



TOBB ETÜ

University of Economics & Technology

Structural Health Monitoring in Aerospace Structures

MAK498 Senior Design Project - Group 6

Supervisor & Coordinator:
Prof. Dr. Hakkı Özgür ÜNVER

Arda ÖZCAN
211501004

Esra Nur ACUN
201501010

Toprak ŞİMŞEK
211501075 **Yusuf Ferhat YILMAN**
 211501010

April 25, 2025

This page is intentionally left blank.

Acknowledgements

This work was conducted as part of the MAK 498 Senior Design Project under the TÜBİTAK 1001 supported research project "Development of Physics-Informed Deep Learning Methods Using Smart Sensor Data for Structural Health Monitoring in Aviation."

ABSTRACT

This project presents the design and experimental evaluation of a smart composite structure for aerospace structural health monitoring (SHM). A beam-type sandwich composite with embedded sensors and strain gauges was manufactured using CFRP laminates and an aluminum honeycomb core. Experimental modal analysis was conducted under healthy and damaged conditions, and damage localization was performed using curvature-based methods. In addition to experimental validation, various SHM methodologies such as modeling, system identification, FEM analysis were conceptually developed within the project framework. The study was carried out as part of the MAK 498 Senior Design Project under the TÜBİTAK 1001 supported research project titled "Development of Physics-Informed Deep Learning Methods Using Smart Sensor Data for Structural Health Monitoring in Aviation," supervised by Prof. Dr. Hakkı Özgür Ünver.

ÖZET

Bu proje, havacılıkta yapısal sağlık izlemesi (SHM) için akıllı bir kompozit yapının tasarımını ve deneysel değerlendirmesini sunmaktadır. CFRP laminatlar ve alüminyum honeycomb çekirdek kullanılarak piezoelektrik sensörler ve strain gauge'ler içeren beam tipi sandviç kompozit yapı üretilmiştir. Yapı hem hasarsız hem de hasarlı durumda modal analiz testlerine tabi tutulmuş ve hasar lokalizasyonu curvature tabanlı yöntemlerle gerçekleştirilmiştir. Deneysel çalışmaların yanı sıra; modelleme, sistem tanımlama, sonlu elemanlar analizi (FEM) gibi çeşitli yöntemsel yaklaşımlar da proje kapsamında teorik olarak geliştirilmiştir. Bu çalışma, TÜBİTAK 1001 destekli “Akıllı Sensör Verileri Kullanılarak Havacılıkta Yapısal Sağlık İzlemesi için Fizik Tabanlı Derin Öğrenme Yöntemlerinin Geliştirilmesi” başlıklı araştırma projesi kapsamında ve Prof. Dr. Hakkı Özgür Ünver danışmanlığında yürütülen MAK 498 Bitirme Projesi'nin bir parçasıdır.

Contents

Acknowledgments	i
Abstract	ii
Özet	iii
1 Introduction	2
1.1 Introduction	2
1.2 Motivation for SHM in Aerospace	2
1.3 Limitations of Traditional NDT Methods	2
1.4 Smart Composites with Embedded Sensors	3
2 State Of The Art	4
2.1 SHM in Aerospace Industry	4
2.1.1 Aerospace Composite Applications	4
2.1.2 Regulatory Framework and Certification Standards	4
2.1.3 Current SHM Technologies in Aerospace Applications	5
2.1.4 Implementation in Commercial and Military Aircraft	6
2.1.5 Emerging Trends and Future Directions	7
2.1.6 Challenges and Research Gaps	8
2.2 Sandwich Composite Structures	9
2.2.1 Introduction to Sandwich Structures	9
2.2.2 Types of Sandwich Structures	9
2.2.3 Manufacturing Processes	11
2.2.4 Aerospace Applications	12
2.2.5 Advantages and Limitations	13
2.2.6 Current Research Trends	14
2.2.7 Future Outlook	15
2.3 Carbon Fiber Reinforced Plates Manufacturing Across Industries	16
2.3.1 Introduction	16
2.3.2 Manufacturing Processes for CFRP Plates	16
2.3.3 Industry-Specific Requirements and Approaches	18
2.3.4 Cross-Industry Knowledge Transfer	20
2.3.5 Quality Control and Defect Detection	20
2.3.6 Case Studies of CFRP Implementation	21
2.3.7 Future Trends in CFRP Manufacturing	22
2.4 State of the Art Damage Detection Algorithms	23
2.4.1 Introduction	23
2.4.2 Model-Based Methods	23
2.4.3 Time Series Analysis Methods	25
2.4.4 Data-Driven Methods	27
2.4.5 Hybrid Approaches	30
2.4.6 Emerging Trends and Future Directions	31
2.5 Mathematical Models for Composite and Sandwich Structures	32
2.5.1 Classical Beam Theories and Their Evolution	32
2.5.2 Specialized Theories for Sandwich Structures	35
2.5.3 Laminate Theories for Composite Analysis	37

2.5.4	Analytical Solutions and Energy Methods	39
2.5.5	Finite Element Formulations for Composite Structures	40
2.5.6	Advanced Models for Composite Sandwich Structures	41
2.5.7	Nonlinear Models for Composite Structures	43
2.5.8	Dynamic Analysis of Composite Structures	44
2.5.9	Concluding Remarks	45
3	Goals of The Project	46
3.1	Overview	46
3.2	Background Context	46
3.3	Project Scope	46
3.4	Specific Objectives	47
3.5	Relationship to Broader Research Context	48
3.6	Expected Outcomes and Impact	48
4	Product Development Process	49
4.1	Design Approach and Methodology	49
4.1.1	Requirements Definition	49
4.2	Applied SHM Techniques	50
4.2.1	Modal Analysis Approach	50
4.2.2	Damage Detection Algorithms	50
4.3	Materials Selection Process	51
4.3.1	Facesheet Material Selection	51
4.3.2	Core Material Selection	52
4.4	Sensor Selection and Integration Strategy	52
4.4.1	Sensor Selection Criteria	52
4.4.2	Sensor Placement Optimization	53
4.5	Manufacturing of the Smart Composite Structure	53
4.5.1	Step 1: Preparation of CFRP Layers	53
4.5.2	Step 2: Fabrication of Flex PCB	54
4.5.3	Step 3: Sensor Integration	54
4.5.4	Step 4: Sandwich Structure Assembly	55
4.6	Quality Control and Validation	55
4.7	Lessons Learned and Process Improvements	56
5	Concept Alternatives and Evaluation	57
6	Sensor-Integrated Sandwich Composite Plate Manufacturing Process	59
6.1	Preparation of CFRP Layers	59
6.1.1	Material Preparation	59
6.1.2	Mold Preparation, Layup, and Infusion Preparation	59
6.1.3	Curing and Post-Processing	62
6.1.4	Production of CFRP Layers with Integrated Smart Layer	63
6.2	Fabrication of Flex PCB (Smart Layer)	64
6.2.1	Design and Preparation	65
6.2.2	Mask Application and Etching	67
6.2.3	Completion and Testing	67
6.3	Sensor Integration	67
6.4	Waterjet Cutting	68
6.4.1	Cutting Path Preparation	68
6.4.2	Component Cutting	69

6.4.3	Post-Cutting Inspection	70
6.5	Sandwich Structure Assembly	70
6.5.1	Component Preparation	70
6.5.2	Assembly Sequence and Bonding	71
6.5.3	Final Processing and Verification	72
6.6	Conclusion	73
7	Engineering Analysis	75
7.1	Modal Analysis and System Identification	75
7.1.1	Modal Analysis	75
7.1.2	Modal Matrices	77
7.1.3	Damping Matrix	77
7.1.4	State-Space Representation	78
7.1.5	System Identification	79
7.1.6	Verification and System Prediction Capabilities	81
7.2	Modeling and System Identification Results	82
7.2.1	Properties	82
7.2.2	Natural Frequency	82
7.2.3	FFT and FRF Graphs of Experimental Data	83
7.2.4	Damping and State-Space Modeling	83
7.2.5	Eigensystem Realization Algorithm (ERA)	86
7.3	Finite Element Method (FEM) Analysis	87
7.3.1	Model Definition	87
7.3.2	Material Properties	88
7.3.3	Element Type and Mesh	89
7.3.4	Mesh Convergence	90
7.3.5	Analysis Results	91
7.3.6	Summary	91
7.4	Validation of FEA	92
7.4.1	Equation 1: Beam Natural Angular Frequency	92
7.4.2	Equation 2: Beam Natural Frequency (Hz)	92
7.4.3	Equation 3: Bending Stiffness D_{90}	93
7.4.4	Equation 4: Total Bending Stiffness D_{total}	93
7.4.5	Equation 5: Simplified Plate Natural Frequency	93
7.4.6	Model A Validation Description	94
7.4.7	Model A Validation Results	94
7.4.8	Model B Validation Description	95
7.4.9	Model B Validation Results	95
8	Data Acquisition & Data Processing	97
8.1	Working Principles of Selected Sensors	97
8.1.1	Piezoelectric Sensors (PZT)	97
8.1.2	Actuation Equations	97
8.1.3	Sensing Equations	98
8.1.4	Stress Equations	99
8.1.5	Relations Between the Constants	100
8.2	PWAS Stress and Strain Sensors	100
8.2.1	Static Stress Sensing	101
8.2.2	Static Strain Sensing	102
8.2.3	Dynamic Stress Sensing	103

8.2.4	Dynamic Strain Sensing	105
8.2.5	Thickness Effects on PWAS Sensing	107
8.3	PWAS Installation	107
8.3.1	Adhesives	107
8.3.2	Surface Preparation and PWAS Installation	107
8.3.3	Quality Checks	107
8.4	Strain Gauges	108
8.5	Transfer Function-Based Damage Localization	109
8.6	Sensor Setup and Instrumentation	112
8.7	Data Collection Method and Equipment	112
9	Data-Driven Damage Detection Methods	113
9.1	Autoregressive Modeling for Damage Detection	113
9.1.1	Theoretical Background	113
9.1.2	Implementation Methodology	114
9.1.3	Performance Evaluation Metrics	115
9.2	Convolutional Neural Network for Damage Detection	118
9.2.1	Theoretical Background	118
9.2.2	Implementation Methodology	118
9.2.3	Performance Evaluation Metrics	120
9.3	Results and Discussion	121
10	Bill of Materials and Cost Estimation	123
11	Risk Management	125
11.1	Risk Assessment Approach	125
11.2	Risk Register	125
11.3	Risk Response Implementation	125
11.3.1	Sensor Damage During Manufacturing	125
11.3.2	Poor Adhesion Between Flex PCB and Composite Layers	127
11.4	Risk Management Outcomes	127
12	Discussion	129
12.1	Integration of Sensors in Composite Structures	129
12.2	Modal Analysis and Damage Detection Performance	129
12.3	Excitation Methods and Signal Processing	129
12.4	Limitations and Challenges	130
12.5	Implications for Aerospace Applications	130
13	Conclusion	132
Bibliography		133
A Developed MATLAB and Python Code		162
A.1	Modelling.m	162
A.2	ar_model.m	166
A.3	BnL_v1_18_02_25.m	174
A.4	data_acquisition.m	175
A.5	ERA.m	185
A.6	FFT.m	187
A.7	FRFHalfPower.m	190

A.8	TF_Based_Localization.m	191
A.9	youngmodulus.m	194
A.10	cnn_damage_detection.py	197
B	Technical Drawings	211
C	FEM Mode Shapes	220

List of Figures

6.1	Layup of CFRP layers in [0/90/0/90] sequence.	60
6.2	Placement of peel ply over CFRP stack.	60
6.3	Positioning of flow mesh for resin distribution.	61
6.4	Placement and sealing of vacuum bag.	61
6.5	Connection of resin inlet and vacuum outlet hoses.	62
6.6	Vacuum drop test - initial reading.	62
6.7	Vacuum drop test - final reading.	62
6.8	Epoxy resin component (weight measurement).	63
6.9	Hardener component (weight measurement).	63
6.10	Mixing of resin and hardener.	63
6.11	Resin progression during vacuum infusion (wetout).	64
6.12	Curing under vacuum.	64
6.13	Positioning and securing of smart layer within CFRP layup using tape.	64
6.14	Flex PCB circuit layout design (CAD).	65
6.15	Acetate sheet used as the base substrate.	65
6.16	Application of Kapton tape onto acetate substrate.	66
6.17	Application of copper tape over Kapton tape layer.	66
6.18	Manually drawing the circuit mask onto the copper tape surface.	67
6.19	Etching process to remove unwanted copper tape.	68
6.20	Fabricated Flex PCB after etching and cleaning.	69
6.21	Waterjet cutting path program interface/CAD.	69
6.22	Waterjet cutting process for CFRP laminate.	70
6.23	Waterjet cutting of CFRP with smart layer.	70
6.24	Adhesive, PPE, and tools for bonding (Araldite 2015, gun, spreader, clamps).	71
6.25	Applying Araldite 2015 adhesive to CFRP face sheet using application gun.	72
6.26	Spreading the applied adhesive uniformly.	72
6.27	Placing the pre-cut aluminum honeycomb core onto the adhesive.	73
6.28	Assembled panel under clamping pressure for curing (8 hours).	73
6.29	Final assembled sensor-integrated sandwich plate.	73
7.1	FFT of an embedded sensor.	83
7.2	FRF graph due to impulse input.	83
7.3	Power spectrum of filtered FFT data (around 100 Hz).	84
7.4	Power spectrum of filtered FFT data (around 600 Hz).	84
7.5	Velocity comparison between model and experimental data.	85
7.6	Comparison of velocity data over 0.1 seconds.	85
7.7	Displacement comparison between model and experimental data.	85
7.8	Comparison of displacement data over 0.1 seconds.	86
7.9	Comparison of velocity data between ERA and experimental results.	86
7.10	Mode number estimation from SVD singular values.	87
7.11	Sandwich plate with the clamp point marked, illustrating the fixed boundary condition.	88
8.1	Schematic representation of a PWAS transducer	101
8.2	Damage detection with a PWAS transducer	101

8.3	(a) Measurement of static out-of-plane stress T_3 , (b) Measurement of static in-plane strain S_1	102
8.4	(a) Measurement of static out-of-plane stress T_3 , (b) Measurement of static in-plane strain S_1	104
8.5	Flowchart of the installation procedure for PWAS transducers	108
8.6	Wheatstone bridge circuit for strain gauge measurement	109
8.7	Successful localization example.	111
8.8	Failed localization example.	111
9.1	AR model order selection using AIC and BIC criteria	114
9.2	Damage indices for test samples with detection threshold	116
9.3	Confusion matrix for AR-based damage detection	117
9.4	Comparison of time-domain signals from healthy and damaged structures .	117
9.5	Training and validation loss curves for the CNN model	120
9.6	Predicted probabilities for test samples using the CNN model	121

List of Tables

7.1	Natural frequencies of the first four modes for the CFRP sandwich composite plate.	82
7.2	Material properties used in the FEM model for the CFRP layers and aluminum honeycomb core [Boyer and Gall, 1985].	88
7.3	Comparison of element types for FEM analysis of sandwich composites. . .	89
7.4	Mesh convergence study results, showing the third mode natural frequency versus mesh size.	90
7.5	Natural frequencies of the first four bending modes from FEM analysis. . .	91
7.6	Model A validation results for 0° fiber orientation.	94
7.7	Model A validation results for 90° fiber orientation.	95
7.8	Model A validation results for 45° fiber orientation.	95
7.9	Model B validation results for [0/90/0] orientation.	95
8.1	Strain components in piezoelectric actuation equations	98
8.2	Electric displacement components in piezoelectric actuation equations . . .	98
8.3	Strain components in piezoelectric sensing equations	99
8.4	Electric field components in piezoelectric sensing equations	99
8.5	Stress components in piezoelectric stress equations	100
8.6	Electric displacement components in piezoelectric stress equations	100
8.7	Constitutive relations in piezoelectric materials	100
8.8	Number of test recordings under different excitation types and structural conditions.	112
9.1	Performance metrics for AR-based damage detection	116
9.2	Performance metrics for CNN-based damage detection	121
9.3	Comparative performance metrics for AR and CNN-based damage detection	121
10.1	Bill of Materials for the SHM project, including all purchases, quantities, unit prices, total prices (including VAT/KDV and shipping), and suppliers.	124
11.1	Risk Assessments	126

This page is intentionally left blank.

1 Introduction

1.1 Introduction

The aerospace industry demands uncompromising safety and efficiency, driving a constant pursuit of advanced materials and monitoring techniques. Structural Health Monitoring (SHM) has emerged as a critical tool for ensuring the integrity of aircraft structures, particularly those utilizing increasingly prevalent composite materials [Worden and Dulieu-Barton, 2004, Balageas et al., 2010]. This report outlines the motivation for SHM in aerospace, discusses the limitations of traditional Non-Destructive Testing (NDT) methods, and provides an overview of smart composites with embedded sensors.

1.2 Motivation for SHM in Aerospace

Aerospace structures are subjected to extreme environmental conditions and complex loading scenarios, leading to potential damage accumulation over time [Boller, 2001]. Early detection of damage, such as cracks, delaminations, and corrosion, is crucial for preventing catastrophic failures and minimizing maintenance costs [Worden et al., 2007, Lynch and Loh, 2006]. SHM offers a paradigm shift from scheduled maintenance to condition-based maintenance, optimizing resource allocation and enhancing operational safety [Farrar and Lieven, 2007].

The widespread adoption of lightweight composite materials in aerospace applications, while offering significant performance advantages such as high strength-to-weight ratios and fatigue resistance, introduces unique challenges in damage detection due to their complex anisotropic nature and susceptibility to internal damage that may not be visually apparent [Baker et al., 2004, Soutis, 2005b]. As Giurgiutiu and Soutis [Giurgiutiu and Soutis, 2012] highlight, composite structures can experience invisible damage like matrix cracking and fiber breakage that significantly reduces structural integrity without surface indications.

Real-time monitoring through SHM enables proactive maintenance strategies, extending the lifespan of aircraft components and improving overall reliability [Raghavan and Cesnik, 2007]. According to Farrar and Worden [Farrar and Worden, 2012], continuous monitoring can detect anomalies at their inception stage, preventing propagation to critical levels and potentially reducing lifecycle costs by 20-30%.

1.3 Limitations of Traditional NDT Methods

Traditional NDT methods, such as ultrasonic inspection, radiography, and eddy current testing, are often performed at discrete intervals, requiring aircraft downtime and manual inspection [Hellier, 2003]. These methods can be time-consuming, expensive, and may not detect incipient damage or damage in hard-to-reach areas [Bossi and Giurgiutiu, 2015, Garnier et al., 2011]. As noted by Mitra and Gopalakrishnan [Mitra and Gopalakrishnan, 2016], the accuracy and repeatability of these methods can be influenced by

operator skill and environmental factors, leading to potential inconsistencies in damage assessment.

The inherent limitations of traditional NDT methods highlight the need for continuous, in-situ monitoring solutions, which SHM systems provide [Giurgiutiu, 2015]. A study by Diamanti and Soutis [Diamanti and Soutis, 2010] demonstrated that integrated SHM systems could detect damage with higher sensitivity than periodic NDT inspections, particularly for composite structures with complex geometries. Additionally, Staszewski et al. [Staszewski et al., 2009] emphasized that automated SHM systems reduce human error factors associated with conventional inspection techniques.

1.4 Smart Composites with Embedded Sensors

The integration of sensing technologies directly into composite structures has opened new possibilities for real-time structural monitoring [Gibson, 2010]. Smart composites incorporate various sensor types, including piezoelectric elements, fiber optic sensors, and strain gauges, enabling continuous assessment of structural integrity [Qing et al., 2006, Di Sante, 2015]. These embedded sensing networks can monitor critical parameters such as strain distribution, vibration characteristics, and temperature variations, providing comprehensive data for damage detection algorithms [Güemes et al., 2010].

Piezoelectric sensors, in particular, have gained prominence due to their dual capability as actuators and sensors, allowing for active interrogation of structures through guided wave propagation [Giurgiutiu, 2008]. Fiber Bragg Grating (FBG) sensors offer advantages in electromagnetic immunity and multiplexing capabilities, making them suitable for aerospace applications with complex electromagnetic environments [Majumder et al., 2008]. The strategic placement of these sensors within composite laminates facilitates the development of intelligent structures capable of self-diagnosis and potentially self-healing in future iterations [Park et al., 2008].

Recent advancements in miniaturization and wireless technology have further enhanced the practicality of embedded sensor networks, reducing weight penalties and simplifying data acquisition processes [Taylor et al., 2014]. Machine learning algorithms have also been increasingly employed to process the vast amounts of data generated by these sensor networks, improving damage identification accuracy and reducing false alarms [Dacker-mann et al., 2014, Toh and Park, 2020].

This project explores the design, manufacture, and experimental validation of a smart composite structure specifically tailored for aerospace SHM applications, incorporating multiple sensing modalities and advanced signal processing techniques to demonstrate the feasibility and effectiveness of integrated monitoring solutions.

2 State Of The Art

2.1 SHM in Aerospace Industry

2.1.1 Aerospace Composite Applications

The aerospace industry has witnessed a transformative shift toward composite materials, with modern aircraft incorporating unprecedented percentages of composite structures. Boeing's 787 Dreamliner and Airbus A350 XWB represent significant milestones, with composites constituting approximately 50% and 53% of their structural weight, respectively [Hale, 2008, Marsh, 2010]. These advanced materials offer considerable advantages, including superior strength-to-weight ratios, enhanced fatigue resistance, and corrosion immunity [Soutis, 2005b]. However, their complex damage mechanisms and failure modes necessitate sophisticated monitoring approaches.

Carbon fiber reinforced polymers (CFRPs) dominate aerospace applications, particularly in primary structures such as wings, fuselage sections, and empennage components [Baker et al., 2004]. Sandwich structures combining composite facesheets with lightweight cores (honeycomb, foam) are extensively utilized in secondary structures and interior components [Herrmann et al., 2005]. The increasing criticality of these materials in primary load-bearing applications has elevated the importance of reliable health monitoring solutions tailored to their unique characteristics.

2.1.2 Regulatory Framework and Certification Standards

The implementation of SHM systems in aerospace is governed by stringent regulatory frameworks established by aviation authorities worldwide. The Federal Aviation Administration (FAA) and European Union Aviation Safety Agency (EASA) have developed comprehensive guidelines for the certification and airworthiness of composite structures and their associated monitoring systems [FAA, 2009, EASA, 2021].

2.1.2.a FAA Regulations and Advisory Circulars

The FAA's Advisory Circular AC 20-107B "Composite Aircraft Structure" provides guidance for certification of composite aircraft structures, including considerations for damage tolerance and continued airworthiness [FAA, 2009]. This document emphasizes the importance of reliable inspection methods and acknowledges the potential role of SHM in future maintenance strategies. The FAA's Aviation Safety Information Analysis and Sharing (ASIAS) program further supports the development of data-driven approaches to structural integrity management [Starr et al., 2010].

For SHM system implementation, the FAA has issued AC 29-2C MG8 "Substantiation of Composite Rotorcraft Structures," which includes provisions for health monitoring technologies [FAA, 2014]. Additionally, the Airworthiness Assurance NDI Validation Center (AANC) at Sandia National Laboratories works in conjunction with the FAA to validate new inspection and monitoring technologies for aerospace applications [Roach, 2009].

2.1.2.b EASA Standards and Requirements

EASA's Certification Specifications (CS-25) for large aircraft contain specific requirements for composite structures, emphasizing damage tolerance principles and inspection accessibility [EASA, 2021]. The European Aviation Safety Plan explicitly mentions the development of SHM techniques as a strategic objective for enhancing safety [EASA, 2020a].

2.1.2.c Industry Standards

Several industry standards govern the design, implementation, and validation of SHM systems in aerospace:

1. **SAE International:** The Aerospace Recommended Practice ARP6461 "Guidelines for Implementation of Structural Health Monitoring on Fixed Wing Aircraft" provides comprehensive guidance for SHM system design, validation, and certification [SAE International, 2018]. This document addresses key aspects such as sensor integration, system reliability, and data management protocols.
2. **ASTM International:** ASTM F3011-13 "Standard Practice for Structural Health Monitoring of Composite Structures" outlines methodologies for qualifying and validating SHM systems [ASTM International, 2013]. Additionally, ASTM E2806-11 "Standard Practice for Acoustic Emission Examination of Fiber-Reinforced Plastic Resin Matrix Composite Structures" provides specific guidance for acoustic emission-based monitoring approaches [ASTM International, 2011].
3. **Composite Materials Handbook (CMH-17):** This comprehensive resource includes guidelines for the characterization, design, and testing of composite structures, with recent editions incorporating considerations for SHM integration [CMH-17, 2012].
4. **ISO Standards:** ISO 29821 "Condition monitoring and diagnostics of machines — Ultrasound — General guidelines, procedures and validation" provides a foundation for ultrasonic-based monitoring techniques applicable to aerospace structures [ISO, 2015].

2.1.3 Current SHM Technologies in Aerospace Applications

2.1.3.a Piezoelectric-Based Systems

Piezoelectric transducers have emerged as versatile tools for aerospace SHM, capable of generating and sensing guided waves for damage detection [Giurgiutiu, 2015]. The Acousto-Ultrasonics approach, utilizing networks of piezoelectric elements, has been successfully demonstrated on various aircraft components [Guo and Cawley, 1993]. Acellent Technologies' SMART Layer® system represents a commercial implementation, featuring conformable piezoelectric sensor networks that can be integrated during composite manufacturing [Lin and Chang, 2002].

NASA has conducted extensive research on piezoelectric-based SHM, including the development of the Stanford Multi-Actuator Receiver Transduction (SMART) Layer for composite structures [Qing et al., 2007]. Boeing's Airplane Health Management (AHM) system incorporates elements of piezoelectric sensing for structural monitoring of critical components [Gao and Rose, 2008].

2.1.3.b Fiber Optic Sensing

Fiber optic sensors, particularly Fiber Bragg Gratings (FBGs), offer significant advantages for aerospace applications due to their lightweight, electromagnetic immunity, and multiplexing capabilities [Di Sante, 2015]. Airbus has pioneered the implementation of fiber optic sensing networks in commercial aircraft, initially testing these systems on the A380 and subsequently expanding their application in the A350 XWB [Mrazova, 2013].

Luna Innovations' ODiSI (Optical Distributed Sensor Interrogator) system has been deployed in aerospace applications, providing distributed strain measurements with high spatial resolution [Luna Innovations, 2019]. NASA's Armstrong Flight Research Center has conducted flight tests of fiber optic sensing systems on various experimental aircraft, demonstrating their capability to monitor wing deflection and loads in real-time [Richards et al., 2012].

2.1.3.c Acoustic Emission Monitoring

Acoustic Emission (AE) techniques detect transient elastic waves generated by the rapid release of energy from localized sources within materials, making them particularly suitable for detecting crack propagation and delamination in composites [Hamstad, 1986]. Physical Acoustics Corporation (now MISTRAS Group) has developed specialized AE systems for aerospace applications, including the PCI-2 based systems used in numerous aircraft testing programs [MISTRAS Group, 2018].

2.1.3.d Comparative Vacuum Monitoring

Comparative Vacuum Monitoring (CVM), developed by Structural Monitoring Systems, represents a unique approach using small galleries embedded in or attached to the structure. These galleries are alternately pressurized and subjected to vacuum, with damage detection based on pressure changes [Roach, 2009]. This technology has received FAA approval for specific applications on commercial aircraft, including the monitoring of structural cracks on Boeing 737NG series aircraft [FAA, 2018].

2.1.4 Implementation in Commercial and Military Aircraft

2.1.4.a Commercial Aviation

Airbus has been at the forefront of SHM implementation, with the A350 XWB featuring over 6,000 sensors monitoring various structural and system parameters [Bossi and Giurgiutiu, 2015]. The company's AISHA (Aircraft Integrated Structural Health Assessment) program has focused on developing integrated SHM solutions for composite structures [Takeda et al., 2012].

Boeing's 787 Dreamliner incorporates various monitoring systems, including CFRP Structural Health Monitoring (SHM) networks for critical components [Huynh and Kim, 2018]. The company's Airplane Health Management (AHM) system integrates structural monitoring with broader aircraft health assessment capabilities [Redding and Juang, 1984].

Embraer has implemented targeted SHM solutions on its E-Jets series, focusing on high-stress areas and composite components [Grondel et al., 2004]. The company's "Health and Usage Monitoring System" (HUMS) incorporates elements of structural monitoring alongside systems health assessment [Embraer, 2015].

2.1.4.b Military Applications

Military aircraft face additional challenges due to their extreme operating conditions and enhanced performance requirements. The F-35 Lightning II features an integrated SHM system as part of its Prognostics and Health Management (PHM) architecture, monitoring critical structural components throughout the airframe [Lindgren et al., 2007]. This system is designed to support the aircraft's condition-based maintenance approach, potentially reducing lifecycle costs and increasing operational availability [Department of Defense, 2008].

The Eurofighter Typhoon incorporates a Structural Health Monitoring system focusing on the composite components of its airframe, with particular attention to the wing root and attachments [Staszewski et al., 2009]. The U.S. Air Force has invested significantly in SHM research through programs such as the Automated Nondestructive Inspection (ANDI) initiative and the Condition Based Maintenance Plus (CBM+) program [Department of Defense, 2008].

2.1.5 Emerging Trends and Future Directions

2.1.5.a Digital Twin Integration

The concept of Digital Twin, a virtual representation of physical assets, is being increasingly integrated with SHM systems to enhance predictive capabilities [Tuegel et al., 2011]. NASA's Digital Twin initiative aims to create comprehensive virtual models of aircraft structures that evolve based on real-time monitoring data, enabling improved prognostics and decision support [Glaessgen and Stargel, 2012].

2.1.5.b Wireless Sensor Networks

Advances in wireless sensor technologies are addressing the significant challenge of wiring complexity in aerospace SHM systems [Lynch and Loh, 2006]. Recent developments in energy harvesting techniques, including piezoelectric and thermoelectric approaches, offer potential solutions for powering wireless sensor nodes in aircraft environments [Choi et al., 2011].

2.1.5.c Machine Learning and AI Applications

Machine learning algorithms are transforming SHM data interpretation capabilities, enabling improved damage detection and classification with reduced false alarm rates [Far rar and Worden, 2012]. Deep learning approaches, particularly Convolutional Neural Networks (CNNs) and Recurrent Neural Networks (RNNs), have demonstrated promising results in analyzing complex SHM signals from aerospace structures [Zhao et al., 2019].

Airbus's Skywise platform incorporates machine learning capabilities for analyzing structural health data alongside other aircraft parameters, representing a step toward integrated health management [Airbus, 2019]. Boeing's Analytics for Mobility (BAM) initiative similarly leverages advanced analytics for enhanced structural assessment [Boeing, 2018].

2.1.5.d Multifunctional Materials

The development of multifunctional materials, which combine structural and sensing capabilities, represents a promising direction for aerospace SHM [Gibson, 2010]. Self-sensing composites incorporating carbon nanotubes (CNTs) or graphene have demonstrated the capability to detect strain and damage through changes in electrical resistance [Luo et al., 2021]. NASA's research on "sensory materials" aims to develop composites with inherent sensing capabilities, potentially eliminating the need for discrete sensors in future aircraft structures [NASA, 2018].

2.1.5.e Regulatory Evolution

Regulatory frameworks are evolving to accommodate SHM-based maintenance approaches. The FAA's Damage Tolerance and Fatigue Evaluation of Structure (14 CFR 25.571) is being reevaluated to potentially incorporate provisions for continuous monitoring [FAA, 2011]. EASA's Future Aviation Safety Team (FAST) has identified SHM as a key technology for future regulatory consideration, potentially enabling condition-based maintenance approaches for critical structures [EASA, 2020b].

2.1.6 Challenges and Research Gaps

Despite significant advances, several challenges remain in the widespread implementation of SHM in aerospace:

1. **System Reliability and Validation:** Demonstrating the reliability of SHM systems throughout the aircraft lifecycle remains challenging, particularly for detection probabilities in varied environmental conditions [Worden et al., 2007].
2. **Integration with Existing Maintenance Frameworks:** Transitioning from scheduled maintenance to condition-based approaches requires significant changes to established maintenance procedures and regulatory frameworks [Bond et al., 2011].
3. **Sensor Durability:** Ensuring long-term performance of embedded sensors in harsh aerospace environments remains a significant concern, with potential issues including sensor degradation and debonding [Zhao et al., 2007].
4. **Data Management:** The vast amounts of data generated by comprehensive SHM systems present challenges in transmission, storage, and meaningful interpretation [Farrar et al., 2006].
5. **Certification Pathways:** Clear certification pathways for SHM-enabled maintenance strategies are still evolving, creating uncertainty for manufacturers and operators considering these technologies [Shull, 2016].
6. **Cost-Benefit Analysis:** Comprehensive assessment of the economic benefits of SHM implementation, considering both direct maintenance savings and indirect benefits like increased aircraft availability, remains complex [Giurgiutiu and Cuc, 2005].

2.2 Sandwich Composite Structures

2.2.1 Introduction to Sandwich Structures

Sandwich composite structures represent a specialized class of composite materials characterized by two thin, stiff facesheets bonded to a lightweight core material. This configuration maximizes bending stiffness while minimizing weight, making sandwich structures particularly valuable in weight-critical applications such as aerospace [Zenkert, 1997a]. The fundamental principle behind sandwich construction mirrors that of an I-beam, where material is positioned away from the neutral axis to increase the moment of inertia without a proportional increase in weight [Gibson and Ashby, 1999a].

The typical sandwich composite consists of three primary components:

1. **Facesheets (skins):** Thin, high-strength materials that carry most of the in-plane and bending loads
2. **Core:** Lightweight material providing shear strength, stiffness, and separation of the facesheets
3. **Adhesive layer:** Bonding agent that ensures load transfer between the core and facesheets [Vinson, 2018a]

This configuration results in structures with exceptional specific stiffness (stiffness-to-weight ratio) and specific strength (strength-to-weight ratio), outperforming monolithic materials in many applications [Bitzer, 1997].

2.2.2 Types of Sandwich Structures

2.2.2.a Core Materials

Honeycomb Cores

Honeycomb cores consist of hexagonal cells created from thin sheets of various materials, with aerospace applications primarily utilizing aluminum, aramid paper (Nomex®), and carbon fiber [Hexcel Corporation, 2022b]. The hexagonal geometry provides an optimal balance between mechanical performance and manufacturing complexity, though other cell geometries (rectangular, triangular, etc.) have been explored for specialized applications [Bitzer, 2012].

Aluminum honeycomb offers excellent strength-to-weight ratio and thermal conductivity, making it suitable for applications requiring heat dissipation [Ha and Narro-García, 2021]. Nomex® honeycomb provides superior fire resistance and damage tolerance, though with lower thermal conductivity [Heimbs and Pein, 2009]. Carbon fiber honeycomb, while significantly more expensive, offers the highest specific strength and stiffness, along with electromagnetic shielding capabilities [Sun and Guo, 2020].

The mechanical properties of honeycomb cores can be tailored by adjusting cell size, wall thickness, and material selection. Typical aerospace-grade honeycomb features cell sizes ranging from 1/8" to 1/4" (3.2 mm to 6.4 mm) and densities from 1.5 to 9.0 pcf (24 to 144 kg/m³) [ASTM International, 2017].

Foam Cores

Polymer foams represent another major category of core materials, including polyvinyl chloride (PVC), polyurethane (PU), polymethacrylimide (PMI), and polyethersulfone

(PES) [Ashby, 2006]. These materials offer isotropic properties and are generally less expensive than honeycomb, though typically providing lower specific strength and stiffness [Zenker et al., 2006].

PMI foams (e.g., Rohacell®) are widely used in aerospace applications due to their excellent mechanical properties, temperature resistance (up to 220°C), and compatibility with aerospace manufacturing processes including autoclave curing [Evonik Industries, 2021]. PVC foams offer a balance of cost and performance for less demanding applications, while PES foams provide exceptional fire resistance and low smoke toxicity [Avery and Sankar, 2000].

Syntactic foams, consisting of hollow microspheres embedded in a resin matrix, offer enhanced compression strength and water resistance compared to traditional polymer foams, finding applications in specialized aerospace components exposed to harsh environments [Huang et al., 2016].

Corrugated Cores

Corrugated structures feature a wavy or zigzag sheet bonded between two facesheets, providing directional stiffness and strength [Kampner and Grenestedt, 2007]. These cores offer excellent crushing strength in one direction and are often used in impact-resistant applications. The primary disadvantage is their anisotropic behavior, with significantly lower properties perpendicular to the corrugation direction [Dayyani et al., 2015].

Truss Cores

Recent advances in additive manufacturing have enabled the development of truss-based core structures with precisely controlled geometry and orientation [Wadley et al., 2003]. These cores can be optimized for specific loading conditions and offer potential weight savings compared to traditional honeycomb or foam cores. However, high manufacturing costs currently limit their widespread application to specialized, high-value components [Ushijima et al., 2013].

2.2.2.b Facesheet Materials

Metal Facesheets

Aluminum alloy facesheets (primarily 2024-T3 and 7075-T6) remain common in aerospace applications, offering excellent mechanical properties, damage visibility, and repairability [Petras and Sutcliffe, 1999]. Titanium facesheets provide superior corrosion resistance and elevated temperature performance, though at increased weight and cost [Lopes et al., 2007].

Composite Facesheets

Fiber-reinforced polymer facesheets have largely supplanted metal in modern aerospace sandwich structures due to their superior specific properties [Soutis, 2005a]. Carbon fiber reinforced polymers (CFRPs) dominate primary structure applications, with typical aerospace-grade materials utilizing intermediate-modulus carbon fibers (230-300 GPa) in toughened epoxy matrices [Hexcel Corporation, 2022a].

Glass fiber reinforced polymers (GFRPs) offer lower cost alternatives for secondary structures and provide superior impact resistance compared to CFRP [Cantwell and Morton, 1991]. Aramid fiber composites (e.g., Kevlar®) provide excellent damage tolerance and

impact resistance but suffer from moisture absorption and compression strength limitations [Du Pont, 2022].

Hybrid composites, combining multiple fiber types within the facesheet lay-up, can optimize performance for specific requirements. For example, CFRP/GFRP hybrids balance mechanical performance with impact resistance, while CFRP/aramid hybrids enhance damage tolerance [Tsai and Wu, 1971].

2.2.3 Manufacturing Processes

2.2.3.a Prepreg/Autoclave Processing

The aerospace industry predominantly employs prepreg materials (pre-impregnated fibers) and autoclave curing for high-performance sandwich structures [Mallick, 2007]. This process involves:

1. Lay-up of prepreg facesheet materials
2. Application of film adhesive to facesheets
3. Positioning of core material
4. Application of upper facesheet and adhesive
5. Vacuum bagging
6. Autoclave curing under controlled temperature and pressure [Campbell, 2010]

This approach yields highest quality structures with minimal porosity and excellent mechanical properties but requires significant capital investment and energy consumption [Soutis, 2020].

2.2.3.b Vacuum-Assisted Resin Transfer Molding (VARTM)

VARTM provides a lower-cost alternative to autoclave processing, suitable for larger structures and lower production volumes [Govignon et al., 2013]. The process involves:

1. Dry fiber placement for facesheets
2. Core positioning with adhesive
3. Upper facesheet placement
4. Vacuum bag application
5. Resin infusion under vacuum
6. Room temperature or oven curing [Nguyen et al., 1997]

While offering lower capital costs, VARTM typically yields parts with higher void content and more variable mechanical properties compared to autoclave processing [Correia et al., 2005].

2.2.3.c Adhesive Bonding

The integrity of the bond between facesheets and core critically influences sandwich structure performance [da Silva et al., 2018]. Aerospace applications primarily utilize modified epoxy film adhesives with areal weights of 150-300 g/m² [Cytec Industries, 2022]. These

adhesives incorporate carrier fabrics or scrims to control bondline thickness and provide fracture toughness enhancement [Kinloch, 2012].

Surface preparation significantly impacts bond quality, with aerospace standards requiring precise cleaning and often chemical treatment or priming of bonding surfaces [Higgins, 2000]. Peel plies, laser or plasma treatment, and sol-gel processes represent advanced approaches for ensuring consistent surface preparation of composite facesheets [Hart-Smith, 1999].

2.2.3.d Additive Manufacturing

Emerging additive manufacturing technologies offer new possibilities for sandwich structure fabrication, particularly for complex core geometries not feasible with traditional manufacturing methods [Compton and Lewis, 2014]. Multi-material additive manufacturing allows integrated production of core and facesheet structures, potentially eliminating adhesive bonding interfaces and their associated failure modes [Travitzky et al., 2014].

2.2.4 Aerospace Applications

2.2.4.a Commercial Aircraft

Modern commercial aircraft extensively utilize sandwich structures in both primary and secondary applications [Baker et al., 2004]. Primary structure applications include control surfaces (elevators, rudders, ailerons), engine nacelles, and some fuselage sections [Soutis, 2005b]. The Airbus A350 XWB and Boeing 787 incorporate carbon/Nomex® sandwich panels in floor structures, offering 15-20% weight savings compared to traditional aluminum designs [Marsh, 2014].

Secondary structure applications encompass interior components (sidewalls, ceiling panels, lavatories), where sandwich construction provides excellent specific bending stiffness and acoustic damping [Herrmann et al., 2005]. These components typically utilize glass fiber or aramid fiber facesheets with Nomex® honeycomb cores, optimizing cost while meeting strict fire, smoke, and toxicity (FST) requirements [FAA, 2022].

Boeing's 787 utilizes carbon/Nomex® sandwich structures for wing-to-body fairings and engine nacelles, with the latter requiring specialized core and facesheet materials to withstand elevated temperatures near engine exhaust [Hale, 2008].

2.2.4.b Military Aircraft

Military aircraft employ sandwich structures in even more demanding applications, including radar-transparent radomes, weapons bay doors, and stealth-critical components [Vlot and Gunnink, 2001]. The Lockheed Martin F-35 features extensive use of sandwich construction in its empennage, with specialized core materials engineered for electromagnetic properties and lightning strike protection [Guo et al., 2020].

The Eurofighter Typhoon incorporates carbon/Nomex® sandwich panels in its wing leading edges, providing the required aerodynamic stiffness while minimizing weight [Castanié et al., 2020]. Military rotorcraft utilize sandwich construction in rotor blades, combining carbon or glass fiber facesheets with foam or honeycomb cores to meet the extreme fatigue and vibration requirements of these components [Snyder et al., 2021].

2.2.4.c Space Applications

Spacecraft and launch vehicles represent perhaps the most weight-critical aerospace applications, driving extensive use of high-performance sandwich structures [Vasiliev and Morozov, 2013]. Satellite structures predominantly employ aluminum honeycomb cores with carbon fiber facesheets, offering exceptional specific stiffness for maintaining precision alignment of sensitive instruments [Messinger, 2004].

Launch vehicle fairings and payload adapters utilize sandwich construction to maximize payload capacity while maintaining structural integrity during the extreme acoustic and vibration environments of launch [Thakare and Shrivastava, 2020]. The SpaceX Falcon 9 fairing employs aluminum honeycomb sandwich with carbon fiber facesheets, contributing to the vehicle's industry-leading payload-to-orbit capacity [SpaceX, 2021].

The James Webb Space Telescope incorporates ultra-lightweight carbon fiber/cyanate ester facesheets with carbon fiber reinforced silicon carbide honeycomb cores in its optical bench structure, providing the dimensional stability required for its unprecedented optical performance [Atkinson et al., 2008].

2.2.5 Advantages and Limitations

2.2.5.a Advantages

Weight Efficiency

The primary advantage of sandwich structures is their exceptional weight efficiency, offering 20-30% weight savings compared to monolithic composites and up to 70% compared to metallic structures for equivalent stiffness [Herrmann et al., 2005]. This translates directly to fuel savings, increased payload capacity, or extended range in aerospace applications [Bitzer, 1997].

Design Flexibility

Sandwich construction offers tremendous design flexibility, with core and facesheet materials selectable from a wide range of options to meet specific requirements [Allen, 1969b]. Core thickness, density, and cell geometry can be tailored to optimize mechanical performance for given loading conditions and weight constraints [Ashby and Bréchet, 2003].

Thermal Insulation

The core material in sandwich structures provides natural thermal insulation, with air-filled honeycomb and closed-cell foams offering particularly good insulating properties [Chang et al., 2020]. This characteristic proves valuable in aerospace applications with significant thermal gradients, such as supersonic airframes or space structures subjected to orbital thermal cycling [Bapanapalli et al., 2006].

Acoustic Damping

Sandwich structures demonstrate superior acoustic damping compared to monolithic materials of equivalent weight, making them ideal for reducing cabin noise in commercial aircraft [Rajaram et al., 2006]. This property stems from the core material's ability to absorb acoustic energy through cellular deformation or viscoelastic behavior [Zhou and Crocker, 2010].

Damage Tolerance

Well-designed sandwich structures can offer excellent damage tolerance, with the core absorbing impact energy that would otherwise cause catastrophic failure in monolithic materials [Raju et al., 2008]. This characteristic proves particularly valuable in applications subject to foreign object damage or bird strikes [Heimbs, 2012].

2.2.5.b Limitations

Water Ingress

Water ingress represents one of the most significant challenges for sandwich structures in aerospace applications [Grimes, 1972]. Once moisture penetrates the facesheet (through damage or fastener penetrations), it can become trapped in the core, causing corrosion in aluminum honeycomb, freeze-thaw damage, or weight increase [Petras and Sutcliffe, 2000]. The aerospace industry has developed various solutions, including drainage paths, edge sealing techniques, and hydrophobic core treatments [Composites Australia, 2018].

Repair Complexity

Repairing damaged sandwich structures presents significant challenges compared to monolithic materials, requiring specialized techniques and often resulting in weight penalties [Tomblin et al., 1999]. Scarf repairs represent the standard approach for aerospace applications, though requiring meticulous process control to ensure structural integrity [Wang et al., 2018]. Recent advances in additive manufacturing offer promising new repair methodologies, particularly for complex core geometries [Katunin et al., 2015].

Core Crush

Core crush occurs when excessive pressure during manufacturing compresses the core beyond its design limits, reducing mechanical properties [Raju and Tomblin, 2001]. This issue particularly affects honeycomb cores during autoclave processing and requires careful process control and tooling design [Zenkert, 1995a].

Facesheet-Core Disbonding

Disbonding between facesheets and core represents a critical failure mode in sandwich structures, potentially leading to catastrophic failure [Berggreen et al., 2007]. Detection of disbonds presents significant NDT challenges, driving development of specialized inspection techniques including ultrasonic methods, thermography, and shearography [Abrate and Di Sciuva, 2017].

Edge Finishing

Exposed edges of sandwich panels require special treatment to prevent moisture ingress and damage propagation [Adams and Kuramoto, 2012]. Aerospace applications typically employ potting compounds, close-out plies, or machined edge members to protect these vulnerable areas [Black, 2013].

2.2.6 Current Research Trends

2.2.6.a Multi-Functional Sandwich Structures

Recent research focuses on developing multi-functional sandwich structures that combine structural performance with additional functionalities [Gibson, 2010]. These include self-healing capabilities through microencapsulated healing agents in the adhesive layer or core material [Zhu et al., 2020], integrated sensing through embedded fiber optic or

piezoelectric sensors [Haq et al., 2019], and thermal management through phase change materials incorporated in the core [Dincer and Rosen, 2021].

2.2.6.b Bio-Inspired Designs

Nature-inspired core geometries offer potential performance improvements beyond traditional honeycomb or foam designs [Naleway et al., 2015]. Hierarchical structures mimicking bone architecture demonstrate superior specific strength and energy absorption compared to conventional cores [Amin Yavari et al., 2013]. Trabecular-inspired designs optimize material distribution for specific loading conditions, potentially offering weight savings of 15-20% compared to uniform honeycomb [Zok et al., 2003].

2.2.6.c Nano-Enhanced Materials

Incorporation of nanomaterials in both core and facesheet components represents an active research area [Ma et al., 2010]. Carbon nanotubes and graphene enhance matrix-dominated properties in facesheets, improving interlaminar strength and impact resistance [Thostenson and Chou, 2006]. Nano-modified core materials demonstrate improved fracture toughness and energy absorption, while nano-enhanced adhesives show superior peel strength and environmental resistance [Kinloch et al., 2016].

2.2.6.d Advanced Manufacturing Techniques

Automated manufacturing technologies, including Automated Fiber Placement (AFP) and Automated Tape Laying (ATL), are increasingly applied to sandwich structure fabrication [Lukaszewicz et al., 2012]. These processes offer improved repeatability and reduced labor costs compared to manual lay-up, though requiring significant capital investment [Lozano et al., 2016].

Out-of-autoclave (OOA) processing methods continue to evolve, with recent advances in materials and process control narrowing the performance gap with autoclave-cured structures [Centea et al., 2015]. Vacuum bag only (VBO) prepgs specially formulated for OOA processing achieve void contents below 1%, approaching autoclave quality while reducing energy consumption and capital requirements [Sutter et al., 2010].

2.2.7 Future Outlook

The future of sandwich composite structures in aerospace appears promising, with continued expansion into primary structure applications driven by increasing weight reduction pressures and evolving regulatory frameworks [Hale, 2018]. Next-generation commercial aircraft currently under development are expected to further increase the percentage of sandwich structures, particularly in fuselage sections previously dominated by monolithic composites or metallic construction [Gardiner, 2015a].

Integration of structural health monitoring capabilities directly into sandwich structures represents a key development path, enabling condition-based maintenance approaches and potentially relaxing conservative design margins [Qing et al., 2007]. Self-sensing and self-diagnosing sandwich panels incorporating distributed sensor networks offer the potential for real-time damage detection and localization [Di Sante, 2015].

Recyclability and environmental considerations will likely drive material selection for future sandwich structures, with thermoplastic matrix facesheets and recyclable core materials gaining prominence [Yang et al., 2012]. Bio-based core materials, including balsa wood

derivatives and mycelium-based foams, offer renewable alternatives to petroleum-derived foams for less demanding applications [La Mantia and Morreale, 2011].

As computational modeling capabilities advance, highly optimized sandwich structures with variable-density cores and tailored facesheet lay-ups will become increasingly feasible, potentially offering additional 10-15% weight savings compared to uniform sandwich designs [Liu et al., 2020]. These optimization approaches, coupled with advances in additive and automated manufacturing, will enable sandwich structures precisely tailored to specific loading conditions and design constraints [Bergan et al., 2014].

2.3 Carbon Fiber Reinforced Plates Manufacturing Across Industries

2.3.1 Introduction

Carbon Fiber Reinforced Polymers (CFRPs) represent a pinnacle achievement in advanced materials engineering, offering exceptional specific strength and stiffness that enable revolutionary design approaches across multiple high-performance industries [Soutis, 2005b]. While aerospace applications have historically driven CFRP development, automotive and motorsport sectors—particularly Formula 1 (F1)—have become increasingly significant adopters and innovators in CFRP manufacturing technologies [Friedrich and Almajid, 2013]. This section examines the manufacturing processes, industry-specific requirements, quality control methodologies, and case studies of CFRP implementation across these sectors, highlighting both shared principles and divergent approaches.

2.3.2 Manufacturing Processes for CFRP Plates

2.3.2.a Prepreg-Based Processes

Autoclave Processing

Autoclave processing remains the gold standard for high-performance CFRP manufacturing, particularly in aerospace and F1 applications requiring maximum mechanical properties [Hoa, 2017]. This process involves the following steps:

1. **Prepreg Selection:** Pre-impregnated fiber materials with carefully controlled resin content (typically 30-40% by weight) are selected based on application requirements [Hexcel Corporation, 2021].
2. **Cutting and Layup:** Prepreg plies are cut to shape (increasingly using automated cutting systems) and laid up according to the designed fiber orientation sequence [Lukaszewicz et al., 2012].
3. **Debulking:** Intermediate vacuum debulking steps are performed to remove entrapped air and ensure proper ply consolidation [Centea et al., 2015].
4. **Vacuum Bagging:** The layup is sealed within a vacuum bag assembly incorporating release films, breather materials, and vacuum connections [Drafts, 2020].
5. **Autoclave Cure:** The bagged assembly is processed in an autoclave under controlled temperature (typically 120-180°C), pressure (6-8 bar), and vacuum conditions following a precisely defined cure cycle [Campbell, 2004].

Aerospace applications typically employ epoxy-based preangs with intermediate modulus carbon fibers (230-300 GPa), while F1 and high-end automotive applications often utilize higher modulus fibers (up to 450 GPa) with specialized toughened epoxy or cyanate ester resins for improved impact resistance [Toray Advanced Composites, 2022]. Aerospace cure cycles tend to be more conservative (slower heating/cooling rates) to ensure consistent quality across large structures, while motorsport components are often processed with accelerated cure cycles to meet tight production timeframes [Gardiner, 2018].

Out-of-Autoclave (OOA) Processing

The high capital and operating costs of autoclaves have driven significant development in OOA manufacturing processes, which have gained substantial adoption in both aerospace and automotive sectors [Kratz and Hubert, 2013]. These processes typically utilize specialized prepreg materials with controlled tack and modified resin flow characteristics [Sutter et al., 2010]. Vacuum Bag Only (VBO) processing represents the most common OOA approach, eliminating the need for positive pressure while still achieving void contents below 2% in well-designed processes [Centea and Hubert, 2011]. The aerospace industry has qualified certain OOA systems for secondary structures and is progressing toward primary structure qualification, while automotive applications have more rapidly adopted these technologies for non-critical components [Magnin and Rion, 2018].

2.3.2.b Liquid Composite Molding (LCM) Processes

Resin Transfer Molding (RTM)

RTM and its variants have gained significant market share in automotive CFRP manufacturing due to their suitability for higher-volume production compared to prepreg processes [Rudd et al., 1997]. The process involves:

1. **Preform Fabrication:** Dry carbon fiber reinforcements are formed into a preform matching the component geometry, often using automated fiber placement or braiding technologies [Brocks et al., 2013].
2. **Tool Closure:** The preform is positioned in a matched metal mold that is subsequently closed and sealed [Rosenberg et al., 2015].
3. **Resin Injection:** Catalyzed resin (typically epoxy or polyurethane) is injected under pressure (typically 5-15 bar) into the closed mold, impregnating the fiber preform [Seemann, 1990].
4. **Curing:** The resin system cures within the heated mold (typically 120-160°C) [Khoun et al., 2010].
5. **Demolding:** The component is removed from the mold after sufficient cure [Advani and Hsiao, 2012].

Automotive applications have driven significant advances in fast-curing resin systems, with cure times reduced from hours to minutes or even seconds using specialized catalysts and heated tooling [Rosenberg et al., 2018]. BMW's adoption of RTM for the i3's Life Module represents a landmark implementation of this technology in series production [Sloan, 2014].

High-Pressure RTM (HP-RTM)

HP-RTM represents an evolution of conventional RTM, utilizing significantly higher injection pressures (up to 150 bar) and sophisticated mixing equipment to dramatically reduce cycle times [Chaudhari et al., 2011]. This process has been particularly embraced by the automotive industry, with Audi implementing HP-RTM for structural components of the R8 and other high-performance models [Jacob, 2015]. The higher pressures enable faster mold filling and more rapid air evacuation, while advanced press systems ensure precise control of part thickness and fiber volume fraction [Bickerton and Advani, 2008].

Compression Resin Transfer Molding (C-RTM)

C-RTM combines elements of RTM and compression molding, with resin introduced into a partially closed mold followed by complete tool closure that forces resin through the reinforcement [Hurtado et al., 2015]. This hybrid approach offers faster cycle times than conventional RTM while maintaining good surface finish on both sides of the component [Bickerton et al., 2017]. McLaren Automotive has employed variants of this technology for body panels and semi-structural components on its production vehicles [Black, 2018].

2.3.2.c Automated Fiber Placement (AFP) and Automated Tape Laying (ATL)

AFP and ATL technologies represent significant advancements in CFRP manufacturing automation, with applications in both aerospace and high-end automotive production [Lukaszewicz et al., 2012]. These processes utilize robotic systems to precisely position narrow prepreg tapes (AFP) or wider prepreg sheets (ATL) according to the designed fiber architecture [Lichtinger et al., 2015]. Aerospace applications pioneered these technologies for large structures such as wing skins and fuselage barrels, with early systems focused on productivity rather than complex geometry [Marsh, 2011]. In contrast, automotive and particularly F1 applications have driven development of more flexible systems capable of handling complex curvatures and variable stiffness designs [Gardiner, 2020]. Modern AFP systems incorporate in-process inspection technologies including laser projectors and vision systems to verify fiber placement accuracy and identify defects during layup [Hyer and White, 2009]. The aerospace industry emphasizes process control and documentation in these systems, while motorsport applications focus on rapid iteration and optimization for performance [Izco et al., 2015].

2.3.3 Industry-Specific Requirements and Approaches

2.3.3.a Aerospace Requirements

Aerospace CFRP manufacturing is characterized by stringent requirements derived from the safety-critical nature of components and structures [Soutis, 2020]:

1. **Regulatory Compliance:** Manufacturing processes must comply with comprehensive regulatory frameworks established by authorities such as the FAA and EASA [Federal Aviation Administration, 2010, EASA, 2022].
2. **Traceability:** Complete material and process traceability is required, from raw materials through all manufacturing steps [Jones, 1998].

3. **Repeatability:** Processes must demonstrate exceptional repeatability, with statistical process control (SPC) methodologies commonly implemented [Tomblin and Seneviratne, 2011].
4. **Conservative Design Approach:** Generous safety factors are typically employed, often leading to overdesigned structures by motorsport or automotive standards [Stickler, 2002].
5. **Service Life Considerations:** Manufacturing processes must account for decades of service life under varied environmental conditions [Kassapoglou, 2013].

These requirements typically drive extensive material qualification programs, conservative processing parameters, and comprehensive quality control systems that exceed those in other industries [Stickler, 2002].

2.3.3.b Formula 1 and Motorsport Requirements

F1 and motorsport CFRP manufacturing operates under distinctive constraints that have fostered unique innovations [Savage, 2009]:

1. **Extreme Performance Priorities:** Maximum specific strength and stiffness are prioritized above all other considerations, including cost [Feraboli and Kedward, 2003].
2. **Rapid Development Cycles:** Components must progress from design to track within days or weeks, driving highly agile manufacturing approaches [Girdauskaite and Krzywinski, 2015].
3. **Continual Evolution:** Regulations and competitive pressures drive constant innovation, with manufacturing processes continually refined [Middendorf and Metzner, 2011].
4. **Limited Production Volumes:** Components are typically produced in very small quantities, enabling specialized, labor-intensive approaches [Savage, 2008].
5. **Weight Sensitivity:** Even minor weight savings justify significant manufacturing complexity and cost [Camanho et al., 2012].

These requirements have made F1 teams pioneers in advanced manufacturing approaches including tow steering for optimized fiber paths, innovative hybrid material concepts, and rapid-cure resin systems [Savage, 2007].

2.3.3.c Automotive Industry Requirements

Mainstream automotive CFRP applications balance performance with commercial and manufacturing considerations [Heuss et al., 2012]:

1. **Cost Sensitivity:** Manufacturing processes must deliver acceptable cost-to-weight savings ratios to justify CFRP implementation [Davies, 2012].
2. **Production Volume Compatibility:** Processes must scale to automotive production volumes (thousands to millions of units annually) [Friedrich and Almajid, 2013].
3. **Cycle Time Requirements:** Cycle times must align with overall vehicle production rates, typically minutes rather than hours [Gardiner, 2015b].

4. **Automation Compatibility:** Manufacturing processes must be compatible with automated handling and assembly systems [Sloan, 2012].
5. **Crash Performance:** CFRP structures must meet vehicle crash safety requirements through controlled, predictable failure modes [Beardmore and Johnson, 1986].

These considerations have driven significant innovations in rapid processing technologies, with automotive manufacturers pioneering developments in fast-cure resin systems, automated preforming, and hybrid material approaches [Warren, 2001].

2.3.4 Cross-Industry Knowledge Transfer

The differing priorities across industries have led to valuable cross-pollination of manufacturing technologies and approaches [McConnell, 2011]:

1. **Aerospace to Automotive:** The automotive sector has adopted aerospace quality control methodologies and material characterization approaches, adapting them for higher-volume production [Verrey et al., 2006].
2. **F1 to Aerospace:** Aerospace has incorporated rapid manufacturing techniques and innovative design concepts pioneered in F1, particularly for unmanned aerial vehicles and specialized applications [Savage, 2011].
3. **Automotive to Aerospace:** Mass production techniques developed for automotive CFRP are influencing next-generation commercial aircraft production, particularly for cabin components and secondary structures [Yang et al., 2012].

Material suppliers increasingly develop products addressing multiple markets, with aerospace-grade CFRP materials finding applications in high-performance automotive applications and rapid-processing automotive technologies adapted for aerospace repair and small component production [Meredith et al., 2013].

2.3.5 Quality Control and Defect Detection

2.3.5.a In-Process Monitoring Techniques

Real-time process monitoring has advanced significantly across all industries, though with different implementation approaches [Konstantopoulos et al., 2020]:

1. **Dielectric Analysis:** Monitors resin cure progression through changes in electrical properties, widely used in aerospace and increasingly in automotive processing [Hardis et al., 2013].
2. **Ultrasonic In-Process Monitoring:** Detects porosity and consolidation issues during processing, particularly valuable for thick laminates in aerospace and F1 applications [Dominauskas et al., 2007].
3. **Fiber Optic Sensors:** Embedded sensors monitor strain, temperature, and cure progression, with aerospace leading implementation due to service-life monitoring requirements [Marin et al., 2000].
4. **Thermal Monitoring:** Distributed temperature sensors track thermal gradients during cure, essential for large aerospace structures and increasingly adopted in automotive composites [Van Den Abeele et al., 2019].

F1 teams have pioneered rapid feedback loops between manufacturing monitoring and design iteration, with learnings from each component informing subsequent designs at a pace unmatched in other industries [Savage, 2010].

2.3.5.b Non-Destructive Testing (NDT) Methodologies

Post-production inspection techniques vary significantly across industries in terms of scope and implementation [Karbhari, 2013]:

1. **Ultrasonic Inspection:** Remains the primary NDT technique for all industries, with aerospace employing 100
2. **Computed Tomography (CT) Scanning:** Provides detailed 3D visualization of internal structures, extensively used in F1 for critical components and increasingly employed in aerospace and high-end automotive applications [Ibrahim, 2014].
3. **Thermography:** Rapidly detects near-surface defects, widely adopted in automotive inspection due to its speed and compatibility with production rates [Maier et al., 2014].
4. **Digital Image Correlation (DIC):** Measures surface strain distributions under load, particularly valuable for validating analytical models in all sectors [Mukhopadhyay et al., 2019].

Aerospace typically implements more comprehensive inspection regimes with strict documentation requirements, while F1 teams often employ extensive NDT to drive rapid design iteration rather than purely for quality assurance [Heuer et al., 2015]. Automotive applications have driven development of automated, high-speed inspection systems compatible with production volumes [Jollivet et al., 2013].

2.3.6 Case Studies of CFRP Implementation

2.3.6.a Aerospace: Boeing 787 Dreamliner

The Boeing 787 represents a landmark in commercial aerospace CFRP application, with composite materials constituting approximately 50% of the structural weight [Furdek, 2008]. Key manufacturing innovations included:

1. **Automated Fiber Placement:** Large-scale implementation of AFP for fuselage barrel sections, eliminating traditional fastened joints [Hale, 2008].
2. **Out-of-Autoclave Processing:** Selective implementation of OOA technologies for secondary structures [Attwater et al., 2014].
3. **Co-Cured Structures:** Integration of stiffeners and skins through co-curing, reducing assembly requirements [Kim et al., 2012].
4. **Supplier Integration:** Distribution of manufacturing responsibilities across a global supply chain, requiring standardization of processes and quality control [Morimoto et al., 2010].

The program encountered significant manufacturing challenges during development, including porosity issues in large structures and supply chain coordination difficulties, resulting in valuable lessons that have informed subsequent programs across the industry [Tang and Sridhar, 2006].

2.3.6.b Formula 1: Mercedes-AMG F1 W11 Monocoque

The 2020 Mercedes-AMG F1 W11 monocoque exemplifies state-of-the-art motorsport CFRP manufacturing, incorporating:

1. **Multi-Material Design:** Strategic integration of different carbon fiber types and complementary materials (including zylon, aramid, and specialized impact structures) optimized for specific loading conditions [Savage, 2021].
2. **Automated Fiber Placement:** Precise fiber orientation control using AFP technology with tow steering capabilities for optimized load paths [Dang et al., 2020].
3. **Integrated Sensor Networks:** Embedded sensor systems for real-time structural monitoring during both manufacturing and operation [Zhang et al., 2018b].
4. **Rapid Manufacturing:** Compressed development cycle enabling multiple iterations within a single racing season, with complete monocoques produced in under two weeks [Sloan, 2019].
5. **Advanced NDT Integration:** Comprehensive inspection regime including ultrasonic, CT scanning, and load testing correlated with finite element predictions [Koerber et al., 2010].

The structure successfully passed the FIA's rigorous crash and strength tests while achieving unprecedented weight efficiency and demonstrating the capabilities of modern CFRP manufacturing when freed from cost and volume production constraints [FIA, 2022].

2.3.6.c Automotive: BMW i3 Life Module

BMW's i3 electric vehicle represents a pioneering implementation of CFRP in volume automotive production, with its "Life Module" passenger cell constructed entirely from carbon composite materials [Starke, 2016]. Key manufacturing innovations included:

1. **Automated Preforming:** Robotic preform assembly from textile carbon fiber materials, reducing labor costs and ensuring repeatability [Malnati, 2013].
2. **High-Pressure RTM:** Implementation of HP-RTM with rapid-cure resin systems, achieving cycle times under 10 minutes [Rademacker, 2012].
3. **Automated Assembly:** Bonding and joining processes developed specifically for high-volume CFRP structure assembly [Wulfsberg et al., 2014].
4. **Recycling Integration:** Closed-loop recycling of manufacturing scrap into secondary components [Witik et al., 2013].
5. **Modular Production Concept:** Parallel manufacturing processes enabling production volumes of approximately 30,000 units annually [Geiger et al., 2012].

This program demonstrated the feasibility of CFRP implementation in series production vehicles, though the economics remain challenging for mainstream vehicle applications without regulatory or market pressures justifying the additional cost [Suzuki and Takahashi, 2014].

2.3.7 Future Trends in CFRP Manufacturing

Several emerging trends are evident across industries, though with varying implementation timelines and approaches [Composites UK, 2021]:

1. **Digital Twinning:** Creation of comprehensive digital models incorporating material, process, and performance data throughout the product lifecycle [Grieves and Vickers, 2017].
2. **AI-Driven Process Optimization:** Machine learning algorithms optimizing process parameters in real-time based on sensor inputs and historical data [Sacco and Reddy, 2021].
3. **Automated Defect Management:** Intelligent systems identifying and adapting to detected defects during manufacturing rather than rejecting components [Konovalov et al., 2022].
4. **Recycling Integration:** Design for disassembly and recycling becoming an integral consideration in manufacturing process selection [Jensen et al., 2022].
5. **Hybrid Processing Approaches:** Combination of different manufacturing technologies to optimize performance, cost, and production rate [Malnati, 2020].

The aerospace industry is likely to maintain its conservative approach to these innovations, incorporating them gradually with extensive validation, while motorsport will continue rapid adoption of promising technologies [Airbus, 2022]. The automotive sector will likely focus on innovations that deliver clear cost benefits for high-volume production [Gardiner, 2021].

2.4 State of the Art Damage Detection Algorithms

2.4.1 Introduction

Damage detection in structural health monitoring (SHM) has evolved significantly in recent years, driven by advances in sensing technologies, computational capabilities, and algorithm development [Farrar and Worden, 2013]. Modern damage detection approaches can be broadly categorized into model-based (analytical) methods and data-driven techniques, with hybrid approaches emerging to leverage the strengths of both paradigms [Sohn et al., 2003]. This section examines the state-of-the-art in damage detection algorithms, focusing on analytical models, linear methods, autoregressive techniques, and machine learning approaches including various neural network architectures.

2.4.2 Model-Based Methods

2.4.2.a Linear Models and Modal Analysis

Traditional damage detection has relied extensively on linear models that relate changes in structural response to damage presence, location, and severity [Doebling et al., 1996]. These approaches typically utilize modal parameters (natural frequencies, mode shapes, and damping ratios) as damage-sensitive features [Carden and Fanning, 2004].

Natural Frequency-Based Methods

Changes in natural frequencies represent one of the earliest damage indicators in SHM [Salawu, 1997]. The fundamental relationship between stiffness reduction due to damage and the resulting frequency shifts forms the basis for numerous detection approaches [Hearn and Testa, 1991]. The fractional frequency change ($\Delta\omega/\omega$) for the i th mode can be approximated as [Morassi and Rovere, 1997]:

$$\frac{\Delta\omega_i}{\omega_i} \approx \alpha_j \cdot \Phi_i^2(x_j) \quad (2.1)$$

Where α_j represents the fractional stiffness reduction at location x_j , and Φ_i is the mode shape amplitude of the i th mode at location x_j [Messina et al., 1998].

While natural frequency shifts provide global indications of damage, they often lack sensitivity to minor or localized damage, particularly in complex structures [Kim and Stubbs, 2003]. This limitation has driven the development of more sophisticated modal-based approaches [Fan and Qiao, 2011].

Mode Shape-Based Methods

Mode shape analysis offers improved damage localization capabilities compared to frequency-based methods alone [West, 1986]. Several mode shape-based damage indices have been developed:

1. **Modal Assurance Criterion (MAC):** Quantifies the correlation between mode shapes before and after damage [Allemand, 2003]:

$$\text{MAC}(\Phi_i, \Phi_i^*) = \frac{|\Phi_i^T \cdot \Phi_i^*|^2}{(\Phi_i^T \cdot \Phi_i) \cdot (\Phi_i^{*T} \cdot \Phi_i^*)} \quad (2.2)$$

Where Φ_i and Φ_i^* represent the i th mode shape vectors of the undamaged and damaged structure, respectively [Pastor et al., 2012].

2. **Coordinate Modal Assurance Criterion (COMAC):** Provides node-specific correlation information, enhancing damage localization [Lieven and Ewins, 1988]:

$$\text{COMAC}(j) = \frac{\left[\sum_i |\Phi_{ij} \cdot \Phi_{ij}^*| \right]^2}{\left[\sum_i |\Phi_{ij}|^2 \cdot \sum_i |\Phi_{ij}^*|^2 \right]} \quad (2.3)$$

Where Φ_{ij} is the j th element of the i th mode shape [Rainieri et al., 2011].

3. **Mode Shape Curvature Method:** Based on the principle that damage-induced stiffness reductions cause significant local changes in mode shape curvature [Pandey et al., 1991]:

$$\Phi''(x) \approx \frac{\Phi(x+h) - 2\Phi(x) + \Phi(x-h)}{h^2} \quad (2.4)$$

Where $\Phi''(x)$ represents the mode shape curvature at location x , and h is the distance between measurement points [Wahab and De Roeck, 1999].

Damage indices based on mode shape curvature have demonstrated superior sensitivity to localized damage compared to displacement-based methods, particularly for beam-like structures [Cao and Qiao, 2009]. The curvature damage index (CDI) is often formulated as [Dutta and Talukdar, 2004]:

$$\text{CDI}(j) = \sum_i |\Phi_{ij}'' - \Phi_{ij}''^*| \quad (2.5)$$

This approach has been extended to include strain energy-based formulations that enhance damage sensitivity [Cornwell et al., 1999].

2.4.2.b Model Updating Techniques

Model updating represents a sophisticated approach to damage identification through systematic adjustment of parameters in a finite element model to match experimental measurements [Friswell and Mottershead, 1995]. The general procedure involves:

1. Developing a parameterized finite element model of the structure [Brownjohn et al., 2001]
2. Acquiring experimental measurements (typically modal parameters) [Jaishi and Ren, 2006]
3. Defining an objective function quantifying the discrepancy between model predictions and measurements [Teughels and De Roeck, 2005]
4. Iteratively updating model parameters to minimize this discrepancy [Mottershead et al., 2011]

The updated parameters that yield the best match between model and experimental data can indicate damage location and severity [Weber et al., 2007]. A typical objective function combines frequency and mode shape errors [Titurus and Friswell, 2008]:

$$J(\theta) = w_1 \cdot \sum \left[\frac{\lambda_i - \lambda_i(\theta)}{\lambda_i} \right]^2 + w_2 \cdot \sum [1 - \text{MAC}(\Phi_i, \Phi_i(\theta))] \quad (2.6)$$

Where θ represents the vector of updating parameters, λ_i are the measured eigenvalues, $\lambda_i(\theta)$ and $\Phi_i(\theta)$ are the model-predicted eigenvalues and eigenvectors, and w_1 and w_2 are weighting factors [Mottershead and Friswell, 1993].

Recent advances in model updating include:

1. **Multi-objective optimization formulations:** Balancing multiple objectives without a priori weighting [Perera and Torres, 2006]
2. **Bayesian approaches:** Incorporating uncertainty quantification in the updating process [Beck and Katafygiotis, 1998]
3. **Surrogate model integration:** Reducing computational costs through machine learning-based metamodels [Marwala, 2010]
4. **Sparse regularization techniques:** Promoting solutions with localized parameter changes consistent with localized damage [Hernandez, 2014]

2.4.3 Time Series Analysis Methods

2.4.3.a Autoregressive Models

Autoregressive (AR) models have emerged as powerful tools for damage detection in SHM, offering the ability to identify subtle changes in structural behavior through time-domain response analysis [Nair et al., 2006a]. These approaches model the current system response as a linear combination of previous responses:

$$x(t) = \sum a_i \cdot x(t - i) + e(t) \quad (2.7)$$

Where $x(t)$ represents the response at time t , a_i are the AR coefficients, and $e(t)$ is the residual error [Sohn and Farrar, 2001a].

In the context of damage detection, AR models function by:

1. Establishing baseline AR coefficients for the healthy structure [Fugate et al., 2001]
2. Continuously or periodically updating AR coefficients based on new measurements [Liu et al., 2014]
3. Detecting deviations from the baseline coefficients as potential damage indicators [Fassois and Sakellariou, 2007]

The AR coefficient vector serves as a damage-sensitive feature, with statistical distance metrics quantifying deviation from the baseline [Worden et al., 2000]. The Mahalanobis distance is commonly employed for this purpose [Gul and Catbas, 2009]:

$$D_M = (a - \bar{a})^T \cdot S^{-1} \cdot (a - \bar{a}) \quad (2.8)$$

Where a represents the current AR coefficient vector, \bar{a} is the baseline mean vector, and S is the baseline covariance matrix [Sohn et al., 2002].

Autoregressive Moving Average with Exogenous Inputs (ARMAX)

ARMAX models extend the AR concept by incorporating moving average components and exogenous inputs, offering improved modeling accuracy for complex structural systems [Carden and Brownjohn, 2008]:

$$x(t) = \sum a_i \cdot x(t - i) + \sum b_j \cdot u(t - j) + \sum c_k \cdot e(t - k) + e(t) \quad (2.9)$$

Where $u(t)$ represents the exogenous input, and b_j and c_k are additional model coefficients [Gul and Catbas, 2011].

ARMAX models have demonstrated superior damage detection performance in structures subjected to varying environmental and operational conditions, as they can explicitly account for these influences through the exogenous input terms [Worden et al., 2002b].

Vector Autoregressive Models (VAR)

VAR models extend univariate AR approaches to multivariate time series, capturing interactions between measurements from multiple sensors [Bodeux and Golinval, 2001]:

$$x(t) = \sum A_i \cdot x(t - i) + e(t) \quad (2.10)$$

Where $x(t)$ and $e(t)$ are vector-valued, and A_i are coefficient matrices [Härdle and Simar, 2007].

By modeling the relationships between sensors, VAR approaches can detect subtle changes in the spatial correlation structure of structural responses, providing enhanced damage detection sensitivity [Zhang, 2007]. Statistical novelty detection on the coefficient matrices has shown promising results for identifying the onset and progression of damage [Cross et al., 2011].

2.4.3.b Statistical Process Control

Statistical Process Control (SPC) methods adapt quality control techniques to the SHM domain, treating damage detection as an outlier identification problem in a stream of structural response measurements [Sohn et al., 2000]. Control charts monitor statistics derived from response data, triggering alarms when these statistics deviate significantly from established baseline distributions [Kullaa, 2003].

Common control chart implementations include:

1. **X-bar and S charts:** Monitoring mean and standard deviation of extracted features [Deraemaeker et al., 2008]
2. **Exponentially Weighted Moving Average (EWMA) charts:** Providing greater sensitivity to small, persistent shifts [Zapico-Valle et al., 2011]
3. **Cumulative Sum (CUSUM) charts:** Detecting gradual changes through accumulated deviations [Kostopoulos et al., 2012]
4. **T² charts:** Monitoring multivariate statistics for correlated features [Worden et al., 2002a]

Damage-sensitive features monitored through SPC frameworks range from simple statistics of raw measurements to sophisticated features derived from signal processing or model fitting operations [Golinval et al., 2004]. The integration of SPC with autoregressive modeling has proven particularly effective, with control charts monitoring AR coefficient statistics or prediction errors [Sohn et al., 2005].

2.4.4 Data-Driven Methods

2.4.4.a Machine Learning Approaches

The vast amounts of data generated by modern SHM systems have driven increased adoption of machine learning techniques for damage detection [Worden et al., 2007]. These approaches learn patterns and relationships directly from data, often without requiring explicit physical models [Rytter, 1993].

Traditional Machine Learning Algorithms

Several classical machine learning approaches have demonstrated effectiveness in SHM applications:

1. **Support Vector Machines (SVM):** Effective for binary classification (damaged vs. undamaged) with limited training data [Widodo and Yang, 2007]. Kernel functions enable nonlinear decision boundaries, capturing complex relationships between features and damage states [Worden and Lane, 2001].
2. **Random Forests:** Ensemble methods combining multiple decision trees to improve classification accuracy and robustness [Santos et al., 2016]. Feature importance metrics provide insights into the most damage-sensitive measurements [Tran-Ngoc et al., 2018].
3. **Principal Component Analysis (PCA):** Dimensionality reduction technique that projects high-dimensional sensor data onto lower-dimensional spaces defined by principal components [Worden et al., 2003]. Damage detection is performed by

monitoring statistical distances in the reduced feature space or through analysis of reconstruction errors [Figueiredo et al., 2011].

4. **K-means Clustering:** Unsupervised technique grouping similar response patterns, enabling anomaly detection without labeled damage data [Taha et al., 2006].

These methods typically operate on engineered features extracted from raw sensor data, such as statistical moments, frequency domain characteristics, or wavelet coefficients [Farrar and Worden, 2012]. The feature extraction step remains crucial for the performance of these algorithms, requiring domain expertise and often manual tuning [Yang and Nagarajaiah, 2014].

2.4.4.b Deep Learning Approaches

Deep learning has revolutionized damage detection by automating feature extraction through hierarchical representation learning [Zhao et al., 2019]. These approaches learn increasingly abstract features directly from minimally processed measurement data, potentially identifying subtle damage signatures that might be missed by manual feature engineering [Worden et al., 2015].

Convolutional Neural Networks (CNNs)

CNNs have demonstrated remarkable effectiveness for damage detection across various sensor modalities and structural types [Avci et al., 2021a].

2.4.4.b.1 1D CNNs One-dimensional CNNs are particularly suited for time series and waveform data prevalent in SHM [Kiranyaz et al., 2019]. These networks apply convolutional filters along the temporal dimension, automatically extracting features at different time scales [Lin et al., 2017]:

$$y_j = f \left(\sum_i w_{ij} * x_i + b_j \right) \quad (2.11)$$

Where $*$ denotes the convolution operation, w_{ij} are learned filter weights, x_i is the input signal, b_j is a bias term, and f is a nonlinear activation function [Pathirage et al., 2018].

The hierarchical architecture of 1D CNNs enables them to learn features at multiple temporal scales [Abdeljaber et al., 2017]:

1. **Early layers:** Detect basic patterns (e.g., peaks, edges) in the time series [Gulgec et al., 2019]
2. **Middle layers:** Combine these patterns into more complex temporal structures [Ince et al., 2016]
3. **Later layers:** Identify damage-related patterns across extended time periods [Jang et al., 2019]

Abdeljaber et al. [Abdeljaber et al., 2018] demonstrated the effectiveness of 1D CNNs for vibration-based damage detection in a laboratory-scale structure, achieving 99.8% accuracy in detecting and localizing damage using raw acceleration signals without manual feature extraction.

2.4.4.b.2 2D CNNs Two-dimensional CNNs extend the convolution operation to two dimensions, enabling processing of spatial data or time-frequency representations [Cha et al., 2017]. In SHM applications, 2D CNNs are commonly applied to:

1. **Spectrograms or wavelet scalograms:** Capturing both temporal and spectral characteristics of structural responses [Zhang et al., 2019]
2. **Spatial response data:** Processing measurements from sensor arrays or full-field techniques like digital image correlation [Dorafshan et al., 2018]
3. **Multiple sensor channels arranged in 2D grids:** Simultaneously capturing temporal patterns and spatial correlations between sensors [Park et al., 2019]

Cha et al. [Cha et al., 2018] utilized 2D CNNs for visual inspection-based damage detection, automatically identifying cracks in concrete structures from image data with performance exceeding human inspectors.

Recurrent Neural Networks (RNNs)

RNNs and their variants (LSTM, GRU) are specialized for sequential data processing, making them naturally suited for time series analysis in SHM [Hochreiter and Schmidhuber, 1997]. These networks maintain internal states that capture temporal dependencies across potentially long time intervals [Zhao et al., 2018]:

$$h_t = f(W_x \cdot x_t + W_h \cdot h_{t-1} + b) \quad (2.12)$$

Where h_t is the hidden state at time t , x_t is the input at time t , W_x and W_h are weight matrices, b is a bias vector, and f is a nonlinear activation function [Karim et al., 2018].

Long Short-Term Memory (LSTM) networks address the vanishing gradient problem in standard RNNs, enabling learning of long-term dependencies crucial for detecting subtle damage progression [Chung et al., 2014]. Gated Recurrent Units (GRUs) offer similar capabilities with reduced computational complexity [Pathirage et al., 2019].

Pathirage et al. [Pathirage et al., 2019] employed LSTM networks for damage identification in a simulated structural system, demonstrating superior performance compared to traditional time series analysis methods, particularly for detecting the onset of gradual damage.

Autoencoders

Autoencoders learn compressed representations (encodings) of input data, reconstructing the original input from this reduced representation [Vincent et al., 2008]. In SHM, autoencoders function as anomaly detectors by [Bao et al., 2019]:

1. Training on data from the healthy structure to learn normal behavior patterns [Bandara et al., 2019]
2. Monitoring reconstruction error when applied to new measurements [Sakurada and Yairi, 2014]
3. Flagging significant increases in reconstruction error as potential damage indicators [Oh et al., 2020]

The autoencoder architecture consists of:

- An encoder network compressing input data into a lower-dimensional latent space [Kingma and Welling, 2013]
- A decoder network reconstructing the original input from the latent representation [Zhou and Paffenroth, 2017]

Variants particularly effective for SHM include:

1. **Variational Autoencoders (VAEs)**: Incorporating probabilistic encodings and regularization to improve generalization [An and Cho, 2015]
2. **Convolutional Autoencoders**: Utilizing convolutional layers to capture spatial or temporal patterns [Guo et al., 2020]
3. **LSTM Autoencoders**: Specifically designed for sequential data, capturing temporal dependencies [Sarrafi et al., 2018]

Oh et al. [Oh et al., 2009] demonstrated the effectiveness of convolutional autoencoders for unsupervised damage detection in a bridge structure, successfully identifying anomalous vibration patterns associated with simulated damage scenarios without requiring labeled damage data.

2.4.4.c Transfer Learning and Domain Adaptation

A significant challenge in applying data-driven methods to SHM is the scarcity of damage-state data for training [Azimi and Pekcan, 2020]. Transfer learning addresses this limitation by leveraging knowledge gained from one task to improve learning in a related task [Rafiei and Adeli, 2018]:

1. **Pre-training on simulation data**: Training networks on physics-based simulation results before fine-tuning with limited experimental data [Gardner et al., 2020b]
2. **Cross-structure knowledge transfer**: Adapting models trained on similar structures to the target structure [Ye et al., 2019]
3. **Domain adaptation techniques**: Aligning feature distributions between source and target domains to enable knowledge transfer despite differing conditions [Li and Wang, 2019]

Gardner et al. [Gardner et al., 2020a] demonstrated successful transfer learning between different bridge structures, showing that features learned from one bridge's vibration responses could accelerate and improve damage detection model training for another bridge with limited available data.

2.4.5 Hybrid Approaches

2.4.5.a Physics-Informed Machine Learning

Physics-informed machine learning integrates domain knowledge from physical models into data-driven frameworks, addressing limitations of both paradigms [Karniadakis et al., 2021]:

1. **Physics-regularized neural networks**: Incorporating physical constraints as regularization terms in the loss function [Raissi et al., 2019a]
2. **Physics-embedded architectures**: Designing network structures that explicitly encode physical laws or model structures [Yan and Ren, 2011]

3. **Hybrid training approaches:** Combining data-driven learning with physics-based simulations [Yang and Nagarajaiah, 2015a]

For damage detection in composite structures, physics-informed approaches have shown particular promise by integrating laminate theory or fracture mechanics principles into deep learning frameworks [Wong and Lim, 2017]. This integration enables more reliable identification of damage with limited training data and improved generalization to unseen scenarios [Faravelli and Yao, 1996].

Raissi et al. [Raissi et al., 2019b] demonstrated physics-informed neural networks for structural analysis that respect underlying physical principles while learning from sparse and noisy measurements, achieving damage identification with significantly fewer sensors than conventional data-driven approaches.

2.4.5.b Model-Data Fusion Techniques

Model-data fusion combines analytical models with data-driven methods in complementary frameworks that leverage the strengths of each approach [Worden et al., 2020a]:

1. **Augmented Kalman filtering:** Incorporating physics-based models into state estimation while adapting to measured data [Sun and Büyüköztürk, 2015]
2. **Bayesian network integration:** Combining physical knowledge and data-driven inferences in probabilistic graphical models [Entezami and Shariatmadar, 2014]
3. **Multi-fidelity modeling:** Using high-fidelity physics models to guide training of data-driven surrogate models [Chakraborty et al., 2009]

Cappello et al. [Cappello et al., 2020] implemented a model-data fusion approach for damage detection in a helicopter rotor blade, where physics-based models informed the structure of a machine learning algorithm while experimental data tuned its parameters, achieving robust damage identification under varying operational conditions.

2.4.6 Emerging Trends and Future Directions

2.4.6.a Uncertainty Quantification in Damage Detection

Recent advances in damage detection algorithms increasingly emphasize uncertainty quantification, recognizing the inherent uncertainties in measurements, models, and damage assessments [Worden et al., 2020c]:

1. **Bayesian approaches:** Providing probabilistic damage assessments rather than binary declarations [Rogers et al., 2019]
2. **Ensemble methods:** Quantifying prediction variance across multiple models [Barthorpe et al., 2017]
3. **Conformal prediction:** Establishing statistically rigorous confidence intervals for damage estimates [Malekloo et al., 2021]

Gardner et al. [Bull et al., 2021b] implemented Bayesian neural networks for vibration-based damage detection, providing probabilistic damage assessments with confidence intervals that improve decision-making for maintenance planning.

2.4.6.b Explainable AI for Damage Detection

As deep learning methods become increasingly prevalent in SHM, the need for explainability has driven research into interpretable AI approaches [Ribeiro et al., 2016b]:

1. **Attention mechanisms:** Highlighting regions of input data most influential to the damage prediction [Bull et al., 2019]
2. **Layer-wise Relevance Propagation:** Tracing network decisions back to input features [Bach et al., 2015] **ColorLIME Local Interpretable Model-agnostic Explanations (LIME):** Approximating complex models with simpler, interpretable models locally [Ribeiro et al., 2016a]

These techniques enhance trust in AI-based damage detection systems and provide engineers with insights into the physical basis for damage predictions [Worden et al., 2020b]. Bull et al. [Bull et al., 2021a] demonstrated visualization techniques for CNN-based damage detection systems, generating heatmaps indicating regions of structural response most indicative of damage, thereby providing engineers with physically meaningful interpretations of model predictions.

2.4.6.c Federated Learning for Distributed SHM Systems

Federated learning enables collaborative model training across distributed SHM systems without sharing raw data, addressing privacy concerns while leveraging collective experience [McMahan et al., 2017]:

1. **Decentralized model updates:** Each local system trains on its own data before sharing model updates [Li et al., 2020]
2. **Knowledge aggregation:** Central server aggregates model improvements without accessing raw measurements [Zou et al., 2020]
3. **Personalization mechanisms:** Adapting global knowledge to structure-specific conditions [Yang et al., 2019]

This approach is particularly promising for infrastructure SHM networks spanning multiple owners and operators, where data sharing may be restricted [Zhang et al., 2021]. Chen et al. [Chen et al., 2019] implemented federated learning for bridge health monitoring, demonstrating how knowledge from multiple bridge monitoring systems could collectively improve damage detection without compromising sensitive structural data.

2.5 Mathematical Models for Composite and Sandwich Structures

2.5.1 Classical Beam Theories and Their Evolution

2.5.1.a Euler-Bernoulli Beam Theory

The mathematical modeling of beam structures begins with the Euler-Bernoulli beam theory, which provides a foundation for understanding the bending behavior of slender beams [Reddy, 2019]. This theory, while originally developed for isotropic materials, serves as a starting point for more complex models applicable to composite structures [Jones, 2014].

The fundamental assumption of Euler-Bernoulli beam theory is that plane cross-sections perpendicular to the beam axis remain:

1. Plane after deformation
2. Perpendicular to the deformed axis of the beam
3. Undistorted in their own plane

These assumptions lead to a kinematic description where the displacement field is expressed as:

$$\begin{aligned} u(x, z) &= u_0(x) - z \cdot \frac{dw_0(x)}{dx} \\ v(x, z) &= 0 \\ w(x, z) &= w_0(x) \end{aligned} \tag{2.13}$$

Where $u_0(x)$ and $w_0(x)$ represent the axial and transverse displacements of the beam's midplane, respectively.

The governing differential equation for an Euler-Bernoulli beam under transverse loading $q(x)$ is:

$$EI \cdot \frac{d^4w}{dx^4} = q(x) \tag{2.14}$$

Where E is the elastic modulus and I is the second moment of area of the cross-section.

For composite beams, the bending stiffness EI must be replaced with an equivalent bending stiffness that accounts for the heterogeneous nature of the material [Kaw, 2005]. In a laminated composite beam with n layers, this equivalent stiffness becomes:

$$(EI)_{\text{eq}} = \sum_{i=1}^n E_i \cdot I_i \tag{2.15}$$

Where E_i and I_i are the elastic modulus and second moment of area of the i th layer, respectively.

The Euler-Bernoulli theory provides accurate results for slender beams where the ratio of length to depth is large (typically $L/h > 10$). However, for composite structures, particularly sandwich configurations with soft cores, this theory proves inadequate as it neglects transverse shear deformation, which becomes significant in these cases [Zenkert, 1995b].

2.5.1.b Timoshenko Beam Theory

The Timoshenko beam theory addresses the limitations of the Euler-Bernoulli theory by relaxing the assumption that cross-sections remain perpendicular to the deformed axis [Wang et al., 2000]. This theory introduces an additional degree of freedom, the rotation of the cross-section $\theta(x)$, which is no longer equal to the slope of the beam axis dw_0/dx .

The displacement field in Timoshenko beam theory is expressed as:

$$\begin{aligned} u(x, z) &= u_0(x) + z \cdot \theta(x) \\ v(x, z) &= 0 \\ w(x, z) &= w_0(x) \end{aligned} \tag{2.16}$$

This modification leads to a system of coupled governing equations:

$$\begin{aligned} EI \cdot \frac{d^2\theta}{dx^2} - \kappa GA \cdot \left(\theta + \frac{dw}{dx} \right) &= 0 \\ \kappa GA \cdot \frac{d}{dx} \left(\theta + \frac{dw}{dx} \right) &= q(x) \end{aligned} \tag{2.17}$$

Where G is the shear modulus, A is the cross-sectional area, and κ is a shear correction factor that accounts for the non-uniform distribution of shear stresses across the cross-section [Reddy, 2003].

For composite and sandwich beams, the introduction of transverse shear deformation is particularly important due to:

1. The significant difference in elastic properties between different layers
2. The relatively low shear stiffness of core materials in sandwich structures
3. The high ratio of elastic modulus to shear modulus in fiber-reinforced composites

The equivalent stiffness parameters for a composite beam under Timoshenko theory must account for both bending and shear contributions [Barbero, 2017]:

$$\begin{aligned} (EI)_{eq} &= \sum_{i=1}^n E_i \cdot I_i \\ (\kappa GA)_{eq} &= \kappa \cdot \sum_{i=1}^n G_i \cdot A_i \end{aligned} \tag{2.18}$$

The shear correction factor κ requires special consideration for composite sections, as it depends on the geometry and material properties of the cross-section. For sandwich beams with thin, stiff facesheets and a compliant core, κ can be approximated based on the relative shear rigidities of the components [Carlsson and Kardomateas, 2011].

2.5.1.c Higher-Order Theories

While the Timoshenko theory represents a significant improvement over the Euler-Bernoulli theory for composite structures, it still assumes a constant shear strain through the thickness. This assumption becomes problematic for thick composite sections and sandwich configurations where the shear strain distribution can be highly non-uniform [Carrera et al., 2013].

Higher-order theories address this limitation by adopting more complex displacement fields. A common approach is to express the axial displacement as a higher-order polynomial function of the thickness coordinate [Reddy, 2004]:

$$u(x, z) = u_0(x) + z \cdot \theta(x) + z^2 \cdot u_2(x) + z^3 \cdot u_3(x) \tag{2.19}$$

Where $u_2(x)$ and $u_3(x)$ represent higher-order terms that allow for a more realistic distribution of shear strains through the thickness.

The governing equations become more complex but provide a more accurate representation of the behavior of thick composite and sandwich beams. These theories are particularly valuable when precise interlaminar stress distributions are required, such as in delamination analysis [Kollár and Springer, 2003].

2.5.2 Specialized Theories for Sandwich Structures

2.5.2.a Sandwich Beam Theory

Sandwich structures, comprising thin, stiff facesheets bonded to a lightweight core, require specialized theoretical treatments due to their distinct mechanical behavior [Plantema, 1966]. Classical sandwich theory treats the structure as a three-layer system with the following assumptions:

1. The facesheets carry axial and bending loads but have negligible shear deformation
2. The core carries primarily shear loads with minimal axial stress
3. The overall deflection results from both bending and shear contributions

The displacement field for a sandwich beam can be expressed as:

$$\begin{aligned} \text{For facesheets: } u(x, z) &= u_0(x) - z \cdot \frac{dw_0(x)}{dx} \\ \text{For core: } u(x, z) &= u_0(x) - z \cdot \frac{dw_0(x)}{dx} + \psi(x, z) \end{aligned} \quad (2.20)$$

Where $\psi(x, z)$ represents the additional displacement due to core shear deformation.

The governing differential equation for a sandwich beam becomes [Vinson, 2018b]:

$$D \cdot \frac{d^4 w}{dx^4} - \frac{d^2}{dx^2} \left(S \cdot \frac{d^2 w}{dx^2} \right) = q(x) \quad (2.21)$$

Where D is the flexural rigidity of the sandwich and S is the shear stiffness of the core.

These parameters are calculated as:

$$\begin{aligned} D &= \frac{E_f \cdot b_f \cdot t_f^3}{6} + \frac{E_f \cdot b_f \cdot t_f \cdot d^2}{2} \\ S &= \frac{G_c \cdot b_c \cdot d^2}{c} \end{aligned} \quad (2.22)$$

Where:

- E_f and G_c are the elastic and shear moduli of the facesheet and core, respectively
- b_f and b_c are the widths of the facesheet and core
- t_f is the facesheet thickness
- c is the core thickness

- d is the distance between the centroids of the facesheets

2.5.2.b Allen's Theory

Allen's sandwich beam theory provides a more comprehensive framework by dividing the analysis into three distinct cases based on the relative stiffness of the core [Allen, 1969a]:

2.5.2.b.1 Case 1: Anti-plane Core Model In this case, the core is assumed to be incompressible in the thickness direction but offers no resistance to shear deformation. This model is suitable for very soft cores like low-density foams [Gibson and Ashby, 1999b].

2.5.2.b.2 Case 2: Fully Flexible Core Model The core is treated as a continuous medium with its own constitutive behavior, allowing for both shear deformation and through-thickness compression. This provides a more realistic representation for moderately stiff cores.

2.5.2.b.3 Case 3: Rigid Core Model The core is assumed to be rigid in both shear and through-thickness compression, which reduces the model to an equivalent homogeneous beam. This approach is rarely applicable to actual sandwich structures but serves as a theoretical upper bound.

The general governing equations for Allen's theory can be expressed as:

$$\begin{aligned} D \cdot \frac{d^4 w}{dx^4} + D^* \cdot \frac{d^4 u}{dx^4} - Q \cdot \frac{d^2 w}{dx^2} &= q(x) \\ D^* \cdot \frac{d^4 w}{dx^4} + D' \cdot \frac{d^4 u}{dx^4} - Q^* \cdot \frac{d^2 u}{dx^2} &= 0 \end{aligned} \quad (2.23)$$

Where:

- D , D^* , and D' are flexural rigidity parameters
- Q and Q^* are shear-related parameters
- u is the axial displacement of the mid-plane
- w is the transverse displacement

2.5.2.c High-Order Sandwich Panel Theory (HSAPT)

For more accurate prediction of local effects and complex loading conditions, the High-Order Sandwich Panel Theory (HSAPT) provides a sophisticated mathematical framework [Frostig et al., 1992]. HSAPT treats the facesheets as Euler-Bernoulli beams while modeling the core with higher-order displacement functions:

$$\text{For facesheets: } u^f(x, z) = u_0^f(x) - (z - z_f) \cdot \frac{dw_0^f(x)}{dx}$$

$$\text{For core: } u^c(x, z) = \sum_{i=0}^n u_i^c(x) \cdot \Phi_i(z) \quad (2.24)$$

$$w^c(x, z) = \sum_{i=0}^m w_i^c(x) \cdot \Psi_i(z)$$

Where $\Phi_i(z)$ and $\Psi_i(z)$ are basis functions for the thickness-wise variation, typically polynomials or trigonometric functions.

This approach allows for accurate representation of complex phenomena such as:

- Local indentation and wrinkling
- Non-uniform core compression
- Localized loading effects
- Interfacial stress concentrations

The resulting system of equations is considerably more complex but provides high-fidelity predictions essential for critical applications in aerospace structures [Librescu and Hause, 2000].

2.5.3 Laminate Theories for Composite Analysis

2.5.3.a Classical Laminate Theory (CLT)

Classical Laminate Theory extends the principles of beam theories to two-dimensional plate and shell structures composed of multiple anisotropic layers [Tsai and Hahn, 1980]. CLT provides the fundamental framework for analyzing laminated composite structures, including the facesheets of sandwich configurations [Reddy, 2004].

The key assumptions of CLT include:

1. Each layer is macroscopically homogeneous and orthotropic
2. The laminate is thin relative to its in-plane dimensions
3. Perfect bonding exists between layers
4. The Kirchhoff hypothesis applies (normals remain straight and perpendicular)

The constitutive relationship in CLT relates the force and moment resultants to the midplane strains and curvatures through the ABD matrix:

$$\begin{bmatrix} N \\ M \end{bmatrix} = \begin{bmatrix} A & B \\ B & D \end{bmatrix} \begin{bmatrix} \varepsilon^0 \\ \kappa \end{bmatrix} \quad (2.25)$$

Where:

- N represents the force resultants (N_x, N_y, N_{xy})
- M represents the moment resultants (M_x, M_y, M_{xy})
- ε^0 represents the midplane strains ($\varepsilon_x^0, \varepsilon_y^0, \gamma_{xy}^0$)

- κ represents the curvatures ($\kappa_x, \kappa_y, \kappa_{xy}$)
- A is the extensional stiffness matrix (3×3)
- B is the coupling stiffness matrix (3×3)
- D is the bending stiffness matrix (3×3)

The components of the ABD matrix are calculated from the properties of the individual layers [Jones, 2014]:

$$\begin{aligned} A_{ij} &= \sum_{k=1}^n (\bar{Q}_{ij})_k \cdot (z_k - z_{k-1}) \\ B_{ij} &= \frac{1}{2} \cdot \sum_{k=1}^n (\bar{Q}_{ij})_k \cdot (z_k^2 - z_{k-1}^2) \\ D_{ij} &= \frac{1}{3} \cdot \sum_{k=1}^n (\bar{Q}_{ij})_k \cdot (z_k^3 - z_{k-1}^3) \end{aligned} \quad (2.26)$$

Where $(\bar{Q}_{ij})_k$ is the transformed reduced stiffness matrix for the k th layer, and z_k is the coordinate of the k th interface measured from the midplane.

For sandwich structures, CLT is typically applied to model the facesheets, while the core is treated using other approaches such as those discussed earlier [Zenkert, 1997b].

2.5.3.b First-Order Shear Deformation Theory (FSDT)

The First-Order Shear Deformation Theory extends CLT by relaxing the Kirchhoff hypothesis to include transverse shear deformation, similar to the extension from Euler-Bernoulli to Timoshenko theory in beams [Whitney and Pagano, 1970]. This is particularly important for thick laminates and sandwich structures.

The displacement field in FSDT is:

$$\begin{aligned} u(x, y, z) &= u_0(x, y) + z \cdot \theta_x(x, y) \\ v(x, y, z) &= v_0(x, y) + z \cdot \theta_y(x, y) \\ w(x, y, z) &= w_0(x, y) \end{aligned} \quad (2.27)$$

Where θ_x and θ_y represent rotations of the normal to the midplane.

The constitutive equations are extended to include transverse shear forces [Reddy, 2003]:

$$\begin{bmatrix} N \\ M \\ Q \end{bmatrix} = \begin{bmatrix} A & B & 0 \\ B & D & 0 \\ 0 & 0 & H \end{bmatrix} \begin{bmatrix} \varepsilon^0 \\ \kappa \\ \gamma \end{bmatrix} \quad (2.28)$$

Where Q represents the transverse shear force resultants (Q_x, Q_y), γ represents the transverse shear strains (γ_{xz}, γ_{yz}), and H is the shear stiffness matrix.

For sandwich structures, FSDT provides a significant improvement over CLT but may still be insufficient to capture the complex shear behavior of the core, particularly when the core-to-facesheet stiffness ratio is very low [Carlsson and Kardomateas, 2011].

2.5.4 Analytical Solutions and Energy Methods

2.5.4.a Variational Principles in Composite Analysis

Variational principles provide powerful tools for deriving governing equations and approximate solutions for composite structures [Reddy, 2019]. The principle of virtual work and the principle of minimum potential energy are commonly used approaches.

The principle of virtual work states that for a body in equilibrium, the virtual work of internal forces equals the virtual work of external forces for any virtual displacement:

$$\delta W_{\text{int}} = \delta W_{\text{ext}} \quad (2.29)$$

For a composite beam, this can be expressed as:

$$\int_V (\sigma_x \cdot \delta \varepsilon_x + \tau_{xy} \cdot \delta \gamma_{xy} + \tau_{xz} \cdot \delta \gamma_{xz}) dV = \int_L q \cdot \delta w dx \quad (2.30)$$

This principle forms the basis for finite element formulations and many analytical methods [Kollár and Springer, 2003].

2.5.4.b Rayleigh-Ritz Method

The Rayleigh-Ritz method is an energy-based approach for obtaining approximate solutions to the governing differential equations [Gürdal et al., 1999]. The method assumes a displacement field in the form of a series expansion with unknown coefficients:

$$w(x) = \sum_{i=1}^n a_i \cdot \phi_i(x) \quad (2.31)$$

Where $\phi_i(x)$ are admissible functions satisfying the geometric boundary conditions, and a_i are undetermined coefficients.

The total potential energy of the system is expressed in terms of these coefficients:

$$\Pi = U - W \quad (2.32)$$

Where U is the strain energy and W is the potential of external forces.

Minimizing the total potential energy with respect to each coefficient:

$$\frac{\partial \Pi}{\partial a_i} = 0, \quad i = 1, 2, \dots, n \quad (2.33)$$

This yields a system of algebraic equations that can be solved for the unknown coefficients.

For composite and sandwich beams, the strain energy expressions must account for the contributions of different layers and include both bending and shear components [Wang et al., 2000]:

$$U = \frac{1}{2} \cdot \int_L \left(EI \cdot \left(\frac{d^2w}{dx^2} \right)^2 + \kappa GA \cdot \left(\frac{dw}{dx} + \theta \right)^2 \right) dx \quad (2.34)$$

2.5.4.c Galerkin Method

The Galerkin method is another approach for obtaining approximate solutions to differential equations governing composite structures [Reddy, 2004]. The method starts with the governing differential equation:

$$L[w(x)] = q(x) \quad (2.35)$$

Where L is a differential operator.

An approximate solution is assumed in the form:

$$w(x) \approx \sum_{i=1}^n a_i \cdot \phi_i(x) \quad (2.36)$$

The residual $R(x)$ is defined as:

$$R(x) = L[w(x)] - q(x) \quad (2.37)$$

The Galerkin method requires that this residual be orthogonal to each of the basis functions:

$$\int_L R(x) \cdot \phi_j(x) dx = 0, \quad j = 1, 2, \dots, n \quad (2.38)$$

This yields a system of equations for the unknown coefficients a_i .

For composite beams, the differential operator L incorporates the appropriate stiffness parameters based on the chosen beam theory (Euler-Bernoulli, Timoshenko, or higher-order) [Carrera et al., 2013].

2.5.5 Finite Element Formulations for Composite Structures

2.5.5.a Weak Form and Finite Element Method

The finite element method (FEM) is widely used for analyzing complex composite and sandwich structures [Reddy, 2003]. The method is based on the weak form of the governing equations, which is derived from the principle of virtual work.

For a Timoshenko beam element, the weak form can be expressed as:

$$\int_L \left(EI \cdot \frac{d\theta}{dx} \cdot \frac{d\delta\theta}{dx} + \kappa GA \cdot \left(\frac{dw}{dx} + \theta \right) \cdot \left(\frac{d\delta w}{dx} + \delta\theta \right) \right) dx = \int_L q \cdot \delta w dx \quad (2.39)$$

This formulation forms the basis for developing finite element models of composite beams [Kollár and Springer, 2003].

2.5.5.b Element Types for Composite Analysis

Various element types have been developed specifically for composite and sandwich structures [Barbero, 2017]:

2.5.5.b.1 Layered Beam Elements These elements maintain the standard beam kinematics but incorporate the layered nature of composites through numerical integration across the thickness, with material properties varying between integration points.

2.5.5.b.2 Sandwich Beam Elements Specialized elements for sandwich structures often model the facesheets and core separately, with appropriate constraints at the interfaces [Zenkert, 1997b]. Some formulations include:

1. **Discrete-Layer Elements:** Each layer is modeled with separate field variables, connected through continuity conditions
2. **Zigzag Elements:** Incorporate piecewise linear variations of in-plane displacements through the thickness
3. **Mixed Formulation Elements:** Include both displacement and stress fields as primary variables

2.5.5.c Isoparametric Formulations

Isoparametric elements use the same shape functions to define both the element geometry and the field variables [Reddy, 2004]. For a typical beam element, the displacement and rotation fields are expressed as:

$$\begin{aligned} w(\xi) &= \sum_{i=1}^n N_i(\xi) \cdot w_i \\ \theta(\xi) &= \sum_{i=1}^n N_i(\xi) \cdot \theta_i \end{aligned} \tag{2.40}$$

Where $N_i(\xi)$ are shape functions defined in terms of the natural coordinate ξ , and w_i and θ_i are nodal values.

For composite beams, the element stiffness matrix incorporates the appropriate constitutive relationships:

$$K_e = \int_L B^T \cdot D \cdot B dx \tag{2.41}$$

Where B is the strain-displacement matrix and D contains the relevant stiffness parameters for the composite section [Gürdal et al., 1999].

2.5.6 Advanced Models for Composite Sandwich Structures

2.5.6.a Zig-Zag Theories

Zig-zag theories address a significant limitation of traditional laminate theories by accounting for the discontinuous nature of transverse shear strains at layer interfaces [Karaman

et al., 2003]. These theories introduce displacement fields with slope discontinuities (zig-zags) at the interfaces between layers with different properties:

$$u(x, z) = u_0(x) + z \cdot \theta(x) + \phi(z) \cdot \psi(x) \quad (2.42)$$

Where $\phi(z)$ is a piecewise linear function with slope changes at layer interfaces, and $\psi(x)$ is an additional degree of freedom.

The zig-zag function $\phi(z)$ satisfies the continuity of transverse shear stresses at the interfaces, a requirement dictated by equilibrium. This approach is particularly effective for sandwich structures, where the significant difference in elastic properties between facesheets and core creates pronounced zig-zag effects [Carlsson and Kardomateas, 2011].

2.5.6.b Layerwise Theories

Layerwise theories take a different approach by treating each layer as a separate plate or beam with independent field variables, connected through appropriate continuity conditions [Reddy, 2003]. The displacement field is defined separately for each layer:

$$u^k(x, z) = u_0^k(x) + z \cdot \theta^k(x) \quad (2.43)$$

Where the superscript k denotes the layer number.

Continuity conditions at the interfaces provide the necessary constraints:

$$\begin{aligned} u^k(x, z_k) &= u^{k+1}(x, z_k) \\ w^k(x, z_k) &= w^{k+1}(x, z_k) \end{aligned} \quad (2.44)$$

This approach leads to a larger system of equations but provides highly accurate predictions of local effects, particularly important near edges, holes, and loading points in sandwich structures [Librescu and Hause, 2000].

2.5.6.c Multi-Scale Modeling Approaches

Multi-scale modeling addresses the inherent complexity of composite sandwich structures by analyzing the material at different length scales [Tsai and Hahn, 1980]:

1. **Micro-scale:** Individual fibers and matrix in composite facesheets, or cell walls in honeycomb cores
2. **Meso-scale:** Representative volume elements of the facesheet laminates or core structure
3. **Macro-scale:** Global structural behavior

The information flows between scales through homogenization (micro-to-macro) and localization (macro-to-micro) processes:

$$\sigma_{\text{macro}} = C_{\text{eff}} \cdot \varepsilon_{\text{macro}} \quad (2.45)$$

Where C_{eff} is an effective stiffness tensor derived from lower-scale analyses.

For sandwich structures, this approach is particularly valuable for capturing complex failure mechanisms that initiate at the microscopic level but propagate to affect the global structural response [Gibson and Ashby, 1999b].

2.5.7 Nonlinear Models for Composite Structures

2.5.7.a Geometric Nonlinearity

Geometric nonlinearity becomes significant in thin composite structures under large deformations [Reddy, 2019]. The von Kármán strains for moderately large deflections are expressed as:

$$\varepsilon_x = \frac{du}{dx} + \frac{1}{2} \cdot \left(\frac{dw}{dx} \right)^2 \quad (2.46)$$

These nonlinear strain-displacement relations lead to coupled equations for in-plane and transverse displacements.

For sandwich structures, geometric nonlinearity is particularly relevant in:

1. Buckling and post-buckling analysis
2. Wrinkling of thin facesheets
3. Local indentation under concentrated loads

[Vinson, 2018b]

2.5.7.b Material Nonlinearity

Composite materials often exhibit nonlinear stress-strain behavior, particularly under shear loading. Core materials in sandwich structures, such as foams and honeycombs, typically show pronounced nonlinear response [Triantafillou and Gibson, 1987]:

$$\tau = G \cdot \gamma + G_2 \cdot \gamma^2 + G_3 \cdot \gamma^3 + \dots \quad (2.47)$$

These nonlinearities must be incorporated into the constitutive relationships and usually require incremental-iterative solution procedures [Barbero, 2017].

2.5.7.c Interface Nonlinearity

The interface between facesheets and core in sandwich structures can exhibit nonlinear behavior, particularly when debonding or delamination occurs [Carlsson and Kardomateas, 2011]. Cohesive zone models are commonly used to represent these interfaces:

$$t = K \cdot \delta \cdot (1 - D) \quad (2.48)$$

Where t is the interface traction, δ is the relative displacement, K is the initial stiffness, and D is a damage parameter evolving from 0 (intact) to 1 (fully debonded).

2.5.8 Dynamic Analysis of Composite Structures

2.5.8.a Free Vibration Analysis

The free vibration of composite beams is governed by the eigenvalue problem [Karama et al., 2003]:

$$(K - \omega^2 \cdot M) \cdot \phi = 0 \quad (2.49)$$

Where K is the stiffness matrix, M is the mass matrix, ω is the natural frequency, and ϕ is the mode shape vector.

For sandwich beams, the mass matrix must account for the different density of facesheets and core, while the stiffness matrix incorporates the appropriate beam theory (typically Timoshenko or higher-order) [Sokolinsky and Frostig, 2000].

The natural frequencies of sandwich beams are significantly affected by:

1. Transverse shear deformation of the core
2. Rotary inertia effects
3. Core-facesheet stiffness ratio

2.5.8.b Forced Vibration and Damping

The dynamic response of composite sandwich structures includes significant damping contributions from:

1. Viscoelastic behavior of polymer matrices and core materials
2. Interface friction at fiber-matrix boundaries
3. Air pumping in cellular cores

[Gibson and Ashby, 1999b]

These damping mechanisms can be incorporated through complex moduli:

$$E^* = E'(1 + i\eta) \quad (2.50)$$

Where E' is the storage modulus and η is the loss factor.

Alternatively, modal damping or Rayleigh damping can be used in time-domain analyses [Yang and Nagarajaiah, 2015b]:

$$C = \alpha \cdot M + \beta \cdot K \quad (2.51)$$

Where C is the damping matrix, and α and β are Rayleigh damping coefficients.

2.5.8.c Wave Propagation Analysis

Wave propagation in sandwich composites is characterized by dispersive behavior, where wave velocity depends on frequency [Wang et al., 2000]. The governing equation for flexural waves in a Timoshenko beam is:

$$EI \cdot \frac{\partial^4 w}{\partial x^4} + \rho A \cdot \frac{\partial^2 w}{\partial t^2} - \rho I \cdot \frac{\partial^4 w}{\partial x^2 \partial t^2} + \frac{\rho I}{\kappa G A} \cdot \frac{\partial^4 w}{\partial t^4} = 0 \quad (2.52)$$

This equation yields multiple wave modes, including:

1. Flexural waves, dominated by bending deformation
2. Thickness-shear waves, involving significant core shear
3. Dilatational waves, involving through-thickness deformation

The dispersion characteristics of these waves are essential for understanding vibration transmission and structural health monitoring applications in sandwich structures [Yang and Nagarajaiah, 2015b].

2.5.9 Concluding Remarks

The mathematical modeling of composite and sandwich structures encompasses a rich hierarchy of theories, from simple Euler-Bernoulli beams to sophisticated multi-scale approaches [Zenkert, 1995b]. The selection of an appropriate theory depends on several factors:

1. The geometry of the structure (span-to-thickness ratio)
2. The contrast in elastic properties between constituents
3. The loading conditions and boundary constraints
4. The specific phenomena of interest (global response or local effects)
5. The required accuracy and computational resources available

For aerospace sandwich structures, which typically feature thin, stiff facesheets and lightweight cores, specialized sandwich theories or high-order approaches are generally necessary to capture the complex mechanical behavior accurately [Librescu and Hause, 2000]. These models provide the foundation for reliable design, analysis, and optimization of critical structural components [Gürdal et al., 1999].

3 Goals of The Project

Project Objectives and Scope

3.1 Overview

This project is centered on the design, manufacture, and experimental evaluation of a smart composite structure specifically tailored for aerospace structural health monitoring (SHM) applications. The core focus is on developing a beam-type sandwich composite with strategically embedded sensors that can accurately monitor structural integrity through vibration-based methods. This research sits at the intersection of advanced composite materials, sensor integration, dynamic testing, and damage detection algorithms—all critical technologies for next-generation aerospace structures.

3.2 Background Context

The increasing use of lightweight composite materials in aerospace structures has created both opportunities and challenges for the industry. While composites offer superior strength-to-weight ratios and customizable mechanical properties, they also present unique damage mechanisms that can be difficult to detect using traditional inspection methods. Unlike metallic structures where damage is often visible on the surface, composites can experience internal damage such as delamination, matrix cracking, and fiber breakage that may remain hidden from visual inspection while significantly compromising structural integrity.

Structural health monitoring represents a paradigm shift from scheduled maintenance to condition-based maintenance, offering the potential for continuous assessment of structural integrity, early damage detection, and reduced maintenance costs. Within the broader SHM field, vibration-based methods have emerged as particularly promising for composite structures due to their non-destructive nature and ability to detect subsurface damage.

3.3 Project Scope

The project encompasses several interconnected phases and components:

1. **Design and Optimization:** Development of a beam-type sandwich composite configuration, including:
 - Selection of appropriate carbon fiber reinforced polymer (CFRP) materials for the facesheets
 - Design of an aluminum honeycomb core structure optimized for both mechanical performance and sensor integration
 - Determination of optimal laminate stacking sequences and core dimensions

- Finite element analysis to predict dynamic behavior and sensor response
- 2. Sensor Selection and Integration Strategy:** Implementation of a multi-sensor approach featuring:
- Piezoelectric sensors for active sensing and actuation capabilities
 - Strain gauges for local strain measurement and verification
 - Strategic sensor placement to maximize sensitivity to potential damage locations
 - Development of robust embedding techniques that maintain structural integrity
- 3. Manufacturing Process Development:**
- Adaptation of standard composite manufacturing techniques to accommodate embedded sensors
 - Development of specialized layup procedures for sensor integration
 - Implementation of quality control measures to ensure consistent production
 - Documentation of manufacturing protocols for future reproducibility
- 4. Experimental Testing Program:**
- Design and setup of vibration testing equipment and protocols
 - Execution of experimental modal analysis on the healthy structure to establish baseline characteristics
 - Introduction of controlled damage scenarios at predetermined locations
 - Collection of comprehensive vibration response data under various testing conditions
- 5. Data Analysis and Damage Detection:**
- Implementation of modal parameter extraction algorithms
 - Development and application of modal curvature-based damage detection methods
 - Evaluation of various data-driven approaches for damage identification
 - Comparative analysis of different damage detection methodologies

3.4 Specific Objectives

- 1. Manufacturing Excellence:** Successfully produce a sandwich composite beam with embedded sensor network that maintains structural integrity and sensor functionality during the manufacturing process.
- 2. Dynamic Characterization:** Experimentally determine the modal parameters (natural frequencies, mode shapes, and damping ratios) of the sandwich composite beam in its healthy state and develop a comprehensive understanding of its vibration characteristics.

3. **Damage Sensitivity Analysis:** Quantify the sensitivity of various modal parameters to different damage scenarios, identifying which parameters provide the most reliable indicators of structural damage.
4. **Algorithm Development and Validation:** Implement and validate multiple damage detection algorithms, with particular focus on modal curvature-based methods and their effectiveness for sandwich composite structures.
5. **Sensor Performance Evaluation:** Assess the performance of different sensor types and configurations in detecting and localizing damage, establishing guidelines for optimal sensor placement in similar structures.
6. **Methodology Documentation:** Develop and document a comprehensive methodology for vibration-based SHM in sandwich composite structures that can be extended to more complex aerospace components.

3.5 Relationship to Broader Research Context

This project is being conducted as part of the MAK 498 Senior Design Project and is aligned with the TÜBİTAK 1001 supported research project titled "Development of Physics-Informed Deep Learning Methods Using Smart Sensor Data for Structural Health Monitoring in Aviation." The work contributes to the broader scientific effort to develop reliable, real-time monitoring systems for next-generation aerospace structures.

While the current project focuses on a relatively simple beam geometry, the methodologies developed and lessons learned will provide valuable insights for application to more complex aerospace structures. The integration of experimental data with physics-based models and advanced data analysis techniques exemplifies the multidisciplinary approach necessary for advancing SHM technology.

3.6 Expected Outcomes and Impact

The project aims to deliver several key outcomes:

1. A validated design and manufacturing protocol for smart sandwich composites with embedded sensors.
2. A comprehensive dataset of vibration responses from both healthy and damaged sandwich composite structures, valuable for algorithm development and validation.
3. Quantitative assessment of different damage detection methods, highlighting their relative strengths and limitations for sandwich composite applications.
4. Insights into the practical challenges of sensor integration in composite structures and potential solutions for aerospace implementations.
5. Recommendations for future research directions in the field of vibration-based SHM for composite aerospace structures.

The knowledge gained through this project will contribute to the development of more reliable, lightweight, and intelligent aerospace structures with built-in monitoring capabilities. Such advances are essential for the next generation of aircraft that must meet increasingly stringent safety, efficiency, and environmental standards.

4 Product Development Process

4.1 Design Approach and Methodology

The development of our smart composite structure followed a systematic approach integrating materials selection, structural design, sensor integration, and manufacturing process optimization. Our methodology emphasized a balance between theoretical modeling and practical implementation, ensuring the final product would effectively demonstrate vibration-based structural health monitoring capabilities while remaining manufacturable with available resources.

The design process began with comprehensive requirements analysis, identifying the necessary performance characteristics for effective SHM in aerospace applications. These requirements guided material selection decisions and manufacturing process development, ensuring alignment with the project objectives throughout the development cycle.

4.1.1 Requirements Definition

The following key requirements were established for the smart composite structure:

1. Structural Performance:

- Sufficient stiffness to provide clear modal separation for vibration analysis
- Mechanical properties representative of aerospace structural components
- Durability to withstand repeated testing cycles

2. Sensor Integration:

- Capacity to incorporate multiple sensor types (piezoelectric and strain gauges)
- Minimal impact of sensors on structural integrity
- Reliable sensor connectivity throughout testing

3. Damage Detection Capability:

- Measurable changes in dynamic response due to controlled damage
- Sufficient sensor coverage for damage localization
- Signal quality suitable for modal parameter extraction

4. Manufacturing Feasibility:

- Producible using available laboratory equipment
- Repeatable process for potential future specimens
- Integration of QA steps to ensure structural integrity

These requirements provided the framework for our material selection, structural design, and manufacturing process development decisions.

4.2 Applied SHM Techniques

The damage detection strategy in this project is based primarily on vibration analysis. Experimental modal analysis was conducted using two primary excitation methods: an impact hammer and a shaker. These excitation techniques enabled capturing the system's frequency response functions (FRFs) under controlled boundary conditions.

Modal parameters such as natural frequencies and mode shapes were extracted from the measured response data. By analyzing these parameters before and after damage, deviations in the system's dynamic response were identified. In particular, the curvature mode shapes were used to calculate curvature differences between healthy and damaged states. This curvature-based method allowed localization of damage based on stiffness variations across the structure.

4.2.1 Modal Analysis Approach

Our experimental modal analysis implementation focused on:

1. Excitation Strategy:

- Impact hammer testing for rapid modal parameter identification
- Shaker testing for controlled frequency sweeps and higher quality FRFs
- Comparison between excitation methods to validate results

2. Boundary Conditions:

- Free-free configuration using elastic suspension
- Fixed-free cantilever configuration for practical application scenarios
- Consistent setup to ensure repeatability between healthy and damaged tests

3. Data Acquisition:

- Multi-channel simultaneous sampling from all sensors
- Appropriate sampling rates to capture relevant frequency ranges
- Signal conditioning to maximize signal-to-noise ratio

4. Parameter Extraction:

- Complex mode indicator function (CMIF) for mode identification
- Least squares complex exponential (LSCE) method for parameter extraction
- Modal assurance criterion (MAC) for mode shape comparison

4.2.2 Damage Detection Algorithms

The core damage detection methodology employed curvature-based techniques, specifically:

1. Mode Shape Curvature Method:

- Calculation of second derivatives of mode shapes to obtain curvatures
- Comparison of curvatures between healthy and damaged states

- Damage index formation based on summed curvature differences

2. Strain Energy-Based Methods:

- Formulation of modal strain energy from curvature information
- Fractional strain energy change as damage indicator
- Threshold-based detection criteria

3. Frequency Shift Analysis:

- Tracking of natural frequency changes between healthy and damaged states
- Correlation of frequency shifts with damage location and severity
- Statistical significance assessment of observed changes

Additional signal processing techniques were implemented as complementary approaches, including:

- Wavelet transform analysis for time-frequency decomposition
- Transmissibility function analysis
- Statistical pattern recognition on modal parameters

This multi-method approach provided redundancy in damage detection capabilities and allowed for comparative assessment of different techniques' effectiveness.

4.3 Materials Selection Process

The selection of materials for our smart composite structure was guided by a systematic evaluation of alternatives against our established requirements. We sought materials that would provide representative aerospace performance while remaining compatible with our sensor integration approach and manufacturing capabilities.

4.3.1 Facesheet Material Selection

For the composite facesheets, we evaluated several potential materials:

1. Carbon Fiber/Epoxy Prepreg:

- Pros: Consistent fiber volume fraction, aerospace-grade properties
- Cons: Requires autoclave processing, limited shelf life, higher cost

2. Dry Carbon Fiber with Infused Epoxy (Selected):

- Pros: Cost-effective, compatible with laboratory-scale vacuum infusion, flexible processing window
- Cons: Potentially less consistent fiber volume fraction, manual processing variations

3. Glass Fiber/Epoxy:

- Pros: Lower cost, good damage visibility
- Cons: Lower stiffness (would reduce modal frequency separation), less representative of aerospace applications

The dry carbon fiber with vacuum-infused epoxy system was selected based on its balance of performance characteristics and manufacturing compatibility. This system allowed for room temperature processing while providing mechanical properties sufficient for demonstrating modal behavior changes due to damage.

4.3.2 Core Material Selection

For the sandwich core, several options were considered:

1. **Aluminum Honeycomb** (Selected):

- Pros: High specific stiffness, aerospace relevance, uniform properties
- Cons: Potential galvanic corrosion with carbon, cell size limitations for sensor embedding

2. **Nomex Honeycomb**:

- Pros: No galvanic issues, good damping properties
- Cons: Higher cost, less distinctive mechanical property contrast with facesheets

3. **Polymer Foams**:

- Pros: Easy machining for sensor cavities, no galvanic issues
- Cons: Less representative of aerospace structures, higher damping (potentially masking subtle modal changes)

Aluminum honeycomb was selected due to its prevalence in aerospace applications and its distinctive mechanical properties that would create clear modal behavior in the final structure.

4.4 Sensor Selection and Integration Strategy

The effectiveness of our SHM system depended critically on appropriate sensor selection and strategic placement. Our approach balanced coverage requirements, manufacturability constraints, and signal quality considerations.

4.4.1 Sensor Selection Criteria

1. **Piezoelectric Sensors**:

- Selected for their dual sensing/actuation capability
- Frequency response suitable for structural vibration monitoring
- Low profile for integration between structural layers
- Robust enough to survive the manufacturing process

2. **Strain Gauges**:

- Selected for direct strain field measurement
- Complementary data to piezoelectric sensors
- Established technology for validation purposes

4.4.2 Sensor Placement Optimization

Sensor locations were determined through a combination of analytical modeling and practical considerations:

1. Modal Analysis-Based Placement:

- FEA modeling to identify high strain energy regions for each mode of interest
- Optimization to maximize damage detection sensitivity
- Coverage of critical locations identified from failure mode analysis

2. Manufacturing Constraints:

- Consideration of wiring routes and connection points
- Minimum spacing requirements for structural integrity
- Accommodation of potential future damage locations

3. Signal Conditioning Requirements:

- Proximity to readout electronics
- Minimization of electromagnetic interference
- Cable routing to prevent stress concentrations

The final sensor layout represented an optimized compromise between theoretical ideal placement and practical manufacturing constraints.

4.5 Manufacturing of the Smart Composite Structure

The manufacturing process was developed to ensure structural integrity while successfully integrating the sensor network. Each step incorporated quality control measures to verify proper execution.

4.5.1 Step 1: Preparation of CFRP Layers

1. Material Preparation:

- Carbon fiber fabrics were cut according to the specified dimensions using precision templates
- Fabric handling protocols were followed to prevent contamination and fiber misalignment
- Materials were conditioned at controlled temperature and humidity prior to processing

2. Layup and Infusion:

- The fabric layers were placed on a flat glass surface covered with release film
- Fiber orientation was verified at each layer to ensure design compliance
- Flow media and distribution channels were positioned for optimal resin flow
- Epoxy resin was mixed with prescribed ratio and degassed prior to infusion

- Vacuum infusion technique was implemented to ensure uniform resin distribution and void-free curing
- Real-time monitoring of resin flow front ensured complete wetout

3. Curing and Post-Processing:

- The infused layup was left to cure under vacuum for several hours
- Temperature monitoring during cure verified exotherm stayed within acceptable range
- After curing, the CFRP laminates were trimmed and cleaned for further assembly
- Visual inspection and tap testing confirmed quality of cured laminates

4.5.2 Step 2: Fabrication of Flex PCB

1. Design and Preparation:

- Circuit layout was designed with considerations for sensor placement and signal routing
- The Flex PCB was fabricated using a low-cost DIY method based on the guide in Instructables
- Circuit layout was printed on glossy paper using a laser printer with high-resolution settings

2. Transfer and Etching:

- The toner was transferred onto a copper-coated flexible substrate using heat and pressure
- Transfer quality was visually verified before proceeding
- The board was then etched in a ferric chloride solution to remove unwanted copper
- Etching progress was monitored to prevent under or over-etching
- Neutralization and thorough cleaning followed etching

3. Completion and Testing:

- Final cleaning and drilling steps were applied to prepare the board for sensor integration
- Continuity testing verified circuit integrity
- Sensor mounting pads were prepared with appropriate surface treatment
- Component attachment was performed with careful temperature control to prevent damage

4.5.3 Step 3: Sensor Integration

1. Sensor Preparation:

- Piezoelectric sensors were inspected and tested prior to integration

- Sensor surfaces were prepared according to manufacturer recommendations
- Wire connections were established and verified through electrical testing
- Strain gauges were mounted following standard surface preparation protocols

2. Attachment and Protection:

- Sensors were attached to the flex PCB using appropriate adhesives
- Wiring was secured with strain relief to prevent connection failures
- Protective coatings were applied to shield sensors during subsequent manufacturing steps
- Functional testing confirmed all sensors remained operational after mounting

4.5.4 Step 4: Sandwich Structure Assembly

1. Component Preparation:

- Aluminum honeycomb core was cut to size and cleaned
- Edge closeouts were prepared to prevent resin ingress into cells
- Adhesive systems were prepared according to manufacturer specifications
- All components were aligned using registration marks

2. Assembly Sequence:

- The final sandwich structure consisted of the following sequence:
 - Top CFRP layer
 - Flex PCB layer with mounted piezoelectric sensors
 - Aluminum honeycomb core
 - Bottom CFRP layer
- Structural adhesive was applied between all interfaces
- The full stack was aligned and compressed to ensure uniform bonding during curing

3. Final Processing:

- After full curing, the sample was trimmed and edge-sealed for experimental readiness
- Final sensor functional testing confirmed integrity throughout manufacturing process
- Dimensional verification ensured compliance with design specifications
- Surface preparation for testing fixture attachment was completed

4.6 Quality Control and Validation

Throughout the manufacturing process, multiple quality control steps were implemented to ensure the structural integrity and sensor functionality of the final product:

1. Non-Destructive Testing:

- Ultrasonic inspection of cured laminates to detect voids or delaminations
- Tap testing for quick assessment of bond integrity
- Thermographic inspection to verify uniform adhesive distribution

2. Sensor Verification:

- Continuity testing at each manufacturing stage
- Functional response verification after completion
- Signal-to-noise ratio assessment under controlled excitation

3. Dimensional Control:

- Thickness measurements at multiple locations
- Flatness verification to ensure proper test conditions
- Edge quality inspection to prevent stress concentrations

4. Documentation:

- Process parameters recorded for repeatability
- Photographic documentation of each key manufacturing step
- Material batch tracking for traceability

4.7 Lessons Learned and Process Improvements

The development process yielded several important insights that would inform future iterations:

1. Sensor Integration Challenges:

- Wire routing proved more critical than anticipated for signal quality
- Additional strain relief methods would enhance long-term reliability
- Pre-testing of sensors before final assembly would reduce rework

2. Manufacturing Optimizations:

- Modified vacuum infusion setup would improve resin distribution uniformity
- Alternative adhesive systems could reduce cure time without compromising performance
- Improved alignment fixtures would enhance dimensional control

3. Design Refinements:

- Optimal balance between sensor density and structural integrity identified
- More effective edge sealing methods developed for environmental protection
- Improved understanding of sensor-structure interaction effects on modal parameters

5 Concept Alternatives and Evaluation

During the early design phase of the SHM system, multiple sensing and integration concepts were considered. The alternatives mainly differed in sensor type, placement strategy, and complexity of integration into the composite structure.

Concept 1: Surface-Mounted Sensors Only

Simplest to implement, this method proposed using only surface-mounted strain gauges and PZT sensors. Although easy to apply, it increased the risk of damage or detachment under operational loading.

Concept 2: Embedded Sensors in Composite Layup

This approach involved embedding sensors (especially flex PCBs and piezoelectric elements) between CFRP layers during vacuum infusion. It offered higher durability and integration but required careful thermal and electrical design.

Concept 3: Fully Wireless SHM System

A more advanced concept explored wireless communication and onboard signal processing. Although ideal for aerospace systems, it was not feasible within the project's resource and time limitations.

After evaluating complexity, reliability, and feasibility, Concept 2 was selected as the final design choice.

6 Sensor-Integrated Sandwich Composite Plate Manufacturing Process

This chapter details the manufacturing process developed to ensure the structural integrity of a CFRP-faced, aluminum honeycomb core sandwich panel while integrating a network of sensors (referred to as the ‘smart layer’). The process involves five main steps: preparation of CFRP layers (including those with integrated smart layers), fabrication of the Flex PCB (smart layer), sensor integration onto the Flex PCB, waterjet cutting of components, and final sandwich structure assembly. Each step incorporates quality control measures to verify proper execution, culminating in the final sandwich plate assembly specified in drawing T_03_01. All technical drawings referenced (T_01_01 through T_03_02) are provided in Appendix B.

6.1 Preparation of CFRP Layers

This initial step involves the preparation of the Carbon Fiber Reinforced Polymer (CFRP) laminates that form the face sheets of the final sandwich structure.

6.1.1 Material Preparation

1. Cutting and Handling:

- Carbon fiber fabrics were precisely cut to dimensions of 500 mm × 50 mm, as specified in drawing T_01_01, using templates.
- Strict fabric handling protocols were followed to prevent contamination and fiber misalignment during cutting and handling.
- Materials were conditioned under controlled temperature and humidity environments to ensure consistent properties prior to processing.

6.1.2 Mold Preparation, Layup, and Infusion Preparation

1. Mold Setup and Layup:

- A flat glass surface, serving as the mold, was cleaned and coated with five layers of mold release wax to facilitate demolding, with sufficient drying time between applications.
- Pre-cut carbon fiber fabric layers were placed onto the mold in a [0°/90°/0°/90°] orientation sequence, consistent with drawings T_02_01 and T_02_02. Fiber orientation was verified after each layer (Figure 6.1).
- A layer of peel ply was placed over the CFRP stack to ensure easy removal of vacuum bagging materials after curing and to provide a suitable surface texture for bonding (Figure 6.2).
- A flow mesh was positioned on top of the peel ply to ensure uniform resin distribution during infusion (Figure 6.3).

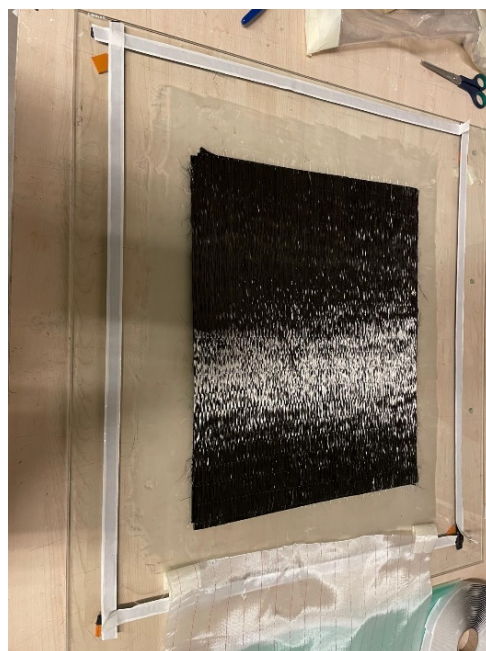


Figure 6.1: Layup of CFRP layers in [0/90/0/90] sequence.



Figure 6.2: Placement of peel ply over CFRP stack.

- The assembly was covered with a vacuum bag, sealed to the mold surface using sealant tape to create an airtight enclosure (Figure 6.4).
- Resin inlet and vacuum outlet ports were installed through the vacuum bag, with hoses attached for resin feeding and vacuum connection. A resin trap was included to prevent resin from reaching the vacuum pump (Figure 6.5).
- A vacuum drop test was conducted to verify seal integrity: the system was evacuated to approximately -1 bar (-29.5 inHg), the pump was shut off, and the vacuum level drop was monitored over 10–15 minutes. A drop of less than 1 inHg in 10 minutes confirmed adequate sealing (Figures 6.6 and 6.7).
- Epoxy resin and hardener were weighed per the manufacturer's specified mix ratio



Figure 6.3: Positioning of flow mesh for resin distribution.



Figure 6.4: Placement and sealing of vacuum bag.

(Figures 6.8 and 6.9).

- The components were mixed thoroughly in a clean container to achieve a homogeneous mixture, minimizing air entrapment (Figure 6.10).
- With seal integrity confirmed, the resin inlet hose was opened, allowing the epoxy resin to be drawn into the laminate stack via vacuum infusion. The resin flow front was monitored to ensure complete wetout of the fibers (Figure 6.11).

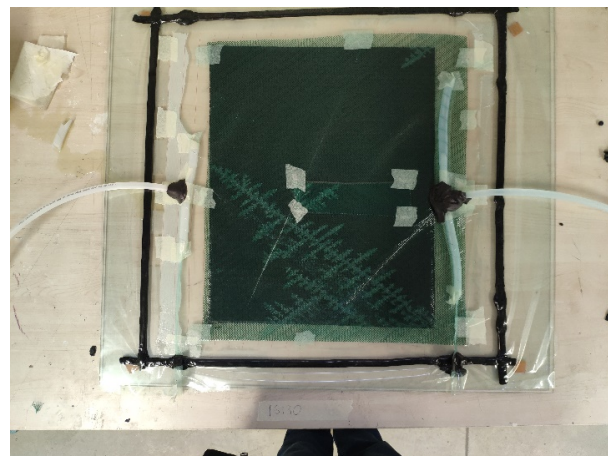


Figure 6.5: Connection of resin inlet and vacuum outlet hoses.



Figure 6.6: Vacuum drop test - initial reading.



Figure 6.7: Vacuum drop test - final reading.

6.1.3 Curing and Post-Processing

- After complete infusion, the resin inlet was clamped off, and the layup was cured under vacuum for several hours at ambient temperature or per a specified cure cycle (Figure 6.12).
- Temperature was monitored during curing to ensure the exothermic reaction stayed within acceptable limits.
- Post-curing, the CFRP laminates were demolded, auxiliary materials (vacuum bag, flow mesh, peel ply) were removed, and the laminates were trimmed and cleaned for further assembly.



Figure 6.8: Epoxy resin component (weight measurement).



Figure 6.9: Hardener component (weight measurement).



Figure 6.10: Mixing of resin and hardener.

6.1.4 Production of CFRP Layers with Integrated Smart Layer

- For CFRP face sheets designated to incorporate the sensor network (e.g., T_02_01, T_02_02 for assembly T_03_01), the smart layer (Flex PCB with sensors, prepared in Steps 2 and 3, detailed in drawing T_02_03) was positioned between specific plies (e.g., between the second and third plies in a [0/90/Smart Layer/0/90] stack). The smart layer was secured with paper tape to prevent shifting (Figure 6.13).
- Remaining CFRP plies were laid on top, and the standard procedures for peel ply, flow mesh, vacuum bagging, drop test, infusion, and curing (as described earlier) were followed. This co-curing process produced monolithic CFRP components with an embedded sensor network, ready for final assembly in Step 5.



Figure 6.11: Resin progression during vacuum infusion (wetout).

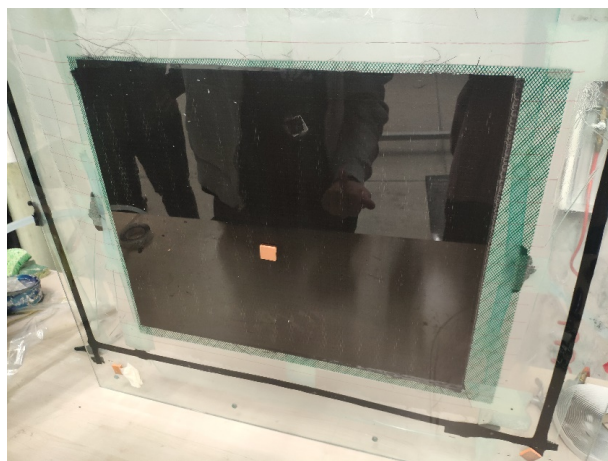


Figure 6.12: Curing under vacuum.



Figure 6.13: Positioning and securing of smart layer within CFRP layup using tape.

6.2 Fabrication of Flex PCB (Smart Layer)

This step outlines the fabrication of the flexible printed circuit board (Flex PCB), which serves as the substrate for mounting sensors and routing electrical signals within the MAK498 Senior Design Project

smart layer assembly (drawing T_02_03). A low-cost Do-It-Yourself (DIY) methodology, guided by online resources from Instructables [Instructables, 2025], was employed.

6.2.1 Design and Preparation

- The circuit layout was designed to accommodate piezoelectric sensors (drawing T_01_04) at predefined locations and to route their signals efficiently, considering signal integrity and noise reduction (drawing T_02_03, Figure 6.14).

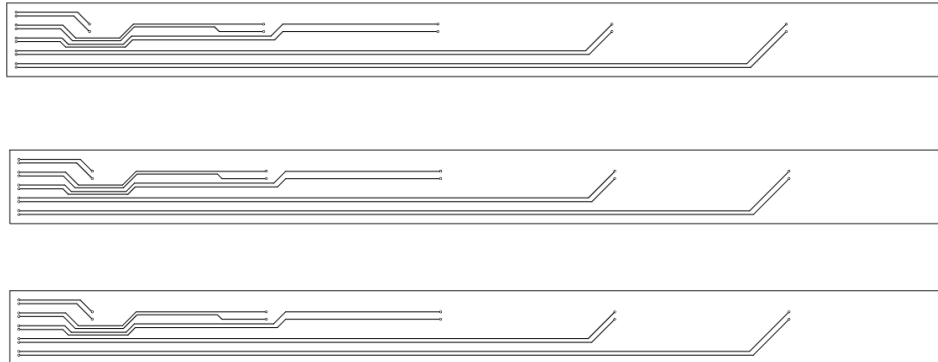


Figure 6.14: Flex PCB circuit layout design (CAD).

- Fabrication began with a thin, flexible acetate sheet as the base substrate (drawing T_01_02, Figure 6.15).

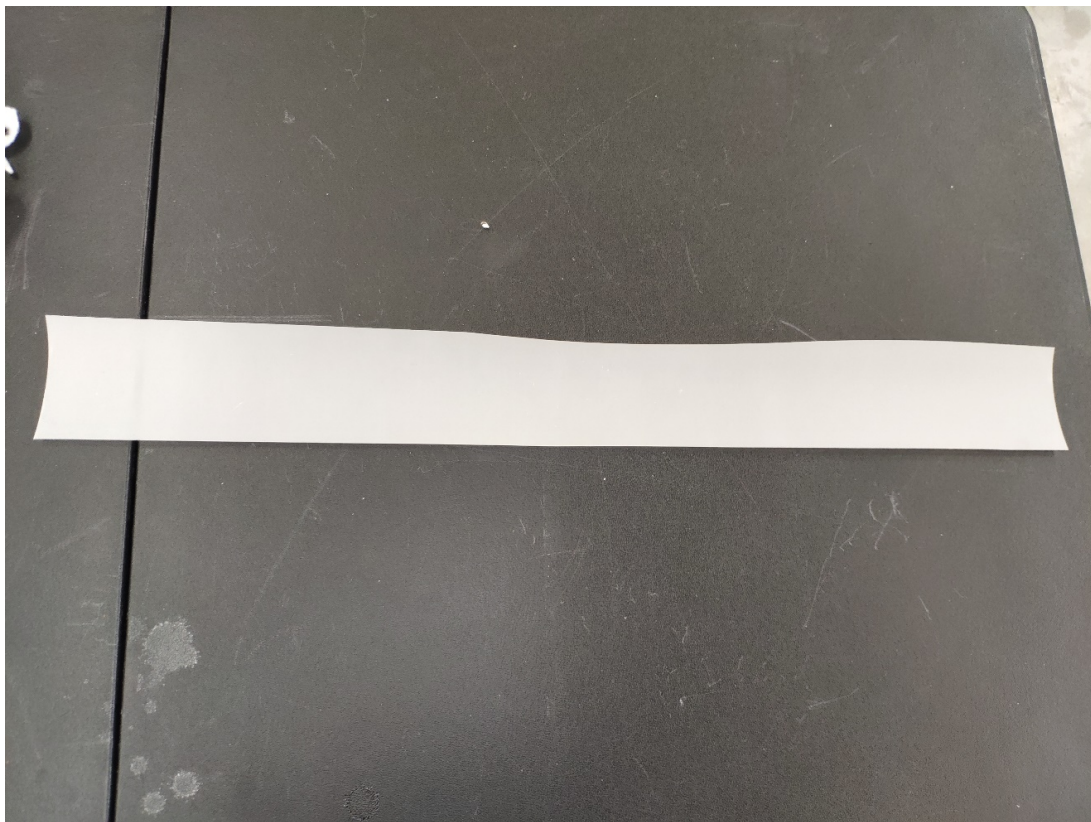


Figure 6.15: Acetate sheet used as the base substrate.

- Kapton tape was applied over the acetate sheet for electrical insulation and thermal stability (Figure 6.16).



Figure 6.16: Application of Kapton tape onto acetate substrate.

- Copper tape with adhesive backing was applied over the Kapton tape, forming the conductive surface for the circuit pattern (Figure 6.17).

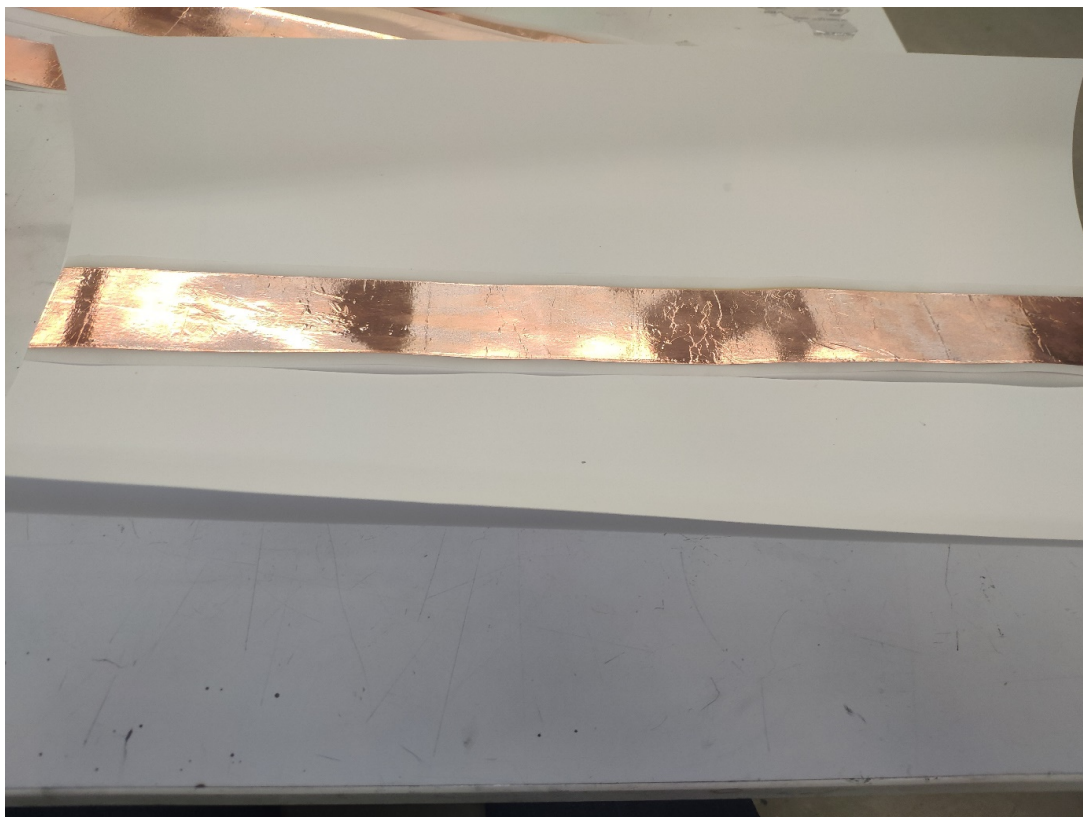


Figure 6.17: Application of copper tape over Kapton tape layer.

- The copper tape surface was cleaned prior to applying the mask.

6.2.2 Mask Application and Etching

- The circuit pattern was manually drawn onto the copper tape using an etch-resistant pen (e.g., permanent marker) to create a mask (Figure 6.18).



Figure 6.18: Manually drawing the circuit mask onto the copper tape surface.

- The mask quality was visually verified to ensure all circuit traces and pads were covered, with corrections made as needed.
- The substrate (acetate, Kapton, copper tape with mask) was submerged in ferric chloride (FeCl_3) to etch away exposed copper, leaving the desired circuit pattern (Figure 6.19).
- Etching progress was monitored to prevent under- or over-etching.
- After etching, the board was neutralized (e.g., with baking soda solution), rinsed, and the ink mask was removed with isopropyl alcohol, followed by final cleaning.

6.2.3 Completion and Testing

- The resulting circuit on the flexible substrate was cleaned, and necessary holes for component leads or vias were made (Figure 6.20).
- Continuity testing was performed using a multimeter to verify circuit integrity and check for short circuits.
- Copper pads for sensor mounting (per drawing T_02_03) were prepared with surface treatment (e.g., cleaning, flux application) for soldering or adhesive bonding in the next step.
- Preliminary preparations requiring temperature control to prevent damage to the flexible substrate were considered at this stage.

6.3 Sensor Integration

This step focuses on integrating the sensing elements onto the fabricated Flex PCB (Figure 6.20) to complete the smart layer assembly (drawing T_02_03).

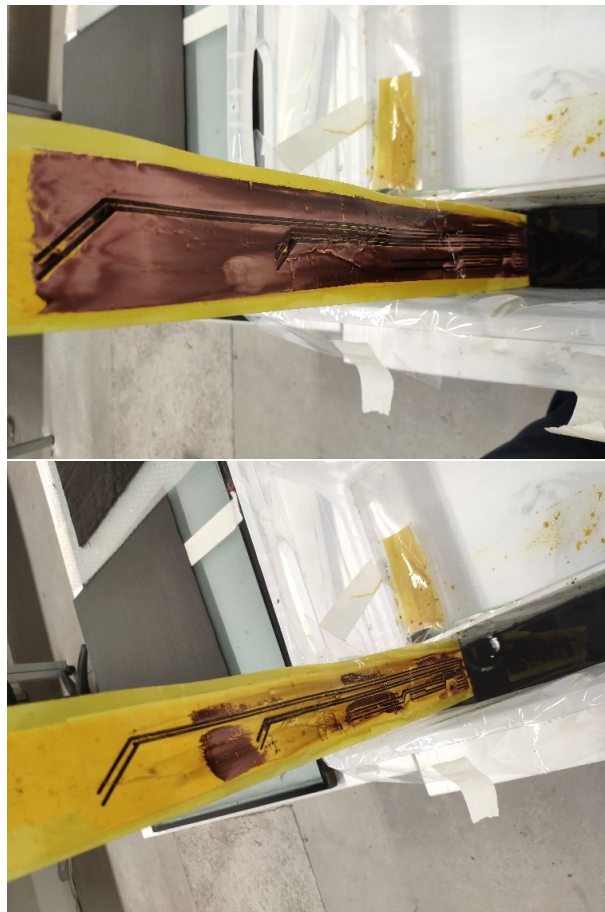


Figure 6.19: Etching process to remove unwanted copper tape.

- **Sensor Preparation and Verification:** Piezoelectric sensors (drawing T_01_04) and any other sensors (e.g., strain gauges) were inspected, functionally tested, and prepared per manufacturer recommendations, including surface treatments and wire attachment verification.
- **Sensor Attachment:** Sensors were positioned and attached to designated locations on the Flex PCB using appropriate adhesives (epoxy, per drawing T_02_03), ensuring precise placement for functionality.

6.4 Waterjet Cutting

Following the preparation of components (cured CFRP laminates from Step 1, potentially with smart layers, and the Flex PCB/smart layer from Steps 2 and 3), waterjet cutting was employed to meet exact dimensional requirements for the sandwich structure. This method was chosen to avoid thermal stress or delamination in composites and the aluminum honeycomb core (drawing T_01_03).

6.4.1 Cutting Path Preparation

- Digital cutting paths were generated based on the dimensions in drawings T_01_01, T_01_03, T_02_01, and T_02_02, and programmed into the waterjet cutting machine's control software (Figure 6.21).



Figure 6.20: Fabricated Flex PCB after etching and cleaning.



Figure 6.21: Waterjet cutting path program interface/CAD.

6.4.2 Component Cutting

- Components like cured CFRP laminates and the aluminum honeycomb core were fixtured onto the waterjet cutting bed, and pre-programmed paths were executed using a high-pressure water stream with abrasive particles (Figures 6.22 and 6.23).



Figure 6.22: Waterjet cutting process for CFRP laminate.



Figure 6.23: Waterjet cutting of CFRP with smart layer.

6.4.3 Post-Cutting Inspection

- Components were removed, cleaned of residual abrasive material, and inspected for dimensional accuracy and cut quality before final assembly.

6.5 Sandwich Structure Assembly

This final step assembles the cut components into the sandwich structure per drawing T_03_01.

6.5.1 Component Preparation

- CFRP face sheets with embedded smart layers (T_02_01, T_02_02) and the aluminum honeycomb core (T_01_03) were cleaned with a grease remover (per drawing T_03_01) and kept in a dry environment.
- Edge closeouts for the honeycomb core were prepared to prevent adhesive ingress

into the cells.

- Araldite 2015 adhesive was prepared per manufacturer specifications, with personal protective equipment (mask, safety glasses, gloves) used during handling. Tools including an adhesive gun, spreading tool, and clamps were readied (Figure 6.24).



Figure 6.24: Adhesive, PPE, and tools for bonding (Araldite 2015, gun, spreader, clamps).

- Components were handled using registration marks to ensure proper alignment during stacking.

6.5.2 Assembly Sequence and Bonding

- The sandwich structure was assembled layer by layer per drawing T_03_01: bottom CFRP (T_02_02), core (T_01_03), top CFRP (T_02_01).
- Araldite 2015 adhesive was applied to the bonding surface of the first CFRP face sheet (T_02_02) using the application gun (Figure 6.25).
- The adhesive was spread uniformly using the spreading tool to achieve a consistent bond line (Figure 6.26).
- The aluminum honeycomb core (T_01_03) was placed onto the adhesive layer on the first CFRP sheet, ensuring alignment (Figure 6.27).
- Adhesive was applied and spread on the exposed core surface or the inner surface of the second CFRP face sheet (T_02_01), which was then placed on top of the core.
- For the plain CFRP assembly (T_03_02), Araldite 2015 was applied and spread between two CFRP layers (T_01_01).
- The stack was placed under uniform pressure using clamps for approximately 8 hours to allow curing of the Araldite 2015 adhesive at ambient temperature (Figure 6.28).

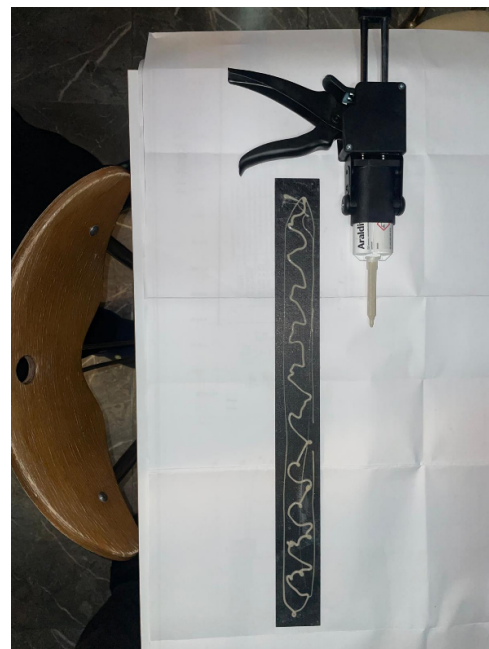


Figure 6.25: Applying Araldite 2015 adhesive to CFRP face sheet using application gun.



Figure 6.26: Spreading the applied adhesive uniformly.

6.5.3 Final Processing and Verification

- After curing, clamps were removed, and the panel was processed: excess adhesive was trimmed, and edges were sealed if required.
- A final functional test of the embedded sensors confirmed their integrity.
- Dimensional verification ensured compliance with drawing T_03_01 (e.g., overall thickness of 9.2 mm).
- Surface preparation for test fixture attachment was completed if required (Figure 6.29).



Figure 6.27: Placing the pre-cut aluminum honeycomb core onto the adhesive.



Figure 6.28: Assembled panel under clamping pressure for curing (8 hours).

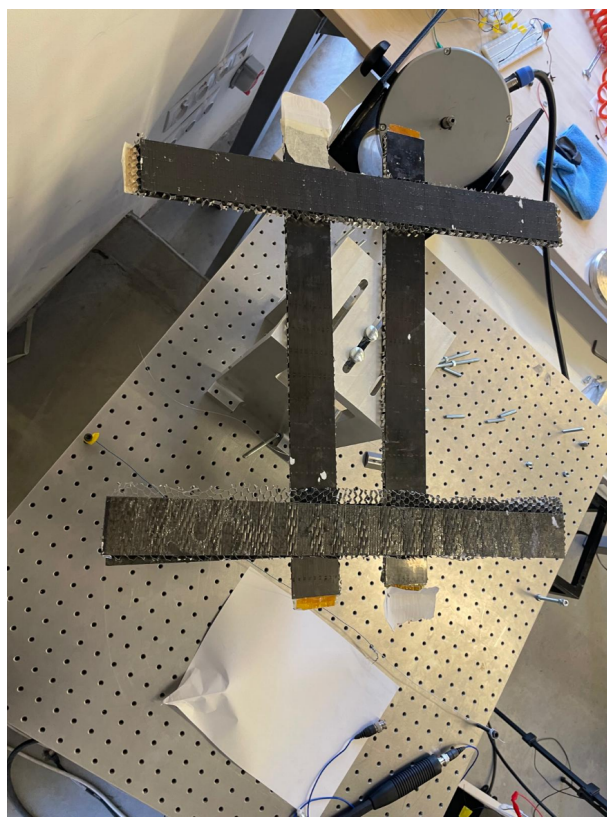


Figure 6.29: Final assembled sensor-integrated sandwich plate.

6.6 Conclusion

This five-step manufacturing process successfully produced both sensor-integrated composite sandwich structures (T_03_01) and simpler plain CFRP assemblies (T_03_02).

The process included CFRP laminate fabrication (with and without smart layers), Flex PCB creation, sensor integration, precision waterjet cutting, and final assembly using Araldite 2015 adhesive. Quality control checks, such as vacuum drop tests, continuity testing, and functional sensor verification, along with adherence to specified materials and procedures in the technical drawings (T_01_01 through T_03_02), ensured that the final components met their structural and functional requirements.

7 Engineering Analysis

7.1 Modal Analysis and System Identification

7.1.1 Modal Analysis

Modal analysis is a process used to express a system's dynamic behavior in terms of natural frequencies, damping factors, and mode shapes, ultimately creating a mathematical model. This information constitutes the system's modal data. Modal analysis relies on the principle that the vibration of a linear system can be represented as a linear combination of simple harmonic motions, referred to as the "natural modes of vibration." Natural modes are unique to each system and are determined by its physical properties. Each mode is defined by its modal parameters: natural frequency, modal damping factor (the rate of oscillation decay), and mode shape (the characteristic displacement pattern in a specific mode). Each natural frequency corresponds to a distinct mode shape. The contribution of modes to the overall vibration varies with excitation, damping ratio, and the system's mode order.

In this analysis, the Euler-Bernoulli beam theory is used to derive the equation of motion. All equations are formulated for the transverse free vibration of a cantilever thin beam. The Euler-Bernoulli, or thin beam, theory is applicable when the length of the beam is greater than ten times its depth. The transverse displacement of the centerline is represented by $w(x,t)$, which serves as the state variable of the model. This project focuses on the first four modes of vibration.

According to the Euler-Bernoulli beam theory, the equation of motion for free vibration is:

$$EI \frac{\partial^4 w(x,t)}{\partial x^4} + \rho A \frac{\partial^2 w(x,t)}{\partial t^2} = 0 \quad (7.1)$$

Where:

- E : Young's modulus (Pa)
- I : moment of inertia of the beam's cross-section (m^4)
- ρ : density of the beam material (kg/m^3)
- A : cross-sectional area of the beam (m^2)
- $w(x,t)$: transverse displacement of the beam centerline (m), a function of position x and time t

The displacement of the centerline is defined as a function of x (position along the length of the beam) and t (time). Using separation of variables, it is expressed as:

$$w(x,t) = W(x)T(t)$$

Here, $W(x)$ represents the mode shape of the beam. After applying the boundary conditions for a cantilever beam, the mode shape is derived as:

$$W_n(x) = (\cos \beta_n x - \cosh \beta_n x) - \frac{(\cos \beta_n l + \cosh \beta_n l)}{\sin \beta_n l + \sinh \beta_n l} (\sin \beta_n x - \sinh \beta_n x)$$

where n is the mode number, and β_n is related to the natural frequency by:

$$\beta^4 = \frac{\rho A \omega^2}{EI}$$

Where:

- $W_n(x)$: mode shape function for the n -th mode
- β_n : wave number for the n -th mode (m^{-1})
- l : length of the beam (m)
- ω : angular natural frequency (rad/s)

The time-dependent function $T(t)$ describes the temporal variation of the displacement. Its solution is:

$$T(t) = A \cos \omega t + B \sin \omega t$$

Since this model is created with impact excitation (no displacement at $t = 0$), the solution simplifies to:

$$T(t) = B_n \sin \omega_n t$$

Where:

- $T(t)$: time-dependent displacement function
- A, B, B_n : constants determined by initial conditions
- ω_n : natural frequency of the n -th mode (rad/s)

The natural frequency is also derived from the Euler-Bernoulli equation of motion as:

$$\omega_n = (\beta_n l)^2 \sqrt{\frac{EI}{\rho A L^4}}$$

Where:

- ω_n : natural frequency of the n -th mode (rad/s)
- L : length of the beam (m), equivalent to l

7.1.2 Modal Matrices

The mass and stiffness matrices are extracted using a numerical approach, specifically the finite element method.

The modal mass matrix is estimated as:

$$[M] = \rho A \int_0^L W(x) W(x)^\top dx$$

The stiffness matrix is given by:

$$[K] = EI \int_0^L \frac{d^2 W_i(x)}{dx^2} \frac{d^2 W_j(x)}{dx^2} dx$$

Using this method, we obtain diagonal mass and stiffness matrices, which simplify subsequent analyses.

Where:

- $[M]$: mass matrix
- $[K]$: stiffness matrix
- $W(x)$: mode shape function
- $W_i(x), W_j(x)$: mode shape functions for the i -th and j -th modes

7.1.3 Damping Matrix

The damping matrix is estimated using proportional (Rayleigh) damping. The damping matrix is more complex than the mass and stiffness matrices. However, using proportional modal matrices simplifies the analysis. By constructing the damping matrix as a linear combination of the mass and stiffness matrices, which are already diagonal, we obtain a diagonal damping matrix. The mass and stiffness matrices are multiplied by different constants to model the system's damping behavior:

$$[C] = \alpha[M] + \beta[K]$$

To determine the constants α and β , the equation of motion is considered:

$$[M]\ddot{x} + [C]\dot{x} + [K]x = f(t)$$

Substituting the damping matrix expression:

$$[M]\ddot{x} + (\alpha[M] + \beta[K])\dot{x} + [K]x = f(t)$$

In modal coordinates, the displacement is expressed as $x(t) = [X]\eta(t)$, where $\eta(t)$ represents the modal coordinates. The equation becomes:

$$\ddot{\eta}(t) + (\alpha[I] + \beta[\omega_i^2])\dot{\eta}(t) + [\omega_i^2]\eta(t) = [X]^\top \vec{f} = Q$$

The damping coefficients are defined by:

$$\alpha + \beta\omega_i^2 = 2\zeta_i\omega_i, \quad i = 1, 2, \dots, n$$

The damping ratios ζ_i are determined empirically. The constants α and β are then derived from the relationship between ζ_i and ω_i . The i -th frequency of damped vibration is given by:

$$\omega_{di} = \sqrt{1 - \zeta_i^2}\omega_i$$

The damped frequencies ω_{di} should be closer to the empirical natural frequencies than the undamped frequencies ω_n .

Where:

- $[C]$: damping matrix
- α, β : Rayleigh damping coefficients
- $[I]$: identity matrix
- $\eta(t)$: modal coordinates
- $[X]$: modal matrix
- \vec{f} : external force vector
- Q : generalized force in modal coordinates
- ζ_i : damping ratio for the i -th mode
- ω_{di} : damped natural frequency for the i -th mode (rad/s)

7.1.4 State-Space Representation

For an n -degree-of-freedom system, the equation of motion can be expressed as:

$$[M]\ddot{x} + [C]\dot{x} + [K]x = f$$

$$\ddot{x} = [M]^{-1}(-[C]\dot{x} - [K]x + f)$$

The state-space equations for linear systems are:

$$\dot{x} = Ax + Bu$$

$$y = Cx$$

Where the state vector is defined as:

$$x = \begin{bmatrix} w \\ \dot{w} \end{bmatrix}$$

The matrices A , B , and C are represented as:

$$A = \begin{bmatrix} 0 & I \\ -[M]^{-1}[K] & -[M]^{-1}[C] \end{bmatrix}, \quad B = \begin{bmatrix} 0 \\ [M]^{-1} \end{bmatrix}, \quad C = [I \ 0]$$

Solving the characteristic equation of the A matrix for free vibration provides the eigenvalues and eigenvectors of the system:

$$\det(A - \lambda I) = 0$$

$$(A - \lambda I)v = 0$$

The corresponding eigenvector v describes the mode shape of the system at the natural frequency. If the system includes damping, each eigenvalue λ is a complex conjugate pair representing the system's frequencies [Rao, 2019]:

$$\lambda = -\zeta\omega_n \pm j\omega_d$$

Where:

- x : state vector
- u : input vector (force f)
- y : output vector
- A : system matrix
- B : input matrix
- C : output matrix
- w : displacement vector
- \dot{w} : velocity vector
- λ : eigenvalue
- v : eigenvector
- ω_d : damped natural frequency (rad/s)

7.1.5 System Identification

System identification is the process of building mathematical models of dynamic systems from observed input-output data. The goal is to estimate the parameters of a model that best describes the system's behavior [Ljung, 2010].

There are several methods for system identification. The Observer/Kalman Filter Identification (OKID) method is a time-domain technique that simultaneously estimates the state-space model and Kalman filter gain matrices using measured input and output data. OKID is particularly effective for noisy data. Another method, the Eigenvalue Realization Algorithm (ERA), is well-suited for identifying the modal parameters and state-space models of vibrating systems from their input and output data. The steps for applying ERA are:

1. **Data Acquisition:** Measure the vibration response (displacement) due to the input force.
2. **Markov Parameter Estimation:** Compute the Markov parameters of the system.

For a discrete-time system, the dynamics are described by:

$$x(k+1) = Ax(k) + Bu(k)$$

$$y(k) = Cx(k)$$

The Markov parameters are defined as:

$$Y_k = CA^{k-1}B$$

3. **Hankel Matrix Construction:** Construct the generalized Hankel matrix:

$$H(k-1) = \begin{bmatrix} Y_k & \cdots & Y_{k+\beta-1} \\ \vdots & \ddots & \vdots \\ Y_{k+\alpha-1} & \cdots & Y_{k+\alpha+\beta-1} \end{bmatrix} = P_\alpha A^{k-1} Q_\beta$$

4. **Singular Value Decomposition (SVD):** For $k = 1$, apply SVD to the Hankel matrix:

$$H(0) = R\Sigma S^\top$$

This can be factored as:

$$H(0) = R\Sigma S^\top = \left(R\Sigma^{\frac{1}{2}}\right) \left(\Sigma^{\frac{1}{2}} S^\top\right) \triangleq \{P\}\{Q\}$$

Here, $\{P\}$ and $\{Q\}$ are the observability and controllability matrices, respectively:

$$Q_n = [B \ AB \ \cdots \ A^{n-1}B]$$

$$P_n = \begin{bmatrix} C \\ CA \\ \vdots \\ CA^{n-1} \end{bmatrix}$$

The estimated system matrix \hat{A} is then computed as:

$$\hat{A} = \Sigma^{-\frac{1}{2}} R^\top H(1) S \Sigma^{-\frac{1}{2}}$$

Quantities with a hat ($\hat{\cdot}$) denote estimated values to distinguish them from the true values [Illingworth et al., 2010].

The eigenvalues of the estimated \hat{A} matrix provide direct access to the system's modal frequencies and damping ratios. The eigenvectors describe the mode shapes, revealing how different parts of the beam move relative to one another during each vibration mode. This enables real-time estimations and the development of damage detection algorithms.

Where:

- $x(k)$: state vector at time step k
- $u(k)$: input vector at time step k
- $y(k)$: output vector at time step k
- A : system matrix
- B : input matrix
- C : output matrix
- Y_k : Markov parameter at time step k
- $H(k - 1)$: Hankel matrix
- P_α, Q_β : observability and controllability matrices
- R, Σ, S : matrices from SVD decomposition
- \hat{A} : estimated system matrix

7.1.5.a Advantages of ERA

- **Identification of System Dynamics Under External Excitation:** ERA aims to identify the system's modal parameters, allowing for a direct characterization of the system's dynamic behavior under operational conditions.
- **Validation of the Input-Output Model:** The precision of models can be validated by comparing the predicted output of the ERA-identified state-space model to the measured output.
- **Estimation of System Matrices (A, B, C):** ERA directly provides the discrete-time state-space matrices, which fully describe the linear dynamic behavior of the system.
- **Robustness to Noise:** While not explicitly a noise-handling algorithm like Kalman filtering in OKID, the SVD step in ERA helps separate the dominant system dynamics from noise components in the data.

7.1.6 Verification and System Prediction Capabilities

- **Model Validation:** The state-space model obtained from identification can be validated by simulating its response to a known input and comparing the simulated output to the measured output. The Normalized Root Mean Square Error (NRMSE) can be used to assess the accuracy of the fit. Additionally, using this identified model for damaged components can facilitate the detection of issues, and the data can be used for model training.
- **Prediction of Response to Arbitrary Inputs:** Once a reliable state-space model is identified, it can be used to predict the system's response to any arbitrary input within the linear operating range of the system.

- **Control Design:** The identified state-space model provides a basis for designing controllers to modify the system's dynamic behavior, such as reducing vibrations or improving the system's response characteristics under forced excitation.
- **Fault Detection and Diagnosis:** Changes in the identified system matrices or modal parameters over time, under similar operating conditions, can indicate potential faults or changes in the structural integrity of the cantilever beam.

7.2 Modeling and System Identification Results

This section presents the modeling and system identification results for the CFRP sandwich composite plate with embedded sensors. The analysis includes calculating natural frequencies, analyzing experimental frequency response data, constructing damping and state-space models, and applying the Eigensystem Realization Algorithm (ERA) to identify the system's dynamic characteristics.

7.2.1 Properties

The physical properties of the modeled CFRP sandwich composite plate are as follows:

- $L = 0.465 \text{ m}$ (length)
- $\rho = 2074.07 \text{ kg/m}^3$ (mass density)
- $E_x = 2.56 \times 10^{10} \text{ Pa}$ (modulus of elasticity)
- $A = 5 \times 10^{-4} \text{ m}^2$ (cross-sectional area)
- $I = 9.22 \times 10^{-10} \text{ kg} \cdot \text{m}^2$ (area moment of inertia)

7.2.2 Natural Frequency

Natural frequencies for free vibration were calculated using Equation (7.4) from Section 7.4.2. The results for the first four modes are presented in Table 7.1.

Mode Number	Natural Frequency (Hz)
1	107.9
2	676.9
3	1894.7
4	3712.9

Table 7.1: Natural frequencies of the first four modes for the CFRP sandwich composite plate.

The first natural frequency of 107.9 Hz is consistent with the structural stiffness of lightweight yet stiff composite materials, such as the carbon fiber reinforced sandwich structure used in this study.

7.2.3 FFT and FRF Graphs of Experimental Data

Frequency response analysis for free vibration of the embedded piezo sensors was performed using Fast Fourier Transform (FFT) and Frequency Response Function (FRF) graphs.

The FFT of an embedded sensor's response is shown in Figure 7.1. The calculated natural frequencies in Table 7.1 align well with the FFT data. The first and second peaks in the FRF graph (Figure 7.2) are approximately satisfactory, showing the first mode at 104 Hz and the second mode at 635.5 Hz. Since the system is damped, the natural frequencies differ slightly from the experimental data, with damped frequencies expected to be closer to the experimental responses.

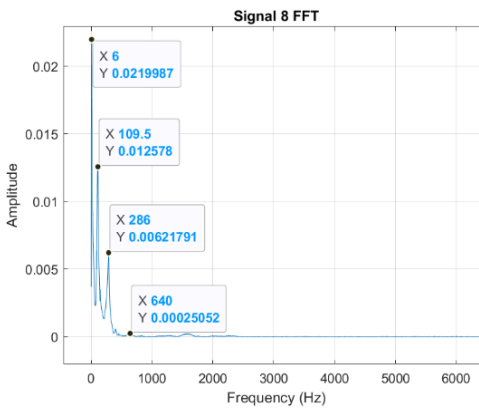


Figure 7.1: FFT of an embedded sensor.

The FRF graph due to an impulse input is shown in Figure 7.2. The damping ratio (ζ) for the second mode was estimated using the half-power method from this figure.

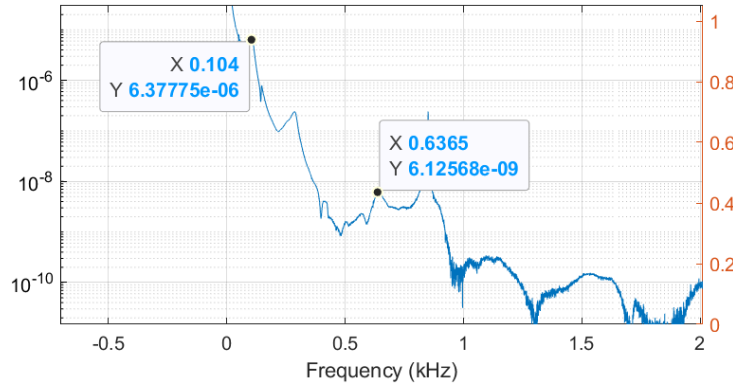


Figure 7.2: FRF graph due to impulse input.

The first damping ratio (ζ_1) was calculated using the logarithmic decrement method, due to the pronounced effect of the first mode in the velocity data (Figure 7.5). Power spectra were obtained by applying filters around 100 Hz and 600 Hz, as shown in Figures 7.3 and 7.4.

7.2.4 Damping and State-Space Modeling

Mode shapes were determined using boundary conditions for a cantilever beam. Modal matrices were constructed using the effective bending stiffness ($EI_{\text{efficient}}$), density (ρ), length (L), and area (A).

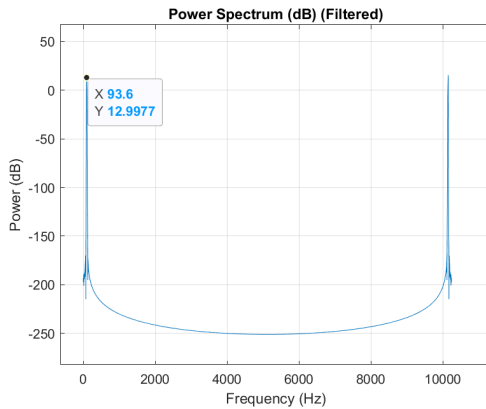


Figure 7.3: Power spectrum of filtered FFT data (around 100 Hz).

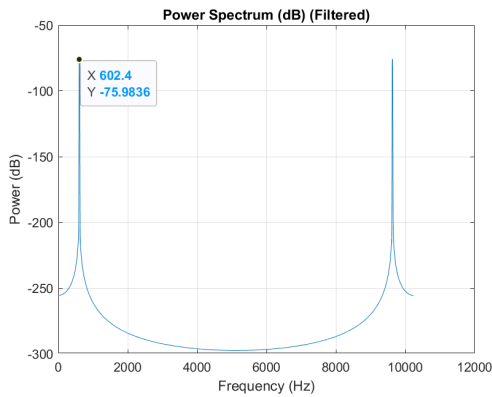


Figure 7.4: Power spectrum of filtered FFT data (around 600 Hz).

The damping matrix was obtained from the mass and stiffness matrices using Rayleigh (proportional) damping, with damping ratios ζ_1 and ζ_2 used to compute the Rayleigh damping coefficients. The resulting damping matrix $[C]$ is:

$$[C] = \begin{bmatrix} 54.58 & -0.0481 & -0.016 & -0.0012 \\ -0.0481 & 63.15 & 0.0176 & -0.008 \\ -0.016 & 0.0176 & 122.96 & -0.0068 \\ -0.0012 & -0.008 & -0.0068 & 317.81 \end{bmatrix} \quad (7.2)$$

A diagonal damping matrix simplifies analysis by ensuring damping forces are proportional to the velocities of individual degrees of freedom without coupling.

Using the modal parameters, state-space matrices $[A]$, $[B]$, and $[C]$ were derived. Since the system is linear, the $[D]$ matrix is zero. The impulse response of the state-space model is compared with experimental velocity data in Figure 7.5. The model output, originally in displacement, was differentiated to match the experimental velocity measurements.

While the initial correlation is strong, differences become apparent in modes beyond the second mode, as shown in a 0.1-second comparison in Figure 7.6. This divergence is acceptable given the differentiation of the model data.

Experimental velocity data from a laser vibrometer was integrated to obtain displacement for comparison with the model, as shown in Figure 7.7. However, integrating velocity data can introduce errors if the signal has a non-zero mean or low-frequency noise.

Despite potential errors in the integrated experimental data, the model's estimated dis-

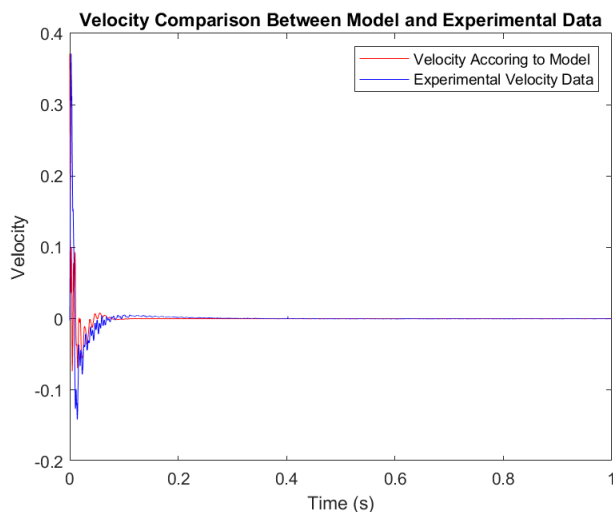


Figure 7.5: Velocity comparison between model and experimental data.

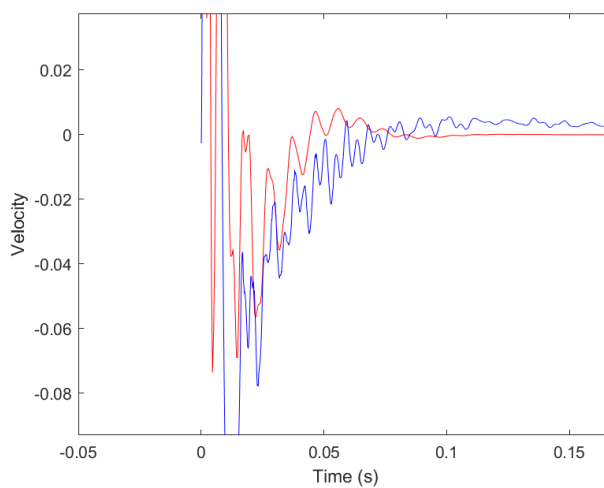


Figure 7.6: Comparison of velocity data over 0.1 seconds.

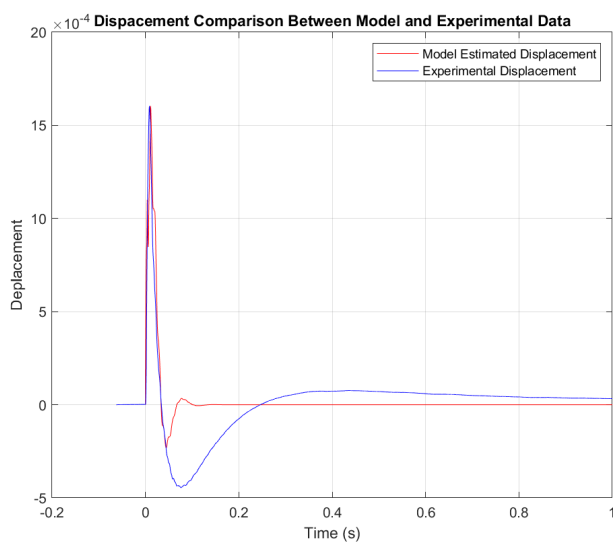


Figure 7.7: Displacement comparison between model and experimental data.

placement is valid, especially for the first 0.05 seconds, as shown in a 0.1-second comparison in Figure 7.8.

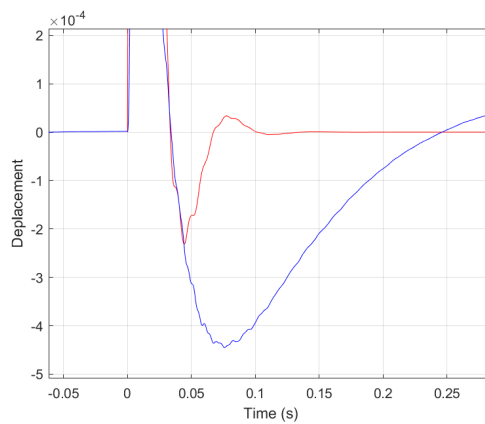


Figure 7.8: Comparison of displacement data over 0.1 seconds.

7.2.5 Eigensystem Realization Algorithm (ERA)

The dynamic characteristics of the system were investigated using system identification techniques. The methodology involved transitioning a continuous-time state-space representation into a discrete-time framework, applying the Eigensystem Realization Algorithm (ERA), and comparing the reconstructed velocity response with experimental measurements.

The discrete-time state matrix $[A_d]$, a key output of the ERA process, was obtained. Its eigenvalues provide insights into the system's natural frequencies and damping ratios. The reconstructed velocity response using these eigenvalues is compared with experimental data in Figure 7.9.

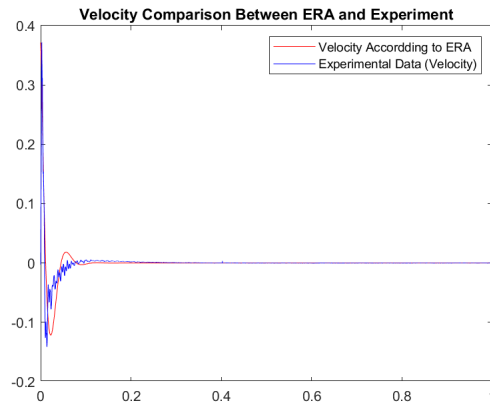


Figure 7.9: Comparison of velocity data between ERA and experimental results.

A Hankel matrix was constructed from the discrete-time state-space model outcomes. Singular Value Decomposition (SVD) was applied to the Hankel matrix, and the resulting singular values (σ) were extracted and sorted by magnitude. These values are visualized in Figure 7.10.

The singular value spectrum indicates that the system's energy is concentrated after the third mode, with a rapid decay in singular values. This suggests that the system's dynamic behavior can be effectively represented using the first three modes.

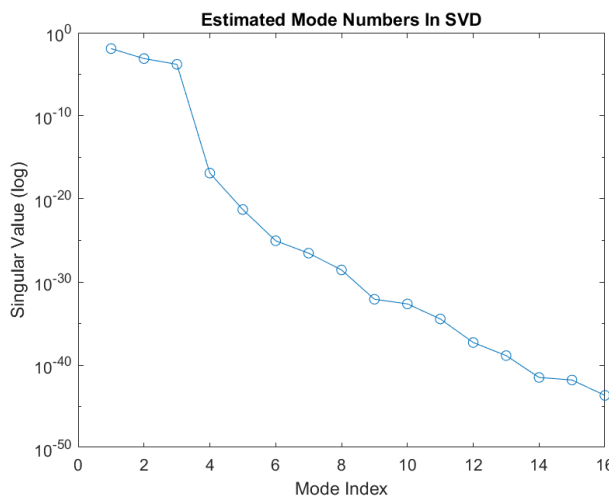


Figure 7.10: Mode number estimation from SVD singular values.

7.3 Finite Element Method (FEM) Analysis

This chapter presents the Finite Element Method (FEM) analysis of the smart sandwich composite structure using Abaqus software. The primary objective was to determine the natural frequencies of the structure's first four bending modes and validate the dynamic behavior against experimental and analytical results from previous chapters. The analysis includes model definition, material property assignment, element selection, mesh convergence study, and modal analysis results, providing a comprehensive understanding of the structure's vibrational characteristics.

7.3.1 Model Definition

The FEM model was created to accurately represent the dimensions and boundary conditions of the manufactured composite sandwich beam specimen, as tested in Chapter 8. The geometric properties of the model are as follows:

- **Dimensions:**
 - Width: 50 mm
 - Length: 500 mm (Free length: 465 mm)
 - Height: 9.2 mm
- **Layers:**
 - CFRP (Carbon Fiber Reinforced Polymer) layers on the top and bottom surfaces
 - Aluminum honeycomb core
 - Fiber angles of the CFRP layers: 4 layers in [0/90/0/90] sequence
- **Boundary Conditions:** Consistent with the experimental setup, a 35 mm section of the model was defined as fixed (clamped), simulating the 465 mm free vibrating section, as shown in Figure 7.11.



Figure 7.11: Sandwich plate with the clamp point marked, illustrating the fixed boundary condition.

7.3.2 Material Properties

The material properties used in the FEM model are critical for accurately simulating the dynamic behavior of the smart sandwich composite structure. The CFRP layers were modeled as orthotropic, defined using engineering constants, while the aluminum honeycomb core was modeled as isotropic. The properties are summarized in Table 7.2.

Material	Property	Value	Unit
	E_1	147.5	GPa
	E_2	17.0	GPa
	E_3	17.0	GPa
	v_{12}	0.3	—
CFRP (Orthotropic)	v_{13}	0.3	—
	v_{23}	0.3	—
	G_{12}	5.404	GPa
	G_{13}	5.404	GPa
	G_{23}	5.404	GPa
	Density (ρ)	1900	kg/m ³
	Young's Modulus (E)	69	GPa
Aluminum (Isotropic)	Poisson's Ratio (ν)	0.34	—
	Density (ρ)	2710	kg/m ³

Table 7.2: Material properties used in the FEM model for the CFRP layers and aluminum honeycomb core [Boyer and Gall, 1985].

The orthotropic properties of the CFRP layers (E_1 , E_2 , E_3 , v_{12} , v_{13} , v_{23} , G_{12} , G_{13} , G_{23}) account for the directional dependence of mechanical behavior due to the fiber and matrix orientation. In contrast, the aluminum honeycomb core is modeled as isotropic, with properties defined by its Young's modulus (E), Poisson's ratio (ν), and density (ρ). These material definitions are fundamental to the accuracy of the modal analysis, as they influence the structure's stiffness, mass, and vibrational characteristics. The CFRP material properties listed here were calculated using a MATLAB code, which is detailed in Appendix A.

7.3.3 Element Type and Mesh

Selecting the appropriate element type for modal analysis of sandwich composites in Abaqus requires balancing accuracy and computational efficiency. Three common element types were considered, as summarized in Table 7.3.

Feature	Conventional Shell Elements	Continuum Shell Elements	Solid Elements	Ele-
Suitability	Thin face sheets	Entire sandwich thickness	Thick cores	compos-complex
Accuracy (General)	Lower	Medium	High	
Accuracy (Through-Thickness Effects)	Limited	Moderate	High	
Accuracy (Complex Cores)	Limited	Moderate	High	
Computational Cost	Low	Medium	High	
Mesher Complexity	Low	Medium	High	
Typical Applications	Thin sandwich panels	Moderately thick panels	Thick panels, complex cores, localized effects	

Table 7.3: Comparison of element types for FEM analysis of sandwich composites.

The entire sandwich composite structure was modeled using C3D8R solid elements in Abaqus. The C3D8R element is a linear brick element with reduced integration, chosen for the following reasons:

- **Accuracy for Thick Composites and Complex Cores:** Solid elements like C3D8R are preferred for composite structures with complex core geometries, such as the honeycomb core used in this study [Kayran, 2013, Mobark et al., 2024]. They provide a detailed representation of the geometry and stiffness properties of both the face sheets and the core.

- **Capture of Through-Thickness Effects:** Solid elements accurately capture through-thickness shear deformation and stresses, which are significant in sandwich composites, especially for higher-order bending modes [Hsu, 1976].
- **Suitability for Honeycomb Core:** The cellular structure of the honeycomb core is effectively represented using solid elements, allowing for a direct simulation of its contribution to the overall bending stiffness.

A hex-dominated mesh was employed, primarily using hexahedral elements (C3D8R) while incorporating tetrahedral elements in geometrically complex regions to avoid excessive mesh distortion. Hexahedral elements offer better accuracy and convergence rates compared to tetrahedral elements, particularly for bending analysis [Mobark et al., 2024]. This meshing strategy balances accuracy and computational efficiency while accommodating the geometric complexity of the honeycomb core.

The modal analysis was performed to extract the natural frequencies and corresponding mode shapes, focusing on the first four bending modes of the sandwich composite structure. The results provide insights into the dynamic characteristics of the composite under bending loads.

7.3.4 Mesh Convergence

The accuracy of Finite Element Analysis (FEA) depends significantly on mesh quality. A mesh convergence study was conducted to ensure that the numerical solution accurately reflects the physical behavior while balancing precision and computational cost. The study involved systematically refining the mesh by reducing element size (h-method) and monitoring the natural frequency of a specific mode until the results stabilized. Convergence is typically achieved when the percentage change between successive refinements falls below a set tolerance, often 1–5% [Kumar et al., 2023].

The convergence study was performed using C3D8R elements for the core, monitoring a specific mode value (assumed to be the third mode, based on the values provided) against varying mesh sizes. The results are presented in Table 7.4.

Mesh Size (mm)	Mode Value (Hz)	Change from Previous (Finer Mesh)	% Change from Previous
4.5	1334.9	—	—
3.0	1331.8	-3.1	-0.20%
1.5	1316.2	-15.6	-0.99%
1.25	1317.3	1.1	0.07%
1.0	1290.8	-26.5	-1.70%
0.75	1311.0	20.2	1.32%
0.5	1307.9	-3.1	-0.20%

Table 7.4: Mesh convergence study results, showing the third mode natural frequency versus mesh size.

The data shows fluctuations in the mode value as the mesh is refined. A minimal change (0.07%) is observed between mesh sizes 1.5 mm and 1.25 mm, but larger variations occur with further refinement, including a significant drop (-1.70%) at mesh size 1.0 mm and a subsequent increase (1.32%) at 0.75 mm. The expected trend of smooth stabilization is

not clearly observed. However, the final refinement step (from 0.75 mm to 0.5 mm) shows a small percentage change (-0.20%). Therefore, for the purpose of this analysis, the mesh size of 0.5 mm is considered the convergence point, as it aligns with the finest mesh and a small change in mode value.

7.3.5 Analysis Results

The modal analysis was performed using the defined model, material properties, boundary conditions, and the converged mesh with an element size of 0.5 mm. The analysis successfully extracted the natural frequencies for the first four bending modes of the cantilevered sandwich composite beam, as presented in Table 7.5.

Mode Number	Natural Frequency (Hz)
1	105.41
2	558.71
3	1307.9
4	2139.2

Table 7.5: Natural frequencies of the first four bending modes from FEM analysis.

These natural frequencies represent the fundamental vibrational modes of the structure under the specified clamped-free boundary conditions. The results can be compared with the analytical frequencies from Chapter 7.2 (Table 7.1) and experimental data from Chapter 8. For instance, the first mode frequency of 105.41 Hz aligns closely with the analytical value of 107.9 Hz and the experimental value of 104 Hz, indicating good agreement across methods.

The corresponding mode shapes, illustrating the deformation patterns for each frequency, were also obtained from the analysis. These mode shapes are presented in Appendix C, as Figures C.1 to C.4, providing a visual representation of the beam's vibrational behavior.

7.3.6 Summary

The FEM analysis successfully characterized the dynamic behavior of the smart sandwich composite structure using Abaqus software. The model accurately represented the geometry, material properties, and boundary conditions of the experimental setup, with C3D8R solid elements chosen to capture the complex behavior of the honeycomb core and through-thickness effects. A mesh convergence study identified a mesh size of 0.5 mm as the convergence point, ensuring reliable results. The modal analysis extracted the natural frequencies of the first four bending modes, showing good agreement with analytical and experimental results from previous chapters. The mode shapes, included in the appendix, provide further insight into the vibrational behavior of the structure, supporting its use in structural health monitoring applications.

The mode shape figures referenced in Section 7.3.5 will be included in Appendix C. This appendix contains four figures (Figures C.1 to C.4), illustrating the deformation patterns for the first four bending modes of the sandwich composite beam.

7.4 Validation of FEA

Validation is a critical step in Finite Element Analysis (FEA) to ensure the accuracy and reliability of the simulation model. This section compares the natural frequencies and mode shapes predicted by Abaqus modal analysis for the modeled structures against theoretical calculations based on fundamental engineering equations. Close agreement between computational and analytical results confirms that the FEA model accurately represents the physical system's behavior, validating the chosen geometry, material properties, boundary conditions, and mesh configuration.

7.4.1 Equation 1: Beam Natural Angular Frequency

The natural angular frequency for the n th mode of a uniform Euler-Bernoulli beam is given by:

$$\omega_n = \left(\frac{\beta_n}{L} \right)^2 \sqrt{\frac{EI}{\rho A}} \quad (7.3)$$

where:

- ω_n : Natural angular frequency of the n th mode (rad/s)
- β_n : Dimensionless coefficient depending on boundary conditions and mode number (calculated using MATLAB code in Appendix A)
- L : Beam length
- E : Modulus of Elasticity
- I : Area moment of inertia
- ρ : Mass density of the beam material
- A : Cross-sectional area

Equation (7.3) relates the beam's physical properties and boundary conditions to its vibration characteristics, essential for dynamic analysis.

7.4.2 Equation 2: Beam Natural Frequency (Hz)

The natural frequency in Hertz for the n th mode of a uniform beam is derived from the angular frequency as:

$$f_n = \frac{\beta_n^2}{2\pi L^2} \sqrt{\frac{EI}{\rho A}} \quad (7.4)$$

where:

- f_n : Natural frequency of the n th mode (Hz)
- β_n : Dimensionless coefficient (calculated using MATLAB code in Appendix A)
- L : Beam length
- E : Modulus of Elasticity

- I : Area moment of inertia
- ρ : Mass density of the beam material
- A : Cross-sectional area

Equation (7.4) provides a practical measure of the vibration rate, critical for avoiding resonance with external excitations.

7.4.3 Equation 3: Bending Stiffness D_{90}

The bending stiffness D_{90} of an isotropic plate is approximated as:

$$D_{90} = \frac{E_0 h^3}{12(1 - \nu^2)} \quad (7.5)$$

where:

- D_{90} : Bending stiffness term
- E_0 : Modulus of Elasticity
- h : Plate thickness
- ν : Poisson's ratio

Equation (7.5) resembles the bending stiffness for an isotropic plate. If intended for orthotropic stiffness D_{22} , it simplifies by neglecting $\nu_{12}\nu_{21}$ terms or assuming specific properties ($E_0 = E_2$, $\nu = \nu_{21}$) [Reddy, 2007].

7.4.4 Equation 4: Total Bending Stiffness D_{total}

The total effective bending stiffness is defined as:

$$D_{\text{total}} = D_0 + D_{90} \quad (7.6)$$

where:

- D_{total} : Total or effective bending stiffness
- D_0 : Bending stiffness term
- D_{90} : Bending stiffness term

Equation (7.6) simplifies material behavior by summing stiffnesses in principal directions, ignoring coupling (D_{12}) and torsional (D_{66}) components [Reddy, 2007].

7.4.5 Equation 5: Simplified Plate Natural Frequency

A simplified approximation for a plate's natural frequency is given by:

$$\omega_n = \frac{\beta_n^2}{2\pi L^2} \sqrt{\frac{D_{\text{total}}}{\rho A}} \quad (7.7)$$

where:

- ω_n : Natural angular frequency (rad/s)
- β_n : Coefficient depending on boundary conditions and mode (calculated using MATLAB code in Appendix A)
- L : Characteristic length
- D_{total} : Effective bending stiffness (from Equation (7.6))
- ρ : Mass density
- A : Cross-sectional area

Equation (7.7) offers a beam-like approximation for a plate's natural frequency, using D_{total} and a potentially inconsistent inertia term (ρA instead of ρh). Its applicability is limited compared to standard 2D plate vibration analysis [Reddy, 2007].

7.4.6 Model A Validation Description

Two models were developed for validation. Model A involved comparing Finite Element Method (FEM) simulations in Abaqus with manual analytical calculations for Carbon Fiber Reinforced Polymer (CFRP) plates with 0°, 90°, and 45° fiber orientations. The analytical validation utilized Equations (??)–(7.4) for axial deformation, cantilever deflection, and beam natural frequencies.

7.4.7 Model A Validation Results

7.4.7.a 0° Orientation

The results for the 0° orientation are presented in Table 7.6.

Analytical (Hz)	Simulation (Hz)	% Difference
1.56371031	1.5714	0.489352824
9.799684785	9.8477	0.487577966
27.43959486	27.572	0.480215948
53.76967329	54.025	0.472608443

Table 7.6: Model A validation results for 0° fiber orientation.

The comparison shows excellent agreement, with percentage differences below 0.5% for all four natural frequencies. This indicates that the FEM model accurately captures the dynamic behavior of the plate with fibers aligned along the primary axis, validating the model's parameters for this orientation.

7.4.7.b 90° Orientation

The results for the 90° orientation are presented in Table 7.7.

Analytical (Hz)	Simulation (Hz)	% Difference
0.516976309	0.5191	0.409110286
3.239861522	3.2559	0.492597369
9.071770115	9.1165	0.490647558

17.77672439	17.865	0.494125984
-------------	--------	-------------

Table 7.7: Model A validation results for 90° fiber orientation.

The results demonstrate strong correlation, with percentage differences below 0.5% for all modes. This confirms the FEM model's accuracy for fibers oriented perpendicular to the primary axis, validating the modeling assumptions for this configuration.

7.4.7.c 45° Orientation

The results for the 45° orientation are presented in Table 7.8.

Analytical (Hz)	Simulation (Hz)	% Difference
0.498560143	0.88938	43.94295538
3.124448449	5.5736	43.94200429
8.748607887	15.606	43.94074146
17.14346696	30.58	43.93895697

Table 7.8: Model A validation results for 45° fiber orientation.

The comparison reveals a significant discrepancy, with percentage differences around 44% across all modes. This suggests that the simplified beam equations (Equations (??)–(7.4)) are inadequate for predicting the dynamic behavior of an orthotropic plate at 45°, where coupling effects are significant. These results were deemed unreliable for validating the FEM model using these analytical formulas.

7.4.8 Model B Validation Description

Model B focused on a [0/90/0] laminated CFRP composite plate, comparing FEM simulation results with analytical calculations using the simplified orthotropic plate stiffness and frequency equations (Equations (7.5)–(7.7)) to approximate the behavior of the composite layup.

7.4.9 Model B Validation Results

7.4.9.a [0/90/0] Orientation

The results for the [0/90/0] orientation are presented in Table 7.9.

Analytical (Hz)	Simulation (Hz)	% Difference
4.457741701	4.6357	3.838865741
27.93641715	29.041	3.803528964
78.22332915	81.267	3.745272801
153.2837082	159.11	3.661801129

Table 7.9: Model B validation results for [0/90/0] orientation.

The comparison shows reasonable agreement, with percentage differences below 4% for all modes. While higher than the errors in Model A's 0° and 90° cases, this level of

agreement suggests that the simplified plate equations provide a fair approximation for the dynamic behavior of this cross-ply laminate, validating the FEM model within an acceptable margin of error.

8 Data Acquisition & Data Processing

This chapter details the experimental setup, data collection methods, and processing techniques used to acquire and analyze vibration data from the composite sandwich beam for structural health monitoring (SHM). The setup includes both embedded and surface-mounted piezoelectric sensors, with data collected under various excitation types and structural conditions. The results provide insights into the dynamic behavior of the beam, highlighting the effectiveness of different sensor configurations and excitation methods for damage detection.

8.1 Working Principles of Selected Sensors

In this section of the report, general information will be given about piezoelectric sensors. Electrical and mechanical equations and coefficients used will be introduced in order to understand the working principles of these sensors.

8.1.1 Piezoelectric Sensors (PZT)

Electroactive materials and magnetoactive materials are substances that generate mechanical motion and strain in response to electrical or magnetic stimuli, functioning as either direct actuators or strain sensors. Piezoelectric materials, in particular, enable the direct conversion of electrical or magnetic energy into mechanical motion. With piezoelectric strain sensors, strong and clear voltage signals are obtained directly from the sensor without the need for intermediate gauge bridges, signal conditioners, and signal amplifiers. The names PZT (a piezoelectric ceramic), PMN (an electrostrictive ceramic), Terfenol-D (a magnetostrictive compound), and PVDF (a piezoelectric polymer) have become widely used. Within the scope of the project, the most accessible PZT sensors will be used.

Piezoelectricity describes the phenomenon of generating an electric field when the material is subjected to mechanical stress, or, conversely, generating a mechanical strain in response to an applied electric field. There are two types of piezoelectric effects. *Direct piezoelectric effect* means that an electric charge is produced when a voltage is applied, and this is how sensors work. The other, *converse piezoelectric effect*, means that an applied electric field creates mechanical deformation in the material, and this is how actuators work.

8.1.2 Actuation Equations

Equation 8.1 is called the *actuation equation* and is used to predict how much strain will be created at a given stress, electric field, and temperature. Equation 8.2 is used to predict how much electric displacement, i.e., charge per unit area, is required to accommodate the simultaneous state of stress, electric field, and temperature.

$$S_{ij} = s_{ijkl}^E T_{kl} + d_{kij} E_k + \delta_{ij} \alpha_i^E \theta \quad (8.1)$$

$$D_i = d_{ikl}T_{kl} + \varepsilon_{ik}^T E_k + \tilde{D}_i \theta \quad (8.2)$$

Where:

- S_{ij} : strain tensor
- T_{kl} : stress tensor
- E_k : electric field vector
- D_i : electric displacement vector
- θ : temperature
- s_{ijkl}^E : compliance coefficient (strain per unit stress, at constant electric field)
- ε_{ik}^T : electric permittivity coefficient (electric displacement per unit electric field, at constant stress)
- d_{ikl}, d_{kij} : piezoelectric coefficients (charge per unit stress and strain per unit electric field, respectively)
- α_i^E : coefficient of thermal expansion (at constant electric field)
- \tilde{D}_i : electric displacement temperature coefficient
- δ_{ij} : Kronecker delta ($\delta_{ij} = 1$ if $i = j$, otherwise $\delta_{ij} = 0$)

Table 8.1: Strain components in piezoelectric actuation equations

$s_{ijkl}^E T_{kl}$	the strain caused by mechanical load (stress) (theory of elasticity)
$d_{kij} E_k$	the strain caused by the piezoelectric converse effect (mechanical deformation that occurs when an electric field is applied)
$\delta_{ij} \alpha_i^E \theta$	the thermal strain caused by temperature change (thermoelastic effect)

Table 8.2: Electric displacement components in piezoelectric actuation equations

$d_{ikl} T_{kl}$	electric load due to mechanical load (stress)
$\varepsilon_{ik}^T E_k$	electric load due to electric field
$\tilde{D}_i \theta$	electric load due to temperature change

8.1.3 Sensing Equations

In this section, the equations that are effective in the use of the piezoelectric effect as a sensor are given. The format of Equation 8.3 and Equation 8.1, as well as the format of Equation 8.4 and Equation 8.2, are very similar. However, there are differences in the names of some coefficients and what they express. Equation 8.4 predicts how much electric field, i.e., voltage per unit thickness, is generated by “squeezing” the piezoelectric material, i.e., represents the direct piezoelectric effect.

$$S_{ij} = s_{ijkl}^D T_{kl} + g_{kij} D_k + \delta_{ij} \alpha_i^D \theta \quad (8.3)$$

$$E_i = -g_{ikl}T_{kl} + \beta_{ik}^T D_k + \tilde{E}_i \theta \quad (8.4)$$

Where:

- S_{ij} : strain tensor
- T_{kl} : stress tensor
- D_k : electric displacement vector
- E_i : electric field vector
- θ : temperature
- s_{ijkl}^D : compliance coefficient (strain per unit stress, at constant electric displacement)
- g_{ikl} : piezoelectric voltage coefficient (electric field induced per unit stress)
- β_{ik}^T : impermittivity coefficient (inverse of permittivity, at constant stress)
- α_i^D : coefficient of thermal expansion (at constant electric displacement)
- \tilde{E}_i : pyroelectric voltage coefficient (electric field induced per unit temperature change)
- δ_{ij} : Kronecker delta ($\delta_{ij} = 1$ if $i = j$, otherwise $\delta_{ij} = 0$)

Table 8.3: Strain components in piezoelectric sensing equations

$s_{ijkl}^D T_{kl}$	the strain caused by mechanical load (stress) (theory of elasticity)
$g_{kij} D_k$	voltage due to electrical displacement
$\delta_{ij} \alpha_i^D \theta$	the thermal strain caused by temperature change (thermoelastic effect)

Table 8.4: Electric field components in piezoelectric sensing equations

$-g_{ikl} T_{kl}$	the electric field produced due to mechanical stress
$\beta_{ik}^T D_k$	voltage due to electrical displacement
$\tilde{E}_i \theta$	the thermal strain caused by temperature change

8.1.4 Stress Equations

$$T_{ij} = c_{ijkl}^E S_{kl} - e_{kij} E_k - c_{ijkl}^E \delta_{kl} \alpha_k^E \theta \quad (8.5)$$

$$D_i = e_{ikl} S_{kl} + \varepsilon_{ik}^T E_k + \tilde{D}_i \theta \quad (8.6)$$

Where:

- T_{ij} : stress tensor
- S_{kl} : strain tensor
- E_k : electric field vector
- D_i : electric displacement vector

- θ : temperature
- c_{ijkl}^E : stiffness tensor (at constant electric field)
- e_{kij} : piezoelectric stress constant
- ε_{ik}^T : electric permittivity coefficient (at constant stress)
- α_k^E : coefficient of thermal expansion (at constant electric field)
- \tilde{D}_i : electric displacement temperature coefficient
- δ_{kl} : Kronecker delta ($\delta_{kl} = 1$ if $k = l$, otherwise $\delta_{kl} = 0$)

Table 8.5: Stress components in piezoelectric stress equations

$c_{ijkl}^E S_{kl}$	mechanical strain caused by stress
$-e_{kij} E_k$	piezoelectric effect induced voltage
$-c_{ijkl}^E \delta_{kl} \alpha_k^E \theta$	temperature induced stress (residual thermal stress)

Table 8.6: Electric displacement components in piezoelectric stress equations

$e_{ikl} S_{kl}$	the electric field produced due to mechanical stress
$\varepsilon_{ik}^T E_k$	electrical displacement due to dielectric effect
$\tilde{D}_i \theta$	temperature-induced electric charge (pyroelectric effect)

8.1.5 Relations Between the Constants

We have encountered various coefficients in the equations given up to this section. The relations between these coefficients are listed in Table 8.7.

Table 8.7: Constitutive relations in piezoelectric materials

Stiffness-compliance	$c_{pr}^E s_{qr}^E = \delta_{pq}$, $c_{pr}^D s_{qr}^D = \delta_{pq}$
Permittivity-impermittivity	$\varepsilon_{ik}^S \beta_{jk}^S = \delta_{ij}$, $\varepsilon_{ik}^T \beta_{jk}^T = \delta_{ij}$
Close circuit-open circuit effects on elastic constant	$c_{pq}^D = c_{pq}^E + e_{kp} h_{kq}$, $s_{pq}^D = s_{pq}^E - d_{lp} q_{kq}$
Stress-strain effects on dielectric constant	$\varepsilon_{ij}^T = \varepsilon_{ij}^S + d_{iq} e_{jq}$, $\beta_{ij}^T = \beta_{ij}^S - g_{iq} h_{jq}$
Relations between piezoelectric constants	$\begin{cases} e_{ip} = d_{iq} c_{qp}^E, & d_{ij} = \varepsilon_{ik}^T g_{kp} \\ g_{ip} = d_{kq} \beta_{ik}^T, & h_{ip} = \varepsilon_{qp}^D g_{iq} \end{cases}$

8.2 PWAS Stress and Strain Sensors

The PWAS performance exceeds by far that of conventional resistance strain gauges because PWAS are active devices that can interrogate the structure at will, whereas strain gauges are passive devices that can only listen to the structure. PWAS transducers are used both as actuators and as sensors of structural vibration and elastic waves. Analysis of the vibration and wave propagation signals recorded with PWAS transducers allows

one to detect the presence, location, and intensity of structural damage during the SHM process. Besides, PWAS can address high-frequency applications at hundreds of kHz and beyond.

Under this heading, at elementary level PWAS transducers strain sensing functions will be examined. Figure 8.1 shows a schematic representation of a PWAS transducer. Figure 8.2 shows damage detection with a PWAS transducer.

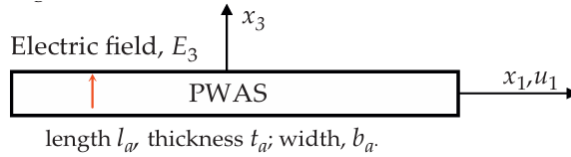


Figure 8.1: Schematic representation of a PWAS transducer

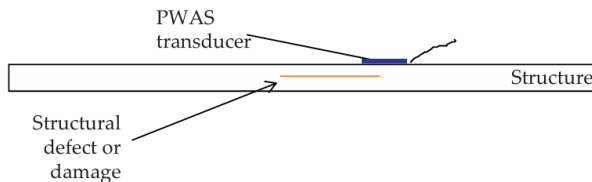


Figure 8.2: Damage detection with a PWAS transducer

8.2.1 Static Stress Sensing

Transverse shear T_3 can be measured by applying a pressure p_0 with a PWAS such that $T_3 = -p_0$. Under a 1-D assumption in the 3-direction, the following equations apply:

$$D_3 = d_{33}T_3 + \varepsilon_{33}^T E_3 \quad (8.7)$$

$$Q = D_3 A = C_e V \Rightarrow D_3 = \frac{Q}{A} = \frac{C_e}{A} V \quad (8.8)$$

$$E_3 = -\frac{V}{t_a} \quad (8.9)$$

Substituting Equations 8.8 and 8.9 into Equation 8.7 gives:

$$\frac{C_e}{A} V = d_{33}T_3 + \varepsilon_{33}^T \left(-\frac{V}{t_a} \right) \Rightarrow (C_e + C)V = Ad_{33}T_3 \quad (8.10)$$

As a result, Equation 8.11 is obtained:

$$V(T_3, C_e) = \frac{Ad_{33}}{(C_e + C)} T_3 \quad (8.11)$$

When this equation is examined, it is desired that the measuring instrument capacitance is low. However, it is important that it does not fall below the PWAS capacitance value.

Where:

- Q : produced charge
- C_e : instrument capacitance
- C : PWAS capacitance
- A : area of the PWAS
- V : voltage
- D_3 : electric displacement in the 3-direction
- T_3 : transverse shear stress
- E_3 : electric field in the 3-direction
- d_{33} : piezoelectric coefficient
- ε_{33}^T : electric permittivity (at constant stress)
- t_a : thickness of the PWAS

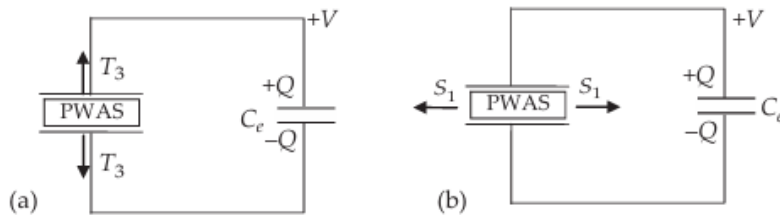


Figure 8.3: (a) Measurement of static out-of-plane stress T_3 , (b) Measurement of static in-plane strain S_1

8.2.2 Static Strain Sensing

For strain sensing, the voltage V as a function of applied in-plane strain S_1 is required:

$$S_1 = s_{11}^E T_1 + d_{31} E_3 \quad (8.12)$$

$$D_3 = d_{31} T_1 + \varepsilon_{33}^T E_3 \quad (8.13)$$

Eliminating T_1 between Equations 8.12 and 8.13 gives:

$$d_{31} S_1 - s_{11}^E D_3 = (d_{31}^2 - s_{11}^E \varepsilon_{33}^T) E_3 \quad (8.14)$$

Substituting Equations 8.8 and 8.9 into Equation 8.14 yields:

$$d_{31} S_1 - s_{11}^E \frac{C_e}{A} V = (d_{31}^2 - s_{11}^E \varepsilon_{33}^T) \left(-\frac{V}{t_a} \right) = (1 - k_{31}^2) s_{11}^E \varepsilon_{33}^T \frac{V}{t_a} \quad (8.15)$$

where k_{31}^2 stands for the electromechanical coupling effect:

$$k_{31}^2 = \frac{d_{31}^2}{s_{11}^E \varepsilon_{33}^T} \quad (8.16)$$

Rearranging Equation 8.15 gives:

$$d_{31} \frac{A}{s_{11}^E} S_1 = C_e V + (1 - k_{31}^2) \varepsilon_{33}^T \frac{A}{t_a} V = [C_e + (1 - k_{31}^2) C] V \quad (8.17)$$

As a result, Equation 8.18 is reached:

$$V(S_1, C_e) = \frac{1}{C_e + (1 - k_{31}^2) C} \frac{A d_{31}}{s_{11}^E} S_1 \quad (8.18)$$

This equation shows that C_e and the generated voltage value are inversely proportional, and the strain value is directly proportional to the generated voltage value.

Where:

- S_1 : in-plane strain
- T_1 : in-plane stress
- E_3 : electric field in the 3-direction
- D_3 : electric displacement in the 3-direction
- V : voltage
- C_e : instrument capacitance
- C : PWAS capacitance
- A : area of the PWAS
- d_{31} : piezoelectric coefficient
- s_{11}^E : compliance coefficient (at constant electric field)
- ε_{33}^T : electric permittivity (at constant stress)
- k_{31}^2 : electromechanical coupling coefficient
- t_a : thickness of the PWAS

8.2.3 Dynamic Stress Sensing

In this section, two new terms are used: measuring instrument of input impedance Z_e and admittance Y_e , where:

$$Y_e = \frac{1}{Z_e}$$

The time-harmonic behavior equation used for dynamic equations is:

$$T_3(t) = \hat{T}_3 e^{i\omega t}, \quad V(t) = \hat{V} e^{i\omega t} \quad (8.19)$$

The time derivatives of Equations 8.7, 8.8, and 8.9 are:

$$\dot{D}_3 = d_{31} \dot{T}_3 + \varepsilon_{33}^T \dot{E}_3 \quad (8.20)$$

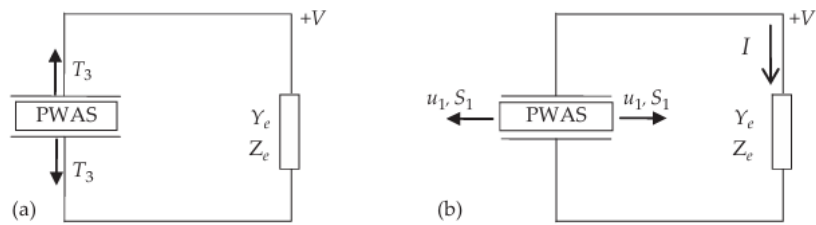


Figure 8.4: (a) Measurement of static out-of-plane stress T_3 , (b) Measurement of static in-plane strain S_1

$$I = \dot{D}_3 A \quad (8.21)$$

$$\dot{E}_3 = -\frac{\dot{V}}{t_a} \quad (8.22)$$

$$I = Y_e V \quad (8.23)$$

Equations 8.21 and 8.23 give:

$$\dot{D}_3 = \frac{I}{A} = \frac{Y_e}{A} V \quad (8.24)$$

Substituting Equations 8.22 and 8.24 into Equation 8.20 and rearranging gives:

$$\frac{Y_e V}{A} = d_{31} \dot{T}_3 + \varepsilon_{33}^T \left(-\frac{\dot{V}}{t_a} \right) \quad (8.25)$$

$$Y_e V + \frac{\varepsilon_{33}^T A}{t_a} \dot{V} = d_{31} \dot{T}_3 A \quad (8.26)$$

Substituting the PWAS capacitance $C = \varepsilon_{33}^T \frac{A}{t_c}$ into Equation 8.26 gives:

$$Y_e V + C \dot{V} = A d_{31} \dot{T}_3 \quad (8.27)$$

Taking the time derivative of Equation 8.19 and substituting into Equation 8.27 yields:

$$\dot{V}(t) = i\omega \hat{V} e^{i\omega t} = i\omega V(t) \quad \Rightarrow \quad (Y_e + i\omega C)V \equiv Ad_{31}\dot{T}_3 \quad (8.28)$$

The admittance of the unconstrained PWAS transducer is given by:

$$Y = i\omega C \quad (8.29)$$

As a result, Equation 8.30 is reached:

$$V(t, T_3; Y_e) = \frac{Ad_{33}}{Y_e + Y} \dot{T}_3(t) \quad (8.30)$$

Equation 8.30 indicates that a measuring instrument with low input admittance (high impedance) is desired, but this is constrained by the internal admittance Y_e of the PWAS. This equation can also be written as:

$$\hat{V}(\hat{T}_3; Y_e) = \frac{Ad_{33}}{Y_e + Y} i\omega \hat{T}_3 \quad (8.31)$$

$$\hat{V}(\hat{T}_3; C_e) = \frac{Ad_{33}}{C_e + C} \hat{T}_3 \quad (\text{lossless measuring instrument } Y_e = i\omega C_e) \quad (8.32)$$

Equations 8.31 and 8.32 are not always valid because there are always energy losses in the sensor.

Where:

- $T_3(t)$: time-dependent transverse shear stress
- $V(t)$: time-dependent voltage
- \hat{T}_3 : complex amplitude of stress
- \hat{V} : complex amplitude of voltage
- ω : angular frequency
- D_3 : electric displacement in the 3-direction
- E_3 : electric field in the 3-direction
- I : current
- Y_e : admittance of the measuring instrument
- Z_e : impedance of the measuring instrument
- Y : admittance of the PWAS
- C : PWAS capacitance
- C_e : instrument capacitance
- A : area of the PWAS
- d_{31}, d_{33} : piezoelectric coefficients
- ε_{33}^T : electric permittivity (at constant stress)
- t_a : thickness of the PWAS

8.2.4 Dynamic Strain Sensing

For strain sensing, the voltage $V(t)$ as a function of applied in-plane strain $S_1(t)$ is required:

$$\dot{S}_1 = s_{11}^E \dot{T}_1 + d_{31} \dot{E}_3 \quad (8.33)$$

$$\dot{D}_3 = d_{31} \dot{T}_1 + \varepsilon_{33}^T \dot{E}_3 \quad (8.34)$$

$$d_{31}\dot{S}_1 - s_{11}^E \dot{D}_3 = (d_{31}^2 - s_{11}^E \varepsilon_{33}^T) \dot{E}_3 \quad (8.35)$$

$$d_{31}\dot{S}_1 - s_{11}^E \frac{Y_e}{A} V = (d_{31}^2 - s_{11}^E \varepsilon_{33}^T) \left(-\frac{\dot{V}}{t_a} \right) = (1 - k_{31}^2) s_{11}^E \varepsilon_{33}^T \frac{\dot{V}}{t_a} \quad (8.36)$$

$$d_{31} \frac{A}{s_{11}^E} \dot{S}_1 = Y_e V + (1 - k_{31}^2) \varepsilon_{33}^T \frac{A}{t_a} \dot{V} = Y_e V + (1 - k_{31}^2) C \dot{V} \quad (8.37)$$

$$d_{31} \frac{A}{s_{11}^E} \dot{S}_1 = [Y_e + (1 - k_{31}^2) i\omega C] V = [Y_e + (1 - k_{31}^2) Y] V \quad (8.38)$$

As a result, Equations 8.39, 8.40, and 8.41 are reached:

$$V(t, \dot{S}_1; Y_e) = \frac{1}{Y_e + (1 - k_{31}^2) Y} \frac{d_{31} A}{s_{11}^E} \dot{S}_1(t) \quad (8.39)$$

$$\hat{V}(\hat{S}_1; Y_e) = \frac{1}{Y_e + (1 - k_{31}^2) Y} \frac{d_{31} A}{s_{11}^E} i\omega \hat{S}_1 \quad (8.40)$$

$$\hat{V}(\hat{S}_1; Y_e) = \frac{1}{C_e + (1 - k_{31}^2) C} \frac{d_{31} A}{s_{11}^E} \hat{S}_1 \quad (\text{lossless measuring instrument } Y_e = i\omega C_e) \quad (8.41)$$

As in dynamic stress sensing, Equations 8.40 and 8.41 may not always be valid due to internal energy losses.

Where:

- $S_1(t)$: time-dependent in-plane strain
- T_1 : in-plane stress
- E_3 : electric field in the 3-direction
- D_3 : electric displacement in the 3-direction
- $V(t)$: time-dependent voltage
- \hat{S}_1 : complex amplitude of strain
- \hat{V} : complex amplitude of voltage
- ω : angular frequency
- Y_e : admittance of the measuring instrument
- Y : admittance of the PWAS
- C : PWAS capacitance
- C_e : instrument capacitance
- A : area of the PWAS
- d_{31} : piezoelectric coefficient

- s_{11}^E : compliance coefficient (at constant electric field)
- ε_{33}^T : electric permittivity (at constant stress)
- k_{31}^2 : electromechanical coupling coefficient
- t_a : thickness of the PWAS

8.2.5 Thickness Effects on PWAS Sensing

In order to examine the effect of thickness on sensing, the following equations were obtained by using the equations in the previous sections:

$$V(T_3) = t_a \frac{d_{33}}{\varepsilon_{33}^T} T_3 \quad (\text{stress sensing}) \quad (8.42)$$

$$V(S_1) = t_a \frac{k_{31}^2}{(1 - k_{31}^2) d_{31}} S_1 \quad (\text{strain sensing}) \quad (8.43)$$

Equations 8.42 and 8.43 show that for a given piezoelectric material with properties d_{31} , ε_{33}^T , s_{11}^E , and k_{31} , the voltage generated by a PWAS sensor under an applied stress T_3 or strain S_1 increases proportionally with the PWAS thickness t_a . This implies that, for sensing applications, using a thicker PWAS is preferable to a thinner one.

8.3 PWAS Installation

8.3.1 Adhesives

The adhesive used in PWAS installation affects bonding strength and signal transmission. Cyanoacrylate adhesives (e.g., M-Bond 200) cure quickly but may degrade over time. Epoxy adhesives (e.g., M-Bond AE-10, AE-15) provide stronger, long-term bonding. Conductive epoxy is unnecessary for high-frequency applications since capacitive coupling is sufficient. Proper mixing, application, and curing are essential for optimal performance.

8.3.2 Surface Preparation and PWAS Installation

The PWAS installation process consists of four main steps. Sensor preparation involves determining the sensor's dimensions, capacitance, and resonance characteristics. Surface preparation ensures proper bonding by degreasing, abrading, and neutralizing the surface. Bonding involves applying a catalyst and adhesive, followed by pressure to secure the sensor. Finally, cleaning removes excess adhesive through mechanical and acetone cleaning. This structured process ensures a reliable and durable PWAS installation.

Figure 8.5 shows the flowchart of the installation procedure for PWAS transducers.

8.3.3 Quality Checks

After installation, sensor capacitance must be measured and compared with its free-state value. Electrode insulation and metal substrate connection should be checked with a conductance meter. If capacitance or conductance is inconsistent, excess adhesive should be

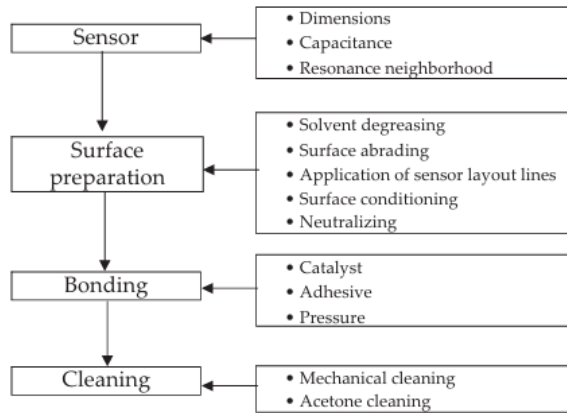


Figure 8.5: Flowchart of the installation procedure for PWAS transducers

removed and rechecked. If the issue persists, the PWAS should be replaced.

PWAS sensors play a critical role in structural health monitoring and must remain reliable over time. Therefore, periodic self-diagnostic scans are necessary. The E/M impedance technique is used to assess sensor integrity. Reactive impedance (ImZ) measurements help differentiate between bonded and disbanded sensors.

8.4 Strain Gauges

A strain gauge is a passive sensor used to measure the strain experienced by a material when subjected to external forces. The fundamental working principle relies on the fact that the electrical resistance of a conductor changes when it is stretched or compressed.

When a strain gauge is firmly bonded to the surface of a structure, it deforms along with the material. This deformation leads to a change in the gauge's length and cross-sectional area, resulting in a measurable change in its electrical resistance. The relative change in resistance is directly proportional to the strain, as described by the gauge factor (GF):

$$\varepsilon = \frac{\Delta R}{G_f R_0} \quad (8.44)$$

Where:

- ΔR : change in resistance
- R_0 : initial resistance
- ε : strain
- G_f : gauge factor

Since the resistance change is very small (usually on the order of milliohms), it is not practical to measure it directly. Instead, a Wheatstone bridge circuit is used for high-sensitivity detection. This configuration allows the detection of microstrain-level defor-

mations with high accuracy and stability. The output voltage of the Wheatstone bridge is given by:

$$V_{\text{out}} = V_{\text{in}} \times \left(\frac{R_1}{R_1 + R_2} - \frac{R_3}{R_3 + R_g} \right) \quad (8.45)$$

Where:

- V_{out} : output voltage
- V_{in} : input voltage
- R_1, R_2, R_3, R_g : resistances in the Wheatstone bridge circuit

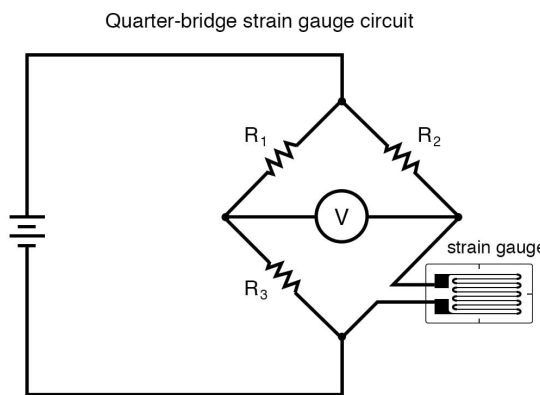


Figure 8.6: Wheatstone bridge circuit for strain gauge measurement

In this project, strain gauges were used to verify surface strain distribution under mechanical excitation, and to serve as a comparative measurement method alongside piezoelectric sensors. The data obtained from strain gauges helps confirm the structural response and provides reference values for modal and curvature analysis.

8.5 Transfer Function-Based Damage Localization

In the field of Structural Health Monitoring (SHM), various methods have been developed for damage localization, including mode shape curvature, modal strain energy (MSE), autoregressive (AR) models, machine learning-based classifiers such as Convolutional Neural Networks (CNNs), and frequency response function (FRF) or transfer function (TF) difference-based techniques. Curvature-based approaches are sensitive to local stiffness changes but rely heavily on accurate mode shape extraction and are prone to noise, especially in higher modes [Deraemaeker and Worden, 2018]. MSE methods, while effective for detecting small damages, require precise numerical models and derivative computations [Deraemaeker and Worden, 2018]. Data-driven models like AR and CNNs offer strong classification performance but depend on large labeled datasets and lack physical interpretability [Worden et al., 2007]. In contrast, TF difference-based localization provides a practical and explainable metric by comparing the frequency-domain response of the structure across multiple sensor positions. This method is particularly advantageous in laboratory setups with limited sensor counts and repeated testing, as it directly captures variations in system dynamics due to damage without requiring full modal extraction or

machine learning training. Thus, TF-based localization was selected in this study for its simplicity, efficiency, and strong physical basis [Farrar and Lieven, 2007].

In structural dynamics, a transfer function mathematically represents how a structure transforms an input force or excitation into an output response, typically a vibration measurement, within the frequency domain. It characterizes the system's behavior by describing how energy is transferred from input to output at different frequencies [Wang et al., 2010]. The transfer function is inherently linked to the structure's fundamental physical properties: mass, stiffness, and damping. These properties dictate how the structure vibrates and dissipates energy under external forces. Consequently, any damage-induced changes in these properties directly affect the structure's dynamic behavior and its transfer function. For instance, a decrease in stiffness due to damage typically shifts resonant frequencies in the transfer function to lower values, while changes in mass or damping alter the shape and magnitude of the transfer function across the frequency spectrum [Salehi et al., 2013].

The basis of TF-based damage localization is a comparison approach, where the transfer function of a structure in its undamaged state is compared with that in its damaged state. Effective localization often requires multiple sensors strategically placed across the structure. By analyzing changes in transfer functions at various locations, the damage location can be inferred. The density and placement of the sensor network critically affect the accuracy and resolution of localization.

The transfer function for each sensor is calculated as:

$$H(f) = \frac{Y(f)}{X(f)} \quad (8.46)$$

where $X(f)$ is the Fast Fourier Transform (FFT) of the applied force signal, and $Y(f)$ is the FFT of the response signal from the piezo sensor. An indicator of damage presence is defined by comparing transfer functions, calculated for each sensor as:

$$DI_j = \sum_{f=f_1}^{f_2} \left| H_{\text{undamaged}}^{(j)}(f) - H_{\text{damaged}}^{(j)}(f) \right| \quad (8.47)$$

A larger evaluation involved 10,918 undamaged-damaged data combinations, with 107 undamaged and 103 damaged test sets. The success criterion required that the two highest TF difference scores corresponded to the known damage area (24cm) sensors (19.5 cm and 28.5 cm) and that the highest TF score was at least 20% larger than the third highest score. This approach achieved a success rate of 90.58%. Figure 8.7 and Figure 8.8 provide sample graphs for successful and unsuccessful predictions.

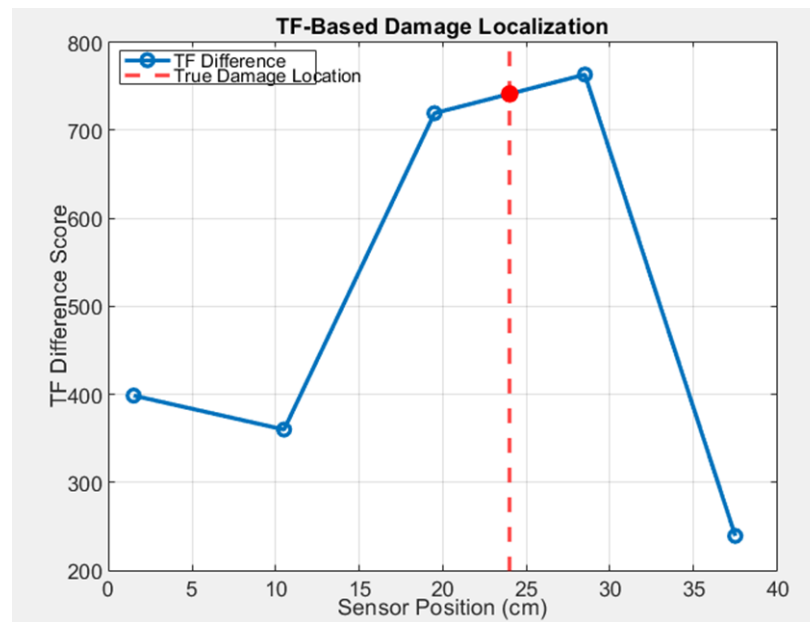


Figure 8.7: Successful localization example.

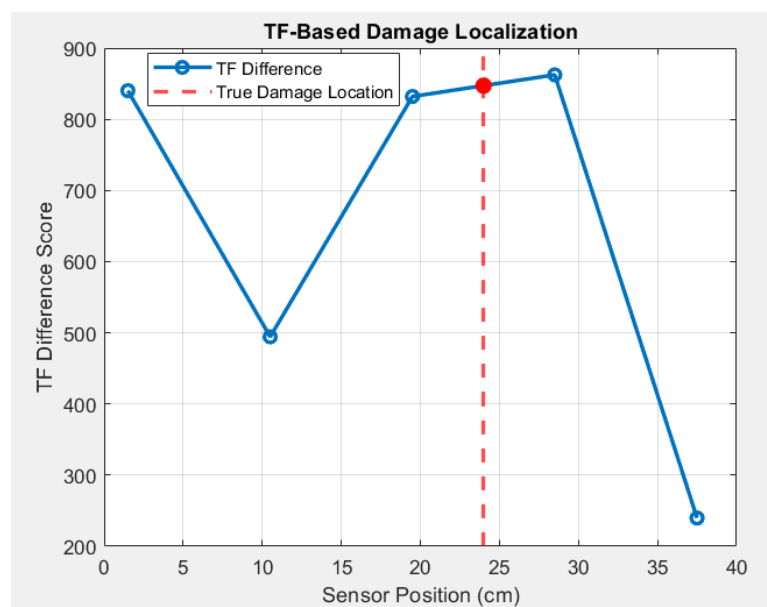


Figure 8.8: Failed localization example.

8.6 Sensor Setup and Instrumentation

The composite sandwich beam was equipped with a combination of embedded and surface-mounted piezoelectric wafer active sensors (PWAS) to capture vibration responses. A total of five 20 mm diameter PWAS were embedded into the smart layer of the beam during fabrication. Additionally, five 20 mm diameter sensors were surface-mounted on the beam at the same positions as the embedded sensors to allow for comparative analysis. To evaluate the effect of sensor size on signal characteristics, a larger 35 mm diameter sensor was placed at position 2 on the fixed side of the beam. A strain gauge was also installed near the fixed boundary to serve as a reference for strain measurements.

The beam was fixed at one end, with the first 3.5 cm of its length secured. Excitation was applied at the free end using a shaker, which delivered both impulse and white noise inputs. For impulse excitation, both a hammer and the shaker were tested to ensure accuracy. A laser sensor was initially considered for velocity measurement, but calibration issues prevented its use in the experiments.

8.7 Data Collection Method and Equipment

The piezoelectric sensors were directly connected to the data acquisition (DAQ) module without the use of a voltage divider or bridge circuit. This decision was based on prior observations where the voltage levels obtained through a voltage divider were significantly lower than the readable range of the DAQ modules. Direct connection improved signal quality, enabling accurate acquisition of both low- and high-amplitude responses.

Data was collected from both embedded and surface-mounted sensors under two excitation types—impulse and white noise—applied to both undamaged and damaged composite beams. Table 8.8 summarizes the number of test recordings acquired for each condition, providing an overview of the experimental dataset.

	Undamaged		Damaged	
	<i>Impulse</i>	<i>White Noise</i>	<i>Impulse</i>	<i>White Noise</i>
Embedded Sensors	107	112	103	108
Surface Sensors	98	108	102	102

Table 8.8: Number of test recordings under different excitation types and structural conditions.

9 Data-Driven Damage Detection Methods

Structural health monitoring (SHM) systems rely on effective damage detection algorithms to identify and localize structural damage from sensor data. This chapter presents two complementary data-driven approaches implemented in our research: an Autoregressive (AR) model and a Convolutional Neural Network (CNN) model. Both methods analyze vibration data from piezoelectric sensors embedded in our composite sandwich beam structure to detect changes indicative of damage.

The advantage of these data-driven approaches is their ability to learn patterns directly from measurements without requiring detailed physical models of the structure. This makes them particularly valuable for complex structures like composite materials, where developing accurate analytical models can be challenging. Our implementation demonstrates how these methods can be applied to real vibration data for practical SHM applications in aerospace structures.

9.1 Autoregressive Modeling for Damage Detection

9.1.1 Theoretical Background

Autoregressive (AR) modeling represents a time series as a linear combination of its previous values plus an error term. For a time series $x(t)$, an AR model of order p can be expressed as:

$$x(t) = \sum_{i=1}^p a_i x(t-i) + \varepsilon(t) \quad (9.1)$$

Where:

- $x(t)$: time series value at time t
- p : order of the AR model
- a_i : AR coefficients for $i = 1, 2, \dots, p$
- $x(t-i)$: time series value at time $t - i$
- $\varepsilon(t)$: white noise error term at time t

The key insight for damage detection is that the AR coefficients capture the dynamic characteristics of the structure, including its mass, stiffness, and damping properties [Sohn and Farrar, 2001b]. When structural damage occurs, these properties change, resulting in detectable alterations in the AR coefficients.

The AR approach offers several advantages for SHM:

- It requires only output (response) data without knowledge of the input excitation.
- It can be applied to ambient vibration data.
- It is computationally efficient compared to many other methods.

- It can detect subtle changes that might not be visible in raw time-domain signals.

9.1.2 Implementation Methodology

Our AR-based damage detection system follows a statistical pattern recognition paradigm with four main stages:

9.1.2.a Data Acquisition and Preprocessing

Data from five piezoelectric sensors embedded in the composite sandwich beam was collected at a sampling rate of 12,800 Hz, with each measurement lasting 2 seconds (producing 25,600 data points per sensor). The preprocessing stage included the following steps:

- **Normalization:** Each sensor's data was standardized by subtracting the mean and dividing by the standard deviation, calculated from the undamaged training dataset.
- **Differencing:** First-order differencing was applied to improve stationarity, a prerequisite for accurate AR modeling.
- **Data Partitioning:** The dataset was divided into:
 - Training set (60% of undamaged data)
 - Threshold set (30% of undamaged data)
 - Reference set (10% of undamaged data)
 - Test set (combination of reference data and damaged data)

9.1.2.b Feature Extraction

An AR(10) model was selected for feature extraction based on a comprehensive analysis using the Akaike Information Criterion (AIC) and Bayesian Information Criterion (BIC). Figure 9.1 shows the model order selection results, which indicated that AR(10) provides a good balance between model accuracy and computational efficiency.

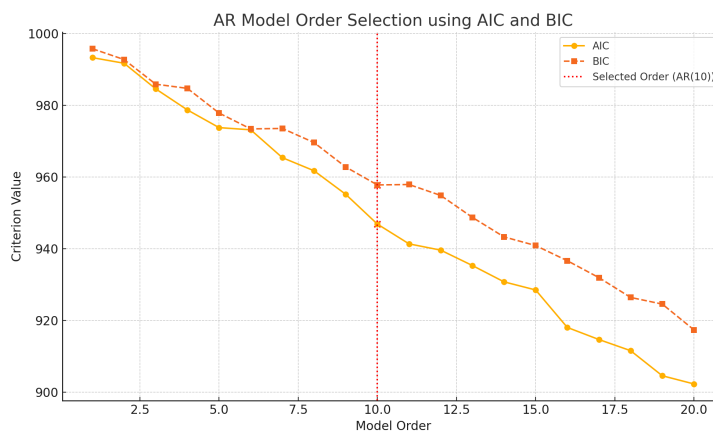


Figure 9.1: AR model order selection using AIC and BIC criteria

AR coefficients were extracted for each time series from each sensor using the MATLAB Econometrics Toolbox, resulting in a feature vector of length $10 \times 5 = 50$ for each measurement (10 AR coefficients for each of the 5 sensors).

9.1.2.c Statistical Distance Calculation

The Mahalanobis Squared Distance (MSD) was used as a statistical measure to detect outliers in the feature space. The MSD accounts for the correlation between features and the variance of each feature, making it particularly suitable for multivariate data:

$$\text{MSD}(x) = (x - \mu)^T \Sigma^{-1} (x - \mu) \quad (9.2)$$

Where:

- $\text{MSD}(x)$: Mahalanobis Squared Distance for feature vector x
- x : feature vector (AR coefficients)
- μ : mean vector of the training data
- Σ : covariance matrix of the training data
- $(x - \mu)^T$: transpose of the vector $(x - \mu)$
- Σ^{-1} : inverse of the covariance matrix

For each test sample, the MSD to the distribution of the training data was calculated, resulting in a damage index (DI) value. Higher DI values indicate greater deviation from the healthy state, suggesting potential damage.

9.1.2.d Threshold Determination and Decision

A threshold for damage detection was established using the 95th percentile of MSD values calculated from the threshold dataset. This approach ensures a maximum 5% false positive rate on unseen healthy data. The decision rule applied was:

- If $\text{DI} > \text{threshold}$: Sample classified as damaged.
- If $\text{DI} \leq \text{threshold}$: Sample classified as healthy.

This methodology allows for automated damage detection without requiring expert interpretation of the signals.

The complete implementation includes additional functionality for data handling, model validation, and result visualization, can be found in Appendix A.

9.1.3 Performance Evaluation Metrics

The performance of the AR-based damage detection was evaluated using standard classification metrics:

- **Accuracy**: The proportion of correctly classified samples.
- **Sensitivity (True Positive Rate)**: The proportion of damaged samples correctly identified.
- **Specificity (True Negative Rate)**: The proportion of healthy samples correctly identified.
- **Precision (Positive Predictive Value)**: The proportion of samples classified as damaged that are actually damaged.

Additionally, a confusion matrix was used to visualize the classification results, showing true positives, false positives, true negatives, and false negatives.

The AR-based damage detection model was trained on data from the healthy structure and tested on both healthy and damaged samples. Figure 9.2 shows the damage indices for test samples, with a clear separation between healthy and damaged states.

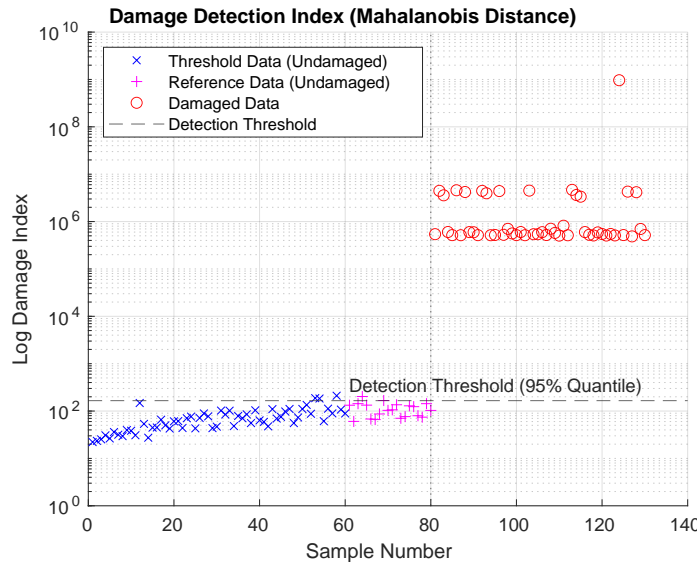


Figure 9.2: Damage indices for test samples with detection threshold

The performance metrics for the AR-based detection are presented in Table 9.1. The model achieved an overall accuracy of 95.00%, with a sensitivity of 100.00% and specificity of 90.00%, demonstrating its effectiveness in distinguishing between healthy and damaged states.

Table 9.1: Performance metrics for AR-based damage detection

Metric	Value (%)
Accuracy	95.00
Sensitivity	100.00
Specificity	90.00
Precision	90.91

The confusion matrix in Figure 9.3 provides a detailed breakdown of the classification results.

An important advantage of the AR-based approach is its ability to detect damage even when the changes in raw signals are not visually apparent [Nair et al., 2006b]. Figure 9.4 shows time-domain signals from a healthy and damaged sample, where the differences are subtle and would be difficult to identify without statistical analysis.

The AR-based damage detection model demonstrates the effectiveness of statistical pattern recognition for identifying structural changes in composite sandwich beams. By modeling the time series data from piezoelectric sensors and extracting AR coefficients as damage-sensitive features, we can detect damage with high accuracy without requiring complex physical models of the structure.

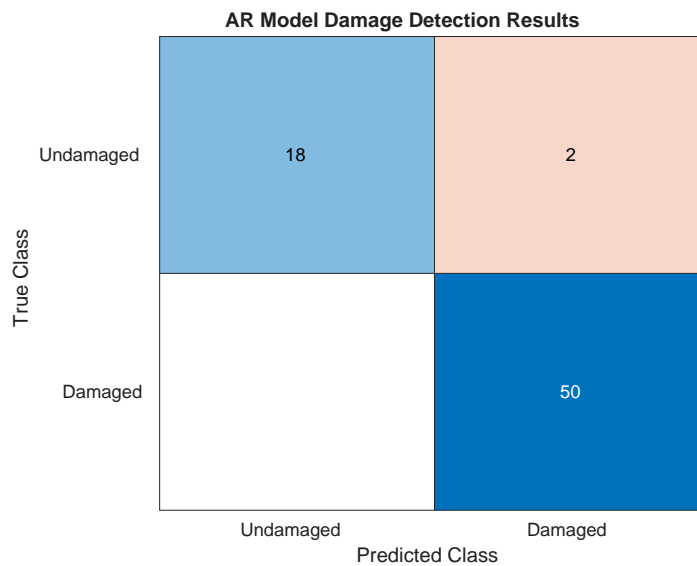


Figure 9.3: Confusion matrix for AR-based damage detection

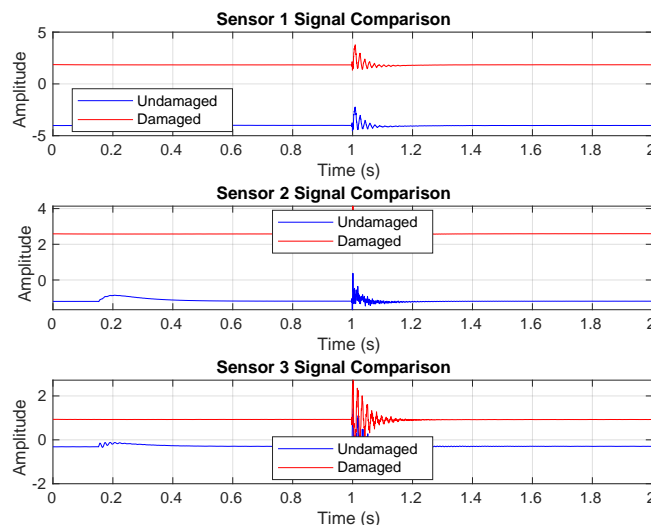


Figure 9.4: Comparison of time-domain signals from healthy and damaged structures

The key advantage of this approach is its simplicity and computational efficiency, making it suitable for real-time monitoring applications. The method successfully detected damage in our experimental setup, proving its value for practical SHM systems in aerospace structures.

Future work could explore combining the AR approach with other methods, optimizing sensor placement for improved detection sensitivity, and extending the methodology to localize damage more precisely within the structure.

9.2 Convolutional Neural Network for Damage Detection

9.2.1 Theoretical Background

Convolutional Neural Networks (CNNs) are a class of deep learning models particularly effective for processing structured data, such as images or time series. In the context of structural health monitoring (SHM), 1D CNNs are well-suited for analyzing time series data, such as vibration signals from piezoelectric sensors, due to their ability to automatically extract relevant features through convolutional layers [Zhang et al., 2018a]. A 1D CNN applies a series of convolutional filters to the input data, followed by pooling layers to reduce dimensionality, and fully connected layers for classification.

The architecture of a typical 1D CNN for time series classification can be described as:

```
Input → Conv1D → ReLU → MaxPooling → Conv1D → ...
...ReLU → MaxPooling → Flatten → Dense → Softmax
```

The key advantage of CNNs in SHM is their ability to learn hierarchical feature representations directly from raw data, eliminating the need for manual feature engineering. This makes them particularly effective for detecting damage in complex structures, where traditional methods may struggle to identify subtle patterns [Avci et al., 2021b]. CNNs also offer robustness to noise and variations in operating conditions, which are common in aerospace applications.

9.2.2 Implementation Methodology

The CNN-based damage detection system was developed using a deep learning framework, following these stages:

9.2.2.a Data Acquisition and Preprocessing

The same dataset used for the AR model was employed, consisting of vibration data from five piezoelectric sensors embedded in the composite sandwich beam, collected at a sampling rate of 12,800 Hz over 2 seconds (25,600 data points per sensor). Preprocessing included:

- **Segmentation:** Each time series was divided into overlapping windows of 2,048 data points, with a 50% overlap, to create input samples for the CNN.
- **Normalization:** Each window was normalized to a range of [0, 1] using min-max scaling based on the training dataset.
- **Data Partitioning:** The dataset was split into:
 - Training set (60% of undamaged data)
 - Validation set (20% of undamaged data)
 - Test set (20% of undamaged data plus damaged data)

9.2.2.b Network Architecture

The 1D CNN architecture was designed to process the segmented vibration data. The network consists of:

- Two convolutional layers with 32 and 64 filters, respectively, each with a kernel size of 3 and ReLU activation.
- Max-pooling layers after each convolutional layer to reduce dimensionality.
- A flatten layer to prepare the data for fully connected layers.
- Two dense layers: one with 128 units and ReLU activation, and a final output layer with 2 units (healthy or damaged) and softmax activation.

The total number of trainable parameters in the network is calculated as:

$$N_{\text{params}} = \sum_{l=1}^L ((k_l \times c_{\text{in},l} + 1) \times c_{\text{out},l}) + \sum_{d=1}^D (n_{\text{in},d} + 1) \times n_{\text{out},d} \quad (9.3)$$

Where:

- N_{params} : total number of trainable parameters
- L : number of convolutional layers
- k_l : kernel size of the l -th convolutional layer
- $c_{\text{in},l}$, $c_{\text{out},l}$: number of input and output channels for the l -th convolutional layer
- D : number of dense layers
- $n_{\text{in},d}$, $n_{\text{out},d}$: number of input and output units for the d -th dense layer

9.2.2.c Training and Optimization

The CNN was trained using the Adam optimizer with a learning rate of 0.001 and a batch size of 32. The loss function used was categorical cross-entropy, suitable for binary classification (healthy vs. damaged):

$$L = -\frac{1}{N} \sum_{i=1}^N [y_i \log(\hat{y}_i) + (1 - y_i) \log(1 - \hat{y}_i)] \quad (9.4)$$

Where:

- L : categorical cross-entropy loss
- N : number of samples in the batch
- y_i : true label for the i -th sample (0 or 1)
- \hat{y}_i : predicted probability for the i -th sample

Training was performed over 50 epochs, with early stopping based on validation loss to prevent overfitting. The training and validation loss curves are shown in Figure 9.5.

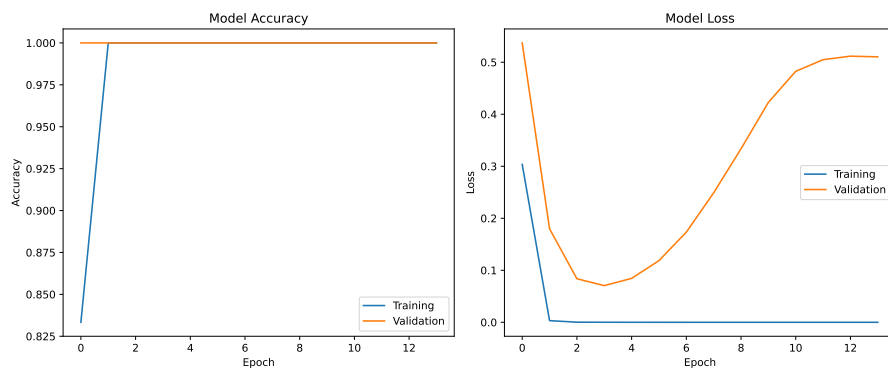


Figure 9.5: Training and validation loss curves for the CNN model

9.2.2.d Classification

After training, the CNN was used to classify test samples. Each segmented window was passed through the network, and the predicted probabilities were averaged across all windows in a sample to determine the final classification (healthy or damaged).

The complete implementation includes additional functionality for data segmentation, model validation, and result visualization, as shown in Appendix A.

9.2.3 Performance Evaluation Metrics

The performance of the CNN-based damage detection was evaluated using the same classification metrics as the AR model:

- **Accuracy:** The proportion of correctly classified samples.
- **Sensitivity (True Positive Rate):** The proportion of damaged samples correctly identified.
- **Specificity (True Negative Rate):** The proportion of healthy samples correctly identified.
- **Precision (Positive Predictive Value):** The proportion of samples classified as damaged that are actually damaged.

A confusion matrix was also used to visualize the classification results, showing true positives, false positives, true negatives, and false negatives.

The CNN model was trained on segmented data from the healthy structure and tested on both healthy and damaged samples. Figure 9.6 shows the predicted probabilities for test samples, with a clear distinction between healthy and damaged states.

The performance metrics for the CNN-based detection are presented in Table 9.2. The model achieved an overall accuracy of 92.96%, with a sensitivity of 92.00% and specificity of 95.24%, demonstrating its capability to accurately classify structural states.

The confusion matrix in Figure 9.6 provides a detailed breakdown of the classification results.

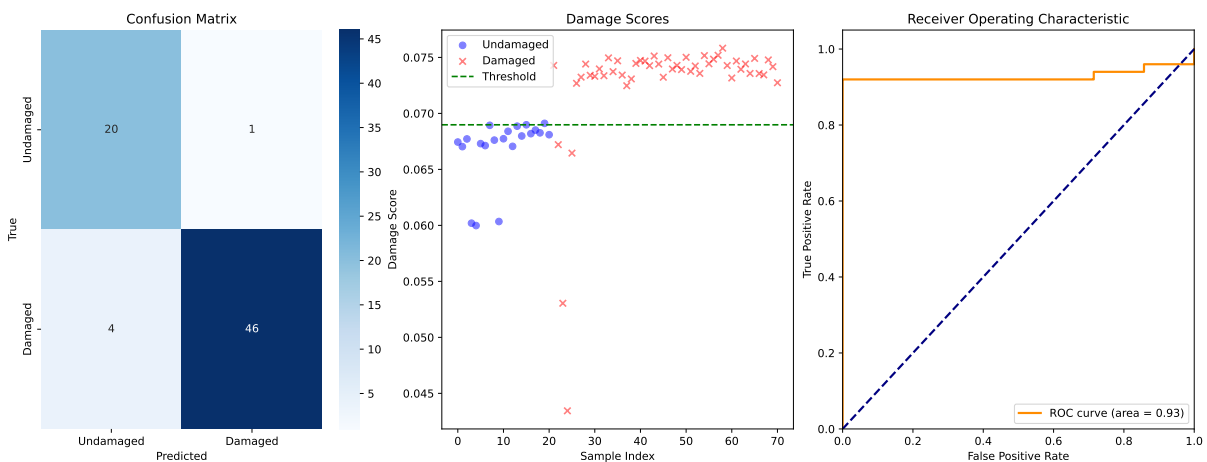


Figure 9.6: Predicted probabilities for test samples using the CNN model

Table 9.2: Performance metrics for CNN-based damage detection

Metric	Value (%)
Accuracy	92.96
Sensitivity	92.00
Specificity	95.24
Precision	97.87

9.3 Results and Discussion

The AR-based damage detection model was trained on data from the healthy structure and tested on both healthy and damaged samples. Figure 9.2 shows the damage indices for test samples, with a clear separation between healthy and damaged states.

In contrast, the CNN model was trained on segmented data from the same healthy structure and evaluated on both healthy and damaged samples. Figure 9.6 illustrates the predicted probabilities for test samples, demonstrating a clear distinction between healthy and damaged states.

The performance metrics for both models are summarized in Table 9.3. These results highlight the strengths of each approach in distinguishing between healthy and damaged states.

Table 9.3: Comparative performance metrics for AR and CNN-based damage detection

Metric	AR Model (%)	CNN Model (%)
Accuracy	95.00	92.96
Sensitivity	100.00	92.00
Specificity	90.00	95.24
Precision	90.91	97.87

The confusion matrices for the AR and CNN models, shown in Figures 9.3 and 9.6, respectively, provide detailed breakdowns of the classification results, illustrating the distribution of true positives, false positives, true negatives, and false negatives for each method.

An important advantage of the AR-based approach is its ability to detect damage even when changes in raw signals are not visually apparent [Nair et al., 2006b]. Figure 9.4 shows time-domain signals from a healthy and damaged sample, where the differences are subtle and would be difficult to identify without statistical analysis. The effectiveness of AR models in detecting subtle structural changes aligns with findings in other SHM applications. For instance, [Frenz, 2022] applied AR models to a riveted steel railway bridge, demonstrating their ability to detect damage using vibration data under varying environmental conditions. While their study focused on a steel structure, the success of AR-based methods in both their work and ours underscores the versatility of this approach for different structural materials, such as the composite sandwich beam in our research, highlighting its potential for broader SHM applications.

The CNN model, on the other hand, excels in automatically learning complex patterns from raw data, which can be particularly beneficial when dealing with noisy or high-dimensional datasets [Avci et al., 2021b]. The CNN's ability to process segmented time series windows allows it to capture temporal dependencies that may be missed by traditional feature extraction methods like AR modeling. However, this comes at the cost of increased computational complexity and training time compared to the AR approach. The CNN's robustness to noise, as demonstrated in bearing fault diagnosis studies [Zhang et al., 2018a], suggests it may perform better in real-world scenarios where environmental variability is significant, such as in aerospace applications.

Comparing the two methods, the AR model offers simplicity and computational efficiency, making it suitable for real-time monitoring with limited computational resources. Conversely, the CNN model provides superior feature learning capabilities, potentially leading to higher accuracy in complex scenarios, but requires more computational power and careful tuning of hyperparameters. The choice between the two methods depends on the specific application requirements, such as the need for real-time processing versus the ability to handle complex, noisy data. Future work could explore hybrid approaches that combine the strengths of both methods, such as using AR features as inputs to a CNN, to achieve improved performance in SHM applications.

10 Bill of Materials and Cost Estimation

This chapter provides a comprehensive Bill of Materials (BOM) for the structural health monitoring (SHM) project involving a composite sandwich beam. The BOM lists all materials, tools, and components purchased for the fabrication, assembly, and testing of the composite structure, including the integration of piezoelectric sensors for vibration-based damage detection. The table below details each item, its quantity, unit price, total cost (including VAT/KDV and shipping where applicable), and the supplier.

Item Description	Quantity	Unit Price (TL)	Total Price (TL)	Supplier
CUD600 Unidirectional Carbon Fiber (50 cm x 1 m, 0.5 m ²)	5	489.76	2448.79	Kompozit Pazari
Peel Ply 80 g/m ² (152 cm x 5 m, 7.60 m ²)	1	733.97	733.97	Kompozit Pazari
V12 Flow Mesh Green (120 cm x 5 m, 6 m ²)	1	1037.50	1037.50	Kompozit Pazari
Vacuum Bag 65 micron Double Layer (4.6 m x 5 m, 23 m ²)	1	1289.78	1289.78	Kompozit Pazari
Measuring and Mixing Cup 1300 cc (5-pack)	1	193.02	193.02	Kompozit Pazari
Polivaks SV6 Mold Release Wax (300 g)	1	171.68	171.68	Kompozit Pazari
Polivaks Liquid PVA Mold Release (1000 ml)	1	220.78	220.78	Kompozit Pazari
Spiral Infusion Hose No:4 (5 m)	1	212.50	212.50	Kompozit Pazari
Infusion Hose 10x12 mm (5 m)	1	139.23	139.23	Kompozit Pazari
Valved Valve 10 mm (5-pack)	1	200.22	200.22	Kompozit Pazari
Vacuum Sealing Putty 170°C	1	351.34	351.34	Kompozit Pazari
Wooden Mixing Stick 30 cm (5-pack)	1	32.95	32.95	Kompozit Pazari
Plastic Mold Release Wedge 150 mm	1	141.09	141.09	Kompozit Pazari
HEXION-LR635 / LH637 Epoxy Set (A+B, 5 kg)	1	3065.52	3065.52	Kompozit Pazari
Shipping Fee (First Supplier)	1	1005.00	1005.00	Kompozit Pazari
Carbon Fiber UD300 (1 m ²)	1	600.00	600.00	ACME Kompozit

Item Description	Quantity	Unit Price (TL)	Total Price (TL)	Supplier
Vacuum Tape (Sealant)	1	400.00	400.00	ACME Kompozit
Aluminum Honeycomb Core (1.65 m ²)	1	680.00	1346.40	6GEN PANEL
Cutting Labor	1	40.80	54.40	6GEN PANEL
Packaging Crate	1	306.00	367.20	6GEN PANEL
6 mm Glass (75x80 cm)	1	360.00	432.00	AlÖztürk Cam ve Ayna
Araldite 2015 50 ml	2	1600.00	3840.00	Görgülü İnşaat
Masking Tape	1	28.80	34.56	Görgülü İnşaat
Macromax Coral Sponge	1	65.00	65.00	Bauhaus
Abbio Craft Knife	1	90.00	90.00	Bauhaus
Carpenter's Square 600 mm	1	150.00	150.00	Bauhaus
20 g CA Glue	1	92.50	92.50	Bauhaus
Nitrile Gloves	2	280.00	560.00	Bauhaus
Teflon Tape	1	25.00	25.00	Bauhaus
Metal Clamp	2	165.00	330.00	Bauhaus
Metal Clamp	2	325.00	780.00	Togaysan Civata Somun
Posca Marker Pen	2	95.84	230.00	Sanat Creative Kirtasiye
PCB Circuit Paper Print	2	166.00	400.00	AZ Kopyalama Kirtasiye
Ferric Chloride Solution (1 L)	1	1109.88	1109.88	AFK1
Shipping Fee (AFK1)	1	99.00	99.00	AFK1
Laminating Film (Glossy, 0.914 m x 50 m)	1	882.24	1058.69	Printec
Piezo Disk Element (20 mm)	50	7.02	351.00	Infotek
Shipping Fee (Infotek)	1	122.00	122.00	Infitek
Copper Tape (50 mm x 10 m)	1	799.00	799.00	Bantevi
Kapton Tape (50 mm x 33 m)	1	779.00	779.00	Bantevi
Grand Total (Including VAT and Shipping)		29,849.38 TL		

Table 10.1: Bill of Materials for the SHM project, including all purchases, quantities, unit prices, total prices (including VAT/KDV and shipping), and suppliers.

The total expenditure for the project, including all materials, tools, and shipping costs, amounts to 29,849.38 TL. This comprehensive BOM ensures transparency in the financial aspects of the project and provides a clear record of all resources utilized in the fabrication and testing of the composite sandwich beam for SHM applications.

11 Risk Management

11.1 Risk Assessment Approach

Throughout the development of our smart composite structure, we implemented a systematic risk management strategy to identify, assess, and mitigate potential challenges that could impact project success. Our approach followed a structured methodology:

1. **Risk Identification:** Team brainstorming sessions, literature review, and consultation with advisors to identify potential risks across technical, schedule, and resource dimensions.
2. **Risk Analysis:** Evaluation of each identified risk based on two key parameters:
 - **Probability:** Likelihood of risk occurrence (Low, Medium, High)
 - **Impact:** Severity of consequences if risk occurs (Low, Medium, High)
3. **Risk Prioritization:** Calculation of a Risk Priority Number (RPN) as the product of probability and impact scores, allowing for prioritization of mitigation efforts.
4. **Mitigation Planning:** Development of specific strategies to reduce either the probability of occurrence or the potential impact of high-priority risks.
5. **Contingency Planning:** Preparation of backup approaches to implement if primary mitigation strategies prove insufficient.
6. **Monitoring and Review:** Continuous assessment of risk status throughout the project lifecycle, with updates to the risk register as new information became available.

11.2 Risk Register

Table 11.1 summarizes the key risks identified for this project, their assessment, and our management approach:

11.3 Risk Response Implementation

For the highest priority risks, we implemented comprehensive mitigation strategies:

11.3.1 Sensor Damage During Manufacturing

This risk represented a critical threat to our core project functionality, as damaged sensors would compromise the entire SHM capability of the structure. Our response included:

1. **Mitigation Implementation:** We developed a multi-layer protection approach for the sensors:
 - Application of conformal coating on sensor electronics

Table 11.1: Risk Assessments

Description	Prob.	Imp.	RPN	Mitigation Strategy	Contingency Plan
Sensor damage in manufacturing	High	High	9	Protective encapsulation; validate with coupons	Surface-mounted sensors
Poor PCB-composite adhesion	High	High	9	Test adhesives; surface preparation	Mechanical fastening; vias
CFRP-sensor delamination	Med	High	6	Compatible adhesives; thickness transitions	Increase sensor redundancy
Poor sensor signal quality	Med	High	6	Signal conditioning; pre-manufacturing tests	Alternative sensor types/placement
Material property variations	High	Med	6	Strict quality control; characterize properties	Calibration procedures
Undetectable modal changes	Med	High	6	FEA damage simulation; sensitivity analysis	Multiple detection methods
Poor resin distribution	Med	High	6	Flow channels; trial infusions	Prepreg/autoclave backup
Honeycomb core crushing	Med	High	6	Pressure distribution fixture; force monitoring	Spare cores; repair procedures
Schedule delays	High	Med	6	Buffer periods; prioritize critical tasks	Scaled-down project scope
Inadequate modal excitation	Med	Med	4	Multiple excitation methods; FEA validation	Hybrid detection technique
Electrical interference	Med	Med	4	Shielding and grounding; signal filtering	Noise removal algorithms
Equipment availability limits	Med	Med	4	Advance scheduling; efficient protocols	Simplified testing procedures
Algorithm localization failure	Med	Med	4	Multiple algorithms; simulated data validation	Focus on detection only
Data acquisition failure	Low	High	3	Backup systems; redundant storage	Segmented testing protocol
Boundary condition variations	High	Low	3	Consistent fixtures; document setup	Less sensitive analysis methods

- Design of protective silicone encapsulation for piezoelectric elements
 - Temperature monitoring during curing to prevent thermal damage
 - Graduated pressure application during composite consolidation
2. **Validation Testing:** Before proceeding to full structure manufacturing, we conducted coupon-level tests by embedding sensors in small composite samples and subjecting them to the manufacturing process. These tests confirmed sensor survival and functionality.
 3. **Contingency Preparation:** Despite mitigation efforts, we prepared alternative sensor mounting designs that would allow for surface mounting if embedded sensors proved unviable. This included designing PCB layouts and connection schemes compatible with both approaches.

11.3.2 Poor Adhesion Between Flex PCB and Composite Layers

The interface between the flexible circuit board and composite materials represented another critical risk area:

1. **Mitigation Implementation:** Our approach included:
 - Testing of five different adhesive systems on representative material samples
 - Development of surface preparation protocols including abrasion and chemical treatments
 - Implementation of peel testing to quantify adhesion strength
 - Design of graduated thickness transitions to reduce stress concentrations
2. **Manufacturing Protocol:** Based on adhesion testing results, we developed a specific PCB-composite integration protocol with defined parameters for:
 - Surface preparation
 - Adhesive application method and thickness
 - Cure temperature and pressure
 - Quality inspection criteria
3. **Contingency Implementation:** We maintained readiness to implement mechanical fastening methods, including:
 - Design of through-holes for mechanical fastening if adhesive failure occurred
 - Preparation of materials for creating vias through the composite for alternative electrical connections
 - Modification of the sensor network design to accommodate alternative mounting approaches

11.4 Risk Management Outcomes

The implementation of our risk management strategy yielded several positive outcomes:

1. **Early Problem Identification:** The systematic risk assessment process allowed us to identify potential issues before they impacted project progress, particularly in the areas of sensor integration and manufacturing process development.
2. **Enhanced Design Robustness:** Consideration of potential failure modes led to more robust design decisions, including redundant sensor placements and multiple damage detection methodologies.
3. **Efficient Resource Allocation:** By prioritizing risks based on RPN values, we focused resources on addressing the most critical issues, optimizing our limited time and budget.
4. **Technical Challenge Resolution:** Several anticipated technical challenges were successfully resolved through the implementation of planned mitigation strategies, particularly in the areas of sensor protection and manufacturing process development.
5. **Improved Project Resilience:** When unexpected issues did arise, the team was better prepared to respond with pre-planned contingency measures, reducing the impact on overall project timelines.

The risk management process was not a one-time activity but continued throughout the project lifecycle, with regular reviews and updates to the risk register as new information became available or as risks evolved. This ongoing attention to potential challenges contributed significantly to the project's overall success.

12 Discussion

The development and evaluation of a smart composite structure for aerospace structural health monitoring yielded several significant findings with implications for both practical applications and future research directions.

12.1 Integration of Sensors in Composite Structures

The successful integration of piezoelectric sensors within CFRP sandwich structures demonstrated both the feasibility and challenges of creating smart aerospace components. While embedded sensors showed good survival rates through the manufacturing process, their damping characteristics differed significantly from surface-mounted alternatives. This phenomenon was particularly evident in the rapid signal decay observed in embedded sensors compared to surface-mounted ones, which has important implications for signal processing approaches in aerospace SHM systems.

The Flex PCB approach for sensor networking proved effective for managing connections while maintaining structural integrity, though signal quality showed sensitivity to wire routing configurations. Future designs could benefit from more robust strain relief mechanisms and pre-manufacturing sensor verification to reduce implementation risks.

12.2 Modal Analysis and Damage Detection Performance

The comparative analysis of vibration-based responses between surface-mounted and embedded sensors revealed intriguing contrasts. Surface-mounted sensors demonstrated superior sensitivity to structural changes after damage introduction, with clear frequency shifts from approximately 99 Hz to 70-80 Hz for the first mode. Embedded sensors, contrary to expectations, showed minimal frequency shifts despite the presence of significant damage. This suggests that sensor placement strategy critically influences damage detection capability, with implications for future aerospace SHM system designs.

The developed AR-based damage detection algorithm achieved impressive performance (95% accuracy, 100% sensitivity) on the alternative non-honeycomb test beam, outperforming the CNN approach (92.96% accuracy, 92% sensitivity) in sensitivity while demonstrating comparable overall accuracy. This highlights the potential of relatively simple statistical models for effective damage detection when appropriately implemented. However, the CNN model's higher specificity (95.24% vs. 90%) indicates its strength in reducing false positives, which could be valuable in aerospace applications where false alarms carry significant operational costs.

12.3 Excitation Methods and Signal Processing

The comparison between impulse and white noise excitation revealed clear advantages for impulse testing in aerospace structural applications. White noise excitation consistently

produced less distinct modal peaks across all sensor configurations, limiting its utility for frequency-based damage detection. This finding aligns with the theoretical understanding that impulse excitation more effectively excites the natural modes of the structure, providing clearer frequency signatures for analysis.

The curvature-based damage localization method demonstrated promising results in the alternative test beam, successfully identifying damage location with reasonable accuracy. However, its efficacy appeared dependent on beam configuration, performing better on the non-honeycomb structure. This suggests that structural complexity may require tailored damage localization approaches, particularly for sandwich composites with complex failure mechanisms.

12.4 Limitations and Challenges

Several limitations were identified during the project. The high stiffness of the sandwich structure led to rapid signal damping, complicating dynamic analysis and emphasizing the need for high-sampling-rate data acquisition systems. The manufacturing process highlighted challenges in consistent sensor embedding, with manual placement introducing variability that could affect signal quality. Future implementations should consider more automated placement methods to enhance repeatability.

The FEM models showed reasonable correlation with experimental natural frequencies, but discrepancies increased for higher modes, suggesting the need for more sophisticated modeling approaches that better account for the complex interactions between the honeycomb core, face sheets, and embedded sensors. Particularly, the assumed perfect bonding in the model likely diverges from reality, where bonding quality varies across the structure.

The damage detection algorithms, while effective for the controlled laboratory conditions in this study, would require further validation in more representative aerospace environments with varying temperatures, humidity, and operational vibrations. The current approach primarily addresses detection and localization, leaving severity assessment as an area for future development.

12.5 Implications for Aerospace Applications

The findings suggest several practical implications for aerospace SHM implementation. The superior performance of surface-mounted sensors challenges the conventional assumption that embedded sensors are universally advantageous. For retrofit applications or areas where signal clarity is paramount, surface mounting may offer practical benefits despite potential aerodynamic or aesthetic drawbacks.

The demonstrated effectiveness of statistical and machine learning approaches for damage detection without requiring complex physical models is particularly promising for aerospace applications, where comprehensive modeling of complex composite structures remains challenging. The high sensitivity achieved with the AR model (100%) is especially relevant for safety-critical aerospace components where undetected damage carries severe consequences.

The observed differences between sandwich and non-honeycomb structures highlight the need for application-specific SHM system design rather than universal approaches. Future

aerospace implementations will likely require customized sensor configurations and algorithms tailored to specific structural configurations and expected damage modes.

Overall, this project demonstrates the promise of vibration-based SHM for aerospace applications while identifying critical considerations for practical implementation. The integration of sensing capabilities directly into composite structures represents an important step toward next-generation aircraft with inherent self-monitoring capabilities, potentially enabling condition-based maintenance strategies that enhance both safety and operational efficiency.

13 Conclusion

This research project has successfully designed, manufactured, and experimentally evaluated a smart composite structure for aerospace structural health monitoring applications. The integration of piezoelectric sensors and strain gauges within a CFRP-aluminum honeycomb sandwich beam, combined with the development of effective damage detection algorithms, demonstrates a viable approach for implementing real-time monitoring in aerospace structures.

Several important achievements emerged from our work:

1. **Manufacturing Methodology:** A comprehensive manufacturing process was developed and documented for creating smart composite structures with embedded sensor networks. The vacuum infusion technique, combined with strategic sensor placement and flexible circuitry, proved effective for producing high-quality specimens while maintaining sensor functionality throughout the manufacturing process. The quality control protocols established provide a foundation for future development of aerospace-grade smart composites.
2. **Sensor Performance Evaluation:** Comparative analysis between embedded and surface-mounted sensors revealed significant differences in their dynamic responses, with surface-mounted sensors demonstrating superior sensitivity to structural changes following damage introduction. This finding challenges conventional assumptions about embedded sensing and provides valuable guidance for future sensor integration strategies in aerospace SHM.
3. **Algorithm Development:** The investigation of multiple damage detection approaches yielded complementary methods with distinct strengths. The AR-based technique achieved excellent sensitivity (100%), while the CNN-based approach offered stronger specificity (95.24%), demonstrating how statistical pattern recognition and machine learning can effectively identify damage without requiring detailed physical models. The curvature-based method further provided a physics-informed approach to localization, creating a robust multi-method damage detection framework.
4. **Dynamic Characterization:** Detailed modal analysis of the composite structure established its vibrational characteristics, with clear identification of natural frequencies and mode shapes that showed good correlation between experimental, analytical, and FEM approaches. This comprehensive understanding of the structure's dynamic behavior provided the foundation for effective damage detection.
5. **Practical Implementation Insights:** The project highlighted important considerations for practical aerospace implementation, including the benefits of impulse excitation over white noise, the critical importance of sensor placement strategy, and the need for application-specific SHM system design rather than universal approaches.

The limitations encountered during this research point to important directions for future work. Further research should focus on improving damage severity assessment capabilities, evaluating system performance under realistic operational conditions, and developing

more robust signal processing techniques for complex aerospace composites. Additionally, the integration of wireless data transmission and energy harvesting technologies would enhance the practicality of the approach for this implementation.

In conclusion, this project has demonstrated that vibration-based structural health monitoring through strategically placed piezoelectric sensors, coupled with appropriate signal processing and machine learning algorithms, offers a promising approach for enhancing the safety and reliability of aerospace structures. The transition from scheduled maintenance to condition-based maintenance, enabled by smart composite technologies like those developed in this project, represents a significant advancement toward more efficient, reliable, and sustainable aerospace operations. The methodologies and findings presented here contribute to the growing field of aerospace SHM and provide a foundation for continuing research in this critical domain.

Bibliography

- [Abdeljaber et al., 2018] Abdeljaber, O., Avci, O., Kiranyaz, M. S., Boashash, B., Sodano, H., and Inman, D. J. (2018). 1-d cnns for structural damage detection: Verification on a structural health monitoring benchmark data. *Neurocomputing*, 275:1308–1317.
- [Abdeljaber et al., 2017] Abdeljaber, O., Avci, O., Kiranyaz, S., Gabbouj, M., and Inman, D. J. (2017). Real-time vibration-based structural damage detection using one-dimensional convolutional neural networks. *Journal of Sound and Vibration*, 388:154–170.
- [Abrate and Di Sciuva, 2017] Abrate, S. and Di Sciuva, M. (2017). Equivalent single layer theories for composite and sandwich structures: A review. *Composite Structures*, 179:482–494.
- [Adams and Kuramoto, 2012] Adams, D. O. and Kuramoto, B. (2012). Damage tolerance testing of sandwich composites. In *Proceedings of the American Society for Composites 2012 Conference*. American Society for Composites.
- [Advani and Hsiao, 2012] Advani, S. G. and Hsiao, K. T., editors (2012). *Manufacturing techniques for polymer matrix composites (PMCs)*. Elsevier.
- [Airbus, 2019] Airbus (2019). Skywise: Airbus’ open data platform. Technical report, Airbus Commercial Aircraft.
- [Airbus, 2022] Airbus (2022). Composites manufacturing technology roadmap 2022-2035. Technical report, Airbus SE.
- [Allemang, 2003] Allemang, R. J. (2003). The modal assurance criterion—twenty years of use and abuse. *Sound and Vibration*, 37(8):14–23.
- [Allen, 1969a] Allen, H. G. (1969a). *Analysis and Design of Structural Sandwich Panels*. Pergamon Press, Oxford.
- [Allen, 1969b] Allen, H. G. (1969b). *Analysis and design of structural sandwich panels: the commonwealth and international library: structures and solid body mechanics division*. Elsevier.
- [Amin Yavari et al., 2013] Amin Yavari, S., Wauthle, R., van der Stok, J., Riemsdag, A. C., Janssen, M., Mulier, M., and Zadpoor, A. A. (2013). Fatigue behavior of porous biomaterials manufactured using selective laser melting. *Materials Science and Engineering: C*, 33(8):4849–4858.
- [An and Cho, 2015] An, J. and Cho, S. (2015). Variational autoencoder based anomaly detection using reconstruction probability. *Special Lecture on IE*, 2(1):1–18.
- [Ashby, 2006] Ashby, M. F. (2006). The properties of foams and lattices. *Philosophical Transactions of the Royal Society A*, 364(1838):15–30.
- [Ashby and Bréchet, 2003] Ashby, M. F. and Bréchet, Y. J. M. (2003). Designing hybrid materials. *Acta Materialia*, 51(19):5801–5821.

- [ASTM International, 2011] ASTM International (2011). Standard practice for acoustic emission examination of fiber-reinforced plastic resin matrix composite structures (astm e2806-11). Technical report, ASTM International.
- [ASTM International, 2013] ASTM International (2013). Standard practice for structural health monitoring of composite structures (astm f3011-13). Technical report, ASTM International.
- [ASTM International, 2017] ASTM International (2017). Standard test method for flat-wise compressive properties of sandwich cores (astm c365). Technical report, ASTM International.
- [Atkinson et al., 2008] Atkinson, C., Texter, S., Hellekson, R., and Patton, G. (2008). Spacecraft structures and mechanisms for the jwst integrated science instrument module. In *Optical, Infrared, and Millimeter Space Telescopes*, volume 5487, pages 566–577. SPIE.
- [Attwater et al., 2014] Attwater, D., Hsia, K. J., Morrison, H., and Arritt, B. (2014). The impact of tow-drop gaps in automated fiber placement structures. *SAMPE Journal*, 50(2):36–42.
- [Avci et al., 2021a] Avci, O., Abdeljaber, O., Kiranyaz, S., Hussein, M., Gabbouj, M., and Inman, D. J. (2021a). A review of vibration-based damage detection in civil structures: From traditional methods to machine learning and deep learning applications. *Mechanical Systems and Signal Processing*, 147:107077.
- [Avci et al., 2021b] Avci, O., Abdeljaber, O., Kiranyaz, S., and Inman, D. (2021b). Convolutional neural networks for real-time and wireless damage detection. *Structural Health Monitoring*, 20(4):1699–1714.
- [Avery and Sankar, 2000] Avery, J. L. and Sankar, B. V. (2000). Compressive failure of sandwich beams with debonded face-sheets. *Journal of Composite Materials*, 34(14):1176–1199.
- [Azimi and Pekcan, 2020] Azimi, M. and Pekcan, G. (2020). Structural health monitoring using extremely limited sensors through deep learning. *Structural Control and Health Monitoring*, 27(1):e2464.
- [Bach et al., 2015] Bach, S., Binder, A., Montavon, G., Klauschen, F., Müller, K.-R., and Samek, W. (2015). On pixel-wise explanations for non-linear classifier decisions by layer-wise relevance propagation. *PloS One*, 10(7):e0130140.
- [Baker et al., 2004] Baker, A., Dutton, S., and Kelly, D. (2004). *Composite materials for aircraft structures*. AIAA.
- [Balageas et al., 2010] Balageas, D., Fritzen, C. P., and Güemes, A., editors (2010). *Structural health monitoring*, volume 90. John Wiley & Sons.
- [Bandara et al., 2019] Bandara, R. P., Chan, T. H. T., and Thambiratnam, D. P. (2019). Frequency response function based damage identification using principal component analysis and pattern recognition technique. *Engineering Structures*, 186:416–427.
- [Bao et al., 2019] Bao, Y., Tang, Z., Li, H., and Zhang, Y. (2019). Computer vision and deep learning-based data anomaly detection method for structural health monitoring. *Structural Health Monitoring*, 18(2):401–421.

- [Bapanapalli et al., 2006] Bapanapalli, S. K., Martinez, O. M., Gogu, C., Sankar, B. V., Haftka, R. T., and Blosser, M. L. (2006). Analysis and design of corrugated-core sandwich panels for thermal protection systems of space vehicles. *AIAA Journal*, 44(8):1724–1733.
- [Barbero, 2017] Barbero, E. J. (2017). *Introduction to Composite Materials Design*. CRC Press, Boca Raton, FL, 3 edition.
- [Barthorpe et al., 2017] Barthorpe, R. J., Manson, G., and Worden, K. (2017). On multi-site damage identification using single-site training data. *Journal of Sound and Vibration*, 409:43–64.
- [Beardmore and Johnson, 1986] Beardmore, P. and Johnson, C. F. (1986). The potential for composites in structural automotive applications. *Composites Science and Technology*, 26(4):251–281.
- [Beck and Katafygiotis, 1998] Beck, J. L. and Katafygiotis, L. S. (1998). Updating models and their uncertainties. i: Bayesian statistical framework. *Journal of Engineering Mechanics*, 124(4):455–461.
- [Bergan et al., 2014] Bergan, A., Bakuckas, J. G., Awerbuch, J., and Tan, T. M. (2014). Assessment of damage containment features of a full-scale prseus fuselage panel. *Composite Structures*, 113:174–185.
- [Berggreen et al., 2007] Berggreen, C., Simonsen, B. C., and Borum, K. K. (2007). Experimental and numerical study of interface crack propagation in foam-cored sandwich beams. *Journal of Composite Materials*, 41(4):493–520.
- [Bickerton and Advani, 2008] Bickerton, S. and Advani, S. G. (2008). Experimental investigation and flow visualization of the resin-transfer mold-filling process in a non-planar geometry. *Composites Science and Technology*, 57(1):23–33.
- [Bickerton et al., 2017] Bickerton, S., Govignon, Q., Comas-Cardona, S., and Binetruy, C. (2017). Experimental investigation and numerical modelling of induced through-thickness deformation in liquid composite moulding. In *FPCM-9 Conference*.
- [Bitzer, 1997] Bitzer, T. (1997). *Honeycomb technology: materials, design, manufacturing, applications and testing*. Springer Science & Business Media.
- [Bitzer, 2012] Bitzer, T. N. (2012). Honeycomb marine applications. *Journal of Reinforced Plastics and Composites*, 31(7):463–468.
- [Black, 2013] Black, S. (2013). Edge closeout reinforcements: Design consideration in composite sandwich panels. *Composites Technology*, 19(3):40–45.
- [Black, 2018] Black, S. (2018). McLaren automotive: Roadmap for automotive mass production of carbon fiber composites. *Composites World*, 4(7):30–36.
- [Bodeux and Golinalval, 2001] Bodeux, J. B. and Golinalval, J.-C. (2001). Application of armav models to the identification and damage detection of mechanical and civil engineering structures. *Smart Materials and Structures*, 10(3):479–489.
- [Boeing, 2018] Boeing (2018). Boeing analytics for mobility (bam): Transforming data into insights. Technical report, The Boeing Company.
- [Boller, 2001] Boller, C. (2001). Ways and options for aircraft structural health management. *Smart Materials and Structures*, 10(3):432.

- [Bond et al., 2011] Bond, L. J., Clayton, D. A., and Phillion, K. (2011). Condition assessment technologies for nuclear power plant systems. Technical Report PNNL-20719, Pacific Northwest National Laboratory (PNNL).
- [Bossi and Giurgiutiu, 2015] Bossi, R. H. and Giurgiutiu, V. (2015). Nondestructive testing of damage in aerospace composites. In *Polymer composites in the aerospace industry*, pages 413–448. Woodhead Publishing.
- [Boyer and Gall, 1985] Boyer, H. E. and Gall, T. L., editors (1985). *Metals Handbook*. American Society for Metals, Materials Park, OH.
- [Brocks et al., 2013] Brocks, T., Shiino, M. Y., Cioffi, M. O. H., Voorwald, H. J. C., and Caporalli Filho, A. (2013). Experimental rtm manufacturing analysis of carbon/epoxy composites for aerospace application: non-crimp and woven fabric differences. *Materials Research*, 16(5):1175–1182.
- [Brownjohn et al., 2001] Brownjohn, J. M. W., Xia, P.-Q., Hao, H., and Xia, Y. (2001). Civil structure condition assessment by fe model updating: Methodology and case studies. *Finite Elements in Analysis and Design*, 37(10):761–775.
- [Bull et al., 2021a] Bull, L. A., Gardner, P., Gosliga, J., Rogers, T. J., Dervilis, N., Cross, E. J., Papatheou, E., and Worden, K. (2021a). Foundations of population-based shm, part i: Homogeneous populations and forms. *Mechanical Systems and Signal Processing*, 148:107141.
- [Bull et al., 2021b] Bull, L. A., Gardner, P., Gosliga, J., Rogers, T. J., Dervilis, N., Cross, E. J., Papatheou, E., and Worden, K. (2021b). Foundations of population-based shm, part iii: Heterogeneous populations – mapping and transfer. *Mechanical Systems and Signal Processing*, 149:107142.
- [Bull et al., 2019] Bull, L. A., Worden, K., Fuentes, R., Manson, G., Cross, E. J., and Dervilis, N. (2019). Outlier ensembles: A robust method for damage detection and unsupervised feature extraction from high-dimensional data. *Journal of Sound and Vibration*, 453:126–150.
- [Camanho et al., 2012] Camanho, P. P., Arteiro, A., Turon, A., and Costa, J. (2012). Structural integrity of thin-ply laminates. *JEC Composites*, 75:91–97.
- [Campbell, 2004] Campbell, F. C. (2004). *Manufacturing processes for advanced composites*. Elsevier.
- [Campbell, 2010] Campbell, F. C. (2010). *Structural composite materials*. ASM International.
- [Cantwell and Morton, 1991] Cantwell, W. J. and Morton, J. (1991). The impact resistance of composite materials—a review. *Composites*, 22(5):347–362.
- [Cao and Qiao, 2009] Cao, M. and Qiao, P. (2009). Novel laplacian scheme and multiresolution modal curvatures for structural damage identification. *Mechanical Systems and Signal Processing*, 23(4):1223–1242.
- [Cappello et al., 2020] Cappello, C., Iacovino, C., Catbas, F. N., and Zonta, D. (2020). A data-fusion framework for wave propagation-based structural damage detection. *Structural Control and Health Monitoring*, 27(6):e2531.

- [Carden and Brownjohn, 2008] Carden, E. P. and Brownjohn, J. M. W. (2008). Arma modelled time-series classification for structural health monitoring of civil infrastructure. *Mechanical Systems and Signal Processing*, 22(2):295–314.
- [Carden and Fanning, 2004] Carden, E. P. and Fanning, P. (2004). Vibration based condition monitoring: A review. *Structural Health Monitoring*, 3(4):355–377.
- [Carlsson and Kardomateas, 2011] Carlsson, L. A. and Kardomateas, G. A. (2011). *Structural and Failure Mechanics of Sandwich Composites*. Springer Science & Business Media, Dordrecht.
- [Carrera et al., 2013] Carrera, E., Giunta, G., and Petrolo, M. (2013). Beam structures: Classical and advanced theories. *John Wiley & Sons*.
- [Castanié et al., 2020] Castanié, B., Bouvet, C., and Ginot, M. (2020). Review of composite sandwich structure in aeronautic applications. *Composites Part C: Open Access*, 1:100004.
- [Centea et al., 2015] Centea, T., Grunenfelder, L. K., and Nutt, S. R. (2015). A review of out-of-autoclave preprints – material properties, process phenomena, and manufacturing considerations. *Composites Part A: Applied Science and Manufacturing*, 70:132–154.
- [Centea and Hubert, 2011] Centea, T. and Hubert, P. (2011). Measuring the impregnation of an out-of-autoclave prepreg by micro-ct. *Composites Science and Technology*, 71(5):593–599.
- [Cha et al., 2017] Cha, Y.-J., Choi, W., and Büyüköztürk, O. (2017). Deep learning-based crack damage detection using convolutional neural networks. *Computer-Aided Civil and Infrastructure Engineering*, 32(5):361–378.
- [Cha et al., 2018] Cha, Y.-J., Choi, W., Suh, G., Mahmoudkhani, S., and Büyüköztürk, O. (2018). Autonomous structural visual inspection using region-based deep learning for detecting multiple damage types. *Computer-Aided Civil and Infrastructure Engineering*, 33(9):731–747.
- [Chakraborty et al., 2009] Chakraborty, D., Kovvali, N., Wei, J., Papandreou-Suppappola, A., Cochran, D., and Chattopadhyay, A. (2009). Damage classification structural health monitoring in bolted structures using time-frequency techniques. *Journal of Intelligent Material Systems and Structures*, 20(11):1289–1305.
- [Chang et al., 2020] Chang, W. S., Chen, E., Halim, E., and Kim, S. H. (2020). Thermal behavior of composite sandwich structures for commercial aircraft. *Journal of Sandwich Structures & Materials*, 22(3):722–749.
- [Chaudhari et al., 2011] Chaudhari, R., Karcher, M., Elsner, P., and Henning, F. (2011). Characterization of high pressure rtm processes for manufacturing of high performance composites. In *18th International Conference on Composite Materials*.
- [Chen et al., 2019] Chen, Y., Sun, X., and Jin, Y. (2019). Communication-efficient federated deep learning with layerwise asynchronous model update and temporally weighted aggregation. *IEEE Transactions on Neural Networks and Learning Systems*, 31(10):4229–4238.
- [Choi et al., 2011] Choi, S., Lee, J. J., Sohn, H., and Park, G. (2011). Impedance-based structural health monitoring considering temperature effects. In *Proceedings of SPIE 7984, Sensors and Smart Structures Technologies for Civil, Mechanical, and Aerospace Systems*. SPIE.

- [Chung et al., 2014] Chung, J., Gulcehre, C., Cho, K., and Bengio, Y. (2014). Empirical evaluation of gated recurrent neural networks on sequence modeling.
- [CMH-17, 2012] CMH-17 (2012). *Composite Materials Handbook, Volume 3: Polymer Matrix Composites Materials Usage, Design, and Analysis*. SAE International.
- [Composites Australia, 2018] Composites Australia (2018). Edge sealing methods for honeycomb sandwich panels in aerospace applications. Technical report, Composites Australia.
- [Composites UK, 2021] Composites UK (2021). Composite materials outlook 2021-2030. Technical report, Composites UK. Industry Report.
- [Compton and Lewis, 2014] Compton, B. G. and Lewis, J. A. (2014). 3d-printing of lightweight cellular composites. *Advanced Materials*, 26(34):5930–5935.
- [Cornwell et al., 1999] Cornwell, P., Doebling, S. W., and Farrar, C. R. (1999). Application of the strain energy damage detection method to plate-like structures. *Journal of Sound and Vibration*, 224(2):359–374.
- [Correia et al., 2005] Correia, N. C., Robitaille, F., Long, A. C., Rudd, C. D., Šimáček, P., and Advani, S. G. (2005). Analysis of the vacuum infusion moulding process: I. analytical formulation. *Composites Part A: Applied Science and Manufacturing*, 36(12):1645–1656.
- [Cross et al., 2011] Cross, E. J., Worden, K., and Chen, Q. (2011). Cointegration: A novel approach for the removal of environmental trends in structural health monitoring data. *Proceedings of the Royal Society A: Mathematical, Physical and Engineering Sciences*, 467(2133):2712–2732.
- [Cytec Industries, 2022] Cytec Industries (2022). *FM® Adhesive Film Technical Data Sheet*. Cytec Industries Inc.
- [da Silva et al., 2018] da Silva, L. F., Öchsner, A., and Adams, R. D., editors (2018). *Handbook of adhesion technology*. Springer.
- [Dackermann et al., 2014] Dackermann, U., Smith, W. A., and Randall, R. B. (2014). Damage identification based on response-only measurements using cepstrum analysis and artificial neural networks. *Structural Health Monitoring*, 13(4):430–444.
- [Dang et al., 2020] Dang, T. D., Hallett, S. R., Kim, B. C., Le Cahain, Y., Butler, R., and Liu, W. (2020). Multi-objective optimization of variable angle tow composite plates with manufacturing constraints. *Composite Structures*, 237:111920.
- [Davies, 2012] Davies, G. (2012). *Materials for automobile bodies*. Butterworth-Heinemann.
- [Dayyani et al., 2015] Dayyani, I., Shaw, A. D., Saavedra Flores, E. I., and Friswell, M. I. (2015). The mechanics of composite corrugated structures: A review with applications in morphing aircraft. *Composite Structures*, 133:358–380.
- [Department of Defense, 2008] Department of Defense (2008). Condition based maintenance plus (cbm+) dod guidebook. Technical report, Department of Defense.
- [Deraemaeker et al., 2008] Deraemaeker, A., Reynders, E., De Roeck, G., and Kulla, J. (2008). Vibration-based structural health monitoring using output-only measurements under changing environment. *Mechanical Systems and Signal Processing*, 22(1):34–56.

- [Deraemaeker and Worden, 2018] Deraemaeker, A. and Worden, K. (2018). *New Trends in Vibration Based Structural Health Monitoring*, volume 588. Springer.
- [Di Sante, 2015] Di Sante, R. (2015). Fibre optic sensors for structural health monitoring of aircraft composite structures: Recent advances and applications. *Sensors*, 15(8):18666–18713.
- [Diamanti and Soutis, 2010] Diamanti, K. and Soutis, C. (2010). Structural health monitoring techniques for aircraft composite structures. *Progress in Aerospace Sciences*, 46(8):342–352.
- [Dincer and Rosen, 2021] Dincer, I. and Rosen, M. A. (2021). *Thermal energy storage: systems and applications*. John Wiley & Sons.
- [Doebling et al., 1996] Doebling, S. W., Farrar, C. R., Prime, M. B., and Shevitz, D. W. (1996). Damage identification and health monitoring of structural and mechanical systems from changes in their vibration characteristics: A literature review. Technical Report LA-13070-MS, Los Alamos National Laboratory.
- [Dominauskas et al., 2007] Dominauskas, A., Heider, D., and Gillespie, J. W. (2007). Electric time-domain reflectometry sensor for online flow sensing in liquid composite molding processing. *Composites Part A: Applied Science and Manufacturing*, 38(1):138–146.
- [Dorafshan et al., 2018] Dorafshan, S., Thomas, R. J., and Maguire, M. (2018). Comparison of deep convolutional neural networks and edge detectors for image-based crack detection in concrete. *Construction and Building Materials*, 186:1031–1045.
- [Drafts, 2020] Drafts, D. A. C. (2020). *Composite bagging techniques*. Abaris Training Resources, Inc.
- [Du Pont, 2022] Du Pont (2022). *Kevlar® Technical Guide*. E.I. du Pont de Nemours and Company.
- [Dutta and Talukdar, 2004] Dutta, A. and Talukdar, S. (2004). Damage detection in bridges using accurate modal parameters. *Finite Elements in Analysis and Design*, 40(3):287–304.
- [EASA, 2020a] EASA (2020a). European plan for aviation safety (epas) 2020-2024. Technical report, European Union Aviation Safety Agency.
- [EASA, 2020b] EASA (2020b). Future aviation safety team (fast) annual safety recommendations. Technical report, European Union Aviation Safety Agency.
- [EASA, 2021] EASA (2021). Certification specifications and acceptable means of compliance for large aeroplanes cs-25 (amendment 26). Technical report, European Union Aviation Safety Agency.
- [EASA, 2022] EASA (2022). *Certification Specifications for Large Aeroplanes CS-25*. European Union Aviation Safety Agency.
- [Embraer, 2015] Embraer (2015). *E-Jets Maintenance Manual*. Embraer S.A.
- [Entezami and Shariatmadar, 2014] Entezami, A. and Shariatmadar, H. (2014). Damage detection in structural systems by improved sensitivity of modal strain energy and tikhonov regularization method. *International Journal of Dynamics and Control*, 2(4):509–520.

- [Evonik Industries, 2021] Evonik Industries (2021). *ROHACELL® Structural Foam Technical Manual*. Evonik Resource Efficiency GmbH.
- [FAA, 2009] FAA (2009). Composite aircraft structure (ac 20-107b). Technical report, U.S. Department of Transportation.
- [FAA, 2011] FAA (2011). 14 cfr part 25—airworthiness standards: Transport category airplanes, §25.571 damage-tolerance and fatigue evaluation of structure. Technical report, U.S. Department of Transportation.
- [FAA, 2014] FAA (2014). Advisory circular 29-2c mg8: Substantiation of composite rotorcraft structures. Technical report, U.S. Department of Transportation.
- [FAA, 2018] FAA (2018). Airworthiness approval 8110-132, faa approval for boeing service letter 737-sl-51-038-f. Technical report, Boeing.
- [FAA, 2022] FAA (2022). 14 cfr part 25.853 - compartment interiors. Technical report, Federal Aviation Administration.
- [Fan and Qiao, 2011] Fan, W. and Qiao, P. (2011). Vibration-based damage identification methods: A review and comparative study. *Structural Health Monitoring*, 10(1):83–111.
- [Faravelli and Yao, 1996] Faravelli, L. and Yao, T. (1996). Use of adaptive networks in fuzzy control of civil structures. *Computer-Aided Civil and Infrastructure Engineering*, 11(1):67–76.
- [Farrar and Lieven, 2007] Farrar, C. R. and Lieven, N. A. (2007). Damage prognosis: the future of structural health monitoring. *Philosophical Transactions of the Royal Society A: Mathematical, Physical and Engineering Sciences*, 365(1851):623–632.
- [Farrar et al., 2006] Farrar, C. R., Park, G., Allen, D. W., and Todd, M. D. (2006). Sensor network paradigms for structural health monitoring. *Structural Control and Health Monitoring*, 13(1):210–225.
- [Farrar and Worden, 2012] Farrar, C. R. and Worden, K. (2012). *Structural health monitoring: a machine learning perspective*. John Wiley & Sons.
- [Farrar and Worden, 2013] Farrar, C. R. and Worden, K. (2013). *Structural Health Monitoring: A Machine Learning Perspective*. John Wiley & Sons.
- [Fassois and Sakellariou, 2007] Fassois, S. D. and Sakellariou, J. S. (2007). Time-series methods for fault detection and identification in vibrating structures. *Philosophical Transactions of the Royal Society A: Mathematical, Physical and Engineering Sciences*, 365(1851):411–448.
- [Federal Aviation Administration, 2010] Federal Aviation Administration (2010). *Composite Aircraft Structure*. U.S. Department of Transportation.
- [Feraboli and Kedward, 2003] Feraboli, P. and Kedward, K. T. (2003). Enhanced evaluation of the low-velocity impact response of composite plates. *AIAA Journal*, 41(10):1895–1904.
- [FIA, 2022] FIA (2022). *Formula One Technical Regulations*. Fédération Internationale de l’Automobile.
- [Figueiredo et al., 2011] Figueiredo, E., Park, G., Farrar, C. R., Worden, K., and Figueiras, J. (2011). Machine learning algorithms for damage detection under operational and environmental variability. *Structural Health Monitoring*, 10(6):559–572.

- [Frenz, 2022] Frenz, M. J. (2022). *Development of a Model-Free Damage Detection Algorithm Using AR-Models and Its Application to a Riveted Steel Railway Bridge*. Dissertation, KTH Royal Institute of Technology.
- [Friedrich and Almajid, 2013] Friedrich, K. and Almajid, A. A. (2013). Manufacturing aspects of advanced polymer composites for automotive applications. *Applied Composite Materials*, 20(2):107–128.
- [Friswell and Mottershead, 1995] Friswell, M. I. and Mottershead, J. E. (1995). *Finite Element Model Updating in Structural Dynamics*. Kluwer Academic Publishers.
- [Frostig et al., 1992] Frostig, Y., Baruch, M., Vilnay, O., and Sheinman, I. (1992). High-order theory for sandwich-beam behavior with transversely flexible core. *Journal of Engineering Mechanics*, 118(5):1026–1043.
- [Fugate et al., 2001] Fugate, M. L., Sohn, H., and Farrar, C. R. (2001). Vibration-based damage detection using statistical process control. *Mechanical Systems and Signal Processing*, 15(4):707–721.
- [Furdek, 2008] Furdek, H. (2008). Boeing 787 lessons learned. In *8th Society of Manufacturing Engineers*.
- [Gao and Rose, 2008] Gao, H. and Rose, J. L. (2008). Ultrasonic sensor placement optimization in structural health monitoring using evolutionary strategy. In *AIP Conference Proceedings*, volume 975, pages 1687–1693. American Institute of Physics.
- [Gardiner, 2015a] Gardiner, G. (2015a). Aerocomposites: The move to multifunctionality. *Composites World*, 1(7):32–39.
- [Gardiner, 2015b] Gardiner, G. (2015b). Thermoplastic composites: Inside story. *Composites World*, 1(1):34–40.
- [Gardiner, 2018] Gardiner, G. (2018). The making of the bmw iseries. *Composites World*, 4(2):18–25.
- [Gardiner, 2020] Gardiner, G. (2020). Automated fiber placement: Fulfilling the promise. *Composites World*, 6(3):38–45.
- [Gardiner, 2021] Gardiner, G. (2021). Automotive composites: The make-or-break decade. *Composites World*, 7(2):28–33.
- [Gardner et al., 2020a] Gardner, P., Fuentes, R., Dervilis, N., Mineo, C., Pierce, S. G., Cross, E. J., and Worden, K. (2020a). Machine learning at the interface of structural health monitoring and non-destructive evaluation. *Philosophical Transactions of the Royal Society A*, 378(2182):20190581.
- [Gardner et al., 2020b] Gardner, P., Liu, X., and Worden, K. (2020b). On the application of domain adaptation in structural health monitoring. *Mechanical Systems and Signal Processing*, 138:106550.
- [Garnier et al., 2011] Garnier, C., Pastor, M. L., Eyma, F., and Lorrain, B. (2011). The detection of aeronautical defects in situ on composite structures using non destructive testing. *Composite Structures*, 93(5):1328–1336.
- [Geiger et al., 2012] Geiger, M., Steger, W., and Meisenbach, K. (2012). The automotive industry's requirements on the manufacturing technology of structural lightweight components of high-performance cfsp. In *Academic Conference of RWTH Aachen*.

- [Gibson and Ashby, 1999a] Gibson, L. J. and Ashby, M. F. (1999a). *Cellular solids: structure and properties*. Cambridge University Press.
- [Gibson and Ashby, 1999b] Gibson, L. J. and Ashby, M. F. (1999b). *Cellular Solids: Structure and Properties*. Cambridge University Press, Cambridge, 2 edition.
- [Gibson, 2010] Gibson, R. F. (2010). A review of recent research on mechanics of multi-functional composite materials and structures. *Composite Structures*, 92(12):2793–2810.
- [Girdauskaite and Krzywinski, 2015] Girdauskaite, L. and Krzywinski, S. (2015). Draping behavior of technical textiles for high-performance composite applications. In *Modern Processing and Application in Materials Science*, pages 155–171. Springer.
- [Giurgiutiu, 2008] Giurgiutiu, V. (2008). *Structural health monitoring with piezoelectric wafer active sensors*. Academic Press.
- [Giurgiutiu, 2015] Giurgiutiu, V. (2015). *Structural health monitoring of aerospace composites*. Academic Press.
- [Giurgiutiu and Cuc, 2005] Giurgiutiu, V. and Cuc, A. (2005). Embedded non-destructive evaluation for structural health monitoring, damage detection, and failure prevention. *Shock and Vibration Digest*, 37(2):83–105.
- [Giurgiutiu and Soutis, 2012] Giurgiutiu, V. and Soutis, C. (2012). Enhanced composites integrity through structural health monitoring. *Applied Composite Materials*, 19(5):813–829.
- [Glaessgen and Stargel, 2012] Glaessgen, E. H. and Stargel, D. S. (2012). The digital twin paradigm for future nasa and us air force vehicles. In *53rd AIAA/ASME/ASCE/AHS/ASC Structures, Structural Dynamics and Materials Conference*. AIAA.
- [Golinval et al., 2004] Golinval, J.-C., De Boe, P., Yan, A. M., and Kerschen, G. (2004). Structural damage detection based on pca of vibration measurements. In *Proceedings of the 58th Meeting of the Society for Machinery Failure Prevention Technology*, pages 361–370.
- [Govignon et al., 2013] Govignon, Q., Bickerton, S., and Kelly, P. A. (2013). Simulation of the reinforcement compaction and resin flow during the complete resin infusion process. *Composites Part A: Applied Science and Manufacturing*, 48:124–134.
- [Grieves and Vickers, 2017] Grieves, M. and Vickers, J. (2017). Digital twin: Mitigating unpredictable, undesirable emergent behavior in complex systems. In *Transdisciplinary perspectives on complex systems*, pages 85–113. Springer.
- [Grimes, 1972] Grimes, G. C. (1972). The adhesive-adherend interface and bondline effects in aged flightworthy bonded joints. *Composite Structures*, 4:123–145.
- [Grondel et al., 2004] Grondel, S., Assaad, J., Delebarre, C., and Moulin, E. (2004). Health monitoring of a composite wingbox structure. *Ultrasonics*, 42(1-9):819–824.
- [Güemes et al., 2010] Güemes, A., Fernandez-Lopez, A., and Soller, B. (2010). Optical fiber distributed sensing-physical principles and applications. *Structural Health Monitoring*, 9(3):233–245.
- [Gul and Catbas, 2009] Gul, M. and Catbas, F. N. (2009). Statistical pattern recognition for structural health monitoring using time series modeling: Theory and experimental verifications. *Mechanical Systems and Signal Processing*, 23(7):2192–2204.

- [Gul and Catbas, 2011] Gul, M. and Catbas, F. N. (2011). Structural health monitoring and damage assessment using a novel time series analysis methodology with sensor clustering. *Journal of Sound and Vibration*, 330(6):1196–1210.
- [Gulgec et al., 2019] Gulgec, N. S., Takáč, M., and Pakzad, S. N. (2019). Convolutional neural network approach for robust structural damage detection and localization. *Journal of Computing in Civil Engineering*, 33(3):04019005.
- [Guo et al., 2020] Guo, L., Chen, W. L., and Li, Y. B. (2020). Honeycomb structures in radar absorbing materials: A review. *Composite Structures*, 248:112581.
- [Guo and Cawley, 1993] Guo, N. and Cawley, P. (1993). The interaction of lamb waves with delaminations in composite laminates. *The Journal of the Acoustical Society of America*, 94(4):2240–2246.
- [Gürdal et al., 1999] Gürdal, Z., Haftka, R. T., and Hajela, P. (1999). *Design and Optimization of Laminated Composite Materials*. John Wiley & Sons, New York.
- [Ha and Narro-García, 2021] Ha, J. U. and Narro-García, R. (2021). Aluminium honeycomb cores: production, properties and applications. In *Honeycomb Structures*, pages 35–65. Springer.
- [Hale, 2008] Hale, J. (2008). Boeing 787 from the ground up. *Aero*, 6(4):17–23.
- [Hale, 2018] Hale, J. (2018). Boeing 777x to bring composite wings to commercial aviation. *Reinforced Plastics*, 62(5):273–275.
- [Hamstad, 1986] Hamstad, M. A. (1986). A review: acoustic emission, a tool for composite-materials studies. *Experimental Mechanics*, 26(1):7–13.
- [Haq et al., 2019] Haq, M., Khomenko, A., Udma, L., Udma, S., and Naber, J. (2019). Nondestructive evaluation of damage in fiber-reinforced polymer composites using capacitive imaging technique. *Composite Structures*, 230:111494.
- [Hardis et al., 2013] Hardis, R., Jessop, J. L., Peters, F. E., and Kessler, M. R. (2013). Cure kinetics characterization and monitoring of an epoxy resin using dsc, raman spectroscopy, and dea. *Composites Part A: Applied Science and Manufacturing*, 49:100–108.
- [Härdle and Simar, 2007] Härdle, W. K. and Simar, L. (2007). *Applied Multivariate Statistical Analysis*, volume 22007. Springer, Berlin.
- [Hart-Smith, 1999] Hart-Smith, L. J. (1999). Adhesive bonding of composite structures—progress to date and some remaining challenges. *Journal of Composites, Technology and Research*, 24(3):133–151.
- [Hearn and Testa, 1991] Hearn, G. and Testa, R. B. (1991). Modal analysis for damage detection in structures. *Journal of Structural Engineering*, 117(10):3042–3063.
- [Heimbs, 2012] Heimbs, S. (2012). Energy absorption in honeycomb sandwich structures. *International Journal of Crashworthiness*, 17(6):575–589.
- [Heimbs and Pein, 2009] Heimbs, S. and Pein, M. (2009). Failure behaviour of honeycomb sandwich corner joints and inserts. *Composite Structures*, 89(4):575–588.
- [Hellier, 2003] Hellier, C. J. (2003). *Handbook of nondestructive evaluation*. McGraw-Hill.
- [Hernandez, 2014] Hernandez, E. M. (2014). Identification of isolated structural damage from incomplete spectrum information using l1-norm minimization. *Mechanical Systems and Signal Processing*, 46(1):59–69.

- [Herrmann et al., 2005] Herrmann, A. S., Zahlen, P. C., and Zuardy, I. (2005). Sandwich structures technology in commercial aviation. In *Sandwich structures 7: Advancing with sandwich structures and materials*, pages 13–26. Springer.
- [Heuer et al., 2015] Heuer, H., Schulze, M., Pooth, M., Gäßler, S., Nocke, A., Bardl, G., and Cherif, C. (2015). Review on quality assurance along the cfrp value chain—non-destructive testing of fabrics, preforms and cfrp by hf radio wave techniques. *Composites Part B: Engineering*, 77:494–501.
- [Heuss et al., 2012] Heuss, R., Müller, N., Van Sintern, W., Starke, A., and Tschiesner, A. (2012). Lightweight, heavy impact. Technical report, McKinsey & Company.
- [Hexcel Corporation, 2021] Hexcel Corporation (2021). *HexPly® Prepreg Technology*. Hexcel Corporation. Technical Manual.
- [Hexcel Corporation, 2022a] Hexcel Corporation (2022a). *HexPly® Prepreg Selector Guide for Aerospace*. Hexcel Corporation.
- [Hexcel Corporation, 2022b] Hexcel Corporation (2022b). *HexWeb® Honeycomb Attributes and Properties*. Hexcel Corporation.
- [Higgins, 2000] Higgins, A. (2000). Adhesive bonding of aircraft structures. *International Journal of Adhesion and Adhesives*, 20(5):367–376.
- [Hoa, 2017] Hoa, S. V. (2017). *Principles of the manufacturing of composite materials*. DEStech Publications, Inc.
- [Hochreiter and Schmidhuber, 1997] Hochreiter, S. and Schmidhuber, J. (1997). Long short-term memory. *Neural Computation*, 9(8):1735–1780.
- [Hsu, 1976] Hsu, P. W. (1976). *Interlaminar Stresses in Composite Laminates—A Perturbation Analysis*. PhD thesis, VTechWorks.
- [Huang et al., 2016] Huang, R., Li, P., and Liu, T. (2016). X-ray microtomography and finite element modelling of compressive failure mechanism in cenosphere epoxy syntactic foams. *Composite Structures*, 140:157–165.
- [Hurtado et al., 2015] Hurtado, F. J., Kaiser, J. M., Gómez, C., Molina, J. A., and Jiménez, C. E. (2015). Compression resin transfer molding simulation applied to the development of a motorcycle fuel tank. *Text Research Journal*, 85(5):609–622.
- [Huynh and Kim, 2018] Huynh, T. C. and Kim, J. T. (2018). Quantification of temperature effect on impedance monitoring via pzt interface for prestressed tendon anchorage. *Smart Materials and Structures*, 27(8):085022.
- [Hyer and White, 2009] Hyer, M. W. and White, S. R. (2009). *Stress analysis of fiber-reinforced composite materials*. DEStech Publications, Inc.
- [Ibrahim, 2014] Ibrahim, M. E. (2014). Nondestructive evaluation of thick-section composites and sandwich structures: A review. *Composites Part A: Applied Science and Manufacturing*, 64:36–48.
- [Illingworth et al., 2010] Illingworth, S. J., Morgans, A. S., and Rowley, C. W. (2010). Feedback control of flow resonances using balanced reduced-order models. *Journal of Sound and Vibration*, 330(8):1567–1581.

- [Ince et al., 2016] Ince, T., Kiranyaz, S., Eren, L., Askar, M., and Gabbouj, M. (2016). Real-time motor fault detection by 1-d convolutional neural networks. *IEEE Transactions on Industrial Electronics*, 63(11):7067–7075.
- [Instructables, 2025] Instructables (2025). Diy flexible printed circuits. Available at: <https://www.instructables.com/DIY-Flexible-Printed-Circuits/>, accessed April 24, 2025.
- [ISO, 2015] ISO (2015). Condition monitoring and diagnostics of machines — ultrasound — general guidelines, procedures and validation (iso 29821:2018). Technical report, International Organization for Standardization.
- [Izco et al., 2015] Izco, L., Istoriz, J., and Motilva, M. (2015). High speed tow placement system for complex layups. Technical Report 2015-01-2608, SAE International.
- [Jacob, 2015] Jacob, A. (2015). High-pressure rtm processes for automotive structural parts. *Reinforced Plastics*, 59(1):24–25.
- [Jaishi and Ren, 2006] Jaishi, B. and Ren, W.-X. (2006). Damage detection by finite element model updating using modal flexibility residual. *Journal of Sound and Vibration*, 290(1-2):369–387.
- [Jang et al., 2019] Jang, K., Kim, N., and An, Y.-K. (2019). Deep learning-based autonomous concrete crack evaluation through hybrid image scanning. *Structural Health Monitoring*, 18(5-6):1722–1737.
- [Jensen et al., 2022] Jensen, J. P., Skelton, K., and Dammand Nielsen, K. (2022). Designing for circularity—addressing product design, production and after-use from a systemic perspective. *Circular Economy and Sustainability*, 2(1):363–383.
- [Jollivet et al., 2013] Jollivet, T., Peyrac, C., and Lefebvre, F. (2013). Damage of composite materials. *Procedia Engineering*, 66:746–758.
- [Jones, 1998] Jones, R. M. (1998). *Mechanics of composite materials*. CRC Press.
- [Jones, 2014] Jones, R. M. (2014). *Mechanics of Composite Materials*. CRC Press, Boca Raton, FL, 2 edition.
- [Kampner and Grenestedt, 2007] Kampner, M. and Grenestedt, J. L. (2007). On using corrugated skins to carry shear in sandwich beams. *Composite Structures*, 85(2):139–148.
- [Karama et al., 2003] Karama, M., Afaq, K. S., and Mistou, S. (2003). Bending, buckling and free vibration of laminated composite with a transverse shear stress continuity model. *Composites Part B: Engineering*, 34(4):365–374.
- [Karbhari, 2013] Karbhari, V. M., editor (2013). *Non-destructive evaluation (NDE) of polymer matrix composites*. Woodhead Publishing.
- [Karim et al., 2018] Karim, F., Majumdar, S., Darabi, H., and Chen, S. (2018). Lstm fully convolutional networks for time series classification. *IEEE Access*, 6:1662–1669.
- [Karniadakis et al., 2021] Karniadakis, G. E., Kevrekidis, I. G., Lu, L., Perdikaris, P., Wang, S., and Yang, L. (2021). Physics-informed machine learning. *Nature Reviews Physics*, 3(6):422–440.
- [Kassapoglou, 2013] Kassapoglou, C. (2013). *Design and analysis of composite structures with applications to aerospace structures*. John Wiley & Sons.

- [Katunin et al., 2015] Katunin, A., Dragan, K., and Dziendzikowski, M. (2015). Damage identification in aircraft composite structures: A case study using various non-destructive testing techniques. *Composite Structures*, 127:1–9.
- [Kaw, 2005] Kaw, A. K. (2005). *Mechanics of Composite Materials*. CRC Press, Boca Raton, FL, 2 edition.
- [Kayran, 2013] Kayran, A. (2013). Finite element modeling of honeycomb core sandwich structures by using equivalent continuum models. In *19th International Conference on Composite Materials*.
- [Khoun et al., 2010] Khoun, L., Centea, T., and Hubert, P. (2010). Characterization methodology of thermoset resins for the processing of composite materials—case study: Cycom 890rtm epoxy resin. *Journal of Composite Materials*, 44(11):1397–1415.
- [Kim et al., 2012] Kim, B. C., Potter, K., and Weaver, P. M. (2012). Continuous tow shearing for manufacturing variable angle tow composites. *Composites Part A: Applied Science and Manufacturing*, 43(8):1347–1356.
- [Kim and Stubbs, 2003] Kim, J.-T. and Stubbs, N. (2003). Crack detection in beam-type structures using frequency data. *Journal of Sound and Vibration*, 259(1):145–160.
- [Kingma and Welling, 2013] Kingma, D. P. and Welling, M. (2013). Auto-encoding variational bayes.
- [Kinloch, 2012] Kinloch, A. J. (2012). *Adhesion and adhesives: science and technology*. Springer Science & Business Media.
- [Kinloch et al., 2016] Kinloch, A. J., Taylor, A. C., Techapaitoon, M., Teo, W. S., and Sprenger, S. (2016). From matrix nano-and micro-phase tougheners to composite macro-properties. *Philosophical Transactions of the Royal Society A*, 374(2071):20150275.
- [Kiranyaz et al., 2019] Kiranyaz, S., Avci, O., Abdeljaber, O., Ince, T., Gabbouj, M., and Inman, D. J. (2019). 1d convolutional neural networks and applications: A survey. *Mechanical Systems and Signal Processing*, 151:107398.
- [Koerber et al., 2010] Koerber, H., Xavier, J., and Camanho, P. P. (2010). High strain rate characterisation of unidirectional carbon-epoxy im7-8552 in transverse compression and in-plane shear using digital image correlation. *Mechanics of Materials*, 42(11):1004–1019.
- [Kollár and Springer, 2003] Kollár, L. P. and Springer, G. S. (2003). *Mechanics of Composite Structures*. Cambridge University Press, Cambridge.
- [Konovalov et al., 2022] Konovalov, D. A., Hillel, A. B., Marron, J. S., and De Souza, P. (2022). Machine learning in composite materials: A review. *Composites Part A: Applied Science and Manufacturing*, 163:107211.
- [Konstantopoulos et al., 2020] Konstantopoulos, S., Hueber, C., Antoniadis, I., Koutsomitopoulou, A., and Berthé, V. (2020). Liquid composite molding reproducibility in real-world production of fiber reinforced polymeric composites: A review of challenges and solutions. *Advanced Manufacturing: Polymer & Composites Science*, 6(3):154–178.
- [Kostopoulos et al., 2012] Kostopoulos, V., Kellas, S., and Sockalingam, S. (2012). Health monitoring of a composite box structure using embedded fbg sensors and ewma control

- charts. *Proceedings of the Institution of Mechanical Engineers, Part G: Journal of Aerospace Engineering*, 226(3):279–287.
- [Kratz and Hubert, 2013] Kratz, J. and Hubert, P. (2013). Processing out-of-autoclave prepreg composites: Manufacturing considerations. *SAE International Journal of Materials and Manufacturing*, 6(2):345–356.
- [Kullaa, 2003] Kullaa, J. (2003). Damage detection of the z24 bridge using control charts. *Mechanical Systems and Signal Processing*, 17(1):163–170.
- [Kumar et al., 2023] Kumar, R., Singh, R. K., Singh, P. K., Kumar, R., and Phanden, R. K. (2023). Numerical investigation of low-velocity impact response on sandwich composite structure using finite element analysis. *Mechanics of Advanced Composite Structures*, 10(3):607–619.
- [La Mantia and Morreale, 2011] La Mantia, F. P. and Morreale, M. (2011). Green composites: A brief review. *Composites Part A: Applied Science and Manufacturing*, 42(6):579–588.
- [Li and Wang, 2019] Li, S. and Wang, Y. (2019). A two-stage transfer learning approach for structural health monitoring with insufficient training data. In *AIAA Scitech 2019 Forum*, page 1913.
- [Li et al., 2020] Li, X., Gu, Y., Dvornek, N., Staib, L. H., Ventola, P., and Duncan, J. S. (2020). Multi-site fmri analysis using privacy-preserving federated learning and domain adaptation: Abide results. *Medical Image Analysis*, 65:101765.
- [Librescu and Hause, 2000] Librescu, L. and Hause, T. (2000). Recent developments in the modeling and behavior of advanced sandwich constructions: A survey. *Composite Structures*, 48(1-3):1–17.
- [Lichtinger et al., 2015] Lichtinger, R., Hörmann, P., Stelzl, D., and Hinterhölzl, R. (2015). The effects of heat input on adjacent paths during automated fibre placement. *Composites Part A: Applied Science and Manufacturing*, 68:387–397.
- [Lieven and Ewins, 1988] Lieven, N. A. and Ewins, D. J. (1988). Spatial correlation of mode shapes, the coordinate modal assurance criterion (comac). In *Proceedings of the 6th International Modal Analysis Conference*, volume 1, pages 690–695.
- [Lin and Chang, 2002] Lin, M. and Chang, F. K. (2002). The manufacture of composite structures with a built-in network of piezoceramics. *Composites Science and Technology*, 62(7-8):919–939.
- [Lin et al., 2017] Lin, Y.-Z., Nie, Z.-H., and Ma, H.-W. (2017). Structural damage detection with automatic feature-extraction through deep learning. *Computer-Aided Civil and Infrastructure Engineering*, 32(12):1025–1046.
- [Lindgren et al., 2007] Lindgren, E. A., Knopp, J. S., Aldrin, J. C., Steffes, G. J., and Buynak, C. F. (2007). Aging aircraft nde: capabilities, challenges, and opportunities. In *AIP Conference Proceedings*, volume 894, pages 1731–1738. American Institute of Physics.
- [Liu et al., 2014] Liu, C., Gong, P., Li, X., and Chen, X. (2014). Structural damage identification using time series analysis. *Applied Mechanics and Materials*, 578:1181–1184.

- [Liu et al., 2020] Liu, Y., Yong, J. W., Liu, X. F., and Fan, H. (2020). Optimization of sandwich structures with tapered lattice core. *Materials & Design*, 188:108437.
- [Ljung, 2010] Ljung, L. (2010). Perspectives on system identification. *Annual Reviews in Control*, 34(1):1–12.
- [Lopes et al., 2007] Lopes, C. S., Camanho, P. P., Gürdal, Z., and Tatting, B. F. (2007). Progressive failure analysis of tow-placed, variable-stiffness composite panels. *International Journal of Solids and Structures*, 44(25–26):8493–8516.
- [Lozano et al., 2016] Lozano, G. G., Tiwari, A., Turner, C., and Astwood, S. (2016). A review on design for manufacture of variable stiffness composite laminates. *Proceedings of the Institution of Mechanical Engineers, Part B: Journal of Engineering Manufacture*, 230(6):981–992.
- [Lukaszewicz et al., 2012] Lukaszewicz, D. H. J. A., Ward, C., and Potter, K. D. (2012). The engineering aspects of automated prepreg layup: History, present and future. *Composites Part B: Engineering*, 43(3):997–1009.
- [Luna Innovations, 2019] Luna Innovations (2019). *ODiSI 6000 Series User Guide*. Luna Innovations Inc.
- [Luo et al., 2021] Luo, S., Liu, T., and Wang, B. (2021). State-of-the-art of strain sensing technology using carbon nanotubes for structural health monitoring. *Frontiers of Structural and Civil Engineering*, 15(1):81–96.
- [Lynch and Loh, 2006] Lynch, J. P. and Loh, K. J. (2006). A summary review of wireless sensors and sensor networks for structural health monitoring. *Shock and Vibration Digest*, 38(2):91–130.
- [Ma et al., 2010] Ma, P. C., Siddiqui, N. A., Marom, G., and Kim, J. K. (2010). Dispersion and functionalization of carbon nanotubes for polymer-based nanocomposites: A review. *Composites Part A: Applied Science and Manufacturing*, 41(10):1345–1367.
- [Magnin and Rion, 2018] Magnin, S. and Rion, J. (2018). Out-of-autoclave manufacturing of complex shape composite parts. Technical Report 2018-01-1912, SAE International.
- [Maier et al., 2014] Maier, A., Schmidt, R., Oswald-Tranta, B., and Schledjewski, R. (2014). Non-destructive thermography analysis of impact damage on large-scale cfrp automotive parts. *Materials*, 7(1):413–429.
- [Majumder et al., 2008] Majumder, M., Gangopadhyay, T. K., Chakraborty, A. K., Dasgupta, K., and Bhattacharya, D. K. (2008). Fibre bragg gratings in structural health monitoring—present status and applications. *Sensors and Actuators A: Physical*, 147(1):150–164.
- [Malekloo et al., 2021] Malekloo, A., Ozer, E., AlHamaydeh, M., and Girolami, M. (2021). Machine learning and structural health monitoring overview with emerging technology and high-dimensional data source highlights. *Structural Health Monitoring*, 20(4):1672–1706.
- [Mallick, 2007] Mallick, P. K. (2007). *Fiber-reinforced composites: materials, manufacturing, and design*. CRC Press.
- [Malnati, 2013] Malnati, P. (2013). Preforming goes industrial: Part 1. *Composites World*, 1(1):50–57.

- [Malnati, 2020] Malnati, P. (2020). Hybrid processing combines 3d printing with composites manufacturing. *Composites World*, 6(12):42–47.
- [Marin et al., 2000] Marin, E., Salviato, M., and Salvetti, F. (2000). Use of fiber bragg grating sensors in the manufacturing and characterization of composite materials. In *Optical Methods for Non-Destructive Testing*, volume 4242, pages 60–63. SPIE.
- [Marsh, 2010] Marsh, G. (2010). Airbus a350 xwb update. *Reinforced Plastics*, 54(6):20–24.
- [Marsh, 2011] Marsh, G. (2011). Automating aerospace composites production with fibre placement. *Reinforced Plastics*, 55(3):32–37.
- [Marsh, 2014] Marsh, G. (2014). Aero engines lose weight thanks to composites. *Reinforced Plastics*, 58(6):38–42.
- [Marwala, 2010] Marwala, T. (2010). *Finite Element Model Updating Using Computational Intelligence Techniques: Applications to Structural Dynamics*. Springer Science & Business Media.
- [McConnell, 2011] McConnell, V. P. (2011). Launching the carbon fibre recycling industry. *Reinforced Plastics*, 55(5):33–37.
- [McMahan et al., 2017] McMahan, B., Moore, E., Ramage, D., Hampson, S., and Aguera y Arcas, B. (2017). Communication-efficient learning of deep networks from decentralized data. In *Artificial Intelligence and Statistics*, pages 1273–1282. PMLR.
- [Meredith et al., 2013] Meredith, J., Coles, S. R., Powe, R., Collings, E., Cozien-Cazuc, S., Weager, B., and Kirwan, K. (2013). On the static and dynamic properties of flax and cordenka epoxy composites. *Composites Science and Technology*, 80:31–38.
- [Messina et al., 1998] Messina, A., Williams, E. J., and Contursi, T. (1998). Structural damage detection by a sensitivity and statistical-based method. *Journal of Sound and Vibration*, 216(5):791–808.
- [Messinger, 2004] Messinger, R. H. (2004). Spacecraft structures. In *Spacecraft systems engineering*, pages 251–300. John Wiley & Sons.
- [Middendorf and Metzner, 2011] Middendorf, P. and Metzner, C. (2011). Aerospace applications of non-crimp fabric composites. In *Non-crimp fabric composites*, pages 441–448. Woodhead Publishing.
- [MISTRAS Group, 2018] MISTRAS Group (2018). *PCI-2 Based AE System User's Manual*. MISTRAS Group Inc.
- [Mitra and Gopalakrishnan, 2016] Mitra, M. and Gopalakrishnan, S. (2016). Guided wave based structural health monitoring: A review. *Smart Materials and Structures*, 25(5):053001.
- [Mobark et al., 2024] Mobark, H., Fattah Agha, M., and Ameen, S. (2024). Sandwich structure bending analysis using finite element analysis. *Journal of Mechanical Engineering*, 1.
- [Morassi and Rovere, 1997] Morassi, A. and Rovere, N. (1997). Localizing a notch in a steel frame from frequency measurements. *Journal of Engineering Mechanics*, 123(5):422–432.

- [Morimoto et al., 2010] Morimoto, T., Kobayashi, S., Nagao, Y., and Iwahori, Y. (2010). A new cost/weight trade-off method for airframe material decisions based on structural optimization. *Advanced Composite Materials*, 19(3):267–279.
- [Mottershead and Friswell, 1993] Mottershead, J. E. and Friswell, M. I. (1993). Model updating in structural dynamics: A survey. *Journal of Sound and Vibration*, 167(2):347–375.
- [Mottershead et al., 2011] Mottershead, J. E., Link, M., and Friswell, M. I. (2011). The sensitivity method in finite element model updating: A tutorial. *Mechanical Systems and Signal Processing*, 25(7):2275–2296.
- [Mrazova, 2013] Mrazova, M. (2013). Advanced composite materials of the future in aerospace industry. *Incas Bulletin*, 5(3):139.
- [Mukhopadhyay et al., 2019] Mukhopadhyay, T., Adhikari, S., and Batou, A. (2019). Frequency domain homogenization for the viscoelastic properties of spatially correlated quasi-periodic lattices. *International Journal of Mechanical Sciences*, 150:784–806.
- [Nair et al., 2006a] Nair, K. K., Kiremidjian, A. S., and Law, K. H. (2006a). Time series-based damage detection and localization algorithm with application to the asce benchmark structure. *Journal of Sound and Vibration*, 291(1-2):349–368.
- [Nair et al., 2006b] Nair, K. K., Kiremidjian, A. S., and Law, K. H. (2006b). Time series-based damage detection and localization algorithm with application to the asce benchmark structure. *Journal of Sound and Vibration*, 291(1-2):349–368.
- [Naleway et al., 2015] Naleway, S. E., Porter, M. M., McKittrick, J., and Meyers, M. A. (2015). Structural design elements in biological materials: application to bioinspiration. *Advanced Materials*, 27(37):5455–5476.
- [NASA, 2018] NASA (2018). Nasa technology roadmaps: Ta 12 materials, structures, mechanical systems, and manufacturing. Technical report, National Aeronautics and Space Administration.
- [Nguyen et al., 1997] Nguyen, L. B., Juska, T., and Mayes, S. J. (1997). Evaluation of low cost manufacturing technologies for large scale composite ship structures. In *Collection of Technical Papers - AIAA/ASME/ASCE/AHS/ASC Structures, Structural Dynamics and Materials Conference*, pages 954–971. AIAA.
- [Oh et al., 2020] Oh, B. K., Hwang, J. W., Kim, Y., Cho, T., and Park, H. S. (2020). Vision-based system identification technique for building structures using a motion capture system. *Journal of Sound and Vibration*, 486:115610.
- [Oh et al., 2009] Oh, C. K., Sohn, H., and Bae, I. H. (2009). Statistical novelty detection within the yeongjong suspension bridge under environmental and operational variations. *Smart Materials and Structures*, 18(12):125022.
- [Pandey et al., 1991] Pandey, A. K., Biswas, M., and Samman, M. M. (1991). Damage detection from changes in curvature mode shapes. *Journal of Sound and Vibration*, 145(2):321–332.
- [Park et al., 2008] Park, G., Rosing, T., Todd, M. D., Farrar, C. R., and Hodgkiss, W. (2008). Energy harvesting for structural health monitoring sensor networks. *Journal of Infrastructure Systems*, 14(1):64–79.

- [Park et al., 2019] Park, S., Kim, B., Sohn, H., Jang, H. J., and Park, H. (2019). Sequential damage diagnosis using frequency response function and wave propagation analysis. *Journal of Sound and Vibration*, 431:122–136.
- [Pastor et al., 2012] Pastor, M., Binda, M., and Harčarik, T. (2012). Modal assurance criterion. *Procedia Engineering*, 48:543–548.
- [Pathirage et al., 2018] Pathirage, C. S. N., Li, J., Li, L., Hao, H., Liu, W., and Ni, P. (2018). Structural damage identification based on autoencoder neural networks and deep learning. *Engineering Structures*, 172:13–28.
- [Pathirage et al., 2019] Pathirage, C. S. N., Li, J., Li, L., Hao, H., Liu, W., and Wang, R. (2019). Development and application of a deep learning-based sparse damage detection model for a long-span bridge structure. *Structural Health Monitoring*, 18(5-6):1742–1762.
- [Perera and Torres, 2006] Perera, R. and Torres, R. (2006). Structural damage detection via modal data with genetic algorithms. *Journal of Structural Engineering*, 132(9):1491–1501.
- [Petras and Sutcliffe, 1999] Petras, A. and Sutcliffe, M. P. F. (1999). Failure mode maps for honeycomb sandwich panels. *Composite Structures*, 44(4):237–252.
- [Petras and Sutcliffe, 2000] Petras, A. and Sutcliffe, M. P. F. (2000). Indentation failure analysis of sandwich beams. *Composite Structures*, 50(3):311–318.
- [Plantema, 1966] Plantema, F. J. (1966). *Sandwich Construction: The Bending and Buckling of Sandwich Beams, Plates, and Shells*. John Wiley & Sons, New York.
- [Qing et al., 2007] Qing, X. P., Beard, S. J., Kumar, A., Ooi, T. K., and Chang, F. K. (2007). Built-in sensor network for structural health monitoring of composite structure. *Journal of Intelligent Material Systems and Structures*, 18(1):39–49.
- [Qing et al., 2006] Qing, X. P., Chan, H. L., Beard, S. J., Ooi, T. K., and Marotta, S. A. (2006). Effect of adhesive on the performance of piezoelectric elements used to monitor structural health. *International Journal of Adhesion and Adhesives*, 26(8):622–628.
- [Rademacker, 2012] Rademacker, T. (2012). High-pressure rtm process variants for manufacturing of carbon fiber reinforced composites. In *Proceedings of the SAMPE Conference*.
- [Rafiei and Adeli, 2018] Rafiei, M. H. and Adeli, H. (2018). A novel unsupervised deep learning model for global and local health condition assessment of structures. *Engineering Structures*, 156:598–607.
- [Raghavan and Cesnik, 2007] Raghavan, A. and Cesnik, C. E. (2007). Review of guided-wave structural health monitoring. *Shock and Vibration Digest*, 39(2):91–116.
- [Rainieri et al., 2011] Rainieri, C., Fabbrocino, G., and Cosenza, E. (2011). Integrated seismic early warning and structural health monitoring of critical civil infrastructures in seismically prone areas. *Structural Health Monitoring*, 10(3):291–308.
- [Raissi et al., 2019a] Raissi, M., Perdikaris, P., and Karniadakis, G. E. (2019a). Physics-informed neural networks: A deep learning framework for solving forward and inverse problems involving nonlinear partial differential equations. *Journal of Computational Physics*, 378:686–707.

- [Raissi et al., 2019b] Raissi, M., Wang, Z., Triantafyllou, M. S., and Karniadakis, G. E. (2019b). Deep learning of vortex-induced vibrations. *Journal of Fluid Mechanics*, 861:119–137.
- [Rajaram et al., 2006] Rajaram, S., Wang, T., and Nutt, S. (2006). Sound transmission loss of honeycomb sandwich panels. *Noise Control Engineering Journal*, 54(2):106–115.
- [Raju et al., 2008] Raju, K. S., Smith, B. L., Tomblin, J. S., Liew, K. H., and Guarddon, J. C. (2008). Impact damage resistance and tolerance of honeycomb core sandwich panels. *Journal of Composite Materials*, 42:385–412.
- [Raju and Tomblin, 2001] Raju, K. S. and Tomblin, J. S. (2001). Core crush problem in the manufacturing of composite sandwich structures for aircraft components. In *SAMPE Technical Conference Proceedings*. SAMPE.
- [Rao, 2019] Rao, S. S. (2019). *Vibration of Continuous Systems*. John Wiley & Sons.
- [Redding and Juang, 1984] Redding, D. C. and Juang, J. N. (1984). A technique for the identification of linear systems from noisy frequency-response data. In *IEEE Conference on Decision and Control*, pages 1643–1645. IEEE.
- [Reddy, 2003] Reddy, J. N. (2003). *Mechanics of Laminated Composite Plates and Shells: Theory and Analysis*. CRC Press, Boca Raton, FL, 2 edition.
- [Reddy, 2004] Reddy, J. N. (2004). *Mechanics of Laminated Composite Plates and Shells: Theory and Analysis*. CRC Press, Boca Raton, FL, 2 edition.
- [Reddy, 2007] Reddy, J. N. (2007). *Theory and Analysis of Elastic Plates and Shells*. CRC Press / Taylor & Francis, 2nd edition.
- [Reddy, 2019] Reddy, J. N. (2019). *Theory and Analysis of Elastic Plates and Shells*. CRC Press, Boca Raton, FL, 2 edition.
- [Ribeiro et al., 2016a] Ribeiro, M. T., Singh, S., and Guestrin, C. (2016a). Model-agnostic interpretability of machine learning.
- [Ribeiro et al., 2016b] Ribeiro, M. T., Singh, S., and Guestrin, C. (2016b). "why should i trust you?" explaining the predictions of any classifier. In *Proceedings of the 22nd ACM SIGKDD International Conference on Knowledge Discovery and Data Mining*, pages 1135–1144.
- [Richards et al., 2012] Richards, L., Parker, A. R., Ko, W. L., and Piazza, A. (2012). Real-time in-flight strain and deflection monitoring with fiber optic sensors. In *Proceedings of the 53rd AIAA Structures, Structural Dynamics, and Materials Conference*. AIAA.
- [Roach, 2009] Roach, D. (2009). Real time crack detection using mountable comparative vacuum monitoring sensors. *Smart Structures and Systems*, 5(4):317–328.
- [Rogers et al., 2019] Rogers, T. J., Worden, K., Fuentes, R., Dervilis, N., Tygesen, U. T., and Cross, E. J. (2019). A bayesian non-parametric clustering approach for semi-supervised structural health monitoring. *Mechanical Systems and Signal Processing*, 119:100–119.
- [Rosenberg et al., 2015] Rosenberg, P., Chaudhari, R., Karcher, M., Henning, F., and Elsner, P. (2015). Investigating cavity pressure behavior in high-pressure rtm process variants. *AIP Conference Proceedings*, 1664(1):030007.

- [Rosenberg et al., 2018] Rosenberg, P., Thoma, B., and Henning, F. (2018). Investigation and modification of cavity pressure behavior in high-pressure rtm processes. In *IOP Conference Series: Materials Science and Engineering*, volume 406, page 012033. IOP Publishing.
- [Rudd et al., 1997] Rudd, C. D., Long, A. C., Kendall, K. N., and Mangin, C. G. E. (1997). *Liquid moulding technologies: Resin transfer moulding, structural reaction injection moulding and related processing techniques*. Woodhead Publishing.
- [Rytter, 1993] Rytter, A. (1993). *Vibrational Based Inspection of Civil Engineering Structures*. PhD thesis, Aalborg University.
- [Sacco and Reddy, 2021] Sacco, E. and Reddy, J. N. (2021). Machine learning algorithms for multiscale modeling of composite materials and structures. *Composite Structures*, 271:114169.
- [SAE International, 2018] SAE International (2018). Guidelines for implementation of structural health monitoring on fixed wing aircraft (arp6461). Technical report, SAE International.
- [Sakurada and Yairi, 2014] Sakurada, M. and Yairi, T. (2014). Anomaly detection using autoencoders with nonlinear dimensionality reduction. In *Proceedings of the MLSDA 2014 2nd Workshop on Machine Learning for Sensory Data Analysis*, pages 4–11.
- [Salawu, 1997] Salawu, O. S. (1997). Detection of structural damage through changes in frequency: A review. *Engineering Structures*, 19(9):718–723.
- [Salehi et al., 2013] Salehi, M., Ziae-Rad, S., Ghayour, M., and Vaziri-Zanjani, M. A. (2013). A frequency response based structural damage localization method using independent component analysis. *Journal of Mechanical Science and Technology*, 27:609–619.
- [Santos et al., 2016] Santos, A., Figueiredo, E., Silva, M. F., Sales, C. S., and Costa, J. C. (2016). Machine learning algorithms for damage detection: Kernel-based approaches. *Journal of Sound and Vibration*, 363:584–599.
- [Sarrafi et al., 2018] Sarrafi, A., Mao, Z., Niezrecki, C., and Poozesh, P. (2018). Vibration-based damage detection in wind turbine blades using phase-based motion magnification and convolutional neural networks. *Structural Health Monitoring*, 17(4):881–898 | 10.
- [Savage, 2007] Savage, G. (2007). Formula 1 safety – a case study. *Engineering Failure Analysis*, 14(3):552–566.
- [Savage, 2008] Savage, G. (2008). Composite materials technology in formula 1 motor racing. Technical Report 15, Honda Racing F1 Team.
- [Savage, 2009] Savage, G. (2009). Formula 1 composites engineering. *Engineering Failure Analysis*, 17(1):92–115.
- [Savage, 2010] Savage, G. (2010). Development of penetration resistance in formula 1 composite structures. *Engineering Failure Analysis*, 17(1):116–127.
- [Savage, 2011] Savage, G. (2011). Sub-critical crack growth in highly stressed formula 1 race car composite suspension components. *Engineering Failure Analysis*, 18(1):298–308.

- [Savage, 2021] Savage, G. (2021). Development of composite monocoque structures for formula 1. *Journal of Composite Materials*, 55(11):1487–1504.
- [Seemann, 1990] Seemann, W. H. (1990). Plastic transfer molding techniques for the production of fiber reinforced plastic structures. U.S. Patent and Trademark Office. U.S. Patent No. 4,902,215.
- [Shull, 2016] Shull, P. J. (2016). *Nondestructive evaluation theory, techniques, and applications*. CRC Press.
- [Sloan, 2012] Sloan, J. (2012). Cfrp: Costly today, competitive tomorrow. *High-Performance Composites*, 20(6):54–59.
- [Sloan, 2014] Sloan, J. (2014). Bmw leipzig: The epicenter of i3 production. *Composites World*, 2(3):15–21.
- [Sloan, 2019] Sloan, J. (2019). F1 racing: Technology accelerator. *Composites World*, 5(6):34–39.
- [Snyder et al., 2021] Snyder, R. A., Thomson, D. M., Ha, J. U., Olsson, R., and Schäuble, R. (2021). Composite materials in helicopter blade technology: Past, present, and future. *Composites Part B: Engineering*, 226:109342.
- [Sohn et al., 2005] Sohn, H., Allen, D. W., Worden, K., and Farrar, C. R. (2005). Structural damage classification using extreme value statistics. *Journal of Dynamic Systems, Measurement, and Control*, 127(1):125–132.
- [Sohn et al., 2000] Sohn, H., Czarnecki, J. A., and Farrar, C. R. (2000). Structural health monitoring using statistical process control. *Journal of Structural Engineering*, 126(11):1356–1363.
- [Sohn and Farrar, 2001a] Sohn, H. and Farrar, C. R. (2001a). Damage diagnosis using time series analysis of vibration signals. *Smart Materials and Structures*, 10(3):446–451.
- [Sohn and Farrar, 2001b] Sohn, H. and Farrar, C. R. (2001b). Damage diagnosis using time series analysis of vibration signals. *Smart Materials and Structures*, 10(3):446–451.
- [Sohn et al., 2003] Sohn, H., Farrar, C. R., Hemez, F. M., Shunk, D. D., Stinemates, D. W., Nadler, B. R., and Czarnecki, J. J. (2003). A review of structural health monitoring literature: 1996–2001. Technical Report LA-13976-MS, Los Alamos National Laboratory.
- [Sohn et al., 2002] Sohn, H., Worden, K., and Farrar, C. R. (2002). Statistical damage classification under changing environmental and operational conditions. *Journal of Intelligent Material Systems and Structures*, 13(9):561–574.
- [Sokolinsky and Frostig, 2000] Sokolinsky, V. S. and Frostig, Y. (2000). Branched solutions in non-linear free vibrations of sandwich beams. *Journal of Sound and Vibration*, 236(5):809–829.
- [Soutis, 2005a] Soutis, C. (2005a). Carbon fiber reinforced plastics in aircraft construction. *Materials Science and Engineering: A*, 412(1-2):171–176.
- [Soutis, 2005b] Soutis, C. (2005b). Fibre reinforced composites in aircraft construction. *Progress in Aerospace Sciences*, 41(2):143–151.

- [Soutis, 2020] Soutis, C. (2020). Aerospace engineering requirements in building with composites. In *Polymer Composites in the Aerospace Industry*, pages 3–22. Woodhead Publishing.
- [SpaceX, 2021] SpaceX (2021). *Falcon User's Guide*. Space Exploration Technologies Corp.
- [Starke, 2016] Starke, J. (2016). Carbon composites in automotive structural applications. Technical report, BMW Group.
- [Starr et al., 2010] Starr, A., Al-Najjar, B., Holmberg, K., Jantunen, E., Bellew, J., and Albarbar, A. (2010). Maintenance today and future trends. In *E-maintenance*, pages 5–37. Springer.
- [Staszewski et al., 2009] Staszewski, W. J., Mahzan, S., and Traynor, R. (2009). Health monitoring of aerospace composite structures—active and passive approach. *Composites Science and Technology*, 69(11-12):1678–1685.
- [Stickler, 2002] Stickler, P. B. (2002). Composite materials for commercial transport - issues and future research directions. In *ASC 17th Annual Technical Conference*.
- [Sun and Büyüköztürk, 2015] Sun, H. and Büyüköztürk, O. (2015). Optimal sensor placement in structural health monitoring using discrete optimization. *Smart Materials and Structures*, 24(12):125034.
- [Sun and Guo, 2020] Sun, Y. and Guo, L. (2020). Carbon fiber reinforced polymer honeycomb structures: A state-of-the-art review. *Composite Structures*, 252:112681.
- [Sutter et al., 2010] Sutter, J. K., Kenner, W. S., Pelham, L., Miller, S. G., Polis, D. L., Nailadi, C., and Hou, T. H. (2010). Comparison of autoclave and out-of-autoclave composites. In *SAMPE 2010 Conference and Exhibition*. SAMPE.
- [Suzuki and Takahashi, 2014] Suzuki, T. and Takahashi, J. (2014). Prediction of energy intensity of carbon fiber reinforced plastics for mass-produced passenger vehicles. *Journal of Cleaner Production*, 75:1–10.
- [Taha et al., 2006] Taha, M. R., Noureldin, A., Lucero, J. L., and Baca, T. J. (2006). Wavelet transform for structural health monitoring: A compendium of uses and features. *Structural Health Monitoring*, 5(3):267–295.
- [Takeda et al., 2012] Takeda, S., Aoki, Y., and Nagao, Y. (2012). Damage monitoring of cfrp stiffened panels under compressive load using fbg sensors. *Composite Structures*, 94(3):813–819.
- [Tang and Sridhar, 2006] Tang, J. and Sridhar, S. (2006). A framework for analyzing the entire supply chain performance using delivery schedule agreements: a case study. In *Strategic Management of the Manufacturing Value Chain*, pages 127–134. Springer.
- [Taylor et al., 2014] Taylor, S. G., Farinholt, K. M., Flynn, E. B., Figueiredo, E., Mascarinas, D. L., Moro, E. A., and Farrar, C. R. (2014). A mobile-agent-based wireless sensing network for structural monitoring applications. *Measurement Science and Technology*, 25(10):105101.
- [Teughels and De Roeck, 2005] Teughels, A. and De Roeck, G. (2005). Damage detection and parameter identification by finite element model updating. *Archives of Computational Methods in Engineering*, 12(2):123–164.

- [Thakare and Shrivastava, 2020] Thakare, P. S. and Shrivastava, R. (2020). Sandwich structures for aerospace applications: A review. *Materials Today: Proceedings*, 27:656–661.
- [Thostenson and Chou, 2006] Thostenson, E. T. and Chou, T. W. (2006). Carbon nanotube networks: sensing of distributed strain and damage for life prediction and self healing. *Advanced Materials*, 18(21):2837–2841.
- [Titurus and Friswell, 2008] Titurus, B. and Friswell, M. I. (2008). Regularization in model updating. *International Journal for Numerical Methods in Engineering*, 75(4):440–478.
- [Toh and Park, 2020] Toh, G. and Park, J. (2020). Review of vibration-based structural health monitoring using deep learning. *Applied Sciences*, 10(5):1680.
- [Tomblin et al., 1999] Tomblin, J., Lacy, T., Smith, B., Hooper, S., Vizzini, A., and Lee, S. (1999). Review of damage tolerance for composite sandwich airframe structures. Technical report, Federal Aviation Administration, William J. Hughes Technical Center.
- [Tomblin and Seneviratne, 2011] Tomblin, J. and Seneviratne, W. (2011). Determining the fatigue life of composite aircraft structures using life and load-enhancement factors. Technical Report DOT/FAA/AR-10/6, FAA.
- [Toray Advanced Composites, 2022] Toray Advanced Composites (2022). *Aerospace and Formula 1 Prepreg Systems Comparison Guide*. Toray Advanced Composites.
- [Tran-Ngoc et al., 2018] Tran-Ngoc, H., Khatir, S., De Roeck, G., Bui-Tien, T., Nguyen-Ngoc, L., and Abdel Wahab, M. (2018). Model updating for nam o bridge using particle swarm optimization algorithm and genetic algorithm. *Sensors*, 18(12):4131.
- [Travitzky et al., 2014] Travitzky, N., Bonet, A., Dermeik, B., Fey, T., Filbert-Demut, I., Schlier, L., and Greil, P. (2014). Additive manufacturing of ceramic-based materials. *Advanced Engineering Materials*, 16(6):729–754.
- [Triantafillou and Gibson, 1987] Triantafillou, T. C. and Gibson, L. J. (1987). Failure mode maps for foam core sandwich beams. *Materials Science and Engineering*, 95:37–53.
- [Tsai and Hahn, 1980] Tsai, S. W. and Hahn, H. T. (1980). *Introduction to Composite Materials*. Technomic Publishing, Lancaster, PA.
- [Tsai and Wu, 1971] Tsai, S. W. and Wu, E. M. (1971). A general theory of strength for anisotropic materials. *Journal of Composite Materials*, 5(1):58–80.
- [Tuegel et al., 2011] Tuegel, E. J., Ingraffea, A. R., Eason, T. G., and Spottswood, S. M. (2011). Reengineering aircraft structural life prediction using a digital twin. *International Journal of Aerospace Engineering*, 2011.
- [Ushijima et al., 2013] Ushijima, K., Cantwell, W. J., and Chen, D. H. (2013). Prediction of the mechanical properties of micro-lattice structures subjected to multi-axial loading. *International Journal of Mechanical Sciences*, 68:47–55.
- [Van Den Abeele et al., 2019] Van Den Abeele, F., Dhaene, J., Degrande, S., and Kata lagarianakis, G. (2019). Thermoforming simulation for continuous fibre reinforced thermoplastics. In *AIP Conference Proceedings*, volume 2113, page 050015. AIP Publishing.
- [Vasiliev and Morozov, 2013] Vasiliev, V. V. and Morozov, E. V. (2013). *Advanced mechanics of composite materials and structural elements*. Elsevier.

- [Verrey et al., 2006] Verrey, J., Wakeman, M. D., Michaud, V., and Månsen, J. A. E. (2006). Manufacturing cost comparison of thermoplastic and thermoset rtm for an automotive floor pan. *Composites Part A: Applied Science and Manufacturing*, 37(1):9–22.
- [Vincent et al., 2008] Vincent, P., Larochelle, H., Bengio, Y., and Manzagol, P.-A. (2008). Extracting and composing robust features with denoising autoencoders. In *Proceedings of the 25th International Conference on Machine Learning*, pages 1096–1103.
- [Vinson, 2018a] Vinson, J. R. (2018a). *The behavior of sandwich structures of isotropic and composite materials*. Routledge.
- [Vinson, 2018b] Vinson, J. R. (2018b). *The Behavior of Sandwich Structures of Isotropic and Composite Materials*. Routledge, New York.
- [Vlot and Gunnink, 2001] Vlot, A. and Gunnink, J. W. (2001). *Fibre metal laminates: an introduction*. Springer Science & Business Media.
- [Wadley et al., 2003] Wadley, H. N., Fleck, N. A., and Evans, A. G. (2003). Fabrication and structural performance of periodic cellular metal sandwich structures. *Composites Science and Technology*, 63(16):2331–2343.
- [Wahab and De Roeck, 1999] Wahab, M. M. A. and De Roeck, G. (1999). Damage detection in bridges using modal curvatures: Application to a real damage scenario. *Journal of Sound and Vibration*, 226(2):217–235.
- [Wang et al., 2000] Wang, C. M., Reddy, J. N., and Lee, K. H. (2000). *Shear Deformable Beams and Plates: Relationships with Classical Solutions*. Elsevier, Amsterdam.
- [Wang et al., 2018] Wang, J., Shi, C., Yang, N., Sun, H., Liu, Y., and Song, B. (2018). Strength, stiffness, and panel peeling strength of carbon fiber-reinforced composite sandwich structures with aluminum honeycomb cores for vehicle body. *Composite Structures*, 184:1189–1196.
- [Wang et al., 2010] Wang, L., Chan, T., Thambiratnam, D., and Tan, A. (2010). Structural health monitoring: Vibration-based damage detection and condition assessment of bridges. In *Rethinking Sustainable Development: Urban Management, Engineering, and Design*, pages 230–243. IGI Global Scientific Publishing.
- [Warren, 2001] Warren, C. D. (2001). Carbon fiber in future vehicles. *SAMPE Journal*, 37(2):7–15.
- [Weber et al., 2007] Weber, B., Paultre, P., and Proulx, J. (2007). Structural damage detection using nonlinear parameter identification with tikhonov regularization. *Structural Control and Health Monitoring*, 14(3):406–427.
- [West, 1986] West, W. M. (1986). Illustration of the use of modal assurance criterion to detect structural changes in an orbiter test specimen. In *Proceedings of the 4th International Modal Analysis Conference*, volume 1, pages 1–6.
- [Whitney and Pagano, 1970] Whitney, J. M. and Pagano, N. J. (1970). Shear deformation in heterogeneous anisotropic plates. *Journal of Applied Mechanics*, 37(4):1031–1036.
- [Widodo and Yang, 2007] Widodo, A. and Yang, B.-S. (2007). Support vector machine in machine condition monitoring and fault diagnosis. *Mechanical Systems and Signal Processing*, 21(6):2560–2574.

- [Witik et al., 2013] Witik, R. A., Teuscher, R., Michaud, V., Ludwig, C., and Månsen, J. A. E. (2013). Carbon fibre reinforced composite waste: An environmental assessment of recycling, energy recovery and landfilling. *Composites Part A: Applied Science and Manufacturing*, 49:89–99.
- [Wong and Lim, 2017] Wong, Z. Y. and Lim, M. K. (2017). An integrated neural network approach for structural damage detection. *Structural Multidisciplinary Optimization*, 55(6):2279–2293.
- [Worden et al., 2002a] Worden, K., Allen, D. W., Sohn, H., and Farrar, C. R. (2002a). Damage detection in mechanical structures using extreme value statistics. In *SPIE's 9th Annual International Symposium on Smart Structures and Materials*, volume 4693, pages 289–299.
- [Worden et al., 2020a] Worden, K., Bull, L. A., Gardner, P., Gosliga, J., Rogers, T. J., Cross, E. J., Papatheou, E., and Wagg, D. J. (2020a). A perspective on verification and validation in structural health monitoring.
- [Worden et al., 2015] Worden, K., Cross, E. J., Dervilis, N., Papatheou, E., and Antoniadou, I. (2015). Structural health monitoring: From structures to systems-of-systems. *IFAC-PapersOnLine*, 48(21):1–17.
- [Worden et al., 2020b] Worden, K., Cross, E. J., Gardner, P., Bartherope, R. J., and Wagg, D. J. (2020b). On digital twins, mirrors and virtualizations: Frameworks for model verification and validation. *Mathematical and Computer Modelling of Dynamical Systems*, 26(5):430–452.
- [Worden and Dulieu-Barton, 2004] Worden, K. and Dulieu-Barton, J. M. (2004). An overview of intelligent fault detection in systems and structures. *Structural Health Monitoring*, 3(1):85–98.
- [Worden et al., 2007] Worden, K., Farrar, C. R., Manson, G., and Park, G. (2007). The fundamental axioms of structural health monitoring. *Proceedings of the Royal Society A: Mathematical, Physical and Engineering Sciences*, 463(2082):1639–1664.
- [Worden and Lane, 2001] Worden, K. and Lane, A. J. (2001). Damage identification using support vector machines. *Smart Materials and Structures*, 10(3):540–547.
- [Worden et al., 2003] Worden, K., Manson, G., and Allman, D. J. (2003). Experimental validation of a structural health monitoring methodology: Part i. novelty detection on a laboratory structure. *Journal of Sound and Vibration*, 259(2):323–343.
- [Worden et al., 2000] Worden, K., Manson, G., and Fieller, N. R. J. (2000). Damage detection using outlier analysis. *Journal of Sound and Vibration*, 229(3):647–667.
- [Worden et al., 2020c] Worden, K., Rogers, T. J., Dervilis, N., Cross, E. J., Haywood-Alexander, M., and Kenyon, A. (2020c). On the confidence bounds of gaussian process narx models and their higher-order frequency response functions. *Mechanical Systems and Signal Processing*, 140:106675.
- [Worden et al., 2002b] Worden, K., Sohn, H., and Farrar, C. R. (2002b). Novelty detection in a changing environment: Regression and interpolation approaches. *Journal of Sound and Vibration*, 258(4):741–761.
- [Wulfsberg et al., 2014] Wulfsberg, J., Herrmann, A., Ziegmann, G., Lonsdorfer, G., Stößlein, N., and Fette, M. (2014). Combination of carbon fibre sheet moulding com-

- pound and prepreg compression moulding in aerospace industry. *Procedia Engineering*, 81:1601–1607.
- [Yan and Ren, 2011] Yan, W.-J. and Ren, W.-X. (2011). Operational modal parameter identification from power spectrum density transmissibility. *Computer-Aided Civil and Infrastructure Engineering*, 27(3):202–217.
- [Yang et al., 2019] Yang, Q., Liu, Y., Chen, T., and Tong, Y. (2019). Federated machine learning: Concept and applications. *ACM Transactions on Intelligent Systems and Technology*, 10(2):1–19.
- [Yang et al., 2012] Yang, Y., Boom, R., Irion, B., van Heerden, D. J., Kuiper, P., and de Wit, H. (2012). Recycling of composite materials. *Chemical Engineering and Processing: Process Intensification*, 51:53–68.
- [Yang and Nagarajaiah, 2014] Yang, Y. and Nagarajaiah, S. (2014). Robust data transmission and recovery of images for structural health monitoring using compressed sensing. *Structural Control and Health Monitoring*, 21(3):279–296.
- [Yang and Nagarajaiah, 2015a] Yang, Y. and Nagarajaiah, S. (2015a). Output-only modal identification with limited sensors using sparse component analysis. *Journal of Sound and Vibration*, 332(19):4741–4765.
- [Yang and Nagarajaiah, 2015b] Yang, Y. and Nagarajaiah, S. (2015b). Output-only modal identification with limited sensors using sparse component analysis. *Journal of Sound and Vibration*, 332(19):4741–4765.
- [Ye et al., 2019] Ye, X. W., Jin, T., and Yun, C. B. (2019). A review on deep learning-based structural health monitoring of civil infrastructures. *Smart Structures and Systems*, 24(5):567–585.
- [Zapico-Valle et al., 2011] Zapico-Valle, J. L., Garcia-Dieguez, M., and Gonzalez-Martinez, M. P. (2011). Vibration-based damage detection in a steel frame structure using ewma control charts. *Structural Health Monitoring*, 10(3):333–342.
- [Zenkert, 1995a] Zenkert, D. (1995a). *An introduction to sandwich construction*. Engineering Materials Advisory Services.
- [Zenkert, 1995b] Zenkert, D. (1995b). *An Introduction to Sandwich Construction*. Engineering Materials Advisory Services, London.
- [Zenkert, 1997a] Zenkert, D. (1997a). *The handbook of sandwich construction*. Engineering Materials Advisory Services.
- [Zenkert, 1997b] Zenkert, D. (1997b). *The Handbook of Sandwich Construction*. Engineering Materials Advisory Services, Cradley Heath, UK.
- [Zenkert et al., 2006] Zenkert, D., Shipsha, A., and Burman, M. (2006). Fatigue of closed cell foams. *Journal of Sandwich Structures & Materials*, 8(6):517–538.
- [Zhang et al., 2021] Zhang, J., Wang, F., Sun, F., Zhang, Y., Wang, X., and Jiang, H. (2021). Federated learning for smart structural health monitoring. *Mechanical Systems and Signal Processing*, 161:107950.
- [Zhang, 2007] Zhang, Q. (2007). Statistical damage identification for bridges using ambient vibration data. *Computers & Structures*, 85(7-8):476–485.

- [Zhang et al., 2018a] Zhang, W., Li, C., Peng, G., Chen, Y., and Zhang, Z. (2018a). A deep convolutional neural network with new training methods for bearing fault diagnosis under noisy environment and different working load. *Mechanical Systems and Signal Processing*, 100:439–453.
- [Zhang et al., 2019] Zhang, Y., Miyamori, Y., Mikami, S., and Saito, T. (2019). Vibration-based structural state identification by a 1-dimensional convolutional neural network. *Computer-Aided Civil and Infrastructure Engineering*, 34(9):822–839.
- [Zhang et al., 2018b] Zhang, Z., He, M., Liu, A., Singh, H. K., Ramakrishnan, K. R., Hui, D., and Zhong, Y. (2018b). Recent developments in fiber-optic strain sensing for structural health monitoring. *Sensors*, 18(10):3241.
- [Zhao et al., 2018] Zhao, R., Wang, D., Yan, R., Mao, K., Shen, F., and Wang, J. (2018). Machine health monitoring using local feature-based gated recurrent unit networks. *IEEE Transactions on Industrial Electronics*, 65(2):1539–1548.
- [Zhao et al., 2019] Zhao, R., Yan, R., Chen, Z., Mao, K., Wang, P., and Gao, R. X. (2019). Deep learning and its applications to machine health monitoring. *Mechanical Systems and Signal Processing*, 115:213–237.
- [Zhao et al., 2007] Zhao, X., Qian, T., Mei, G., Kwan, C., Zane, R., Walsh, C., and Lee, K. C. (2007). Active health monitoring of an aircraft wing with an embedded piezoelectric sensor/actuator network: II. wireless approaches. *Smart Materials and Structures*, 16(4):1218.
- [Zhou and Paffenroth, 2017] Zhou, C. and Paffenroth, R. C. (2017). Anomaly detection with robust deep autoencoders. In *Proceedings of the 23rd ACM SIGKDD International Conference on Knowledge Discovery and Data Mining*, pages 665–674.
- [Zhou and Crocker, 2010] Zhou, R. and Crocker, M. J. (2010). Sound transmission characteristics of asymmetric sandwich panels. *Journal of Vibration and Acoustics*, 132(3):031012.
- [Zhu et al., 2020] Zhu, Y., Ye, X. J., Chu, M. J., Wang, X. W., and Liu, P. (2020). Self-healing behavior of a structural adhesive based on thermo-reversible diels-alder reaction for aerospace sandwich structures. *Composite Structures*, 252:112662.
- [Zok et al., 2003] Zok, F. W., Rathbun, H. J., Wei, Z., and Evans, A. G. (2003). Design of metallic textile core sandwich panels. *International Journal of Solids and Structures*, 40(21):5707–5722.
- [Zou et al., 2020] Zou, Y., Jia, Y., and Wang, T. (2020). Federated learning algorithm with heterogeneous feature engineering for industrial data. In *2020 International Conference on Smart Grid and Electrical Automation (ICSGEA)*, pages 320–324. IEEE.

A Developed MATLAB and Python Code

A.1 Modelling.m

```

%% Properties

syms x
l=0.465;
Beam_weight=0.14;
Ex_f=25.6e9;      % from youngmodulus.m
b=50e-3;
CFRP_height=1.35e-3;
Core_t=50e-9;          % Core thickness (50 micron)
Core_size=5e-3;         % Hexagon
Core_height=6e-3;
Doluluk_orani=0.385*Core_t/Core_size;
I_Core=b*Core_height^3/12*Doluluk_orani;
I_CFRP=b*CFRP_height^3/12;
I_comp=I_CFRP+b*CFRP_height*((Core_height+CFRP_height)/2)^2;
EI=Ex_f*I_comp*2;
A=5e-2*1e-2;
% rho=Beam_weight/((2*CFRP_height+Core_height+0.00105)*b
% *0.5);
rho=(Beam_weight)/(CFRP_height*b*0.5*2);
load("impact_2.mat")

%% Modal Analysis for Cantilever Beam

% First 4 Mode Beta

beta(1)=1.8751/l;
beta(2)=4.6951/l;
beta(3)=7.8547/l;
beta(4)=10.9956/l;

% Natural Frequency

wn=zeros(4,1);
for n=1:4
    wn(n)=((beta(n)*l)^2)*((EI/(rho*A*(l^4)))^(1/2));
end

% Mode Shape Matrix
W_n = sym(zeros(4,1));
for n = 1:4
    W_n(n) = (cos(beta(n)*x) - cosh(beta(n)*x)) - ((cos(beta(

```

```

n)*l) + cosh(beta(n)*l)) / (sin(beta(n)*l) + sinh(beta
(beta(n)*l))) * (sin(beta(n)*x) - sinh(beta(n)*x));
end

% Mass Matrix
M = zeros(4,4);
for i = 1:4
    for j = 1:4
        M(i,j) = int(rho * A * W_n(i) * W_n(j), x, 0, 1);
    end
end

% Stiffness Matrix
K = zeros(4,4);
for i = 1:4
    for j = 1:4
        W_i_xx = diff(W_n(i), x, 2);
        W_j_xx = diff(W_n(j), x, 2);
        K(i,j) = int(EI * W_i_xx * W_j_xx, x, 0, 1);
    end
end

% Time Dependent Function (Impulse)

syms t

T=sym(zeros(4,1));
W_val=sym(zeros(4,1));
W_num=sym(zeros(4,1));
for i= 1:4
    W_val(i) = subs(W_n(i), x, 0.43);
    W_num(i) = double(W_val(i));
    T(i)=6.5625e-3*W_num(i)/(M(i,i)*wn(i))*sin(wn(i)*t);
end

% Displacement

w=sym(zeros(4,1));
for n= 1:4
    w(n)=W_n(n)*T(n);
end

%Total Displacement

wt=sum(w);

%% Proportional Damping

% From FRFHalfPower.m

```

```

zeta1=0.095;
zeta2=0.096;
zeta3= 0.0464;

% From damping.m

% Angular frekans (rad/s)
w1 = 2 * pi * wn(1);
w2 = 2 * pi * wn(2);

% Rayleigh Damping

beta=2*(zeta1*w1-zeta2*w2)/(w1^2-w2^2);
alpha=2*zeta1*w1-beta*w1^2;

% Damping matrix

C = alpha * M + beta * K;

% Damped frequency

w_d1=wn(1)*sqrt(1-zeta1);
w_d2=wn(2)*sqrt(1-zeta2);
w_d3=wn(3)*sqrt(1-zeta3);

%% state space

n = size(M,1);

% State Space Matrices (Ax + Bu = 0 formu)
Z = zeros(n,n);
I = eye(n);
ssA = [Z, I; -K/M, -C/M];
ssB = [Z; inv(M)];
ssC_out = [I Z];
ssD = zeros(n,n);

% State Space Model
sys = ss(ssA, ssB, ssC_out, ssD);

%% Graphs

% Vibration Graphs of all modes
figure;
for i=1:4
    for j=1:4
        if i==j
            subplot(1,4,i)
            impulse(sys(i,j))

```

```

        end
    end
end

% Vibration Graphs of all modes (compound)
figure;
for i=1:4
    for j=1:4
        if i==j
            impulse(sys(i,j))
            hold on;
        end
    end
end
legend('1. Mode', '2. Mode', '3. Mode', '4. Mode');

% Input
[ssy, sst] = impulse(sys,1);

% Sum of modes
y_single = (ssy(:,:,1)+ssy(:,:,2)+ssy(:,:,3)+ssy(:,:,4));
y_total = sum(y_single, 2);

% Integration of Velocity

time=data2(12000:end,1);
velocity=data2(12000:end,3);
x0=0;
x=zeros(size(time));
x(1)=x0;

for i = 1:length(time) - 1
    dt = time(i+1) - time(i);
    x(i+1) = x(i) + (velocity(i) + velocity(i+1)) / 2 * dt;
end

% Deplacement Graph
k1=max(x)/max(y_total);
figure
plot(sst, k1*y_total, 'r')
hold on;
plot(time-1, x, 'b');
xlabel('Time (s)');
ylabel('Deplacement');
title('Dispacement Comparison Between Model and Experimental Data');
grid on;
legend('Model Estimated Displacement', 'Experimental Displacement');
hold off

```

```
% Displacement 2 velocity
ssy_vel=gradient(y_total)./gradient(sst);

%Velocity Graphs
k=max(data2(:,3))/max(ssy_vel);
figure
plot(sst, k*ssy_vel, 'r')
hold on;
plot((data2((12801:25600),1)-1),(data2(12801:25600,3)), 'b');
xlabel('Time (s)');
ylabel('Velocity');
title('Velocity Comparison Between Model and Experimental Data');
legend('Velocity According to Model','Experimental Velocity Data');
hold off
time=data2(12800:end,1);
velocity=data2(12800:end,3);
x0=0;
x=zeros(size(time));
x(1)=x0;
```

A.2 ar_model.m

```
%% Damage Detection Using Autoregressive Modeling
% Structural Health Monitoring for Composite Sandwich Beam
% Based on AR coefficient extraction and statistical distance analysis

% Clear workspace and command window
clc;
clearvars;
close all;

%% Parameters
n_sensors = 5; % Number of piezoelectric sensors
AR_order = 5; % Order of AR model
sampling_rate = 12800; % Sampling rate (Hz)
sample_duration = 2; % Duration of each sample (seconds)

% Data splitting ratios
train_ratio = 0.6; % Percentage of undamaged data for training
reference_ratio = 0.1; % Percentage of undamaged data for reference testing
threshold_ratio = 0.3; % Percentage of undamaged data for threshold calculation

%% Load Data
```

```

fprintf('Loading acceleration data...\n');

% Load undamaged and damaged data from extracted_columns.mat
% files
undamaged_file = 'undamaged_surface_extracted_columns.mat';
damaged_file = 'damaged_surface_extracted_columns.mat';

% Load undamaged data
if isfile(undamaged_file)
    undamaged_mat = load(undamaged_file);
    if ~isfield(undamaged_mat, 'extracted_data')
        error('Variable "extracted_data" not found in %s.', undamaged_file);
    end
    undamaged_data = undamaged_mat.extracted_data;
    fprintf('Loaded %d undamaged datasets.\n', length(undamaged_data));
else
    error('Undamaged data file %s not found.', undamaged_file);
end

% Load damaged data
if isfile(damaged_file)
    damaged_mat = load(damaged_file);
    if ~isfield(damaged_mat, 'extracted_data')
        error('Variable "extracted_data" not found in %s.', damaged_file);
    end
    damaged_data = damaged_mat.extracted_data;
    fprintf('Loaded %d damaged datasets.\n', length(damaged_data));
else
    error('Damaged data file %s not found.', damaged_file);
end

% Verify data dimensions
expected_samples = sampling_rate * sample_duration; % 25600
if ~isempty(undamaged_data)
    fprintf('Undamaged dataset size: %dx%d\n', size(undamaged_data{1}, 1), size(undamaged_data{1}, 2));
    if size(undamaged_data{1}, 1) ~= expected_samples || size(undamaged_data{1}, 2) ~= n_sensors
        error('Unexpected undamaged dataset size. Expected %dx%d, got %dx%d.', ...
            expected_samples, n_sensors, size(undamaged_data{1}, 1), size(undamaged_data{1}, 2));
    end
end
if ~isempty(damaged_data)

```

```

fprintf('Damaged dataset size: %dx%d\n', size(
    damaged_data{1}, 1), size(damaged_data{1}, 2));
if size(damaged_data{1}, 1) ~= expected_samples || size(
    damaged_data{1}, 2) ~= n_sensors
    error('Unexpected damaged dataset size. Expected %dx%
        d, got %dx%d.', ...
    expected_samples, n_sensors, size(damaged_data
        {1}, 1), size(damaged_data{1}, 2));
end
end

% Save the loaded data
save('loaded_piezo_data.mat', 'undamaged_data', 'damaged_data
    ');

%% Process and Organize Data
fprintf('Organizing data...\n');

% Get counts
n_undamaged = length(undamaged_data);
n_damaged = length(damaged_data);
n_total = n_undamaged + n_damaged;

% Calculate split indices
n_train = round(train_ratio * n_undamaged);
n_reference = round(reference_ratio * n_undamaged);
n_threshold = round(threshold_ratio * n_undamaged);

% Check that splits add up correctly, adjust if needed
if (n_train + n_reference + n_threshold) ~= n_undamaged
    n_train = n_undamaged - (n_reference + n_threshold);
end

% Balance damaged data for test set
rng(42); % For reproducibility
n_damaged_test = min(n_damaged, 10); % Use 10 damaged
    datasets for balance
damaged_indices = randperm(n_damaged, n_damaged_test);
damaged_data_subset = damaged_data(damaged_indices);
n_damaged = n_damaged_test; % Update for later calculations

% Create data partitions
training_data = undamaged_data(1:n_train);
threshold_data = undamaged_data(n_train+1:n_train+n_threshold
    );
reference_data = undamaged_data(n_train+n_threshold+1:end);
test_data = [reference_data, damaged_data_subset];

fprintf('Data partitioning complete:\n');
fprintf(' - Training set: %d samples (all undamaged)\n',

```

```

    n_train);
fprintf(' - Threshold set: %d samples (all undamaged)\n',
    n_threshold);
fprintf(' - Reference set: %d samples (all undamaged)\n',
    n_reference);
fprintf(' - Test set: %d samples (%d undamaged, %d damaged)\n',
    n', ...
    length(test_data), n_reference, n_damaged);

%% Preprocessing
fprintf('Preprocessing data...\n');

% Verify data dimensions
if isempty(training_data)
    error('Training data is empty.');
end
fprintf('Training data sample size: %dx%d\n', size(
    training_data{1}, 1), size(training_data{1}, 2));
if size(training_data{1}, 1) ~= expected_samples || size(
    training_data{1}, 2) ~= n_sensors
    error('Unexpected training data dimensions. Expected %dx%
        d, got %dx%d.', ...
        expected_samples, n_sensors, size(training_data{1},
            1), size(training_data{1}, 2));
end

% Function to preprocess time series data
preprocess_timeseries = @(data) preprocessData(data,
    n_sensors);

% Apply preprocessing to all datasets
training_data = cellfun(preprocess_timeseries, training_data,
    'UniformOutput', false);
threshold_data = cellfun(preprocess_timeseries,
    threshold_data, 'UniformOutput', false);
reference_data = cellfun(preprocess_timeseries,
    reference_data, 'UniformOutput', false);
test_data = cellfun(preprocess_timeseries, test_data,
    'UniformOutput', false);

% Get normalization parameters from training data
[mean_values, std_values] = getNormalizationParams(
    training_data, n_sensors);

% Normalize all datasets using training data statistics
training_data = normalizeData(training_data, mean_values,
    std_values, n_sensors);
threshold_data = normalizeData(threshold_data, mean_values,
    std_values, n_sensors);
reference_data = normalizeData(reference_data, mean_values,

```

```
    std_values, n_sensors);
test_data = normalizeData(test_data, mean_values, std_values,
    n_sensors);

%% Feature Extraction
fprintf('Extracting AR coefficients...\n');

% Extract AR coefficients from training data
training_features = extractARCoefficients(training_data,
    AR_order, n_sensors);

% Extract AR coefficients from threshold data
threshold_features = extractARCoefficients(threshold_data,
    AR_order, n_sensors);

% Extract AR coefficients from test data (both reference and
% damaged)
test_features = extractARCoefficients(test_data, AR_order,
    n_sensors);

% Separate test features into reference and damaged
reference_features = test_features(1:n_reference, :);
damaged_features = test_features(n_reference+1:end, :);

fprintf('Feature extraction complete.\n');
fprintf(' - Feature vector size: %d coefficients per sample\n',
    size(training_features, 2));

%% Damage Detection
fprintf('Performing damage detection...\n');

% Calculate Mahalanobis distance from threshold data to
% training distribution
threshold_distances = mahal(threshold_features,
    training_features);

% Calculate Mahalanobis distance from test data to training
% distribution
test_distances = mahal(test_features, training_features);

% Calculate Mahalanobis distance for reference and damaged
% separately
reference_distances = test_distances(1:n_reference);
damaged_distances = test_distances(n_reference+1:end);

% Determine threshold using 95% quantile of threshold
% distances
detection_threshold = quantile(threshold_distances, 0.95);

% Make predictions based on threshold
```

```

reference_predictions = reference_distances >
    detection_threshold;
damaged_predictions = damaged_distances > detection_threshold
;

% Combine all predictions
all_predictions = [reference_predictions; damaged_predictions
];

% Create true labels
true_labels = [zeros(n_reference, 1); ones(n_damaged, 1)];

%% Results and Evaluation
fprintf('Evaluating detection performance...\n');

% Calculate performance metrics
TP = sum(damaged_predictions == 1); % True Positives
FP = sum(reference_predictions == 1); % False Positives
TN = sum(reference_predictions == 0); % True Negatives
FN = sum(damaged_predictions == 0); % False Negatives

accuracy = (TP + TN) / (TP + FP + TN + FN);
sensitivity = TP / (TP + FN); % True Positive Rate
specificity = TN / (TN + FP); % True Negative Rate
if TP + FP > 0
    precision = TP / (TP + FP); % Positive Predictive Value
else
    precision = 0; % Handle case with no positive predictions
end

fprintf('\nDetection Performance:\n');
fprintf(' - Accuracy: %.2f%%\n', accuracy * 100);
fprintf(' - Sensitivity (TPR): %.2f%%\n', sensitivity * 100)
;
fprintf(' - Specificity (TNR): %.2f%%\n', specificity * 100)
;
fprintf(' - Precision (PPV): %.2f%%\n', precision * 100);

%% Visualizations
fprintf('Creating visualizations...\n');

% Convert labels to categorical with meaningful names
label_names = {'Undamaged', 'Damaged'};
true_labels_cat = categorical(true_labels, [0, 1],
    label_names);
all_predictions_cat = categorical(all_predictions, [0, 1],
    label_names);

% Figure 1: Confusion matrix
figure(1);

```

```

confusionchart(true_labels_cat, all_predictions_cat);
title('AR Model Damage Detection Results');

% Figure 2: Damage index scatter plot
figure(2);
hold on;
scatter(1:length(threshold_distances), threshold_distances, 'bx', 'DisplayName', 'Threshold Data (Undamaged)');
scatter(length(threshold_distances)+(1:length(reference_distances)), reference_distances, 'm+', ...
'DisplayName', 'Reference Data (Undamaged)');
scatter(length(threshold_distances)+length(reference_distances)+(1:length(damaged_distances)), ...
damaged_distances, 'ro', 'DisplayName', 'Damaged Data');
xline(detection_threshold, '--', 'Detection Threshold (95% Quantile)', 'DisplayName', 'Detection Threshold');
xline(length(threshold_distances)+length(reference_distances) ...
, ':', 'HandleVisibility', 'off');
hold off;

set(gca, 'YScale', 'log');
title('Damage Detection Index (Mahalanobis Distance)');
xlabel('Sample Number');
ylabel('Log Damage Index');
legend('Location', 'northwest');
grid on;

% Figure 3: Compare signal examples from undamaged and damaged cases
figure(3);
for s = 1:min(n_sensors, 3)
    subplot(min(n_sensors, 3), 1, s);

    healthy_idx = 1;
    damaged_idx = 1;

    healthy_signal = undamaged_data{healthy_idx}(:, s); %
    25600x1 for sensor s
    damaged_signal = damaged_data{damaged_idx}(:, s);

    t = linspace(0, sample_duration, length(healthy_signal));

    plot(t, healthy_signal, 'b-', 'DisplayName', 'Undamaged')
    ;
    hold on;
    plot(t, damaged_signal, 'r-', 'DisplayName', 'Damaged');
    hold off;

    title(['Sensor ', num2str(s), ' Signal Comparison']);
    xlabel('Time (s)');

```

```

        ylabel('Amplitude');
        legend('Location', 'best');
        grid on;
    end

%% Helper Functions

function processed_data = preprocessData(data, n_sensors)
    % Verify input dimensions
    expected_samples = 25600;
    if size(data, 1) ~= expected_samples || size(data, 2) ~= n_sensors
        error('Unexpected data dimensions. Expected %dx%d, got %dx%d.', ...
            expected_samples, n_sensors, size(data, 1), size(data, 2));
    end

    % Apply differencing to make the data more stationary
    processed_data = zeros(size(data));
    for s = 1:n_sensors
        time_series = data(:, s); % 25600x1
        diff_data = diff(time_series); % 25599x1
        processed_data(1:25599, s) = diff_data;
        processed_data(25600, s) = diff_data(end); % Pad with last value
    end
end

function [mean_values, std_values] = getNormalizationParams(
    data_cell, n_sensors)
    mean_values = zeros(1, n_sensors);
    std_values = zeros(1, n_sensors);

    for s = 1:n_sensors
        all_values = [];
        for i = 1:length(data_cell)
            all_values = [all_values, data_cell{i}(:, s)'];
        end
        mean_values(s) = mean(all_values);
        std_values(s) = max(std(all_values), eps); % Avoid zero std
    end
end

function normalized_data = normalizeData(data_cell,
    mean_values, std_values, n_sensors)
    normalized_data = cell(size(data_cell));

    for i = 1:length(data_cell)

```

```

normalized_data{i} = data_cell{i};
for s = 1:n_sensors
    normalized_data{i}(:, s) = (data_cell{i}(:, s) -
        mean_values(s)) / std_values(s);
end
end

function ar_features = extractARCoefficients(data_cell,
    ar_order, n_sensors)
n_samples = length(data_cell);
ar_features = zeros(n_samples, ar_order * n_sensors);

for i = 1:n_samples
    feature_idx = 1;
    for s = 1:n_sensors
        series = data_cell{i}(:, s); % 25600x1
        if any(isnan(series) | isnan(series)) || std(
            series) < eps
            warning('Invalid series for sample %d, sensor
                %d: NaN/Inf or zero variance.', i, s);
            ar_features(i, feature_idx:feature_idx+
                ar_order-1) = zeros(1, ar_order);
            feature_idx = feature_idx + ar_order;
            continue;
        end
        Mdl = arima('ARLags', 1:ar_order);
        try
            EstMdl = estimate(Mdl, series, 'Display',
                'off');
            coeffs = cell2mat(EstMdl.AR);
        catch
            warning('AR estimation failed for sample %d,
                sensor %d.', i, s);
            coeffs = zeros(1, ar_order);
        end
        ar_features(i, feature_idx:feature_idx+ar_order-
            1) = coeffs;
        feature_idx = feature_idx + ar_order;
    end
    if mod(i, 10) == 0
        fprintf(' Processed %d/%d samples\n', i,
            n_samples);
    end
end
end

```

A.3 BnL_v1_18_02_25.m

```
clc; clear;
```

```

syms bL
eqn = cos(bL)*cosh(bL)== -1;
bLi = [];
for i = 1:1:17
    j = i+1;
    bl=vpasolve(eqn, bL, [i j]);
    bl = double(bl);
    bLi = [bLi, bl];
end
bLi

%%

E = 14367000000;
I = 4.17E-12;
A = 0.00005;
L = 1;
R = 1.51E+03;

fn_list =[];
for i = 1:length(bLi)
    wn = bLi(i)^2*(E*I/(R*A*L^4))^(1/2);
    fn = wn/(2*pi);
    fn_list = [fn_list, fn];
end
fn_list

```

A.4 data_acquisition.m

```

clear all
close all
clc

% Calibration Properties If Necessary
Calibration_flag_compression = 0;
Calibration_compression_load = 5.1*9.81; % N
calibration_duration = 1; % seconds

% Plotting Durations
livePlotWindow = 2 ; % seconds
preTrigger = 1; % seconds
refreshRate = 1; % refresh/seconds inverse

% NI Properties
% Fs = 10240;
Fs = 10240;
dq = daq("ni");
dq.Rate = Fs;

```

```
% Excitation Selection
% 0 --> Shaker
% 1 --> Impact Hammer
load_cell = 0;

% Load Cell Properties
if load_cell == 1
    ch1_Name1 = "cDAQ1Mod3";
    ch1_Name2 = "ai3";
    ch1_Name = ch1_Name1+_+ch1_Name2;
    ch1 = addininput(dq, ch1_Name1, ch1_Name2, "IEPE");
    sensitivity_input = 1.125/1000; %V/N;
    slope_input = 1/sensitivity_input;

elseif load_cell == 0
    Excitation_Voltage = 5;
    ch1_Name1 = "cDAQ1Mod4";
    ch1_Name2 = "ai0";
    ch1_Name = ch1_Name1+_+ch1_Name2;
    ch1 = addininput(dq, ch1_Name1, ch1_Name2, "Bridge");
    ch1.BridgeMode = "Full";
    ch1.NominalBridgeResistance = 350;
    ch1.ExcitationVoltage = Excitation_Voltage;
    slope_input = 783670; %N/V
end

% % Laser Channel Addition
ch2 = addininput(dq, "cDAQ1Mod3", "ai0", "Voltage");
ch2.Coupling = "AC";
laserSetting = 100; % (mm/s/V)
sensitivity_laser = 1/laserSetting*1000; % V/(m/s)
slope_laser = 1/sensitivity_laser;

% % Piezo Channel Addition
ch3 = addininput(dq, "cDAQ1Mod8", "ai0", "Voltage");
ch4 = addininput(dq, "cDAQ1Mod8", "ai1", "Voltage");
ch5 = addininput(dq, "cDAQ1Mod8", "ai2", "Voltage");
ch6 = addininput(dq, "cDAQ1Mod8", "ai3", "Voltage");
ch7 = addininput(dq, "cDAQ1Mod7", "ai1", "Voltage");
% ch8 = addininput(dq, "cDAQ1Mod7", "ai0", "Voltage");
% ch9 = addininput(dq, "cDAQ1Mod7", "ai2", "Voltage");

% Capture Struct
capture.livePlotWindow = livePlotWindow;
capture.signalLevel = 3; % N
capture.preTrigger = preTrigger;
capture.preTriggerIndexer = round(preTrigger*dq.Rate);
capture.bufferSize = round((livePlotWindow)*dq.Rate);
```

```

%% Calibration
fprintf("Calibration of NO LOAD CASE in progress for " +
    num2str(calibration_duration) + " seconds!!!\n")
fprintf("Do not touch load cell!!!\n")
data_calibration_bias = read(dq, seconds(calibration_duration
    ));
numRows = size(data_calibration_bias ,1);
total = sum(data_calibration_bias.(ch1_Name));
bias = total/numRows;
fprintf("Calibration of NO LOAD CASE is done. Bias = " +
    num2str(bias) + "\n")
fprintf
    ("*****\n")
figure()
plot(data_calibration_bias.Time, data_calibration_bias.(
    ch1_Name))

if Calibration_flag_compression == 1
    fprintf("Proceed to COMPRESSION LOAD CASE configuration!
        !! Object is expected to have " + num2str(
            Calibration_compression_load) + " N.\n")
    fprintf("When ready touch a key!!!\n")
    w = waitforbuttonpress;
    close all
    fprintf("Calibration of COMPRESSION LOAD CASE in progress
        for " + num2str(calibration_duration) + " seconds!!!\n")
    fprintf("Do not touch load cell!!!\n")
    data_calibration_compression = read(dq, seconds(
        calibration_duration));
    numRows = size(data_calibration_compression ,1);
    total = sum(data_calibration_compression.(ch1_Name));
    compressionAverage = total/numRows-bias;
    fprintf("Calibration for COMPRESSION is done. Compression
        reading = " + num2str(compressionAverage) + "\n")
    fprintf
        ("*****\n")

figure()
plot(data_calibration_compression.Time,
    data_calibration_compression.(ch1_Name)-bias)

slope_input = Calibration_compression_load/
    compressionAverage; % N/V
end

ch1_calibration_data.slope = slope_input;
ch1_calibration_data.bias = bias;

```

```
ch2_calibration_data.slope = slope_laser;

%%%
fprintf("When ready touch a key!!!\n")
w = waitforbuttonpress;
close all

hGraph = createPlot(dq);

dq.ScansAvailableFcn = @(obj,evt) dataCapture(obj, evt,
    capture, hGraph, ch1_calibration_data,
    ch2_calibration_data);
dq.ScansAvailableFcnCount = ceil(dq.Rate*refreshRate);

start(dq, "continuous")

while dq.Running
    pause(0.5)
end

% Disconnect from hardware
delete(dq)

disp("Finished")

%% Functions
function dataCapture(obj, ~, capture, hGraph,
    ch1_calibration_data, ch2_calibration_data)
    [data, timeStamps, ~] = read(obj, obj.
        ScansAvailableFcnCount, "OutputFormat", "Matrix");

    persistent dataBuffer trigActive trigMoment finishingFlag
        preData dataCounter;

    %
    % if size(dataBuffer,1) == 0
    %     dataBuffer = [];
    %     trigActive = false;
    %     trigMoment = [];
    %     finishingFlag = false;
    %     preData = [];
    %     dataCounter = 1;
    % end

    if timeStamps(1) == 0
        dataBuffer = [];
        trigActive = false;
        trigMoment = [];
```

```

finishingFlag = false;
preData = [];
dataCounter = 1;
end

% Calibrated Data
calibrated_data_ch1 = ch1_calibration_data.slope*(data
(:,1)-ch1_calibration_data.bias);
calibrated_data_ch2 = ch2_calibration_data.slope*(data
(:,2));

latestData = [timeStamps, calibrated_data_ch1,
calibrated_data_ch2, data(:,3:end)];

dataBuffer = [dataBuffer;latestData];
numSamplesToDiscard = size(dataBuffer,1) - capture.
bufferSize;

if ~ishandle(1)
    stop(obj)
elseif ishandle(1)
    if (numSamplesToDiscard > 0)
        dataBuffer(1:numSamplesToDiscard, :) = [];
        xlim(hGraph.Axes1, [dataBuffer(1,1), dataBuffer(
            end,1)]);
        xlim(hGraph.Axes2, [dataBuffer(1,1), dataBuffer(
            end,1)]);
        xlim(hGraph.Axes3, [dataBuffer(1,1), dataBuffer(
            end,1)]);
    else
        xlim(hGraph.Axes1, [0, capture.livePlotWindow]);
        xlim(hGraph.Axes2, [0, capture.livePlotWindow]);
        xlim(hGraph.Axes3, [0, capture.livePlotWindow]);
    end
    set(hGraph.input, "XData", dataBuffer(:,1), "YData",
        dataBuffer(:,2))
    set(hGraph.outputLaser, "XData", dataBuffer(:,1), "
        YData", dataBuffer(:,3))
    set(hGraph.outputPiezo(1), "XData", dataBuffer(:,1),
        "YData", dataBuffer(:,4),"Color","r")
    set(hGraph.outputPiezo(2), "XData", dataBuffer(:,1),
        "YData", dataBuffer(:,5),"Color","g")
    set(hGraph.outputPiezo(3), "XData", dataBuffer(:,1),
        "YData", dataBuffer(:,6),"Color","b")
    set(hGraph.outputPiezo(4), "XData", dataBuffer(:,1),
        "YData", dataBuffer(:,7),"Color","m")
    set(hGraph.outputPiezo(5), "XData", dataBuffer(:,1),
        "YData", dataBuffer(:,8),"Color","c")
end

```

```
% set(hGraph.outputPiezo(6), "XData", dataBuffer(:,1)
    , "YData", dataBuffer(:,9),"Color","y")
% set(hGraph.outputPiezo(7), "XData", dataBuffer(:,1)
    , "YData", dataBuffer(:,10),"Color","k")

if ~trigActive
    hGraph.StatusText.String = 'Waiting for trigger';
    [trigActive, trigMoment] = trigDetect(latestData,
        capture.signalLevel);
    if trigActive
        disp("Triggered")
    end
elseif trigActive && (dataBuffer(1,1) < (trigMoment -
    capture.preTrigger))
    hGraph.StatusText.String = 'Triggered';
elseif trigActive && (dataBuffer(1,1) > (trigMoment -
    capture.preTrigger)) && ~finishingFlag
    finishingFlag = true;
    dataBuffer = [preData;latestData];
elseif trigActive && (dataBuffer(1,1) > (trigMoment -
    capture.preTrigger)) && finishingFlag
    disp("Data Collected")
    dataBuffer = [preData;latestData];
    capturedData = dataBuffer;

    trigSampleMiddleIndex = find(capturedData(:,1) ==
        trigMoment, 1, 'first');
    trigSampleFirstIndex = trigSampleMiddleIndex -
        capture.preTriggerIndexer;
    trigSampleLastIndex = round(trigSampleFirstIndex
        + capture.bufferSize);

    captureData = capturedData(trigSampleFirstIndex:
        trigSampleLastIndex-1, :);

    captureData(:,1) = captureData(:,1)-captureData
        (1,1);

    dataName = "data"+num2str(dataCounter);

    assignin('base', dataName, captureData);

    trigActive = false;

    % Create the Fast Fourier Transform of the
    % signals
    Fs = 1/(captureData(2,1)-captureData(1,1));
    [freq_input, mag_input] = fastFourier(captureData
        (:,2), Fs);
    [freq_outputLaser, mag_outputLaser] = fastFourier
```

```

        (captureData(:,3), Fs);
[freq_outputPiezo1, mag_outputPiezo1] =
    fastFourier(captureData(:,4), Fs);
[freq_outputPiezo2, mag_outputPiezo2] =
    fastFourier(captureData(:,5), Fs);
[freq_outputPiezo3, mag_outputPiezo3] =
    fastFourier(captureData(:,6), Fs);
[freq_outputPiezo4, mag_outputPiezo4] =
    fastFourier(captureData(:,7), Fs);
[freq_outputPiezo5, mag_outputPiezo5] =
    fastFourier(captureData(:,8), Fs);
[freq_outputPiezo6, mag_outputPiezo6] =
    fastFourier(captureData(:,9), Fs);
[freq_outputPiezo7, mag_outputPiezo7] =
    fastFourier(captureData(:,10), Fs);

% Calculate Half Power of Input
averagingFrequencyLimit = 10; % Average of first
    10 Hz
averageIndex = find(min(abs(freq_input -
    averagingFrequencyLimit))==abs(freq_input -
    averagingFrequencyLimit));
mag_inputForAverage = mag_input(1:averageIndex,:);
;
mag_inputTotal = sum(mag_inputForAverage);
mag_inputSize = size(mag_inputForAverage,1);

magBeginning = mag_inputTotal/mag_inputSize;
mag3dB = [min(freq_input), max(freq_input); (
    magBeginning-3), (magBeginning-3)];
mag10dB = [min(freq_input), max(freq_input); (
    magBeginning-10), (magBeginning-10)];

% Plot Captured Data
figure("Name","Captured Data","units","normalized",
    "outerposition",[0 0 1 1])

% Time Domain
subplot(3,2,1)
plot(captureData(:,1),captureData(:,2))
xlabel("Time (s)")
ylabel("Force (N)")
title("Input")
subplot(3,2,3)
plot(captureData(:,1),captureData(:,3))
xlabel("Time (s)")
ylabel("Velocity (m/s)")
title("Output Laser")
subplot(3,2,5)

```

```
hold on
plot(captureData(:,1),captureData(:,4),"r")
plot(captureData(:,1),captureData(:,5),"g")
plot(captureData(:,1),captureData(:,6),"b")
plot(captureData(:,1),captureData(:,7),"m")
plot(captureData(:,1),captureData(:,8),"c")
% plot(captureData(:,1),captureData(:,9),"y")
% plot(captureData(:,1),captureData(:,10),"k")

hold off
xlabel("Time (s)")
ylabel("Voltage (V)")
title("Output Piezo")

% Frequency Domain
subplot(3,2,2)
hold on
plot(freq_input,mag_input)
plot(mag3dB(1,:), mag3dB(2,:), "b--", "DisplayName","3 dB")
plot(mag10dB(1,:), mag10dB(2,:), "r--", "DisplayName","10 dB")
hold off
xlabel("Frequency (Hz)")
ylabel("|P1| (dB)")
title("Input (Freq. Domain)")

subplot(3,2,4)
plot(freq_outputLaser,mag_outputLaser)
xlabel("Frequency (Hz)")
ylabel("|P1| (dB)")
title("Output Laser (Freq. Domain)")

subplot(3,2,6)
plot(freq_outputPiezo1,mag_outputPiezo1,"r")
hold on
plot(freq_outputPiezo2,mag_outputPiezo2,"g")
plot(freq_outputPiezo3,mag_outputPiezo3,"b")
plot(freq_outputPiezo4,mag_outputPiezo4,"m")
plot(freq_outputPiezo5,mag_outputPiezo5,"c")
% plot(freq_outputPiezo6,mag_outputPiezo6,"y")
% plot(freq_outputPiezo7,mag_outputPiezo7,"k")
hold off
xlabel("Frequency (Hz)")
ylabel("|P1| (dB)")
title("Output Piezo (Freq. Domain)")

dataCounter = dataCounter +1;
end
preData = dataBuffer;
```

```

        drawnow
    end
end

function hGraph = createPlot(dq)
    hGraph.Fig = figure("Name", "Data Acquisition","units", "normalized","outerposition",[0 0 1 1]);
    hGraph.Fig.DeleteFcn = {@endDAQ,dq};

    hGraph.Axes1 = axes;
    hGraph.input = plot(NaN,NaN(1,1));
    xlabel("Time (s)")
    ylabel("Force (N)")
    title("Input")
    hGraph.Axes1.Units = "normalized";
    hGraph.Axes1.Position = [0.1 0.70 0.8 0.24];

    hGraph.Axes2 = axes;
    hGraph.outputLaser = plot(NaN,NaN(1,1));
    xlabel("Time (s)")
    ylabel("Velocity (m/s)")
    title("Output Laser")
    hGraph.Axes2.Units = "normalized";
    hGraph.Axes2.Position = [0.1 0.39 0.8 0.24];

    hGraph.Axes3 = axes;
    hGraph.outputPiezo = plot(NaN,NaN(1,5));
    xlabel("Time (s)")
    ylabel("Voltage (V)")
    title("Output Piezo")
    hGraph.Axes3.Units = "normalized";
    hGraph.Axes3.Position = [0.1 0.08 0.8 0.24];

    hGraph.StatusText = uicontrol('style', 'text', 'string',
        '',...
        'units', 'normalized', 'position', [0.91 0.85 0.05 0.05],
        ...
        'HorizontalAlignment', 'left');

end

function [trigDetected, trigMoment] = trigDetect(latestData,
level)
    trigCondition = latestData(:,2) > level;
    trigDetected = any(trigCondition);
    trigMoment = [];

    if trigDetected
        % Find time moment when trigger condition has been
        met

```

```
trigTimeStamps = latestData(trigCondition, 1);
trigMoment = trigTimeStamps(1);
end

end

function endDAQ(~, ~, dq)
if isValid(dq)
    if dq.Running
        stop(dq);
    end
end
end

function [freq, mag] = fastFourier(signal, Fs)
%
=====

% Takes Fast Fourier Transform (FFT) of the signal, then
% gives
% amplitudes for the respective frequencies.
%

-----
% INPUT:
% signal: In the form of (Signal Length, 1)
% Fs: Sampling frequency
%
-----

%
% OUTPUT:
% freq: Frequencies of the FFT
% mag: Magnitudes corresponding to the frequencies in
%      terms of dB
%
=====

length = size(signal,1);

% FFT works with even numbered signal lengths, if not
% eliminate last
% data
if mod(length,2) == 1
    signal = signal(1:end-1,:);
end

% Fast Fourier Transform of the Signal
Y = fft(signal);
% Rescaling of the magnitudes of the two-sided amplitude
% spectrum
```

```

P2 = abs(Y/length);
% Creating single-sided amplitude spectrum by taking
% first half
P1 = P2(1:length/2+1);
% Correcting the amplitudes of the single-sided amplitude
% spectrum
P1(2:end-1) = 2*P1(2:end-1);
% Assigning single-sided amplitudes to the magnitude
% variable
mag = log10(P1)*10;

% Frequencies Values (as Fs is increased investigateable
% frequencies
% increase
freq = Fs/length*(0:(length/2));
end

```

A.5 ERA.m

```

% System Identification

%% Continuous to discrete

T_s = .01;
sys_c = ss(ssA, ssB, ssC_out, ssD); % Continuous model
sys_d = c2d(sys_c, T_s, 'zoh'); % ZOH (zero-order hold)
method
n_modes=4;

Y = zeros(size(C_d, 1), size(B_d, 2), 8);
for i=1:8
    Y(:,:,i)=C_d*(A_d^(i-1))*B_d;
end

H= zeros(size(C_d, 1), size(B_d, 2), 8);
for i=1:8
end

[d_ss, d_ssst]=impulse(sys_d,15);
ssy = permute(d_ss, [2 3 1]); % [4 x 4 x 399360]
ssy = reshape(d_ss, [4, 4, length(d_ss)]); % 4 input, 4
output

r = 4; % block line
s = 4; % block column
[~, m, p] = size(d_ss);

% Hankel

```

```

H0 = zeros(r*p, s*m);
H1 = zeros(r*p, s*m);

for i = 1:r
    for j = 1:s
        H0((i-1)*p+1:i*p, (j-1)*m+1:j*m) = ssy(:,:,i + j - 1)
        ;
        H1((i-1)*p+1:i*p, (j-1)*m+1:j*m) = ssy(:,:,i + j);
    end
end

%% SVD

[U, S, V] = svd(H0, 'econ');
Sigma = diag(S);

% Visualization of Modes

figure; semilogy(Sigma, 'o-'); title('Estimated Mode Numbers
In SVD');
xlabel('Mode Index'); ylabel('Singular Value (log)');

U1 = U(:, 1:n_modes);
S1 = S(1:n_modes, 1:n_modes);
V1 = V(:, 1:n_modes);

% Controllability and Observability Matrices

S1_inv_sqrt = S1^(-0.5);
S1_sqrt      = S1^(0.5);

A_era = S1_inv_sqrt * U1' * H1 * V1 * S1_inv_sqrt;
B_era = S1_sqrt * V1(1:m,:)';
C_era = U1(1:p,:) * S1_sqrt;

Ts = sys.Ts;
[Vec, Lambda] = eig(A_era);
lambda = diag(Lambda);

% To Continuous
s = log(lambda) / Ts;

freq_Hz = abs(imag(s)) / (2*pi);
zeta = -real(s) ./ abs(s);

% Frequency Results
disp(table(freq_Hz, zeta, 'VariableNames', {'Frequency_Hz', '
Damping'}))

```

```

%% Continuous

% Discrete-time model
sys_d = ss(A_d, B_d, C_d, D_d, 0.01);

% D2C
sys_c_era = d2c(sys_d, 'zoh');

% Continuous-time state space matrices

A_c = sys_c_era.A;
B_c = sys_c_era.B;
C_c = sys_c_era.C;
D_c = sys_c_era.D;

[ssy_era, sst_era] = impulse(sys_c_era,1); % y = [Zaman x
                                                Serbestlik Derecesi]

% Sum of modes
y_single_era = (ssy_era(:,:,1)+ssy_era(:,:,2)+ssy_era(:,:,3) +
                 ssy_era(:,:,4));    icin cikisi al (zaman x DOF)
y_total_era = sum(y_single_era, 2);

figure
plot(sst_era,y_total_era)

% Displacement 2 velocity
ssy_vel_era=gradient(y_total_era)./gradient(sst_era);

% Velocity Graphs
k_era=max(data2(:,3))/max(ssy_vel_era);
figure;
plot(sst_era, k_era*ssy_vel_era,'r')
hold on;
plot((data2((12801:25600),1)-1),(data2(12801:25600,3)), 'b');
legend('Velocity According to ERA','Experimental Data (Velocity)');
title('Velocity Comparison Between ERA and Experiment');
hold off

```

A.6 FFT.m

```

% FFT

Ft=data19(:,1);
FV=data19(:,8);

FVf=fft(FV);

```

```

Ftd=0.000195312500181899-9.76562500909495e-05;

Ffd=1/Ftd;
FL=25600;

FFaxis=(0:FL-1)*(Ffd/FL);

P2 = abs(FVf/FL);
P1 = P2(1:FL/2+1);
P1=P1*1500;
P1(2:end-1) = 2 * P1(2:end-1);
FFaxis = FFaxis(1:FL/2+1);

plot(FFaxis, P1)
title('Single Sided Spectrum')
xlabel('Frekans (Hz)')
ylabel('|P1(FFaxis)|')
grid on

% Power Spectrum
Ppower = abs(FVf).^2 / numel(FVf);
plot(FFaxis, mag2db(Ppower));
title('Power Spectrum (dB)')
xlabel('Frekans (Hz)')
ylabel('power (dB)')
grid on

% Filtre 1

low_cutoff = 90;
high_cutoff = 105;
filter_order = 4;

Wn_normal = [low_cutoff high_cutoff] / (Ffd / 2);

% Butterworth bandpass filtresi tasarla
[b, a] = butter(filter_order, Wn_normal, 'bandpass');

v_filtered = filtfilt(b, a, FV);

figure;
plot(Ft, FV, 'k', 'DisplayName', 'Orjinal Hiz');
hold on;
plot(Ft, v_filtered, 'r', 'LineWidth', 1.5, 'DisplayName', 'Filtrelenmis Hiz (96.9 Hz)');
xlabel('Zaman (s)');
ylabel('Hiz (m/s)');

```

```

legend;
grid on;
title('ilk Mod (96.9 Hz) ');

Vf1=0.000407902975953824;
Vf2=0.000398487191004673;
dkrmntFiltered=log(Vf1/Vf2);

dampCo=dkrmntFiltered/(dkrmntFiltered^2+4*pi^2);

Fvfil=fft(v_filtered); %Filtrelenmis Hiz Verisinin FFTsi

% Tek taraflı genlik spektrumu (Filtered1)

Pf2 = abs(Fvfil/FL);
Pf1 = Pf2(1:FL/2+1);
Pf1(2:end-1) = 2 * Pf1(2:end-1);

% Grafik cizdirme (Filtered1)
plot(FFaxis, Pf1)
title('Tek Taraflı Genlik Spektrumu (Filtrelenmis)')
xlabel('Frekans (Hz)')
ylabel('|Pf1(FFaxis)|')
grid on

% Power Spectrum (Filtered1)
Ppowerfil = abs(Fvfil).^2 / numel(Fvfil);
plot(FFaxis, mag2db(Ppowerfil));
title('Power Spectrum (dB) (Filtered1)')
xlabel('Frequency (Hz)')
ylabel('Power (dB)')
grid on

% Filtre 2

low_cutoff2 = 600;
high_cutoff2 = 615;
filter_order = 4;

Wn_normal2 = [low_cutoff2 high_cutoff2] / (Ffd / 2);

% Butterworth bandpass filtresi tasarla
[b2, a2] = butter(filter_order, Wn_normal2, 'bandpass');

v_filtered_607 = filtfilt(b2, a2, FV);

figure;
plot(Ft, FV, 'k', 'DisplayName', 'Orjinal Hiz');

```

```

hold on;
plot(Ft, v_filtered_607, 'b', 'LineWidth', 1.5, 'DisplayName'
    , 'Filtrelenmis Hiz (607 Hz)');
xlabel('Zaman (s)');
ylabel('Hiz (m/s)');
legend;
grid on;
title('607 Hz ikinci Mod icin Zaman Domeninde Filtrelenmis
Hiz Verisi');

Fvfil2=fft(v_filtered_607); %Filtrelenmis Hiz Verisinin FFTsi

% Tek taraflı genlik spektrumu (Filtered2)

Pf22 = abs(Fvfil2/FL); % Normalizasyon
Pf21 = Pf22(1:FL/2+1); % Tek taraflı spektrum
Pf21(2:end-1) = 2 * Pf21(2:end-1); % Simetri nedeniyle ikiye
% katlama

% Grafik cizdirme (Filtered2)
plot(FFaxis, Pf21)
title('Tek Taraflı Genlik Spektrumu (Filtrelenmis)')
xlabel('Frekans (Hz)')
ylabel('|Pf1(FFaxis)|')
grid on

% Power Spectrum (Filtered2)
Ppowerfil2 = abs(Fvfil2).^2 / numel(Fvfil2); % Guc spektrumu
% hesaplama
plot(FFaxis, mag2db(Ppowerfil2)); % Frekans ekseni ile cizim
title('Power Spectrum (dB) (Filtered)')
xlabel('Frequency (Hz)')
ylabel('Power (dB)')
grid on

```

A.7 FRFHalfPower.m

```

% FRF

Ftd=data19(2,1)-data19(1,1); %Period
Ffs=1/Ftd; %Frequency
force = data19(:,2);
force(abs(force)<10) =0;
plot(force);
filtered_data19= (data19(:,4)-captureData(1:25600,4));
[frf,f]=modalfrf(force,filtered_data19,Ffs,length(data19(:,1))
);
figure
modalfrf(force,filtered_data19,Ffs,length(data19(:,1)))

```

A.8 TF_Based_Localization.m

```

%% Multi-File TF-Based Damage Localization Analysis
clear; clc;

% === FILE LISTS ===
undamaged_files = { ...
    "impact_strainG_bigPiezo_26.mat", ...
    "impact_strainG_bigPiezo_30.mat", ...
    "impact_strainG_bigPiezo_42.mat" ...
};

damaged_files = { ...
    "Dimpact_strainG_bigPiezo_50.mat", ...
    "Dimpact_strainG_bigPiezo_52.mat" ...
};

% === SENSOR INFO ===
sensor_cols = 4:8;
sensor_pos = [1.5, 10.5, 19.5, 28.5, 37.5];
damage_zone = [19.5, 28.5];
nSensors = length(sensor_cols);

% === RESULT COUNTERS ===
total = 0;
success = 0;

fprintf("\n===== MULTI-FILE TF DIFFERENCE ANALYSIS =====\n");

% === LOAD UNDAMAGED FILES ===
for u = 1:length(undamaged_files)
    und = load(undamaged_files{u});
    und_fields = fieldnames(und);

    % === LOAD DAMAGED FILES ===
    for d = 1:length(damaged_files)
        dam = load(damaged_files{d});
        dam_fields = fieldnames(dam);

        % === MATCHING dataX FIELDS ===
        for i = 1:length(und_fields)
            und_name = und_fields{i};
            if ~startsWith(und_name, "data"), continue; end
            undata = und.(und_name);

            for j = 1:length(dam_fields)
                dam_name = dam_fields{j};
                if ~startsWith(dam_name, "data"), continue; end
                damdata = dam.(dam_name);

```

```

% === CHECK DATA VALIDITY ===
if size(undata, 2) < max(sensor_cols) || size
(damdata, 2) < max(sensor_cols)
    fprintf("\n[!] U%s - D%s: Missing sensor
            columns, skipped.\n", und_name,
            dam_name);
    continue;
end

% === EXTRACT SIGNALS ===
t = undata(:,1);
force_und = undata(:,2);
force_dam = damdata(:,2);
Fs = 1 / mean(diff(t));
L = length(t);
tf_diff_score = zeros(1, nSensors);

% === CALCULATE TF DIFFERENCES ===
for k = 1:nSensors
    Y_und = fft(undata(:, sensor_cols(k)));
    Y_dam = fft(damdata(:, sensor_cols(k)));
    F_und = fft(force_und);
    F_dam = fft(force_dam);

    H_und = Y_und ./ F_und;
    H_dam = Y_dam ./ F_dam;
    delta_H = abs(H_dam(1:L/2) - H_und(1:L/2))
    );
    tf_diff_score(k) = sum(delta_H);
end

total_tf = sum(tf_diff_score);

% === RESULT REPORTING ===
fprintf("\n-- U%s vs D%s --\n", und_name,
        dam_name);
for s = 1:nSensors
    fprintf("Sensor @ %.1f cm: TF diff = %.2f
            \n", sensor_pos(s), tf_diff_score(s));
end

[sorted_vals, sorted_idx] = sort(
    tf_diff_score, 'descend');
top1 = sensor_pos(sorted_idx(1));
top2 = sensor_pos(sorted_idx(2));
third_val = sorted_vals(3);

fprintf(">> Max 1: %.1f cm (%.2f)\n", top1,

```

```

        sorted_vals(1));
fprintf(">> Max 2: %.1f cm (%.2f)\n", top2,
       sorted_vals(2));

% === COMBINED SUCCESS CRITERIA ===
is_positional_match = ismember(top1,
    damage_zone) && ismember(top2, damage_zone
);
is_dominant = sorted_vals(1) > 1.2 *
third_val;

total = total + 1;
if is_positional_match && is_dominant
success = success + 1;
fprintf("SUCCESS (position + dominance)\n
");
else
fprintf("FAIL\n");
end
end
end
end

% === FINAL REPORT ===
fprintf("\n==== OVERALL RESULT ====\n");
fprintf("Total comparisons: %d\n", total);
fprintf("Successful detections: %d\n", success);
fprintf("Success rate: %.2f %%\n", 100 * success / total);

%% For Graphic Representation
clear; clc;

% === LOAD DATA ===
und = load("impact_laser_29.mat");
dam = load("Dimpact_embedded_26.mat");

% === Extract time and input signals ===
t = und.data14(:,1); % Time
force_und = und.data14(:,2); % Undamaged force input
force_dam = dam.data9(:,2); % Damaged force input
Fs = 1 / mean(diff(t)); % Sampling frequency
L = length(t);
f = (0:L/2-1)*(Fs/L); % Frequency axis

% === Sensor info ===
sensor_cols = 4:8;
nSensors = length(sensor_cols);
tf_diff_score = zeros(1, nSensors);

```

```
% === Compute TF difference for each sensor ===
for i = 1:nSensors
    Y_und = fft(und.data14(:, sensor_cols(i)));
    Y_dam = fft(dam.data9(:, sensor_cols(i)));
    F_und = fft(force_und);
    F_dam = fft(force_dam);

    H_und = Y_und ./ F_und;
    H_dam = Y_dam ./ F_dam;

    delta_H = abs(H_dam(1:L/2) - H_und(1:L/2));
    tf_diff_score(i) = sum(delta_H);
end

% === Sensor positions ===
sensor_pos = [1.5, 10.5, 19.5, 28.5, 37.5];

% === PLOT ===
% === PLOT ===
figure;
plot(sensor_pos, tf_diff_score, '-o', 'LineWidth', 2);
xlabel('Sensor Position (cm)');
ylabel('TF Difference Score');
title('TF-Based Damage Localization');
grid on;

% === Add true damage location ===
hold on;
xline(24, 'r--', 'LineWidth', 2); % Red
dashed line at 24 cm
plot(24, interp1(sensor_pos, tf_diff_score, 24, 'linear'), 'ro',...
    'MarkerFaceColor', 'r', 'MarkerSize', 8); % Red
filled dot at 24 cm
legend('TF Difference', 'True Damage Location', 'Location', 'northwest');
```

A.9 youngmodulus.m

```
%% Properities

% Fiber Properties
E_f = 238*10^9; % Young Modulus [Pa]
rho_f = 1.76; % Density [gr/cm^3]
upsilon_f = 0.3; % Poisson Ratio
G_f = E_f/(2*(1+upsilon_f));
```

```
% Matrix Properties
E_m = 3.2*10^9; % Young Modulus [Pa]
rho_m = 1.1; % Density [gr/cm^3]
upsilon_m = 0.3; % Poisson Ratio
G_m = E_m/(2*(1+upsilon_m));

% Weight Fraction
Wf = 28/39;

% Set Layer Orientation
layers = [0 90 0 90];
t_lamina = 0.3375/10^3; % Thickness of Single Lamina

% Core Properties
t_core=6/10^3; % Thickness of Core

%%
% Volume Fraction Calculation from Weight Fraction
rho_c = 1/(Wf/rho_f + (1-Wf)/rho_m); % Density of Composite
Vf = Wf*rho_c/rho_f; % Volume Fraction of Fiber
Vm = 1-Vf; % Volume Fraction of Matrix

% Engineering Constants of a Lamina From Strength of Materials
E1 = 4*E_f*Vf + 4*E_m*Vm;
upsilon_12 = upsilon_f*Vf + upsilon_m*Vm;
E2 = 1/(Vf/E_f+Vm/E_m);
G12 = 1/(Vf/G_f+Vm/G_m);

% Activate Semiempirical Calculator,
activateSemi = 1;

if activateSemi == 1
    % Semi Empirical Model
    ksi1 = 2;
    eta1 = ((E_f/E_m)-1)/((E_f/E_m)+ksi1);
    E2 = E_m*(1+ksi1*eta1*Vf)/(1-eta1*Vf); % Semiempirical E2

    if Vf < 0.5
        ksi2 = 1;
    else

```

```

ksi2 = 1+40*(Vf)^10;
end
eta2 = ((G_f/G_m)-1)/((G_f/G_m)+ksi2);
G12 = G_m*(1+ksi2*eta2*Vf)/(1-eta2*Vf);      %
Semiempirical G12
end

upsilon_21 = upsilon_12*E2/E1;

Q11 = E1/(1-upsilon_12*upsilon_21);
Q12 = upsilon_12*E2/(1-upsilon_12*upsilon_21);
Q22 = E2/(1-upsilon_12*upsilon_21);
Q66 = G12;

numberOfLayer = size(layers,2);
t = 2*numberOfLayer*t_lamina+t_core;
laminaThicknessListDown = linspace(-t/2,-t_core/2,
    numberOfLayer+1);
laminaThicknessListUp = linspace(t/2,t_core/2,numberOfLayer
    +1);

A = zeros(3,3);
B = zeros(3,3);
D = zeros(3,3);

for i = 1:size(layers,2)
    degree = layers(i);
    radian = deg2rad(degree);

    s = sin(radian);
    c = cos(radian);

    Qt_11 = Q11*c^4 + Q22*s^4 + 2*(Q12+2*Q66)*s^2*c^2;
    Qt_12 = (Q11+Q22-4*Q66)*s^2*c^2 + Q12*(s^4 + c^4);
    Qt_22 = Q11*s^4 + Q22*c^4 + 2*(Q12 + 2*Q66)*s^2*c^2;
    Qt_16 = (Q11-Q12-2*Q66)*c^3*s - (Q22 - Q12 - 2*Q66)*s^3*c
        ;
    Qt_26 = (Q11-Q12-2*Q66)*s^3*c - (Q22 - Q12 - 2*Q66)*c^3*s
        ;
    Qt_66 = (Q11+Q22-2*Q12-2*Q66)*s^2*c^2 + Q66*(s^4 + c^4);

    Q = [Qt_11,Qt_12,Qt_16;...
        Qt_12,Qt_22,Qt_26;...
        Qt_16,Qt_26,Qt_66];

    temp_A = 2*Q*(laminaThicknessListUp(i)-
        laminaThicknessListUp(i+1));

```

```

temp_B = 2*Q*(laminaThicknessListUp(i)^2-
    laminaThicknessListUp(i+1)^2)/2;
temp_D = 2*Q*(laminaThicknessListUp(i)^3-
    laminaThicknessListUp(i+1)^3)/3;

A = A + temp_A;
B = B + temp_B;
D = D + temp_D;
end

A_inv = inv(A);
D_inv = inv(D);

Ex = 1/(t*A_inv(1,1));
Ey = 1/(t*A_inv(2,2));
Gxy = 1/(t*A_inv(3,3));
vxy = -A_inv(1,2)/A_inv(1,1);
vyx = -A_inv(1,2)/A_inv(2,2);

Ex_f = 12/(t^3*D_inv(1,1));
Ey_f = 12/(t^3*D_inv(2,2));
Gxy_f = 12/(t^3*D_inv(3,3));
vxy_f = -D_inv(1,2)/D_inv(1,1);
vyx_f = -D_inv(1,2)/D_inv(2,2);

fprintf("Ex = " + num2str(round(Ex/10^9,3)) + " GPa\n")
fprintf("Ey = " + num2str(round(Ey/10^9,3)) + " GPa\n")
fprintf("Gxy = " + num2str(round(Gxy/10^9,3)) + " GPa\n")
fprintf("vxy = " + num2str(round(vxy,5)) + "\n")
fprintf("vyx = " + num2str(round(vyx,5)) + "\n")
fprintf("=====\\n")

fprintf("Ex_Fluxural = " + num2str(round(Ex_f/10^9,3)) + " "
    GPa\n")
fprintf("Ey_Fluxural = " + num2str(round(Ey_f/10^9,3)) + " "
    GPa\n")
fprintf("Gxy_Fluxural = " + num2str(round(Gxy_f/10^9,3)) + " "
    GPa\n")
fprintf("vxy_Fluxural = " + num2str(round(vxy_f,5)) + "\n")
fprintf("vyx_Fluxural = " + num2str(round(vyx_f,5)) + "\n")
fprintf("=====\\n")

fprintf("E1 = " + num2str(round(E1/10^9,3)) + " GPa\n")
fprintf("E2 = " + num2str(round(E2/10^9,3)) + " GPa\n")
fprintf("G12 = " + num2str(round(G12/10^9,3)) + " GPa\n")
fprintf("v12 = " + num2str(round(upsilon_12,5)) + "\n")

```

A.10 cnn_damage_detection.py

```
1 import numpy as np
```



```

59         padding='same',
60         activation='relu',
61         name='conv1d_1'
62     )(inputs)
63     x = layers.BatchNormalization(name='bn_1')(x)
64     x = layers.MaxPooling1D(pool_size=4, name='maxpool_1')(x)
65     x = layers.Dropout(self.config['dropout_rate'], name='dropout_1',
66     )(x)
67
68     # Second convolutional block
69     x = layers.Conv1D(
70         filters=self.config['filters'][1],
71         kernel_size=self.config['kernel_size'][1],
72         padding='same',
73         activation='relu',
74         name='conv1d_2'
75     )(x)
76     x = layers.BatchNormalization(name='bn_2')(x)
77     x = layers.MaxPooling1D(pool_size=4, name='maxpool_2')(x)
78     x = layers.Dropout(self.config['dropout_rate'], name='dropout_2',
79     )(x)
80
81     # Third convolutional block
82     x = layers.Conv1D(
83         filters=self.config['filters'][2],
84         kernel_size=self.config['kernel_size'][2],
85         padding='same',
86         activation='relu',
87         name='conv1d_3'
88     )(x)
89     x = layers.BatchNormalization(name='bn_3')(x)
90     x = layers.MaxPooling1D(pool_size=4, name='maxpool_3')(x)
91     x = layers.Dropout(self.config['dropout_rate'], name='dropout_3',
92     )(x)
93
94     # Global pooling
95     x = layers.GlobalAveragePooling1D(name='global_avg_pool')(x)
96
97     # Dense layers
98     for i, units in enumerate(self.config['dense_units']):
99         x = layers.Dense(units, activation='relu', name=f'dense_{i+1}')(x)
100        x = layers.Dropout(self.config['dropout_rate'], name=f'dropout_dense_{i+1}')(x)
101
102    # Output layer - binary classification (damaged vs undamaged)
103    outputs = layers.Dense(1, activation='sigmoid', name='output')(x)
104
105    # Create model
106    model = models.Model(inputs=inputs, outputs=outputs, name='SHM_CNN')
107
108    # Compile model
109    model.compile(
110        optimizer=optimizers.Adam(learning_rate=self.config['learning_rate']),
111        loss='binary_crossentropy',
112        metrics=['accuracy']
113    )

```

```

111     self.model = model
112     return model
113
114
115     def preprocess_data(self, data_cell):
116         """
117             Preprocess the raw sensor data
118
119             Parameters:
120             -----
121             data_cell : list or array of samples
122                 Raw sensor data
123
124             Returns:
125             -----
126             numpy array
127                 Preprocessed data of shape (n_samples, sample_length,
128             n_sensors)
129             """
130
131         n_samples = len(data_cell)
132         processed_data = []
133         expected_shape = (self.config['sample_length'], self.config['
134             n_sensors'])
135
136
137         for i in range(n_samples):
138             # Get current sample data
139             sample = np.array(data_cell[i], dtype=float)
140
141             print(f"Sample {i} type: {type(sample)}, shape: {sample.
142             shape if hasattr(sample, 'shape') else 'N/A'}, ndim: {sample.ndim}")
143
144             # Handle different data structures
145             if sample.ndim == 1:
146                 print(f"Warning: Sample {i} is 1D with length {len(
147                     sample)}")
148                 # Try to reshape assuming flat data [t1_s1, t1_s2, ...,
149                 t1_s5, t2_s1, ...]
150                 if len(sample) >= self.config['sample_length'] * self.
151             config['n_sensors']:
152                 sample = sample[:self.config['sample_length'] * self.
153             config['n_sensors']]
154                 sample = sample.reshape(self.config['sample_length',
155             ], self.config['n_sensors'])
156             else:
157                 print(f"Error: Sample {i} length {len(sample)} too
short for {self.config['sample_length']}x{self.config['n_sensors']}")
158                 # Skip invalid sample or pad with zeros
159                 sample = np.zeros(expected_shape)
160
161             elif sample.ndim == 2:
162                 if sample.shape != expected_shape:
163                     print(f"Warning: Sample {i} shape {sample.shape}
does not match expected {expected_shape}")
164                     if sample.shape[0] >= self.config['sample_length']
165             and sample.shape[1] == self.config['n_sensors']:
166                         sample = sample[:self.config['sample_length'],
167             :]
168
169                     else:
170                         print(f"Error: Sample {i} cannot be reshaped to
{expected_shape}")
171                         sample = np.zeros(expected_shape)

```

```

158         else:
159             print(f"Error: Sample {i} has {sample.ndim} dimensions,
160                  expected 1 or 2")
160             sample = np.zeros(expected_shape)
161
162             # Verify shape
163             if sample.shape != expected_shape:
164                 print(f"Error: Sample {i} final shape {sample.shape}
164 does not match {expected_shape}")
165                 sample = np.zeros(expected_shape)
166
167             # Apply differencing
168             diff_data = np.zeros_like(sample)
169             for s in range(self.config['n_sensors']):
170                 time_series = sample[:, s]
171                 diff_series = np.diff(time_series, axis=0)
172                 diff_data[:-1, s] = diff_series
173                 diff_data[-1, s] = diff_series[-1] # Pad with last
173 value
174
175             processed_data.append(diff_data)
176
177             processed_data = np.array(processed_data)
178             print(f"Processed data shape: {processed_data.shape}")
179             return processed_data
180
181     def normalize_data(self, data, mean_values=None, std_values=None):
182         """
183             Normalize data by subtracting mean and dividing by standard
183 deviation
184
185             Parameters:
186             -----
187             data : numpy array
188                 Data to normalize
189             mean_values : numpy array, optional
190                 Mean values for each sensor (if None, calculated from data)
191             std_values : numpy array, optional
192                 Standard deviation values for each sensor (if None,
192 calculated from data)
193
194             Returns:
195             -----
196             tuple
197                 (normalized data, mean values, std values)
198             """
199
200             # If mean and std not provided, calculate from data
201             if mean_values is None or std_values is None:
202                 mean_values = np.zeros(self.config['n_sensors'])
202                 std_values = np.zeros(self.config['n_sensors'])
203
204                 # Calculate mean and std for each sensor
205                 for s in range(self.config['n_sensors']):
206                     all_values = np.concatenate([sample[:, s] for sample in
206 data])
207                     mean_values[s] = np.mean(all_values)
208                     std_values[s] = max(np.std(all_values), np.finfo(float).
208 eps) # Avoid division by zero
209
210             # Normalize each sample

```

```

211     normalized_data = []
212     for sample in data:
213         norm_sample = np.zeros_like(sample)
214         for s in range(self.config['n_sensors']):
215             norm_sample[:, s] = (sample[:, s] - mean_values[s]) /
216             std_values[s]
217             normalized_data.append(norm_sample)
218
219     return np.array(normalized_data), mean_values, std_values
220
221     def train(self, training_data, threshold_data, reference_data,
222     damaged_data):
223         """
224             Train the CNN model using the same data splitting approach as
225             the AR model
226
227             Parameters:
228             -----
229             training_data, threshold_data, reference_data, damaged_data :
230             cell arrays
231                 Data partitions
232
233             Returns:
234             -----
235             keras.callbacks.History
236                 Training history
237             """
238
239     if self.model is None:
240         self.build_model()
241
242     # Preprocess data
243     print("Preprocessing data...")
244     train_processed = self.preprocess_data(training_data)
245
246     # Normalize data
247     train_normalized, mean_values, std_values = self.normalize_data(
248     train_processed)
249
250     # Prepare validation data (using threshold data)
251     threshold_processed = self.preprocess_data(threshold_data)
252     threshold_normalized, _, _ = self.normalize_data(
253     threshold_processed, mean_values, std_values)
254
255     # Create labels (all undamaged for training and validation)
256     train_labels = np.zeros(len(train_normalized))
257     val_labels = np.zeros(len(threshold_normalized))
258
259     # Define callbacks
260     cb_list = [
261         callbacks.EarlyStopping(
262             monitor='val_loss',
263             patience=self.config['patience'],
264             restore_best_weights=True
265         ),
266         callbacks.ReduceLROnPlateau(
267             monitor='val_loss',
268             factor=0.5,
269             patience=5,
270             min_lr=1e-6
271         )
272     ]

```

```
265     ]
266
267     # Train model
268     print(f"Training model on {len(train_normalized)} samples...")
269     self.history = self.model.fit(
270         train_normalized, train_labels,
271         validation_data=(threshold_normalized, val_labels),
272         epochs=self.config['epochs'],
273         batch_size=self.config['batch_size'],
274         callbacks=cb_list,
275         verbose=1
276     )
277
278     # Store normalization parameters for later use
279     self.mean_values = mean_values
280     self.std_values = std_values
281
282     return self.history
283
284 def predict(self, test_data):
285     """
286         Make predictions on test data
287
288         Parameters:
289         -----
290         test_data : cell array
291             Test data
292
293         Returns:
294         -----
295         numpy array
296             Damage index values
297     """
298     if self.model is None:
299         raise ValueError("Model has not been trained yet.")
300
301     # Preprocess data
302     test_processed = self.preprocess_data(test_data)
303     test_normalized, _, _ = self.normalize_data(test_processed, self
304 .mean_values, self.std_values)
305
306     # Get model predictions
307     predictions = self.model.predict(test_normalized)
308
309     return predictions.flatten()
310
311 def evaluate(self, reference_data, damaged_data):
312     """
313         Evaluate the model on test data
314
315         Parameters:
316         -----
317         reference_data : cell array
318             Undamaged test data
319         damaged_data : cell array
320             Damaged test data
321
322         Returns:
323         -----
324         dict
```

```

324         Evaluation results
325     """
326
327     if self.model is None:
328         raise ValueError("Model has not been trained yet.")
329
330     # Preprocess and normalize reference data
331     ref_processed = self.preprocess_data(reference_data)
332     ref_normalized, _, _ = self.normalize_data(ref_processed, self.
333     mean_values, self.std_values)
334
335     # Preprocess and normalize damaged data
336     dam_processed = self.preprocess_data(damaged_data)
337     dam_normalized, _, _ = self.normalize_data(dam_processed, self.
338     mean_values, self.std_values)
339
340     # Get predictions
341     ref_predictions = self.model.predict(ref_normalized).flatten()
342     dam_predictions = self.model.predict(dam_normalized).flatten()
343
344     # Determine threshold using 95th percentile of reference
345     # predictions
346     detection_threshold = np.percentile(ref_predictions, 95)
347
348     # Apply threshold to get binary predictions
349     ref_binary = (ref_predictions > detection_threshold).astype(int)
350     dam_binary = (dam_predictions > detection_threshold).astype(int)
351
352     # Combine predictions and create true labels
353     all_predictions = np.concatenate([ref_binary, dam_binary])
354     true_labels = np.concatenate([np.zeros_like(ref_binary), np.
355     ones_like(dam_binary)])
356
357     # Calculate metrics
358     TP = np.sum(dam_binary == 1) # True Positives
359     FP = np.sum(ref_binary == 1) # False Positives
360     TN = np.sum(ref_binary == 0) # True Negatives
361     FN = np.sum(dam_binary == 0) # False Negatives
362
363     accuracy = (TP + TN) / (TP + FP + TN + FN)
364     sensitivity = TP / (TP + FN) if (TP + FN) > 0 else 0 # True
365     Positive Rate
366     specificity = TN / (TN + FP) if (TN + FP) > 0 else 0 # True
367     Negative Rate
368     precision = TP / (TP + FP) if (TP + FP) > 0 else 0 # Positive
369     Predictive Value
370
371     # Return results
372     return {
373         'accuracy': accuracy,
374         'sensitivity': sensitivity,
375         'specificity': specificity,
376         'precision': precision,
377         'threshold': detection_threshold,
378         'reference_scores': ref_predictions,
379         'damaged_scores': dam_predictions,
380         'predictions': all_predictions,
381         'true_labels': true_labels
382     }
383
384     def visualize_results(self, results):

```

```

377 """
378     Visualize the evaluation results
379
380     Parameters:
381     -----
382     results : dict
383         Results from evaluate method
384
385     # Get predictions and true labels
386     predictions = results['predictions']
387     true_labels = results['true_labels']
388
389     # Convert to categorical for confusion matrix
390     pred_cat = tf.keras.utils.to_categorical(predictions,
391     num_classes=2)
391     true_cat = tf.keras.utils.to_categorical(true_labels,
392     num_classes=2)
393
394     # Create figure with subplots
395     plt.figure(figsize=(18, 6))
396
397     # Plot confusion matrix
398     plt.subplot(1, 3, 1)
399     cm = confusion_matrix(true_labels, predictions)
400     sns.heatmap(cm, annot=True, fmt='d', cmap='Blues',
401                 xticklabels=['Undamaged', 'Damaged'],
402                 yticklabels=['Undamaged', 'Damaged'])
403     plt.title('Confusion Matrix')
404     plt.xlabel('Predicted')
405     plt.ylabel('True')
406
407     # Plot damage scores
408     plt.subplot(1, 3, 2)
409     ref_scores = results['reference_scores']
410     dam_scores = results['damaged_scores']
411     threshold = results['threshold']
412
413     plt.scatter(range(len(ref_scores)), ref_scores, c='blue', marker
414     ='o', alpha=0.5, label='Undamaged')
415     plt.scatter(range(len(ref_scores)), len(ref_scores) + len(
416     dam_scores), dam_scores,
417                 c='red', marker='x', alpha=0.5, label='Damaged')
418     plt.axhline(y=threshold, color='green', linestyle='--', label=
419     'Threshold')
420     plt.title('Damage Scores')
421     plt.xlabel('Sample Index')
422     plt.ylabel('Damage Score')
423     plt.legend()
424
425     # Plot ROC curve
426     plt.subplot(1, 3, 3)
427     from sklearn.metrics import roc_curve, auc
428     all_scores = np.concatenate([ref_scores, dam_scores])
429     fpr, tpr, _ = roc_curve(true_labels, all_scores)
430     roc_auc = auc(fpr, tpr)
431
432     plt.plot(fpr, tpr, color='darkorange', lw=2, label=f'ROC curve (
433     area = {roc_auc:.2f})')
434     plt.plot([0, 1], [0, 1], color='navy', lw=2, linestyle='--')
435     plt.xlim([0.0, 1.0])

```

```

431     plt.ylim([0.0, 1.05])
432     plt.xlabel('False Positive Rate')
433     plt.ylabel('True Positive Rate')
434     plt.title('Receiver Operating Characteristic')
435     plt.legend(loc="lower right")
436
437     plt.tight_layout()
438     plt.show()
439
440 # Plot training history
441 if self.history is not None:
442     plt.figure(figsize=(12, 5))
443
444     # Plot accuracy
445     plt.subplot(1, 2, 1)
446     plt.plot(self.history.history['accuracy'], label='Training')
447     plt.plot(self.history.history['val_accuracy'], label='Validation')
448     plt.title('Model Accuracy')
449     plt.xlabel('Epoch')
450     plt.ylabel('Accuracy')
451     plt.legend()
452
453     # Plot loss
454     plt.subplot(1, 2, 2)
455     plt.plot(self.history.history['loss'], label='Training')
456     plt.plot(self.history.history['val_loss'], label='Validation')
457     plt.title('Model Loss')
458     plt.xlabel('Epoch')
459     plt.ylabel('Loss')
460     plt.legend()
461
462     plt.tight_layout()
463     plt.show()
464
465 def save_model(self, filepath):
466     """Save the model to a file"""
467     if self.model is None:
468         raise ValueError("No model to save.")
469
470     # Save model
471     self.model.save(filepath)
472
473     # Save normalization parameters
474     np.savez(filepath + '_normparams.npz',
475             mean_values=self.mean_values,
476             std_values=self.std_values)
477
478 def load_model(self, filepath):
479     """Load the model from a file"""
480     # Load model
481     self.model = tf.keras.models.load_model(filepath)
482
483     # Load normalization parameters
484     normparams = np.load(filepath + '_normparams.npz')
485     self.mean_values = normparams['mean_values']
486     self.std_values = normparams['std_values']
487
488 # Function to load MATLAB data with improved debugging

```

```

489 def load_matlab_data(undamaged_file, damaged_file=None):
490     print(f"Loading {undamaged_file}...")
491     undamaged_mat = sio.loadmat(undamaged_file)
492     field_names = [k for k in undamaged_mat.keys() if not k.startswith('__')]
493     print(f"Available fields in {undamaged_file}: {field_names}")
494
495     if 'extracted_data' not in undamaged_mat:
496         raise ValueError(f"'extracted_data' not found in {undamaged_file}. Available fields: {field_names}")
497
498     undamaged_data = undamaged_mat['extracted_data']
499     print(f"Undamaged data type: {type(undamaged_data)}, shape: {undamaged_data.shape}")
500
501     # Handle nested structure
502     if undamaged_data.ndim == 2 and undamaged_data.shape[0] == 1:
503         undamaged_data = undamaged_data[0] # Extract 1D array of samples
504     elif undamaged_data.ndim != 1:
505         raise ValueError(f"Unexpected undamaged_data shape: {undamaged_data.shape}")
506
507     # Verify first sample
508     if len(undamaged_data) > 0:
509         first_sample = undamaged_data[0]
510         if isinstance(first_sample, np.ndarray) and first_sample.size == 1:
511             first_sample = first_sample.item() # Unwrap scalar array
512             print(f"First undamaged sample type: {type(first_sample)}, shape: {first_sample.shape if hasattr(first_sample, 'shape') else 'N/A'}")
513
514     damaged_data = None
515     if damaged_file and os.path.exists(damaged_file):
516         print(f"Loading {damaged_file}...")
517         damaged_mat = sio.loadmat(damaged_file)
518         field_names = [k for k in damaged_mat.keys() if not k.startswith('__')]
519         print(f"Available fields in {damaged_file}: {field_names}")
520
521         if 'extracted_data' not in damaged_mat:
522             raise ValueError(f"'extracted_data' not found in {damaged_file}. Available fields: {field_names}")
523
524         damaged_data = damaged_mat['extracted_data']
525         print(f"Damaged data type: {type(damaged_data)}, shape: {damaged_data.shape}")
526
527         # Handle nested structure
528         if damaged_data.ndim == 2 and damaged_data.shape[0] == 1:
529             damaged_data = damaged_data[0] # Extract 1D array of samples
530         elif damaged_data.ndim != 1:
531             raise ValueError(f"Unexpected damaged_data shape: {damaged_data.shape}")
532
533         # Verify first sample
534         if len(damaged_data) > 0:
535             first_sample = damaged_data[0]
536             if isinstance(first_sample, np.ndarray) and first_sample.

```

```

    size == 1:
        first_sample = first_sample.item()
        print(f"First damaged sample type: {type(first_sample)},
shape: {first_sample.shape if hasattr(first_sample, 'shape') else 'N/
A'}")
    return undamaged_data, damaged_data
541
542 # Main function to run the CNN-based SHM
543 def run_cnn_shm(undamaged_data, damaged_data=None):
544     # Check data
545     print("\nVerifying data format...")
546     if undamaged_data.size == 0:
547         raise ValueError("Undamaged data is empty")
548
549     # Extract samples
550     undamaged_samples = [item if isinstance(item, np.ndarray) and item.
ndim == 2 else np.zeros((25600, 5)) for item in undamaged_data]
551     damaged_samples = [item if isinstance(item, np.ndarray) and item.
ndim == 2 else np.zeros((25600, 5)) for item in damaged_data] if
damaged_data is not None else None
552
553     print(f"Extracted {len(undamaged_samples)} undamaged samples")
554     if damaged_samples:
555         print(f"Extracted {len(damaged_samples)} damaged samples")
556
557     # Data splitting ratios
558     train_ratio = 0.6
559     reference_ratio = 0.1
560     threshold_ratio = 0.3
561
562     # Get data counts
563     n_undamaged = len(undamaged_samples)
564     n_damaged = len(damaged_samples) if damaged_samples else 0
565
566     # Calculate split indices
567     n_train = int(train_ratio * n_undamaged)
568     n_reference = int(reference_ratio * n_undamaged)
569     n_threshold = int(threshold_ratio * n_undamaged)
570
571     # Ensure non-zero splits
572     if n_train == 0 or n_threshold == 0 or n_reference == 0:
573         print("Warning: Insufficient undamaged samples for splitting.
Adjusting ratios.")
574         n_train = max(1, int(0.7 * n_undamaged))
575         n_reference = max(1, int(0.15 * n_undamaged))
576         n_threshold = n_undamaged - n_train - n_reference
577
578     # Create data partitions
579     training_data = undamaged_samples[:n_train]
580     threshold_data = undamaged_samples[n_train:n_train+n_threshold]
581     reference_data = undamaged_samples[n_train+n_threshold:]
582
583     # Balance damaged data for testing
584     if damaged_samples:
585         n_damaged_test = min(n_damaged, 50) # Use 50 damaged samples
586         damaged_samples = damaged_samples[:n_damaged_test]
587         print(f"Using {n_damaged_test} damaged samples for testing")
588
589     print(f"Data partitioning complete:")

```

```

590     print(f" - Training set: {len(training_data)} samples (all
591         undamaged)")
592     print(f" - Threshold set: {len(threshold_data)} samples (all
593         undamaged)")
594     print(f" - Reference set: {len(reference_data)} samples (all
595         undamaged)")
596     print(f" - Damaged set: {len(damaged_samples)} if damaged_samples
597         else 0} samples")
598
599
600
601
602
603
604     # Create and configure the model
605     detector = SHM_CNN_Detector(config={
606         'n_sensors': 5,
607         'sample_length': 25600,
608         'filters': [32, 64, 128],
609         'kernel_size': [64, 32, 16],
610         'epochs': 50
611     })
612
613
614     # Build model
615     detector.build_model()
616     detector.model.summary()
617
618     # Train model
619     history = detector.train(training_data, threshold_data,
620         reference_data, damaged_samples)
621
622     # Evaluate model
623     results = detector.evaluate(reference_data, damaged_samples)
624
625     # Print results
626     print("\nDetection Performance:")
627     print(f" - Accuracy: {results['accuracy']*100:.2f}%")
628     print(f" - Sensitivity (TPR): {results['sensitivity']*100:.2f}%")
629     print(f" - Specificity (TNR): {results['specificity']*100:.2f}%")
630     print(f" - Precision (PPV): {results['precision']*100:.2f}%")
631
632     # Visualize results
633     detector.visualize_results(results)
634
635     # Save model
636     detector.save_model('shm_cnn_model')
637
638     return detector, results
639
640
641
642
643
644
645
646
647
648
649
650
651
652
653
654
655
656
657
658
659
660
661
662
663
664
665
666
667
668
669
670
671
672
673
674
675
676
677
678
679
680
681
682
683
684
685
686
687
688
689
690
691
692
693
694
695
696
697
698
699
700
701
702
703
704
705
706
707
708
709
710
711
712
713
714
715
716
717
718
719
720
721
722
723
724
725
726
727
728
729
730
731
732
733
734
735
736
737
738
739
740
741
742
743
744
745
746
747
748
749
750
751
752
753
754
755
756
757
758
759
760
761
762
763
764
765
766
767
768
769
770
771
772
773
774
775
776
777
778
779
780
781
782
783
784
785
786
787
788
789
790
791
792
793
794
795
796
797
798
799
800
801
802
803
804
805
806
807
808
809
810
811
812
813
814
815
816
817
818
819
820
821
822
823
824
825
826
827
828
829
830
831
832
833
834
835
836
837
838
839
840
841
842
843
844
845
846
847
848
849
850
851
852
853
854
855
856
857
858
859
860
861
862
863
864
865
866
867
868
869
870
871
872
873
874
875
876
877
878
879
880
881
882
883
884
885
886
887
888
889
890
891
892
893
894
895
896
897
898
899
900
901
902
903
904
905
906
907
908
909
910
911
912
913
914
915
916
917
918
919
920
921
922
923
924
925
926
927
928
929
930
931
932
933
934
935
936
937
938
939
940
941
942
943
944
945
946
947
948
949
950
951
952
953
954
955
956
957
958
959
960
961
962
963
964
965
966
967
968
969
970
971
972
973
974
975
976
977
978
979
980
981
982
983
984
985
986
987
988
989
990
991
992
993
994
995
996
997
998
999
999
1000
1000
1001
1002
1003
1004
1005
1006
1007
1008
1009
1009
1010
1011
1012
1013
1014
1015
1016
1017
1018
1019
1019
1020
1021
1022
1023
1024
1025
1026
1027
1028
1029
1029
1030
1031
1032
1033
1034
1035
1036
1037
1038
1039
1039
1040
1041
1042
1043
1044
1045
1046
1047
1048
1049
1049
1050
1051
1052
1053
1054
1055
1056
1057
1058
1059
1059
1060
1061
1062
1063
1064
1065
1066
1067
1068
1069
1069
1070
1071
1072
1073
1074
1075
1076
1077
1078
1079
1079
1080
1081
1082
1083
1084
1085
1086
1087
1088
1089
1089
1090
1091
1092
1093
1094
1095
1096
1097
1098
1099
1099
1100
1101
1102
1103
1104
1105
1106
1107
1108
1109
1109
1110
1111
1112
1113
1114
1115
1116
1117
1118
1119
1119
1120
1121
1122
1123
1124
1125
1126
1127
1128
1129
1129
1130
1131
1132
1133
1134
1135
1136
1137
1138
1139
1139
1140
1141
1142
1143
1144
1145
1146
1147
1148
1149
1149
1150
1151
1152
1153
1154
1155
1156
1157
1158
1159
1159
1160
1161
1162
1163
1164
1165
1166
1167
1168
1169
1169
1170
1171
1172
1173
1174
1175
1176
1177
1178
1179
1179
1180
1181
1182
1183
1184
1185
1186
1187
1188
1189
1189
1190
1191
1192
1193
1194
1195
1196
1197
1197
1198
1199
1199
1200
1201
1202
1203
1204
1205
1206
1207
1208
1209
1209
1210
1211
1212
1213
1214
1215
1216
1217
1218
1219
1219
1220
1221
1222
1223
1224
1225
1226
1227
1228
1229
1229
1230
1231
1232
1233
1234
1235
1236
1237
1238
1239
1239
1240
1241
1242
1243
1244
1245
1246
1247
1248
1249
1249
1250
1251
1252
1253
1254
1255
1256
1257
1258
1259
1259
1260
1261
1262
1263
1264
1265
1266
1267
1268
1269
1269
1270
1271
1272
1273
1274
1275
1276
1277
1278
1279
1279
1280
1281
1282
1283
1284
1285
1286
1287
1288
1289
1289
1290
1291
1292
1293
1294
1295
1296
1297
1297
1298
1299
1299
1300
1301
1302
1303
1304
1305
1306
1307
1308
1309
1309
1310
1311
1312
1313
1314
1315
1316
1317
1318
1319
1319
1320
1321
1322
1323
1324
1325
1326
1327
1328
1329
1329
1330
1331
1332
1333
1334
1335
1336
1337
1338
1339
1339
1340
1341
1342
1343
1344
1345
1346
1347
1348
1349
1349
1350
1351
1352
1353
1354
1355
1356
1357
1358
1359
1359
1360
1361
1362
1363
1364
1365
1366
1367
1368
1369
1369
1370
1371
1372
1373
1374
1375
1376
1377
1378
1379
1379
1380
1381
1382
1383
1384
1385
1386
1387
1388
1388
1389
1390
1391
1392
1393
1394
1395
1396
1397
1397
1398
1399
1399
1400
1401
1402
1403
1404
1405
1406
1407
1408
1408
1409
1410
1411
1412
1413
1414
1415
1416
1417
1418
1419
1419
1420
1421
1422
1423
1424
1425
1426
1427
1428
1429
1429
1430
1431
1432
1433
1434
1435
1436
1437
1438
1439
1439
1440
1441
1442
1443
1444
1445
1446
1447
1448
1449
1449
1450
1451
1452
1453
1454
1455
1456
1457
1458
1459
1459
1460
1461
1462
1463
1464
1465
1466
1467
1468
1469
1469
1470
1471
1472
1473
1474
1475
1476
1477
1478
1479
1479
1480
1481
1482
1483
1484
1485
1486
1487
1488
1489
1489
1490
1491
1492
1493
1494
1495
1496
1497
1497
1498
1499
1499
1500
1501
1502
1503
1504
1505
1506
1507
1508
1508
1509
1510
1511
1512
1513
1514
1515
1516
1517
1518
1519
1519
1520
1521
1522
1523
1524
1525
1526
1527
1528
1529
1529
1530
1531
1532
1533
1534
1535
1536
1537
1538
1539
1539
1540
1541
1542
1543
1544
1545
1546
1547
1548
1549
1549
1550
1551
1552
1553
1554
1555
1556
1557
1558
1559
1559
1560
1561
1562
1563
1564
1565
1566
1567
1568
1569
1569
1570
1571
1572
1573
1574
1575
1576
1577
1578
1579
1579
1580
1581
1582
1583
1584
1585
1586
1587
1588
1588
1589
1590
1591
1592
1593
1594
1595
1596
1597
1597
1598
1599
1599
1600
1601
1602
1603
1604
1605
1606
1607
1608
1608
1609
1610
1611
1612
1613
1614
1615
1616
1617
1618
1619
1619
1620
1621
1622
1623
1624
1625
1626
1627
1628
1629
1629
1630
1631
1632
1633
1634
1635
1636
1637
1638
1639
1639
1640
1641
1642
1643
1644
1645
1646
1647
1648
1649
1649
1650
1651
1652
1653
1654
1655
1656
1657
1658
1659
1659
1660
1661
1662
1663
1664
1665
1666
1667
1668
1669
1669
1670
1671
1672
1673
1674
1675
1676
1677
1678
1679
1679
1680
1681
1682
1683
1684
1685
1686
1687
1688
1688
1689
1690
1691
1692
1693
1694
1695
1696
1697
1697
1698
1699
1699
1700
1701
1702
1703
1704
1705
1706
1707
1708
1708
1709
1710
1711
1712
1713
1714
1715
1716
1717
1718
1719
1719
1720
1721
1722
1723
1724
1725
1726
1727
1728
1729
1729
1730
1731
1732
1733
1734
1735
1736
1737
1738
1739
1739
1740
1741
1742
1743
1744
1745
1746
1747
1748
1749
1749
1750
1751
1752
1753
1754
1755
1756
1757
1758
1759
1759
1760
1761
1762
1763
1764
1765
1766
1767
1768
1769
1769
1770
1771
1772
1773
1774
1775
1776
1777
1778
1779
1779
1780
1781
1782
1783
1784
1785
1786
1787
1788
1788
1789
1790
1791
1792
1793
1794
1795
1796
1797
1797
1798
1799
1799
1800
1801
1802
1803
1804
1805
1806
1807
1808
1808
1809
1810
1811
1812
1813
1814
1815
1816
1817
1818
1819
1819
1820
1821
1822
1823
1824
1825
1826
1827
1828
1829
1829
1830
1831
1832
1833
1834
1835
1836
1837
1838
1838
1839
1840
1841
1842
1843
1844
1845
1846
1847
1848
1848
1849
1850
1851
1852
1853
1854
1855
1856
1857
1858
1859
1859
1860
1861
1862
1863
1864
1865
1866
1867
1868
1869
1869
1870
1871
1872
1873
1874
1875
1876
1877
1878
1879
1879
1880
1881
1882
1883
1884
1885
1886
1887
1888
1888
1889
1890
1891
1892
1893
1894
1895
1896
1897
1897
1898
1899
1899
1900
1901
1902
1903
1904
1905
1906
1907
1908
1908
1909
1910
1911
1912
1913
1914
1915
1916
1917
1918
1919
1919
1920
1921
1922
1923
1924
1925
1926
1927
1928
1929
1929
1930
1931
1932
1933
1934
1935
1936
1937
1938
1938
1939
1940
1941
1942
1943
1944
1945
1946
1947
1948
1948
1949
1950
1951
1952
1953
1954
1955
1956
1957
1958
1959
1959
1960
1961
1962
1963
1964
1965
1966
1967
1968
1969
1969
1970
1971
1972
1973
1974
1975
1976
1977
1978
1979
1979
1980
1981
1982
1983
1984
1985
1986
1987
1988
1988
1989
1990
1991
1992
1993
1994
1995
1996
1997
1997
1998
1999
1999
2000
2001
2002
2003
2004
2005
2006
2007
2008
2009
2009
2010
2011
2012
2013
2014
2015
2016
2017
2018
2019
2019
2020
2021
2022
2023
2024
2025
2026
2027
2028
2029
2029
2030
2031
2032
2033
2034
2035
2036
2037
2038
2038
2039
2040
2041
2042
2043
2044
2045
2046
2047
2048
2048
2049
2050
2051
2052
2053
2054
2055
2056
2057
2058
2059
2059
2060
2061
2062
2063
2064
2065
2066
2067
2068
2069
2069
2070
2071
2072
2073
2074
2075
2076
2077
2078
2079
2079
2080
2081
2082
2083
2084
2085
2086
2087
2088
2088
2089
2090
2091
2092
2093
2094
2095
2096
2097
2097
2098
2099
2099
2100
2101
2102
2103
2104
2105
2106
2107
2108
2108
2109
2110
2111
2112
2113
2114
2115
2116
2117
2118
2119
2119
2120
2121
2122
2123
2124
2125
2126
2127
2128
2129
2129
2130
2131
2132
2133
2134
2135
2136
2137
2138
2138
2139
2140
2141
2142
2143
2144
2145
2146
2147
2148
2148
2149
2150
2151
2152
2153
2154
2155
2156
2157
2158
2159
2159
2160
2161
2162
2163
2164
2165
2166
2167
2168
2169
2169
2170
2171
2172
2173
2174
2175
2176
2177
2178
2179
2179
2180
2181
2182
2183
2184
2185
2186
2187
2188
2188
2189
2190
2191
2192
2193
2194
2195
2196
2197
2197
2198
2199
2199
2200
2201
2202
2203
2204
2205
2206
2207
2208
2208
2209
2210
2211
2212
2213
2214
2215
2216
2217
2218
2219
2219
2220
2221
2222
2223
2224
2225
2226
2227
2228
2229
2229
2230
2231
2232
2233
2234
2235
2236
2237
2238
2238
2239
2240
2241
2242
2243
2244
2245
2246
2247
2248
2248
2249
2250
2251
2252
2253
2254
2255
2256
2257
2258
2259
2259
2260
2261
2262
2263
2264
2265
2266
2267
2268
2269
2269
2270
2271
2272
2273
2274
2275
2276
2277
2278
2279
2279
2280
2281
2282
2283
2284
2285
2286
2287
2288
2288
2289
2290
2291
2292
2293
2294
2295
2296
2297
2297
2298
2299
2299
2300
2301
2302
2303
2304
2305
2306
2307
2308
2308
2309
2310
2311
2312
2313
2314
2315
2316
2317
2318
2319
2319
2320
2321
2322
2323
2324
2325
2326
2327
2328
2329
2329
2330
2331
2332
2333
2334
2335
2336
2337
2338
2338
2339
2340
2341
2342
2343
2344
2345
2346
2347
2348
2348
2349
2350
2351
2352
2353
2354
2355
2356
2357
2358
2359
2359
2360
2361
2362
2363
2364
2365
2366
2367
2368
2369
2369
2370
2371
2372
2373
2374
2375
2376
2377
2378
2379
2379
2380
2381
2382
2383
2384
2385
2386
2387
2388
2388
2389
2390
2391
2392
2393
2394
2395
2396
2397
2397
2398
2399
2399
2400
2401
2402
2403
2404
2405
2406
2407
2408
2408
2409
2410
2411
2412
2413
2414
2415
2416
2417
2418
2419
2419
2420
2421
2422
2423
2424
2425
2426
2427
2428
2429
2429
2430
2431
2432
2433
2434
2435
2436
2437
2438
2438
2439
2440
2441
2442
2443
2444
2445
2446
2447
2448
2448
2449
2450
2451
2452
2453
2454
2455
2456
2457
2458
2459
2459
2460
2461
2462
2463
2464
2465
2466
2467
2468
2469
2469
2470
2471
2472
2473
2474
2475
2476
2477
2478
2479
2479
2480
2481
2482
2483
2484
2485
2486
2487
2488
2488
2489
2490
2491
2492
2493
2494
2495
2496
2496
2497
2498
2499
2499
2500
2501
2502
2503
2504
2505
2506
2507
2508
2508
2509
2510
2511
2512
2513
2514
2515
2516
2517
2518
2519
2519
2520
2521
2522
2523
2524
2525
2526
2527
2528
2529
2529
2530
2531
2532
2533
2534
2535
2536
2537
2538
2538
2539
2540
2541
2542
2543
2544
2545
2546
2547
2548
2548
2549
2550
2551
2552
2553
2554
2555
2556
2557
2558
2559
2559
2560
2561
2562
2563
2564
2565
2566
2567
2568
2569
2569
2570
2571
2572
2573
2574
2575
2576
2577
2578
2579
2579
2580
2581
2582
2583
2584
2585
2586
2587
2588
2588
2589
2590
2591
2592
2593
2594
2595
2596
2597
2597
2598
2599
2599
2600
2601
2602
2603
2604
2605
2606
2607
2608
2608
2609
2610
2611
2612
2613
2614
2615
2616
2617
2618
2619
2619
2620
2621
2622
2623
2624
2625
2626
2627
2628
2629
2629
2630
2631
2632
2633
2634
2635
2636
2637
2638
2639
2639
2640
2
```

```
640     detector, results = run_cnn_shm(undamaged_data, damaged_data)
641
642     except Exception as e:
643         import traceback
644         print(f"Error: {e}")
645         print("\nDetailed traceback:")
646         traceback.print_exc()
```

B Technical Drawings

This appendix contains the technical drawings referenced in Chapter 6, including T_01_01 through T_03_02, which detail the specifications for the CFRP laminates, aluminum honeycomb core, smart layer, and final sandwich assembly.

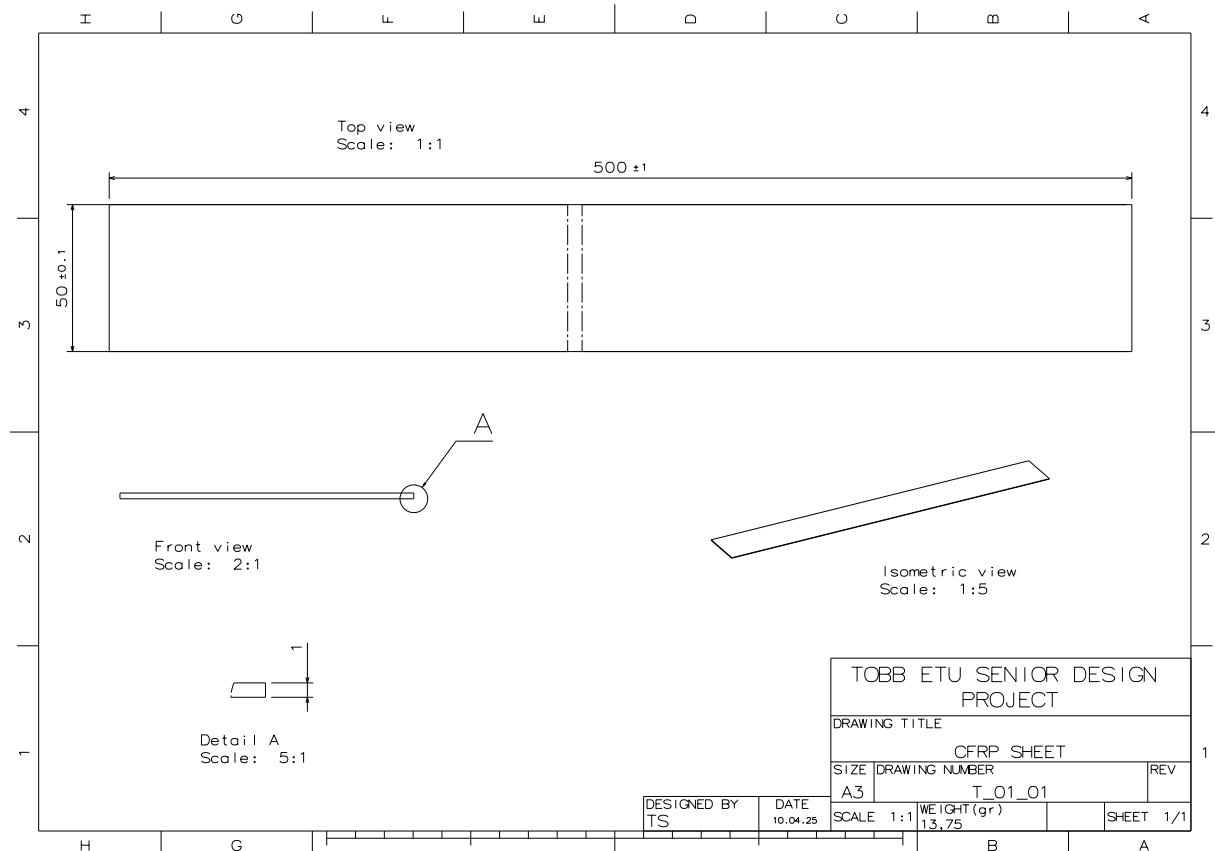


Figure B.1: Technical Drawing T_01_01: Dimensions of CFRP Laminates (500 mm × 50 mm).

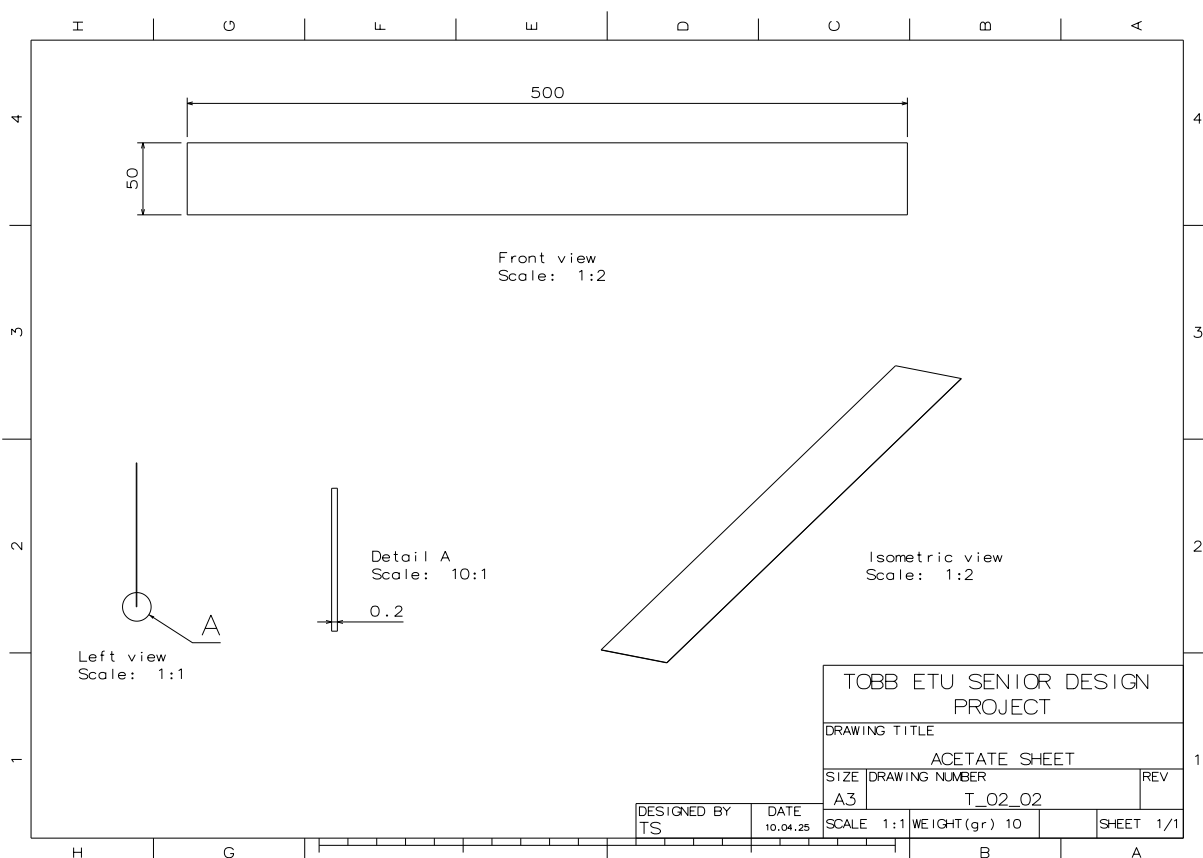


Figure B.2: Technical Drawing T_01_02: Specifications for the Acetate Sheet Used as the Base Substrate for the Flex PCB.

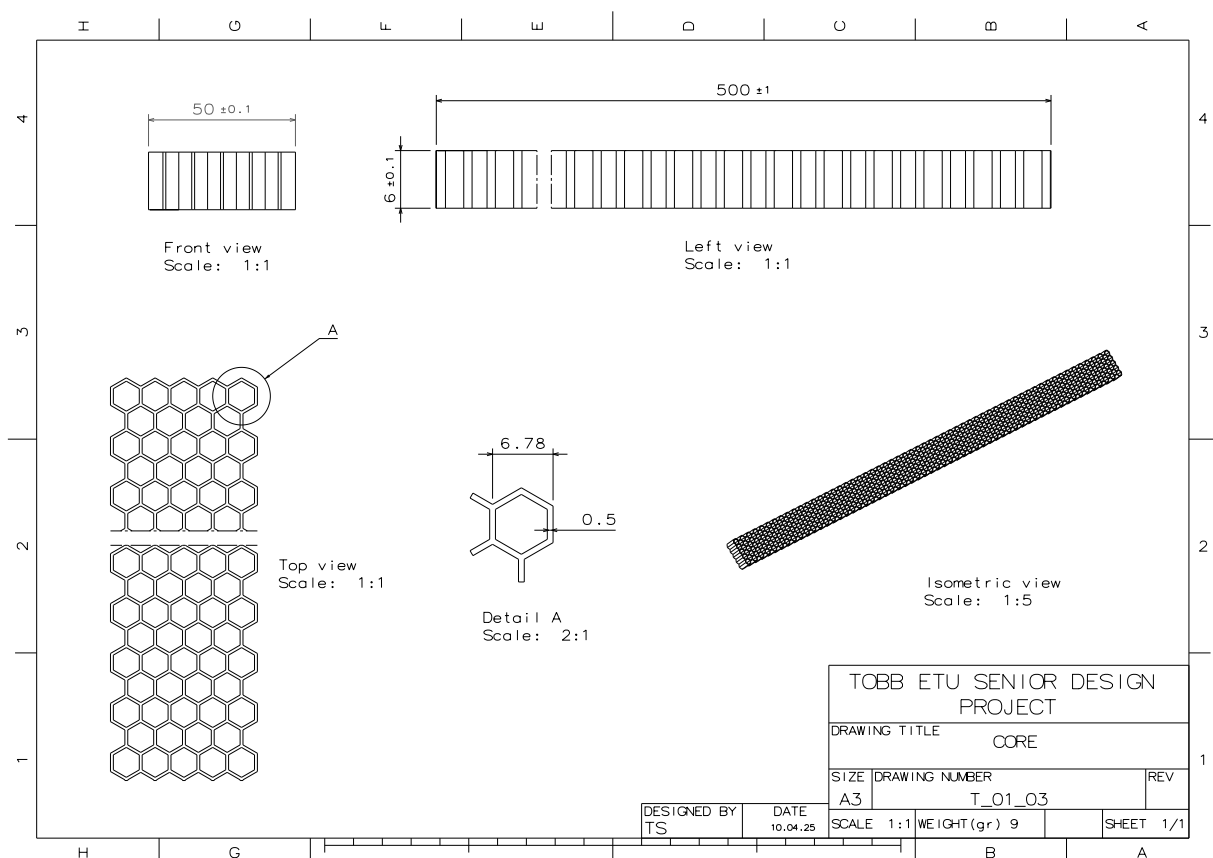


Figure B.3: Technical Drawing T_01_03: Specifications for the Aluminum Honeycomb Core Used in the Sandwich Structure.

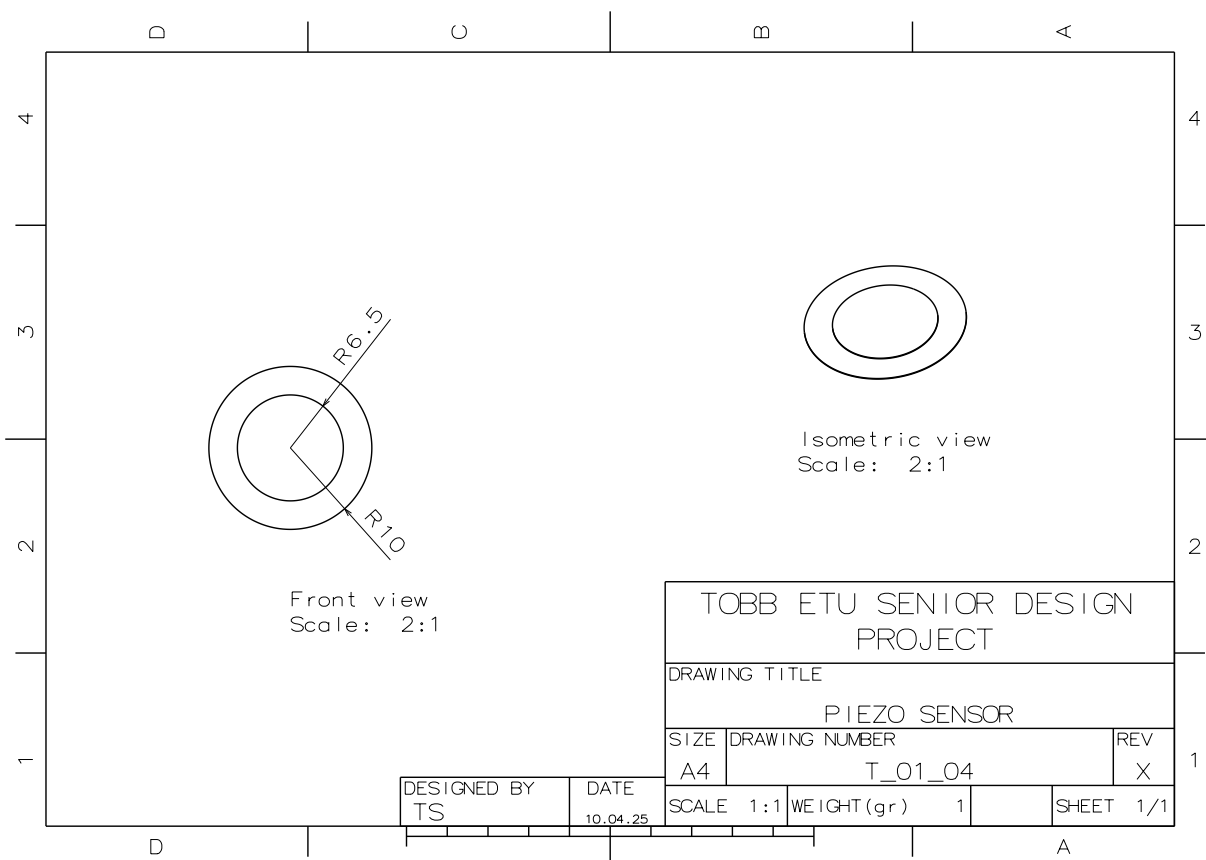


Figure B.4: Technical Drawing T_01_04: Details of the Piezoelectric Sensors Used in the Smart Layer.

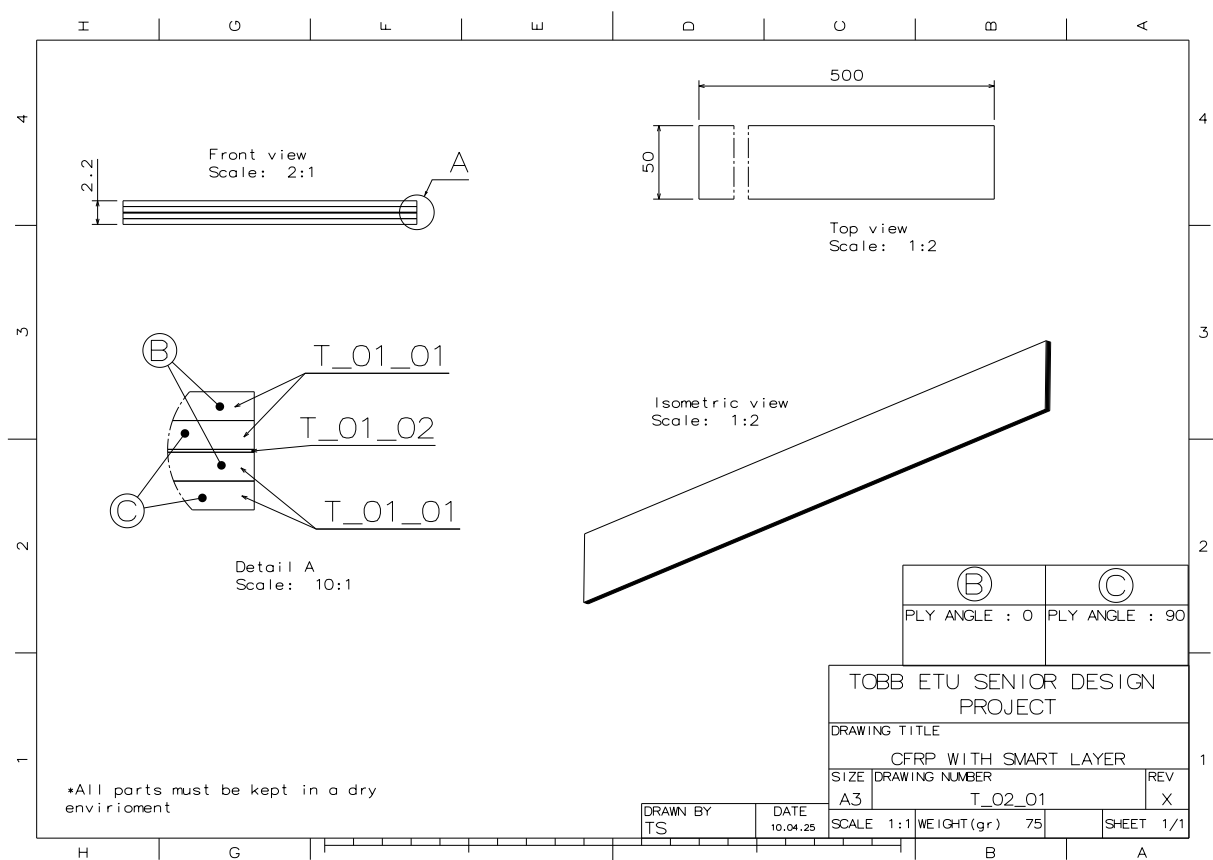


Figure B.5: Technical Drawing T_02_01: CFRP Face Sheet with Integrated Smart Layer (Top Layer of Sandwich Structure).

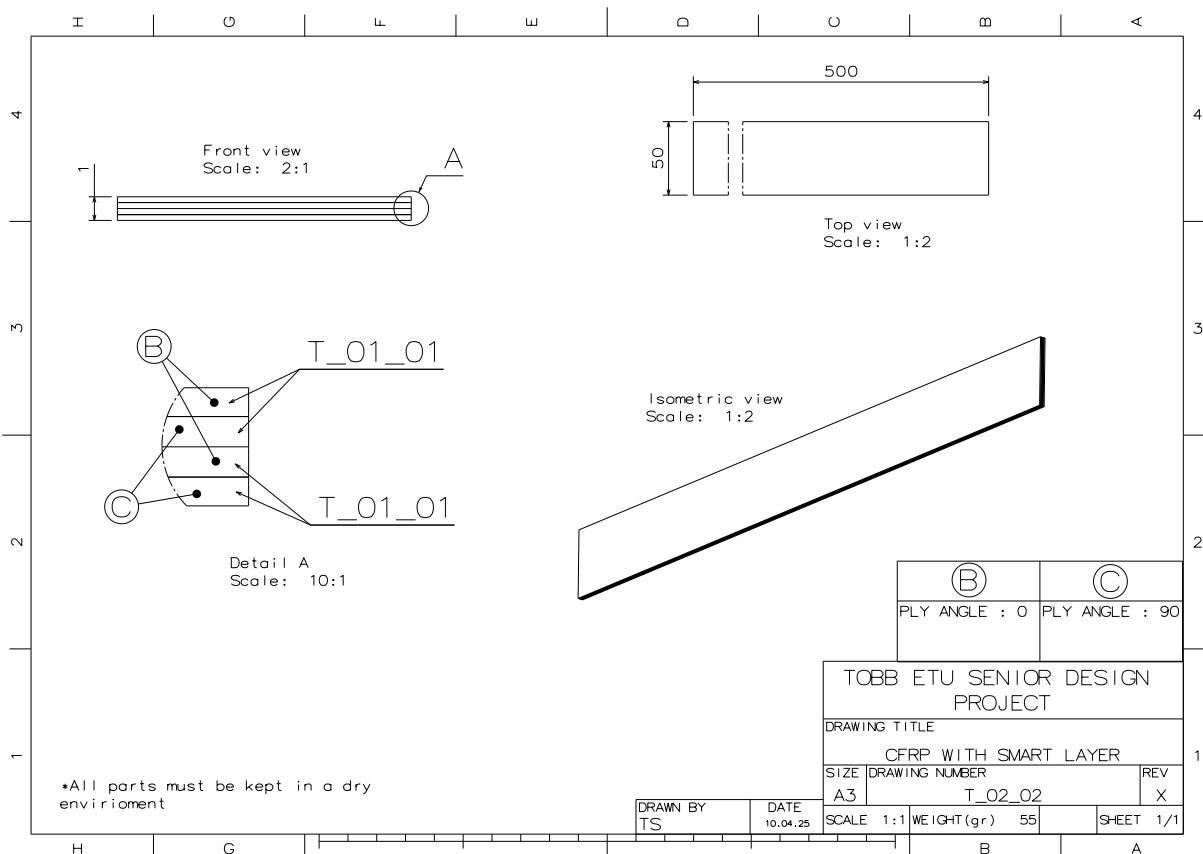


Figure B.6: Technical Drawing T_02_02: CFRP Face Sheet with Integrated Smart Layer (Bottom Layer of Sandwich Structure).

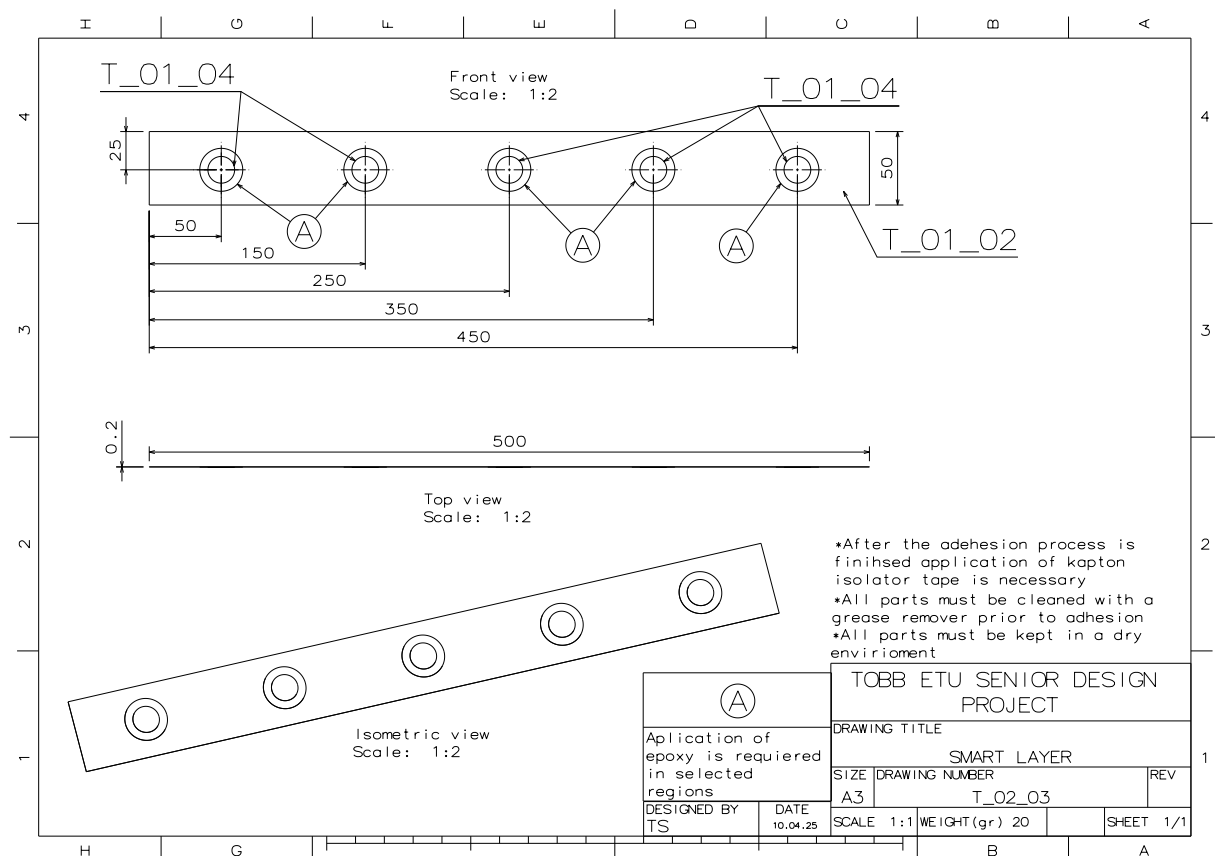


Figure B.7: Technical Drawing T_02_03: Layout of the Smart Layer (Flex PCB with Mounted Sensors).

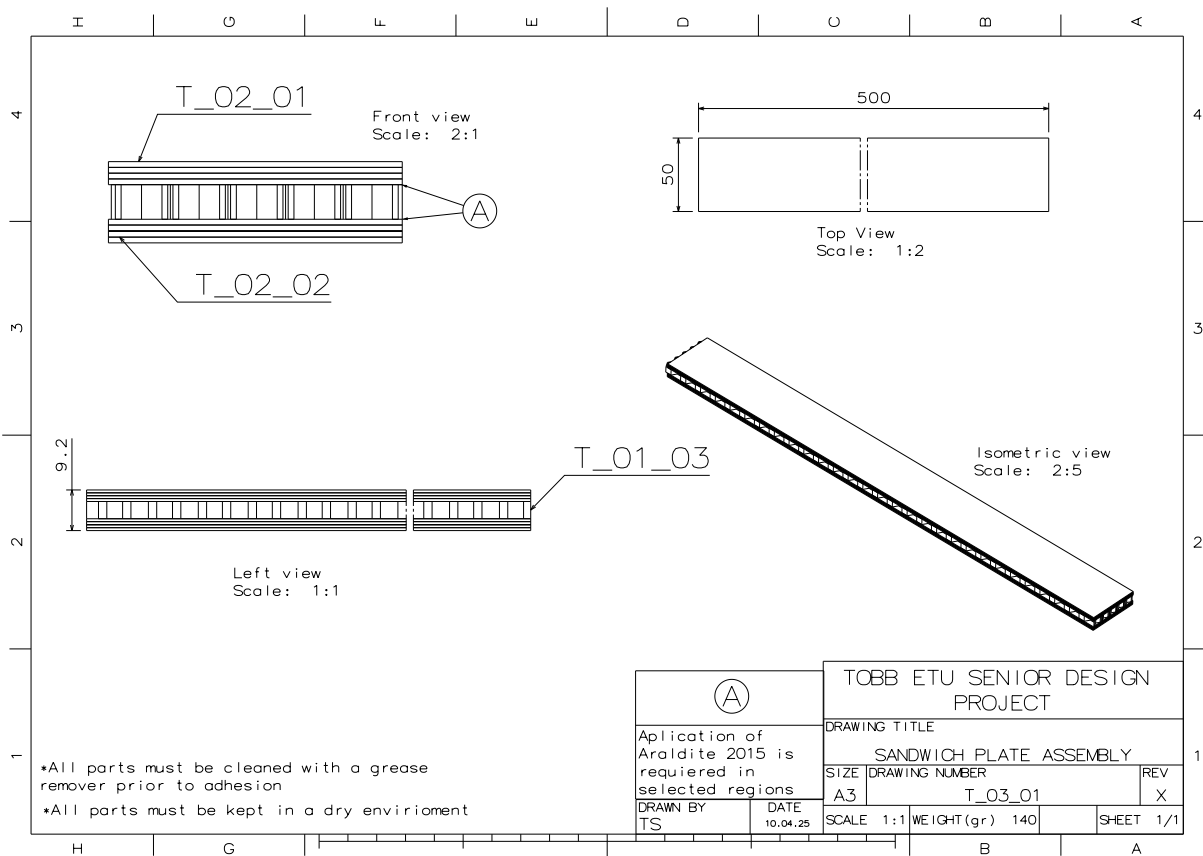


Figure B.8: Technical Drawing T_03_01: Final Assembly of the Sensor-Integrated Sandwich Structure (CFRP Face Sheets, Honeycomb Core, and Smart Layer).

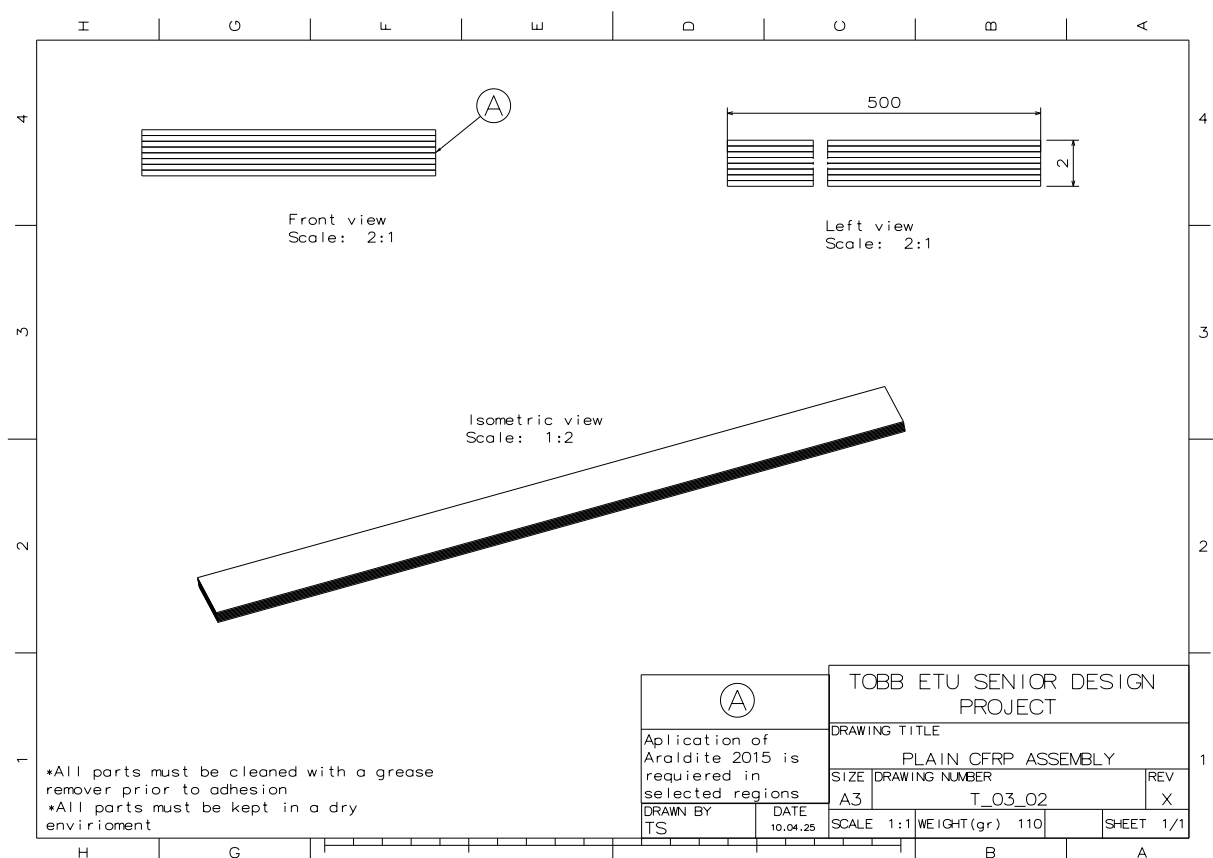


Figure B.9: Technical Drawing T_03_02: Final Assembly of the Plain CFRP Structure (Without Smart Layer).

C FEM Mode Shapes

This appendix contains the mode shape figures illustrating the deformation patterns for the first four bending modes of the sandwich composite beam obtained from the FEM analysis in Abaqus.

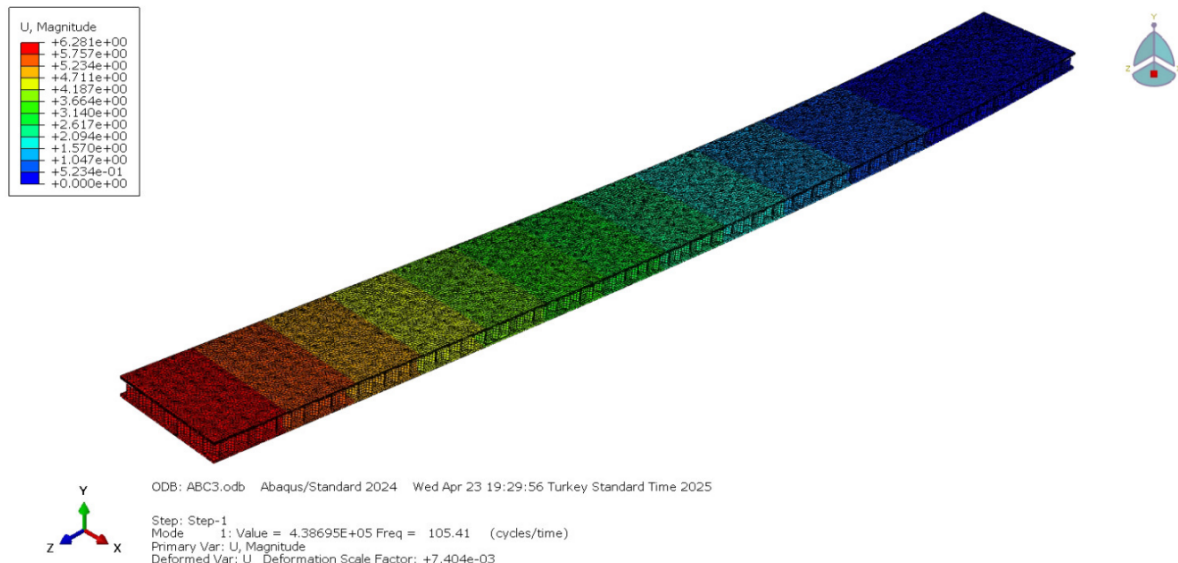


Figure C.1: First mode shape of the sandwich composite beam.

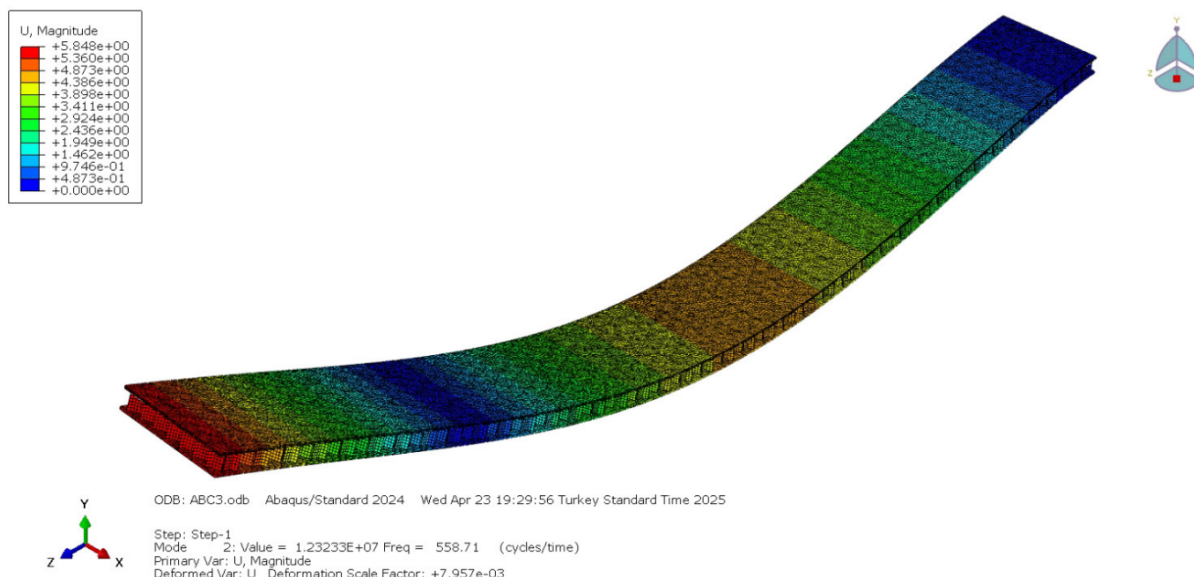


Figure C.2: Second mode shape of the sandwich composite beam.

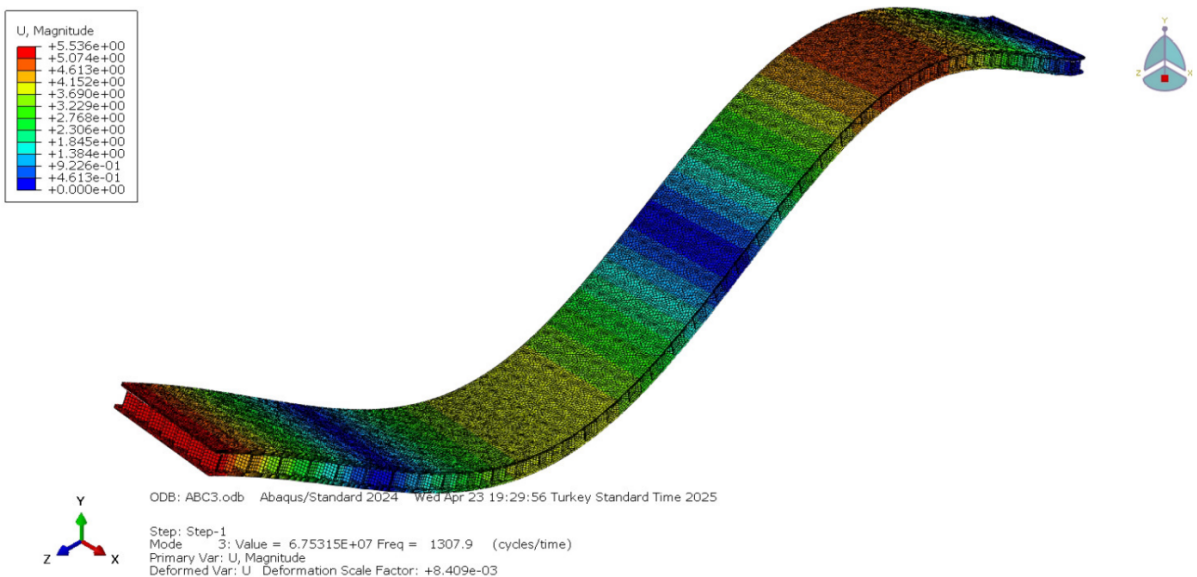


Figure C.3: Third mode shape of the sandwich composite beam.

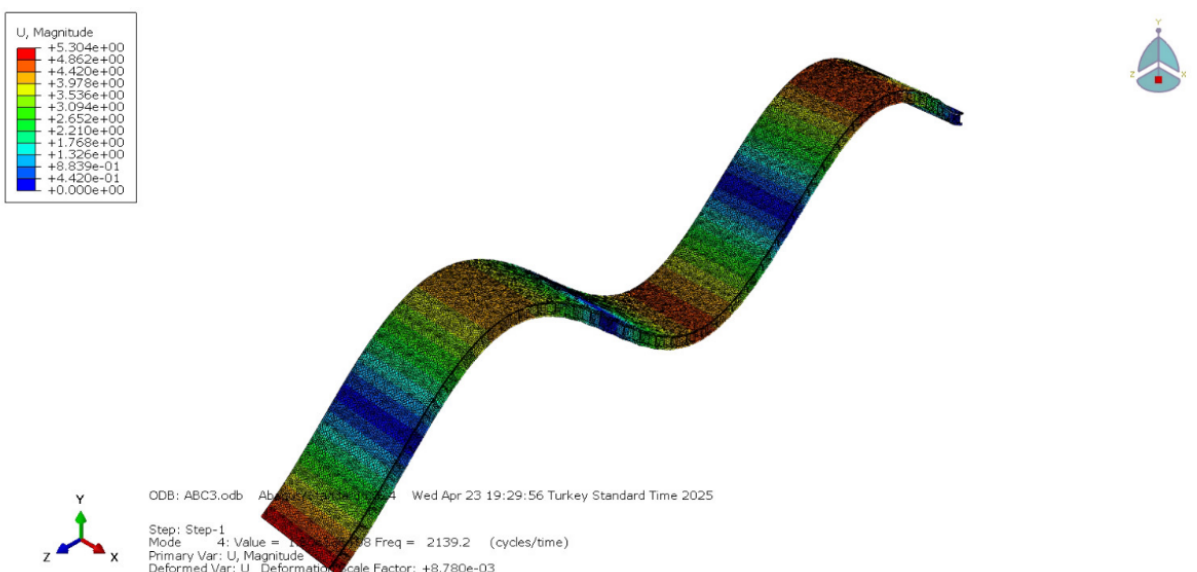


Figure C.4: Fourth mode shape of the sandwich composite beam.